Université de Paris

Département de Physique
École normale supérieure

Université de Paris

Ecole doctorale 564 : Physique en île de France
Laboratoire de physique de l'Ecole Normale Supérieure (LPENS)

Kinetic locking and nanometric monitoring of the extension of nucleic acids with high-resolution magnetic tweezers.

THESE DE DOCTORAT

de

PHYSIQUE

Présentée par :

Martin RIEU

Soutenue publiquement le 15 mars 2021 devant un jury composé de :

Jean-Louis Mergny	Directeur de recherche	Ecole polytechnique	Président
Nynke Dekker	Professeure	Université de technologie de Delft	Rapportrice
Laurent Cognet	Directeur de recherche	Université de Bordeaux	Rapporteur
Michelle Wang	Professeure	Université Cornell	Examinatrice
Felix Ritort	Professeur	Université de Barcelone	Examinateur
Vincent Croquette	Directeur de recherche	Ecole Normale Supérieure	Directeur de thèse
Jean-François Allemand	Professeur	Ecole Normale Supérieure	Co-directeur de thèse

Titre : Verrouillage cinétique et suivi nanométrique de l'extension d'acides nucléiques au moyen de pinces magnétiques super-résolues.

Résumé :

Les pinces magnétiques constituent l'une des techniques utilisées pour manipuler des molécules biologiques uniques. La micromanipulation de ces molécules permet en particulier d'étudier leurs propriétés thermodynamiques ainsi que leur interaction avec les protéines impliquées dans leur réplication et leur traduction. Ces données sont obtenues en mesurant les changements d'extension d'acides nuclétiques accrochées entre une bille magnétique et une surface fonctionnalisée. Le suivi optique de la position en 3D de la bille magnétique permet de mesurer ces changements. Jusqu'à présent, la limite de résolution de ce suivi se situe autour de 2 nanomètres. Ce travail introduit une technique de superrésolution optique, la stéréo-interférométrie en fond noir, qui permet d'augmenter significativement la résolution optique du suivi et d'atteindre des échelles sous-nanométriques. Nous allons présenter des applications de cette nouvelle résolution à l'étude de la cinétique d'hybridisation d'oligonucléotides courts ainsi qu'à l'étude des interactions entre hélicases et acides nucléiques. Nous allons ensuite décrire comment les couplages hydrodynamiques près de la surface induisent une diminution drastique de la résolution spatio-temporelle de notre appareil malgré l'amélioration de la résolution optique. Enfin, nous allons introduire une nouvelle méthode basée sur ces pinces magnétiques superrésolues, que nous appelons verrouillage cinétique : en utilisant une épingle à cheveux d'acides nucléiques fluctuant rapidement, elle permet la détection d'évènements d'accrochage qui ne mettent en jeu aucun changement mesurable d'extension.

Mots clefs:

Pinces magnétiques, molécule unique, acides nucléiques, biophysique, spectroscopie de force, superrésolution, suivi 3D, hélicases, verrouillage cinétique, stéréoscopie, interférométrie

Title: Kinetic locking and nanometric monitoring of the extension of nucleic acids with high-resolution magnetic tweezers.

Abstract:

Magnetic tweezers (MT) are one of the techniques used to micromanipulate biomolecules. In particular, micromanipulating nucleic acids with MT allows one to investigate their thermodynamical properties as well as their interaction with proteins involved in their replication, their transcription or their topological rearrangement. These studies are performed by measuring the extension changes of nucleic acids tethered between a micrometric magnetic bead and a surface. The optical measurement of the 3D position of the magnetic bead allows detecting these changes. So far, the resolution of this tracking is roughly 2 nm. This work will introduce a superresolution technique, Stereo Darkfield Interferometry, that allowed us to increase significantly the optical resolution of the tracking, down to the subnanometer range. We will also describe how the hydrodynamic couplings close to the glass surface result in a dramatic loss of spatio-temporal resolution in spite of the enhancement of the optical precision. We will show some applications of this new resolution to the characterization of helicases and to the study of the hybridization of short oligonucleotides. We will also present a MT-based method, that we called kinetic locking. Based on a DNA fluctuating probe, it enables measurements that do not involve measurable extension changes.

Keywords:

Magnetic tweezers, single molecule, nucleic acids, biophysics, force spectroscopy, superresolution, helicases, 3D-tracking, kinetic locking, stereoscopy, interferometry

À Nanie

Contents

Remerciements

Merci Maman, Papa, pour votre dévouement et votre patience. Merci d'avoir cultivé ma curiosité comme une plante délicate. Merci de m'avoir laissé explorer le monde comme s'il fût une assiette savoureuse, quitte à m'y brûler la langue. Merci Elsa, Julie, Sylvain, pour votre amour et votre générosité inconditionnelle.

Chacun dans mon laboratoire sait qu'il ne serait pas grand chose sans Vincent Croquette. Il incarne l'élégance de la science et la simplicité des belles idées. Merci de tout cœur, Vincent, pour tout ce que tu m'as appris et tout le temps que tu m'as accordé.

Je remercie Jean-François Allemand pour son œuvre doctorale fondatrice, son soutien indéfectible et ses relectures minutieuses.

Ce travail n'aurait pas été possible sans les tutelles de David Bensimon, Fatima Hamouri, Thibault Vieille, Maartje Pontier, Gaël Radou, François-Xavier Lyonnet du Moutier et Jessica Valle-Orero.

Il n'aurait pas non plus vu le jour sans les discussions captivantes et collaborations généreuses avec Hervé Le Hir, Nadia Ruiz-Gutierrez, Joanne Kanaan, Jean-Baptiste Boulé, Thao Tran, Raphaël Jeanneret et Jimmy Ouellet.

Je remercie les rapporteurs de ce travail, Nynke Dekker et Laurent Cognet, et le jury qui me fait l'honneur de l'évaluer : Michelle Wang, Felix Ritort, Jean-Louis Mergny.

Merci à tous les professeurs dévoués et passionnants dont j'ai eu la chance d'être élève : Jean-Christophe Hannachi, Stephan Fauve, Frédéric Chévy, Lydéric Bocquet, Paul Colin, Pierre Gissot, Blandine Durand, Aurélien Moncomble, Hakim Lakmini, Nathalie Chesse, Serge Cibray, Martine Crégut, Bernard Gadat, Sylvie Pardessus, Marc Fournet, Mary Devismes, Madame Pinsonneau, Isabelle Lejault, Patrick Robiano, Madame Sionian, Emmanuel Attali, Monsieur Bariolet, Madame Bellecourt, Madame Salgues, Soazig Levrel, Philippe Rey.

Merci à José Da Silva Quintas, Nabil Garroum, Annie Ribaudeau, Benoît Paulet, Monia Mestar, pour leur soutien quotidien.

Merci à Christophe Goupil et Bérengère Dubrulle.

Merci à Juliette Chatelut, Tiphaine Champetier, Hervé Ménévis, Marie-José Gibrat, d'avoir su, au bon moment, être présents et attentifs.

Merci Paulette, pour toutes nos balades avec Titus.

Merci Christine, Cricri.

Merci Adrien, Clément, Alpha.

Merci Boubou d'être aussi doux, merci Claire d'être aussi belle.

Introduction

Elements of context

This work is dedicated to the enhancement of the resolution of magnetic tweezers, a biophysical technique used to study interactions between biomolecules, and in particular between nucleic acids (NA) and proteins. Protein–NA and NA-NA are essential in many critical biological processes such as replication [Kornberg and Baker, 2005], transcription [Pabo and Sauer, 1992], translation [Noller, 1991], repair [Li, 2008, Kowalczykowski, 2015], recombination [Haber, 1999], and antigen recognition [Yoneyama and Fujita, 2009]. As such, they constitute a large field of research for biologists. Over the last century, biochemists have developed an arsenal of *in vitro* techniques allowing the measurement of interactions between proteins and nucleic acids. They did not only provide thermodynamics equilibrium measurements of these interactions, but also precise kinetic measurements at the millisecond timescale, in particular thanks to the progress of stopped-flow techniques [Jia et al., 1996, Liu et al., 2020, Zheng et al., 2015]. These techniques, inherited from chemistry, are qualified as **bulk**, or *ensemble* techniques, as they consist in performing unique measurements averaged over billions of different molecules. Most of them are based on the optical properties of the biochemical samples: fluorescence, absorbance, circular dichroism, diffraction.

More recently, in the last decades, physicists have developed **single-molecule** (sm) methods [Miller et al., 2017]. As their name implies, they allow one to perform measurements on unique molecules, by opposition with bulk experiments. The goal is to account for the diversity of behaviors that can display a biochemical sample. For example, a protein might overtime undergo conformational changes that will modify its interactions with its partners. A bulk experiment would result in an average measurement of these interactions, while, in theory, single-molecule techniques can unveil the heterogeneity of behaviors that can be observed in a sample. Since aggregated data can not account for the diversity of behaviors and since we do not know how to rigorously aggregate data from many populations into gross indices,

both scales are important to understand complex systems made of many constituents, such as biological or economic systems.

Single-molecule methods can be classified into three main categories: single-molecule microscopy, single-molecule conductance detection and single-molecule micro-manipulation methods. Most **single-molecule microscopy** techniques are based on fluorescence [Moerner and Fromm, 2003, Harms et al., 2001]. They allow detecting the fluorescence signals of single labeled molecules by selectively *switching on* a small sub-sample of all molecules, then switching them off and switching on another sub-sample, and so on until all molecules have been imaged [Betzig et al., 2006,Rust et al., 2006,Sharonov and Hochstrasser, 2006, Cognet et al., 2008, Giannone et al., 2013, Godin et al., 2014]. The diffraction limit is thus overcome by the low density of observable particles at a given time. Super-resolution microscopy can also be performed in 3D, this will be discussed in the first chapter. On the other hand, Förster Resonance Energy Transfer (FRET) [Förster, 1948, Förster, 1982] allows measuring the distance between two fluorophores (in the nanometer range). Based on this sensitivity, single-molecule FRET [Ha, 2001] is able to unveil the dynamics of protein conformation changes [Santoso et al., 2010, Schuler and Eaton, 2008, Gopich and Szabo, 2007] as well as the dynamics of interactions between proteins and nucleic acids [Roy et al., 2008, Paul et al., , Singh et al., 2018, Singh et al., 2016, Comstock et al., 2015]. While less mature, fluorescence-free sm-microscopy techniques have also recently shown promising results for the measurements of biochemical interactions: label-free interference reflection microscopy of large molecules [Ortega-Arroyo and Kukura, 2012, Ortega Arroyo et al., 2014, Andrecka et al., 2016, Taylor and Sandoghdar, 2019, Spindler et al., 2016] and single-molecule Raman spectroscopy [Siddhanta and Narayana, 2012]. **Single-molecule conductance detection** consists in measuring with high precision the electrical current (typically a few picoamperes) going through a nanopore (a nano hole) in a membrane separating to electrolyte solutions at different potentials. When a molecule of interest goes through such a nanopore, it decreases the electrolyte flow and consequently creates a drop in conductance [Dekker, 2007]. This type of experiments allows identifying biomolecules [Rotem et al., 2012, Morin et al., 2018], sequencing DNA [Clarke et al., 2009], identifying epigenetic modifications [Wallace et al., 2010], and more recently, it has also been used to measure the microsecond unfolding dynamics of proteins [Rodriguez-Larrea and Bayley, 2013, Oukhaled et al., 2007] and the interaction of proteins with nucleic acids [Craig et al., 2019, Craig et al., 2017, Caldwell and Spies, 2017, Laszlo et al., 2016, Manrao et al., 2012, Lin et al., 2017].

The technique at the core of this work belongs to the third category of single-molecule techniques:

single-molecule micro-manipulation (smMM), or single-molecule force spectroscopy. These techniques have much in common and consist in attaching single molecules to micro-objects that can be easily manipulated and tracked. When a force is applied to the micro-object, it is transmitted to the studied molecule, which in turn translates in a change of extension. This allows drawing the force-extension curve of the molecule and thus accessing its thermodynamic properties. For example, one of the pioneering measurement by micro-manipulation was to draw the force-extension curve of double-stranded DNA [Smith et al., 1992] and subsequently to show that it could be well fitted by the worm-like chain model (WLC) [Strick et al., 1996, Marko and Siggia, 1995]. On the other hand, these techniques allowed characterizing the dynamics of molecular motors, proteins that perform cyclic micro-mechanical tasks. For example, optical tweezers were used to measure the steps of kinesins along microtubules [Block et al., 1990, Svoboda and Block, 1994] as well as the one of myosin along actin filaments [Finer et al., 1994]. In a serie of bluffing experiments, the team of Kinosita [Yasuda et al., 1998, Adachi et al., 2007, Adachi et al., 2000, Kato-Yamada et al., 1998, Hirono-Hara et al., 2001, Itoh et al., 2004], was able to mechanically drive the synthesis of ATP by F1-ATPase by micromanipulating the *rotor* of the molecular motor with magnetic tweezers. Later, it appeared that monitoring the extension of DNA molecules in presence of molecular motors involved in their replication and transcription could give important insights into their mechanisms. Indeed, transient loops or transitions from single-stranded (ss) to double-stranded (ds) result in a change in extension of the nucleic acids. This observation led to numerous breakthroughs in the understanding of some types of NA-processing molecular motors, such as helicases [Dessinges et al., 2004, Stanley et al., 2006, Lionnet et al., 2007, Johnson et al., 2007, Manosas et al., 2013, Fiorini et al., 2015, Bagchi et al., 2018, Kanaan et al., 2018], polymerases [Yin et al., 1995, Wang et al., 1998, Maier et al., 2000, Manosas et al., 2012a, Manosas et al., 2012b, Righini et al., 2018], topoisomerases [Strick et al., 2000, Dekker et al., 2002, Koster et al., 2005, Charvin et al., 2005, Lipfert et al., 2009, Seol and Neuman, 2011, Mills et al., 2018], or packaging motors [Moffitt et al., 2009]. As a consequence, micro-manipulation of nucleic acids became a standard tool for the study of replisomes, the complexes of enzymes involved in nucleic acid replications. The fact that helicase of the SARS-CoV-2 virus, nsp13, was characterized using this method [Mickolajczyk et al., 2020], just a few months after the start of the epidemics illustrates the normalization of micro-manipulation techniques. Regarding its possible interest for virology, it is also noteworthy that micro-manipulation recently allowed characterizing RNA-dependent RNA polymerases (RdRP), enzymes that are essential for viral replication and thus are considered as important therapeutic targets [Vilfan et al., 2008, Dulin et al.,

2015b, Dulin et al., 2015c, Dulin et al., 2017].

Three main methods are used to micro-manipulate single molecules: atomic force spectroscopy (AFM), optical tweezers (OT), and magnetic tweezers (MT) [Neuman and Nagy, 2008]. AFM is mostly known as a precise imaging technique that consists of scanning the surface of a material with a cantilever and measuring the bending of the cantilever with a laser beam [Eaton and West, 2010]. However, it can also be operated as a micro-manipulating device by attaching one side of a molecule on a surface and the other side on the tip of the cantilever. From the position of the tip of the cantilever, measured through the deflection of the laser beam, and from the position of the base of the cantilever attached to a nano-positioning device, one can deduce the force and the extension of the molecule [Hinterdorfer and Dufrêne, 2006, Zlatanova et al., 2000, Rief et al., 1997]. Optical tweezers [Ashkin, 1997] allow attaching a molecule between microspheres that are trapped optically at the focusing point of a laser beam. The traps can here again be nano-positioned and the force can be deduced from the position of the micro-spheres in their optical traps, allowing the measurements of the force-extension curves [Wang et al., 1997, Fazal and Block, 2011]. Magnetic tweezers consist in attaching a molecule between a surface and a magnetic microbead: a force is applied to the bead by approaching magnets and the position of the bead is tracked by holographic imaging. We refer the reader interested in the technical details of each technique to the numerous and comprehensive reviews written on the subject [Neuman and Nagy, 2008, Miller et al., 2018, Perkins, 2014, Sullan et al., 2013, De Vlaminck and Dekker, 2012, Ribeck and Saleh, 2008, Manosas et al., 2010]. We will focus here on some metrological aspects.

To our knowledge, all smMM biological measurements involving extension changes smaller than 2 nanometers or shorter than the millisecond involve either OT or AFM but never magnetic tweezers. For this reason, MT have earned the reputation to have a lower spatio-temporal resolution. In spite of this lower resolution, magnetic tweezers present some precious advantages. First, thanks to the homogeneity of the magnetic field, the force applied on the bead is not coupled to its position. Thus, it makes possible to work at constant force[1]. This constant force simplifies the acquisition of controlled thermodynamic data. Second, MT display a larger force operational range, from 10^{-3} to several hundreds of piconewtons. Third, MT represent a method of choice to produce rotational stress in single-molecules and measure its effect[2]. Finally, and most importantly, MT are intrinsically parallelizable, allowing the tracking of several

[1] OT can be operated in a constant force regime close to the inflection point of the trapping potential but the range is limited to a few ten of nanometers. In comparison, the force applied on a magnetic field in a typical MT experiments featuring magnets with a 300 microns gap varies of less that 0.3% over a position range of 1 micron.

[2] Some techniques have also been proposed to produce torques with optical tweezers [Pedaci et al., 2011, Pedaci et al., 2012]

hundreds of single molecules at the same time, when OT and AFM are still hard to multiplex. This relatively high-throughput is crucial for single-molecule techniques, since many individual events must be observed in order to deduce relevant parameters. For example, the relative precision on the inference of a Poisson parameter scales as $1/\sqrt{N}$, where N is the number of observed events. In order to deduce the binding rate of a protein with a nucleic acid with a 1% precision, 10.000 binding events must be observed. If the protein can bind with various conformations, each involving a different binding rate, the need of numerous data points becomes even more compelling.

The parallelism of MT has acquired a particular significance in the recent years with the development of a new analytical method based on micro-manipulation. The method allows the detection of specific sequence motifs [Ding et al., 2012], epigenetic modifications [Wang et al., 2020] and secondary structures, such as G-quadruplex [Hodeib, 2017], in nucleic acids. In particular, it offers the promise of a direct read-out of unamplified native NA modifications, which is still the blind spot of next-generation sequencing techniques. The technique consists of converting a portion of double-stranded nucleic acid into a hairpin. This hairpin is then attached between a surface and a magnetic micro-bead and then repetitively opened and closed by applying a force cycle. At high force (~15 pN for DNA, ~18 pN for RNA), the Watson-Crick energy of hybridization of both DNA and RNA is not sufficient to withstand the applied force. Consequently, the hairpin unwinds into a long single-stranded molecule, resulting in a change in extension of the order of one nanometer per unwound base. When the force is lowered again (less than ~8 pN), the hairpin rewinds into a duplex structure. If a secondary structure is present in the nucleic acid, or if a protein binds to the single-stranded NA, it can be observed during the closing of the hairpin as it transiently blocks it in the open state.

The detection method described above reaffirms the interest of reaching a resolution of one nanometer. Indeed, when a base-pair of a hairpin is unwound, it results in a change of extension that corresponds to the length of two bases of single-stranded NA. In the force range that is needed to open/close a hairpin, this length is close to the nanometer. A basepair precision in the framework of a hairpin-based detection thus requires a nanometer resolution. Since the blockage of the hairpin is transient, this resolution must be reached by averaging the signal over a finite time window, typically the second. As a consequence, being able to determine the extension of a molecule with magnetic tweezers and with a spatio-temporal resolution of one nanometer in a fraction of second would me a major milestone.

---

and more recently to induce supercoiling in DNA [King et al., 2019].

An other motivation for reaching such a resolution would be the possibility to gather more data about the precise mechanisms of helicases. Helicases are a broad family of molecular motors whose function is to unwind double-stranded nucleic acids into single-strands [Spies, 2012]. They are involved in many crucial biological processes such as replication, repair [Bernstein et al., 2010], recombination [Wu and Hickson, 2006], RNA splicing [Cordin and Beggs, 2013], translation initiation, or transcription termination [Brennan et al., 1987]. Magnetic tweezers have proven to be a useful technique to study properties of these motors that could not be easily measured in bulk such as processivity, velocity and pausing dynamics [Hodeib et al., 2016]. Again, a hairpin of nucleic acid is tethered between a magnetic bead and the surface, this time at a force smaller than its opening force but large enough so that the hairpin can not encircle the helicase and refold behind it. In this regime, the extension of the nucleic acid is a direct proxy of the number of bases unwound by the helicase. Various mechanisms have been proposed to explain the mechanisms of helicase translocation along nucleic acids. However, large and systematic data covering the accurate sequence-dependence of the discrete unwinding kinetics of helicases are still lacking. Thanks to their good spatio-temporal resolution, optical tweezers were able to capture some traces showing discrete steps of helicases[1] and polymerases [Abbondanzieri et al., 2005, Moffitt et al., 2006, Cheng et al., 2011, Spies, 2014, Qi et al., 2013, Whitley et al., 2016]. Benefiting at the same time from the parallelism of magnetic tweezers and from such a good spatio-temporal resolution could thus represent an important advance for the characterization of helicases.

One of the causes of the better resolution of optical tweezers and AFM is the optical detection method of the microspheres and cantilever. They are indeed based on position sensitive devices, allowing the sampling of positions with microsecond and ångströmic resolutions. Magnetic tweezers, on the other hand, rely on CMOS cameras with many pixels and consequently with larger sampling times (fractions of milliseconds). Furthermore, they are based on microscope-based imaging that so far does not reach the precision of the devices used in OT and AFM. However, the optical localization error is not the only cause of measurement noise. Independently on the localization precision, the three methods also suffer from measurements uncertainties due to the overdamped Brownian motion caused by the hydrodynamic drag applied on the micro-objects. This drag is indeed much larger than the one that would experience a free molecule. By slowing down the random movement of the system, this hydrodynamic drag imposes a limit on the spatio-temporal resolution of the techniques. Nowadays, optical tweezers and AFM are mainly limited by this effect. It ex-

[1] In order to slow down the kinetics of helicases down to observable timescales, low and unphysiological nucleotide concentrations are used.

plains why recent progress of spatio-temporal resolution in OT [Sudhakar et al., 2020] and AFM [Edwards et al., 2015, Edwards et al., 2017, Jacobson et al., 2020] have been supported by the development of new microspheres and cantilevers that display smaller hydrodynamic drag.

Motivated by the above considerations, we will strive to increase the spatio-temporal resolution of magnetic tweezers by using a recently developed optical system. We will seek to provide convincing proof-of-concepts based on precise biophysical measurements. The latter will involve short DNA molecules[1] in order to minimize the Brownian motion of the system. We will explore the interactions of these short molecules with oligonucleotides and proteins.

Outline

First, we will introduce and characterize a 3D-tracking technique for microparticles *Stereo Darkfield Interferometry*. Based on the engineering of the point-spread-function, this microscopy technique will allow us to significantly decrease the optical localization error of fixed magnetic beads from a few nanometers down to a few ångströms. Importantly, this increase in resolution will be performed without the need of averaging many different images, allowing real-time tacking of a whole field of view with ångströmic resolutions.

Armed with this new technique, we will track the extension of short DNA substrates and explain how the Brownian motion of the magnetic bead limits the spatio-temporal resolution of the measurement. In spite of this limitation, we will demonstrate that the gain in optical resolution allows observing nanometric extension steps of nucleic acids with magnetic tweezers. We will apply it to the measurement of the kinetics of hybridization of a short oligonucleotide of 8 bases and to the observation of the stepping dynamics of the helicase Upf1. However this gain in resolution will not allow improving the throughput of helicase stepping experiments compared to previous optical tweezers experiments nor to increase the nucleotide concentration up to physiological levels.

Finally, we will describe a new method of detection of discrete binding events of oligonucleotides and proteins with nucleic acids. Permitted by our new optical resolution and by the intrinsic force stability of magnetic tweezers, it is based on the accurate measurement of the kinetics of the rates of a rapidly fluctuating hairpin. The variation of these rates upon injection of a molecule binding to the fluctuating probe allows accessing precise thermodynamic and kinetic parameters. We will demonstrate the technique

[1] shorter than 140 basepairs of double-stranded DNA

by measuring the binding thermodynamics of oligonucleotides as short as five bases as well as the binding kinetics of the DNA-binding *E. coli* helicase RecQ.

Chapter 1

3D-super resolution tracking with Stereo Darkfield Interferometry

In the last twenty years, particle-tracking and localization-based super-resolution techniques [Moerner and Fromm, 2003] have advanced from a 2D imaging method to the third dimension. While x-y localization is obtained by evaluating the translation of the image compared to the optical axis, localization in the z-direction is made more complicated by the fact that camera images are plane. Thus, the axial position has to be deduced from the dependence of the image of an unfocused particle with the defocus distance *dz*. We will first introduce some basic definitions and concepts that are essential to understand 3D super-resolution and then describe and characterize *Stereo Darkfield Interferometry*, an optical method that allows the real-time tracking of microparticles with subnanometer resolution.

1.1 Real-time tracking 3D super-resolution: fundamental concepts and challenges

When a light-emitting point is observed through an optical system on a camera, it gives rise to a 2D-signal, called a **point-spread function** (PSF). This PSF is the probability distribution of a unique photon scattered or emitted by the imaged particle to reach a given pixel of the camera. It is parametric and depends on the localization of the particle in the object space (x,y,z). A camera allows us to count the number of photons that reached a given pixel during a time called the shutter time τ_s. These counts vary as they are the result of the sampling of the PSF. However, while at very low light intensity these counts display a Poisson

distribution, when many photons are sampled, the distribution of these counts converges to a Gaussian one owing to the law of the large numbers [Poisson, 1837]: their mean is equal to their variance. In other words, if a given pixel receives on average N photons by units of time, the counts vary with a typical spread σ_N of $\sqrt{N}$. This is called the photon noise, or shot noise [Schottky, 1918], and explains the slight variation of an image of a fixed object from one frame to the other. The higher the number of photons received in one pixel during τ_s, the less visible the variation, since the noise-to-signal ratio $\frac{\sigma_N}{N}$ decreases as $\frac{1}{\sqrt{N}}$ [1].

In a camera, the photons received in one pixel during τ_s produce an analog signal converted in an integer comprised between 0 and 2^b, where b in the number of bits of the analog-to-digital converter (typically 8, 10 or 12 for current cameras). A camera is characterized by the maximum number of photons that can be received by a pixel during one frame, called the **well depth** w_d. If this number is larger than w_d, the camera will not distinguish between the different counts and will return the saturating digital value: $2^b - 1$. It follows from the previous definitions that a pixel of an image that has a digital value I_d has received during the shutter time $I_d \times w_d/(2^b - 1)$ photons. $\alpha = w_d/(2^b - 1)$ is the conversion factor between the digital levels and the number of photons, it verifies: $N = \alpha I_d$. If we take the example of an image captured by a 8-bit camera with a well depth $w_d = 10000$, a pixel with value 255 corresponds to a number of collected photons larger than 10000, while a pixel with value 128 corresponds to a number of collected photons comprised between 5000 and $5000 + w_d/256 = 5039$ photons. The error on the photon number due to the digitization is called the **discretization noise**. It is not an important source of noise if it is smaller than the photon noise. In the case of our camera, the photon noise for $I_d = 128$ is roughly $\sqrt{5000} \simeq 70$ and is larger than the discretization noise. Finally, let us note that measuring the photon noise is a way to access experimentally the well depth of the camera. Indeed, imagine that w_d is not known. We expect the typical variation of I_d, σ_{I_d}, to be:

$$\sigma_{I_d}^2 = var(I_d) = var(N/\alpha) = \frac{var(N)}{\alpha^2} = \frac{N}{\alpha^2} = \frac{I_d}{\alpha}$$

Measuring the distribution of I_d thus allows us to measure α and subsequently w_d. Such a typical curve is shown on figure 1-1 and was used to calibrate our camera well depth.

The image of a small fixed particle by a digital camera thus corresponds to the sampling of the PSF with N photons. We recall that the PSF is a 2D-probability distribution (the resulting image is in 2D) that depends

[1] We must note that some light sources display non-Poisonnian statistics [Short and Mandel, 1983, Tapster et al., 1987, Brown and Twiss, 1956], especially at times below the coherence time (typically the microsecond).

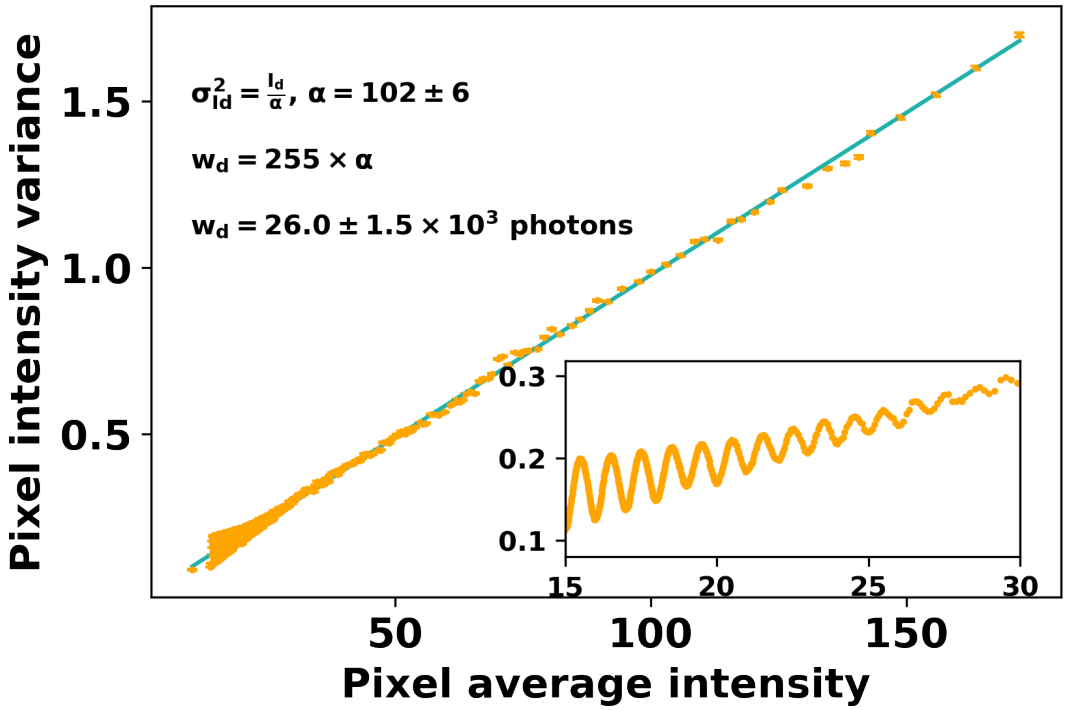

Figure 1-1: **Variance of the numerical intensity of the pixels of a fixed image as a function of their average intensity.** The slope of the curve allows one to retrieve the well depth of the camera. Inset: larger view of the small intensity pixels. The oscillations are due to discretization noise, the pixel intensity value being an integer. The discretization noise is minimal at integer average intensity values and maximal at half-integer intensity values. The curve has been drawn from successive images (128x256 pixels) of a fixed microbead obtained with *Stereo Darkfield Interferometry*, the technique described later in this chapter. The photon sources are red LEDs (Thorlabs, M625L4).

on (x,y,z), the position of the particle. We write PSF = PSF ($\mathbf{p} \mid x, y, z$). $\mathbf{p}$ is the position of the pixel where the photon is observed. The probability of this observation depends on (x,y,z). The principle of 3D super-resolution is to capture images, sampled from the PSF, and to retrieve from these images the parameters x,y,z. If we had access to the exact PSF, these parameters could be theoretically extracted without errors. Because we only have at our disposal samples of the PSF taken by the camera, there exists, however, a limit on the resolution of these parameters that depend on how strong the PSF depend on them and on the number of samples (the number of photons) N at our disposal. Retrieving underlying parameters from sampled distributions belongs to the field of statistical inference and the theory behind it does not belong to the scope of this work. However, it is noteworthy that the theory predicts a maximal precision on the inference of the parameters (x,y,z) that depends on the shape of the PSF. This precision is quantified by the spread of the distribution of the inferred parameter from one frame, called the **frame-to-frame** localization noise: σ_{ff}. The larger this spread, the smaller the localization precision. Writing $\mathbf{x} = (x, y, z)$, the theoretical limit on σ_{ff}, called the Cramér-Rao lower bound (CRLB) reads, assuming some regularity conditions on the PSF [Rao, 1992]:

$$\sigma^2_{ff,x_i} > \frac{[\mathbb{F}(\mathbf{x})]^{-1}_{ii}}{N}. \tag{1.1}$$

$[\mathbb{F}(\mathbf{x})]$ is the Fisher information matrix of the PSF defined by the following equation, where we denote by $\mathbf{x_0}$ the true value of the particle position for which we want to compute the statistical error:

$$\mathbb{F}(\mathbf{x_0})_{ij} = -\int_{\mathbf{p}\in\mathbb{R}^2} \left(\frac{\partial^2 \ln \mathrm{PSF}(\mathbf{p} \mid \mathbf{x})}{\partial x_i \partial x_j} \right)\Big|_{\mathbf{x}_0} \mathrm{PSF}(\mathbf{p} \mid \mathbf{x_0}) \mathrm{d}\mathbf{p}. \tag{1.2}$$

We will see later that the Fisher information reduces to a more intuitive formula for some specific PSF. At this stage, the important message is that the error on the bead localization is limited by a PSF-dependent parameter and that it decreases as $\frac{1}{\sqrt{N}}$, the number of photons collected to assess the position $\mathbf{x}$. We thus have two levers to increase the localization precision: (i) increasing the number of photons N by increasing the light power, or, (ii) engineering the PSF by modifying the optical setup so as to maximize the Fisher information that it contains regarding the particle position. The second point will be the object of the following section. Concerning the number of photons, it can be increased in spite of the well depth of the camera if one increases the acquisition frequency. Indeed, if instead of acquiring one frame per unit of time, one acquires 1000 frames, the pixel is read 1000 times more frequently, allowing us to use 1000 times its full well depth capacity and thus to capture 1000 times more photons. We will now discuss how **real-time tracking** limits this strategy.

Real-time tracking consists of acquiring and analyzing images on the fly in order to only keep the inferred position of the particles. It is opposed to image post-processing, which consists in saving all the raw images during the experiment time in order to analyze them later. Let us perform a short calculation to explain why post-processing is technically impossible for long experiments. Imagine that we want to save the position of several particles imaged on a 4MPx-camera at a kilohertz frequency during one hour. We would then have to save $1000 \times 3600 = 3.600.000$ images. If the images are 8-bit, a 4Mx-images has a size of 4 megabytes (1 byte = 8 bits). Thus, all these images will occupy 14.400.000 megabytes, or 14.4 terabytes. Saving all these images is thus impracticable even with today's large hard-drive capacity. Real-time is thus a necessary feature. However, real-time tracking is limited by the transfer rate between the camera and the computer: the full image needs to be transferred to the computer at a rate larger than the acquisition frequency f. A typical USB-3 connection is limited to 500 MB/s. For 4MB images, it limits the acquisition frequency to f_{max} = 125 Hz. Some fancier PCI-express based hardware allows one to

reach 40 GB/s, but the full-frame acquisition frequency will still be limited to 5000 Hz. If we now consider the well depth of the camera, the number of photons n_p received by one pixel during 1s is thus limited to $n_{p,max} = f_{max} \times w_d$. That is the reason why real-time tracking limits the number of photons received and analyzed by a unit of time. As a consequence, averaging the inferred localization information from many frames acquired at high-acquisition frequencies is a limited solution and one is forced to increase the localization information contained in one single frame. The **frame-to-frame** localization noise is thus the important parameter that needs to be maximized by optical engineering.

Noticeably, since it is the number of photons by pixel that is limited by the well depth, increasing the spatial spread of the PSF over more pixels allows one to increase the number of photons received in one frame for a given well depth. Nevertheless, for most PSF, it is a counterproductive solution. For instance, for a Gaussian PSF of width w, the Fisher information related to the localization (x,y) decreases as $1/w^2$ [Thompson et al., 2002]. On the other hand, the maximal number of photons N_{max} that can fit into such a PSF at fixed well depth evolves as w. Thus, the minimal localization noise (Eq 1.1) evolves as $\sqrt{w}$: in this case, spreading the PSF increases the maximal number of photons but the effect of this increase does not compensate for the loss of Fisher information.

To summarize, given the technical limitation of the cameras and the camera-computer transfer, improving the localization precision of a super-resolution technique must rely on decreasing the frame-to-frame localization noise. For this purpose, the optical system must be designed in order to:

1. maximize the Fisher information contained in the PSF

2. spread the PSF on several pixels without losing Fisher information.

This is the goal of *Stereo Darkfield Interferometry*, the technique that we will describe here after a short description of the state of the art of PSF engineering.

1.2 PSF engineering: a state of the art

1.2.1 High resolution methods

PSF engineering consists in designing optical setups that enhance the Fisher information contained in photons regarding the 3D position of the scatterer. The introduction of spatial phase modulators and other phase customization devices have provided a PSF library with a high information content in all three dimensions:

phase ramp based [Baddeley et al., 2011], tetrapods [Shechtman et al., 2014], elliptical PSF [Kao and Verkman, 1994] [Huang et al., 2008], double-helix PSF [Pavani et al., 2009], self-bending PSF [Jia et al., 2014]. In spite of their high accuracy, all these approaches suffer from the complexity of their experimental implementation. More importantly, 3D-techniques based on these techniques exhibit a strong dependence upon the quantitative measurement of the image shape that increases their sensibility to optical imperfections such as spherical aberration or astigmatism. As a consequence, there is a need for lookup tables calibrated for each individual emitter (or at least for a set of sufficient positions in the field of view) [von Diezmann et al., 2017] that limits their throughput and their usage. A recent technique deserves a particular interest as it exhibits a particularly high Fisher information compared to existing methods as well as a simple experimental implementation: a simple diffraction grating before the camera is sufficient to obtain an interferometric PSF that depends precisely on the z position of the scatterer [Bon et al., 2018]. Nevertheless, all these methods are designed to be used in a fluorescence setup. Because they rely on wavelength filtering, these experiments result automatically in dark fields (no light reaches the camera in the absence of particles). In general, in the case of 3D-microparticle tracking, the image is due to the scattering of the light by the particle and is thus of the same wavelength than the incident light. As a consequence, the incident light cannot easily be filtered out and one must consequently adapt the optical techniques.

The most widely used technique in the field of microparticle scattering, and in particular in the community of magnetic tweezers [Gosse and Croquette, 2002] and single-cell tracking [Taute et al., 2015], relies on analyzing the diameter of the holographic rings appearing in the image of a bead illuminated with a parallel monochromatic incoming wave (figure 1-2.a). As the microparticle scatters the incoming electromagnetic field $\mathbf{E}_{in}$, the spherical scattered field $\mathbf{E}_{scat}$ interferes with $\mathbf{E}_{in}$. Because Mie scattering results in an equal phase for all points in a direction θ compared to the incoming light [Bohren and Huffman, 1983, Chapter 3, section 2], the planar section of the resulting field consists in concentric rings whose radius increases with the distance of the object plane with the particle dz. Thus, the radius of the rings encodes information about the axial position dz while their center encodes information about the lateral positions x and y. The success of the method is due to the simplicity of its implementation: simply imaging a micro-particle through a standard microscope with a parallel monochromatic light is enough to observe these rings. The technique allows, with X100 objectives, axial frame-to-frame localization noises down to ≈ 2 nm (figure 1-2.d). This resolution is mainly limited by the low number of useful photons in a single image. Indeed, the interference contrast is low and the image is dominated by the intensity of the incident wave. Increasing the number of

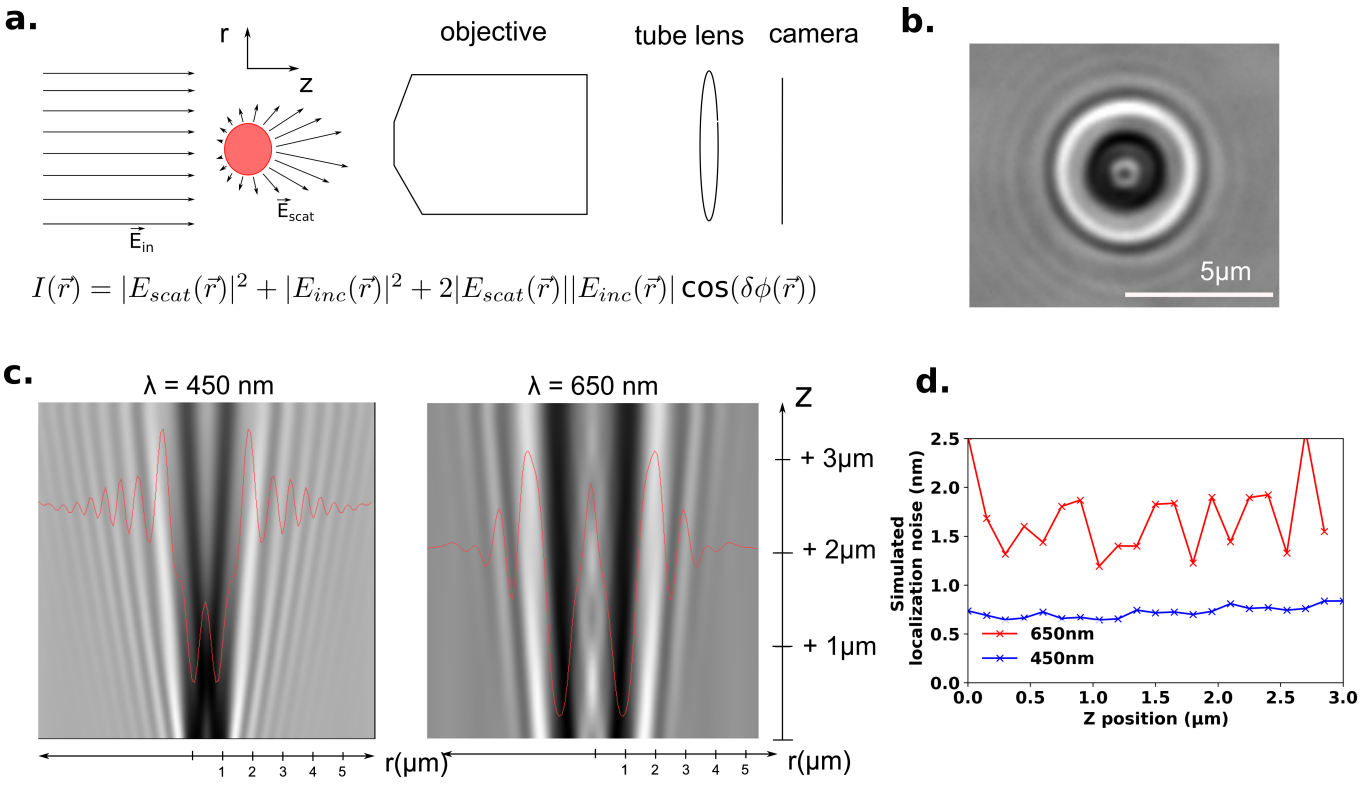

Figure 1-2: **Classical holographic technique used for the 3D-tracking of microbeads. a.** Description of the method. A bead placed close to the front focal plane of an objective is imaged with a parallel incoming light. The scattered light interferes with the incident light, thus encoding phase information into an intensity pattern. **b.** Holographic image of a magnetic bead of diameter 1μm (Thermofisher Dynabeads MyOne T1). **c.** Transverse radial profile of the image as a function of the axial position of the bead z for two different vacuum wavelengths of the incoming light. Light red lines show the intensity profile for $z = 2\mu m$. **d.** Simulated axial localization noise obtained from the images in c for a camera well depth of 30000 electrons. Simulations are performed by sampling 2048 Gaussian noise profiles. These profiles are added to the profiles shown in c. and the inferred z is computed by applying the algorithm presented in [Gosse and Croquette, 2002].

photons participating to the interferometric PSF is thus limited by the fact that the majority of the well depth of the camera is filled by useless photons from the bright field. The only solution to increase the number of photons received by units of time is thus to increase the acquisition frequency. This strategy is used by many authors [Kim and Saleh, 2009, Lansdorp et al., 2013, Dulin et al., 2015a, Huhle et al., 2015], who increase the acquisition frequency of bead imaging up to 10 kHz, in order to reduce the localization noise down to the ångströmic level upon averaging the signal over many frames. As stated earlier, real time acquiring at such frequency is impossible or imposes to reduce the field of view to a few hundreds of pixels. This most probably explains why these authors were not able to demonstrate this resolution through the measurements of nanometric biological signals. In practice, finding well-attached single-molecules requires indeed a large field of view allowing testing multiple beads.

Noticeably, we can imagine two solutions that can participate in increasing the resolution of ring-based

3D tracking. The first consists in decreasing the wavelength of the light in order to encode more information in the PSF. Indeed, the frequency of the concentric circles is proportionally related to the wavelength since two successive peaks correspond to optical paths between scattered and incoming light that differ by a multiple of the wavelength. We illustrate this effect on figure 1-2.c-d and compare the simulated localization noise from the z-dependency of the rings acquired with blue (450 nm) and red (650 nm) light. It is interesting that the simulated frame-to-frame z-resolution goes down to $0.7nm$ for the blue light. Sadly, lowering even more the wavelength of the incoming light is incompatible with the imaging of biological samples due to the toxicity of the highly energetic photons. The second solution would consist in reproducing the methodology of phase-contrast microscopy. In order to increase the contrast of the interferences between incoming and scattered light, a gray filter is introduced after the sample in a phase-contrast microscope in order to fade the incoming light that belongs to a predefined angular cone. The same method could be simply transposed to ring imaging by placing a gray filter in the center of the back-focal plane of the objective, that would fade the parallel incoming light without modifying the intensity of the scattered light [1].

This second method, while interesting in principle, was not tested in the context of this work since two other features of the ring-shaped PSF wanted to be overcome: its non-linearity and its dependence on the particle shape. The non-linearity is the absence of parameters that vary linearly with the axial position of the bead. While the radius of the rings varies almost linearly at large distances from the beads, it is not the case in the region where the contrast is at its highest, close to the focal plane. This is due to the complexity of the scattered electromagnetic field in the region close to the beads that cannot be approximate by the asymptotic Mie formula (equation 1.24). Furthermore, particles of different sizes give rise to quantitatively different images, especially close to the focus. Because of this dependence on the particle shapes, it is necessary to record a reference image library for each particle and different z-position. This annoying calibration step is particularly problematic for freely moving particles, which cannot be immobilized at a particular position to permit the focus sweep necessary for the recording of such a calibration library. Another goal of *Stereo Darkfield Interferometry*, additionally to increase the frame-to-frame localization precision, is also to remove the dependence of the optical response to the particle shape as well as its non-linearity.

[1] Preliminary experiments have been performed in our group by Hugo Trentesaux and Vincent Croquette in 2017.

1.2.2 Stereoscopic methods: the advantage of linearity

Compared to the previous non-linear methods, stereoscopic methods [Sun et al., 2009, Sun et al., 2010, Sancataldo et al., 2017] are more versatile and proficient in the context of heterogeneous and fast-moving particles. The principle and the geometric intuition behind it are illustrated in figure 1-3.a. Stereoscopy consists in separating the image of a particle into two parts: the one that results from a constrained angle range, and the other that results from the symmetric range with respect to the optical axis. When the particle is in focus, both images coincide. However, as the tracked object moves out of focus by dz, the shift between both images dx increases linearly with dz. This linearity is a great feature of the method alleviating the requirement of a calibration step and insuring its independence with respect to the particle size. Importantly, the width of the selected angle range has two effects on the duplicated PSF. The smaller the width, the larger the PSF: this is a result of the larger diffraction related to the reduced aperture. This is illustrated in figure 1-3. The size of the PSF for in-focus particles is smaller in the case of a smaller angle aperture (subfigure b.) than in the case of smaller apertures (subfigure a.). On the other hand, the larger the angular width of the beams, the more important the deformation of the PSF for out-of-focus particles. This is also illustrated in the figure : the PSF for out of focus particles is larger in the case of larger aperture. This effect is related to the concept of **depth of field**. It is the maximum defocus range dz for which the image appears sharp and relatively unmodified compared with the in focus image. This fundamental trade-off between resolution at focus and depth of field is well known to photographers. Increasing the aperture of a photo camera has two effects: it increases the level of detail at focus but reduces it for objects out of focus (background and foreground appear blurred compared with the in-focus image).

The geometric illustration presented above shows that stereoscopy results in the opposite translation of two separate images (1 and 2) resulting from the two illumination directions by a vector $(\varepsilon_X^{1,2}, \varepsilon_X^{1,2})$ as a response to the axial displacement δz of the imaged particle : $\varepsilon_X^1 - \varepsilon_X^2 = 2g_z\delta z$. We will discuss the rigor of this linearity later in this manuscript. We call g_z the z-sensitivity of the stereoscopic method that will depend on the illumination angle. On the other hand, for an aplanetic optical setup, the lateral position (x,y) of the particle is linearly related to the translation of the whole image, that is in this case the average of the translation of the two separate spots forming the PSF : $\varepsilon_X^1 + \varepsilon_X^2 = 2g \times x$ and $\varepsilon_Y^1 + \varepsilon_Y^2 = 2g \times y$. g is the optical magnification of the setup. Inferring the 3D position of the particle (x,y,z) can thus be reduced to the inference of the translation parameters of the two spots, $\varepsilon^{1,2} = (\varepsilon_X^{1,2}, \varepsilon_Y^{1,2})$, such that $PSF^{1,2}(\mathbf{p} \mid (x,y,z)) = PSF^{1,2}(\mathbf{p} - \varepsilon^{1,2})$. Here, $PSF^{1,2}$ denotes the partial PSF formed by each of the two beams in figure 1-3.

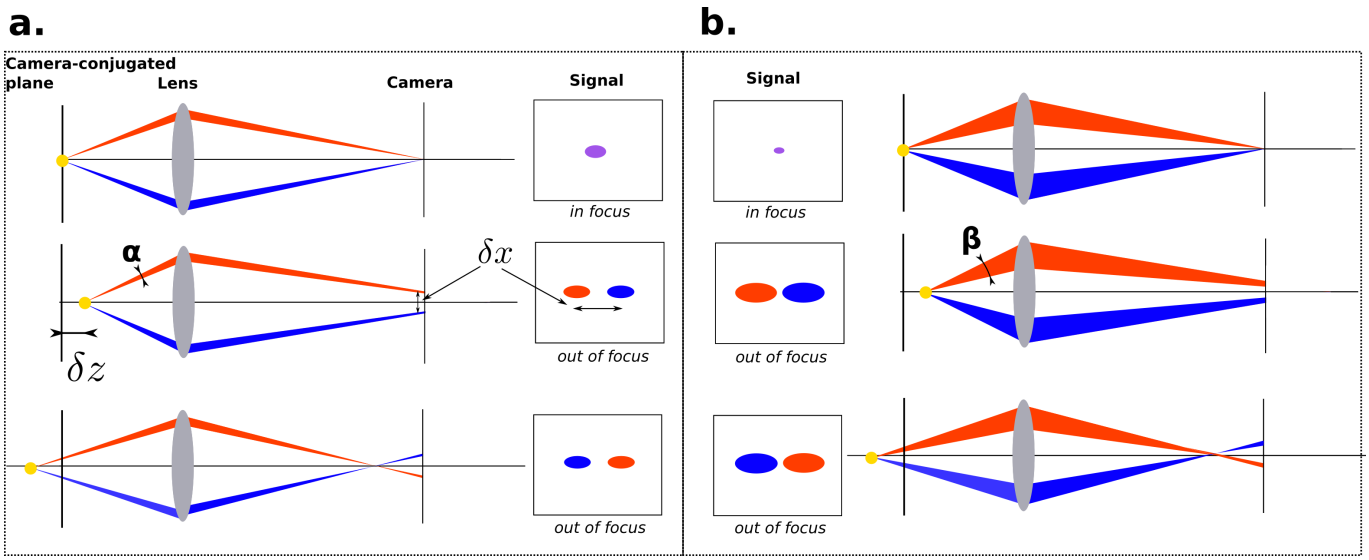

Figure 1-3: **Principle of stereomicroscopy.** Red and blue rays do not have to correspond to different wavelengths. **a.** Stereoscopy consists in comparing the images formed by two beams with symmetric angles with regard to the optical axis. The two images are superimposed at focus and undergo a shear translation as the imaged particle moves away from the front focal plane. **b.** Impact of a larger angular aperture ($\beta > \alpha$) on stereomicroscopy. A larger aperture causes a smaller PSF at focus but a broader PSF out-of-focus, and thus a stronger PSF deformation with defocus.

Calling f one of this partial PSF, the Fisher information matrix (eq 1.2) for the inference of its translation vector ε verifies :

$$\mathbb{F}(\boldsymbol{\varepsilon_0})_{ij} = -\int_{\mathbf{p}\in\mathbb{R}^2} \left(\frac{\partial^2 \ln f(\mathbf{p} \mid \varepsilon)}{\partial \varepsilon_i \partial \varepsilon_j} \right) \Big|_{\varepsilon_0} f(\mathbf{p} \mid \varepsilon_0) \mathrm{d}\mathbf{p}. \tag{1.3}$$

$$= -\int_{\mathbf{p}\in\mathbb{R}^2} \left(\frac{\partial^2 \ln f(\mathbf{p} - \varepsilon)}{\partial \varepsilon_i \partial \varepsilon_j} \right) \Big|_{\varepsilon_0} f(\mathbf{p} - \varepsilon_0) \mathrm{d}\mathbf{p}. \tag{1.4}$$

$$\tag{1.5}$$

This expression does not any more depend on ε_0 , the translation parameter, which is due to the fact that there is no deformation of the PSF as it translates (assuming negligible aberrations): its geometric and thus informational-theoretical properties thus do not depend on their positions. The Fisher information can be further reduced :

$$\mathbb{F}_{ij} = -\int_{\mathbf{p}\in\mathbb{R}^2} \left(\frac{\partial^2 \ln f(\mathbf{p})}{\partial p_i \partial p_j} \right) f(\mathbf{p}) \mathrm{d}\mathbf{p} \tag{1.6}$$

$$= -\int_{\mathbf{p}\in\mathbb{R}^2} \left(\frac{\partial^2 f(\mathbf{p})}{\partial p_i \partial p_j} \right) \mathrm{d}\mathbf{p} + \int_{\mathbf{p}\in\mathbb{R}^2} \left(\frac{\frac{\partial f(\mathbf{p})}{\partial p_i} \frac{\partial f(\mathbf{p})}{\partial p_j}}{f(\mathbf{p})} \right) \mathrm{d}\mathbf{p}. \tag{1.7}$$

$$\tag{1.8}$$

The first terms equals zero for a localized PSF. In order to better understand the second term, let us make the hypothesis that $f(\mathbf{p}) = f_x(p_x)f_y(p_y)$ (that will also be the case for the PSF engineered in this work). In this case $\mathbb{F}$ is diagonal and :

$$\mathbb{F}_{ii} = \int_{\mathbf{p}\in\mathbb{R}^2} \frac{f_i'(p_i)^2}{f_i(p_i)} \mathrm{d}p_i \tag{1.9}$$

This formula shows that the Fisher information related to the translation of the partial PSF is directly related to its spatial variation : the stronger the spatial dependence of the PSF in the direction i, the smaller the statistical noise on the measurement on the translation parameter ε_i. For a Gaussian PSF $f(p_x, p_y) = \frac{1}{2\pi\sigma_x\sigma_y} e^{-\frac{x^2}{2w^2} - \frac{y^2}{2w_y^2}}$, one can check that the formula agrees with the result of Thomson-Webb [Thompson et al., 2002], which states that 2D resolution decreases with the width of a Gaussian-like PSF :

$$\mathbb{F}_{ii} = \frac{1}{w_i^2} \tag{1.10}$$

This explains the relatively low precision per photon of stereoscopic methods: because the numerical aperture is reduced, the PSF is spatially spread and thus the inference of its position is less precise. *Stereo Darkfield Interferometry* is meant to overcome this problem and to maximize all relevant parameters described in the above sections :

- It makes use of stereoscopy in order to ensure **linearity**.
- It uses a greatly reduced angular aperture in order to increase the axial measurement range (the **depth-of-field**).
- The diffraction created by the reduced range of angles also allows to spatially spread the PSF and thus to capture more photons by frame, allowing to make a better use of the **well depth** of the camera.
- The reduced information per photon due to the spatial spread of the PSF is compensated by a **spatial structuration** of the PSF by interferometry, as suggested by Equation 1.8.
- The **dark field** allows us to get rid of the useless photons from the incoming light, allowing us to detect photons scattered by the tracked particle and transporting information about its position.

1.3 Stereo Darkfield Interferometry

1.3.1 Optical setup

Figure 1-4 presents the principle of Stereo Darkfield Interferometry. Illumination is generated by two superluminescent LEDs (SLED) sending collimated parallel beams with symmetric incidence angles of $\pm 39^\circ$ from the optical axis (figure 1-4.a). The microscope is built around an infinity corrected objective and a field lens producing an image on a camera chip. An afocal system built with 4 lenses is used to access the image focal plane of the objective that is physically located inside the objective mount and in most cases not accessible. A black absorbant film with slits is used as a filter in the Fourier plane, *i.e.* the back focal plane. The Fourier filter is built with four symmetrical slits spanning the x axis. In the absence of diffusing particles, no light reaches the camera since the two illumination beams are focused on the black region located between the slits (figure 1-4.b). When a micron size particle is placed in the objective focal plane, the light stemming from each of the sources is diffused in a cone which covers mostly the two closest slits. The slits select two beams that are focused on the camera chip by a lens placed in contact with the slits. When the particle is at the focal plane, the beams originating from both slit pairs coincide. In order to separate them along the y direction for an easier tracking of each translated image, two glass slides tilted with opposite incidences ($\pm 17^\circ$) are placed just behind each slit pairs in close contact with the imaging lens. Their incidence is chosen to be large enough so that the two images coming from both pairs of slits do not coincide. Due to the double-slit configuration, each of the beam pairs issued from the same light source, as in the so-called Young double-slit experiment, gives rise to an interferometric pattern. When the object moves away from the focal plane by δz, both patterns are translated in a shear mode with opposite directions along the x-axis (figure 1-4.c-d).

1.3.2 Translation of the interferometric pattern and theoretical z-sensitivity

We now compute the theoretical translation of both interferometric pattern as the axial position of the particle changes. Notations are defined on figure 1-5. We first compute the phase shift between two rays stemming from the object $O(x_o, z_o)$ when they reach a point of the screen $I(x, z)$ by assuming that the objective is perfectly aplanetic but without assuming the astigmatism along the axial coordinate. For this purpose we use a construction point belonging to the object focal plane whose image would be I. Given the hypothesis of perfect aplanetism, the coordinates of this point are $B(x/g, 0)$, where g is the transverse

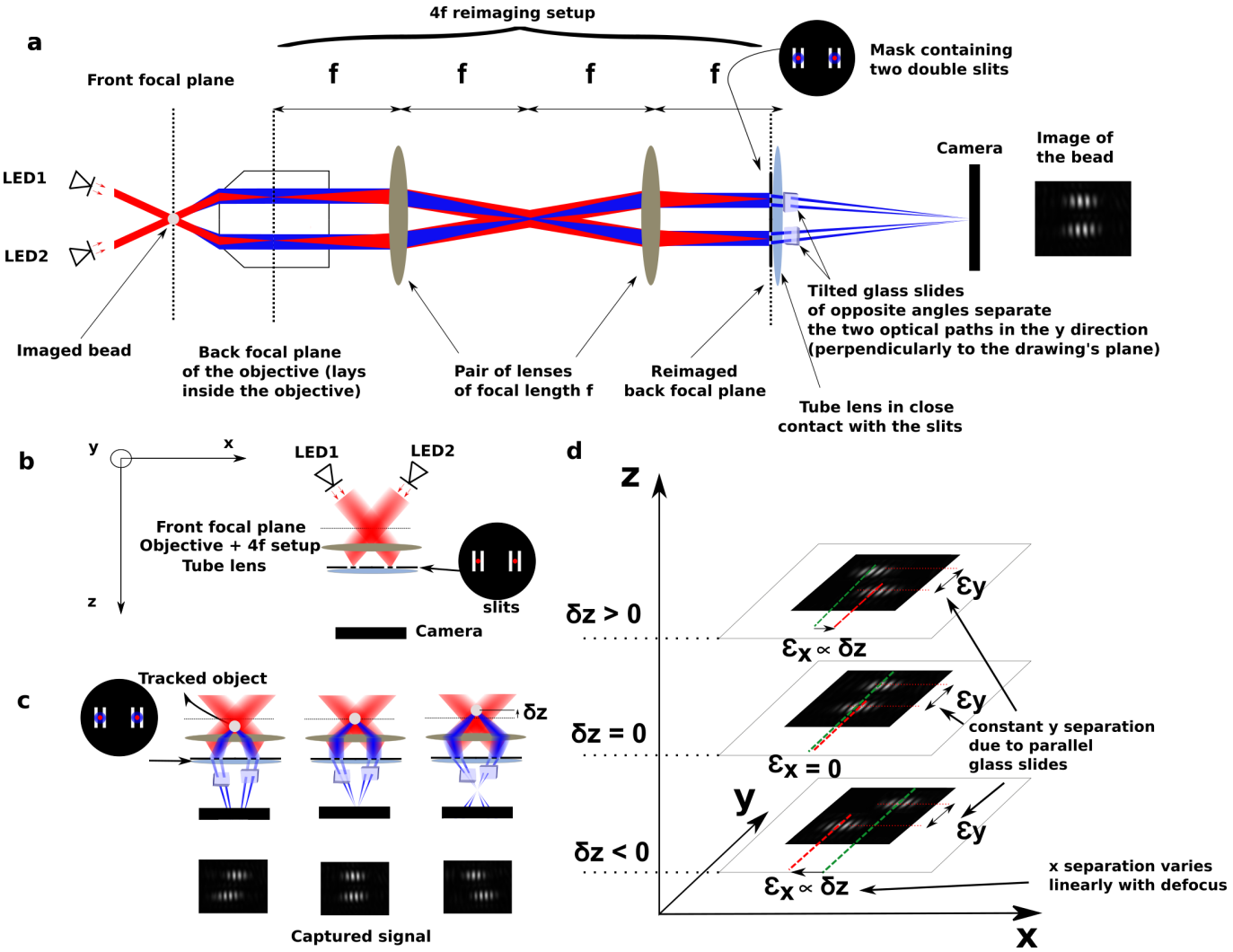

Figure 1-4: **Principles of *Stereo Darkfield Interferometry***. The red and blue colors denote respectively parallel incident light and light diffused by the scatterer (same wavelengths). **a.** Presentation of the optical setup and image of a micrometric bead with *SDI*. **b.** Schematic view of the setup in the absence of scatterer. For the sake of clarity, the objective and the 4f setup are represented as a unique lens. The incoming parallel light is blocked, ensuring darkfield. **c.** When a scatterer is present, the light goes through the slits and creates a PSF consisting of two interference patterns. **d.** Vertical stack of the SDI images (objective 100X) as a function of the defocus (axial position z) of the tracked object. The transverse distance ε_x between the two spots is proportional to the defocus (Figure 1-10.a).

magnification of the setup. All the rays stemming from this point and converging to I have no relative phase shift. Thus, denoting α_1 et α_2 the angles corresponding to the slits, we have:

$$(BI)_{\alpha_1} = (BI)_{\alpha_2} \tag{1.11}$$

, so,

$$(BX_1) + (X_1I) = (BX_2) + (X_2I) \tag{1.12}$$

Incoming parallel rays being conjugated to the plane of the slits, the following relation also holds:

$$(J_1X_1) = (BX_1) \tag{1.13}$$

, and,

$$(J_2X_2) = (BX_2) \tag{1.14}$$

, J_1 being defined in the inset of figure 1-5 and J_2 being the corresponding construction point for α_2. They verify (see figure 1-5):

$$(OJ_i) = \cos(\alpha_i)z_o - \sin(\alpha_i)(x_o - \frac{x}{g}) \tag{1.15}$$

Bringing these relations together, we get

$$\begin{aligned}
\delta(OI) &= (OI)_{\alpha_1} - (OI)_{\alpha_2} \\
&= (OJ_1) + (J_1X_1) + (X_1I) - (OJ_2) - (J_2X_2) - (X_2I) \\
&= (OJ_1) - (OJ_2) \\
&= (\cos(\alpha_1) - \cos(\alpha_2))z_o - (\sin(\alpha_1) - \sin(\alpha_2))(x_o - \frac{x}{g})
\end{aligned} \tag{1.16}$$

Thus,

$$\begin{aligned}
\delta\phi &= \frac{2\pi n\delta(OI)}{\lambda} \\
&= \frac{2\pi n}{\lambda}(\cos(\alpha_1) - \cos(\alpha_2))z_o - (\sin(\alpha_1) - \sin(\alpha_2))(x_o - \frac{x}{g})
\end{aligned} \tag{1.17}$$

We deduce in particular the lateral displacement of the central fringe when the bead is displaced of $\mathrm{d}z_b$ in the axial direction:

$$dx = g\frac{\cos(\alpha_1) - \cos(\alpha_2)}{\sin(\alpha_2) - \sin(\alpha_1)}\mathrm{d}z_b \tag{1.18}$$

Thus, the axial magnification g_z defined previously is written (recalling that g is the transverse magnification):

$$g_z = g\frac{\cos(\alpha_1) - \cos(\alpha_2)}{\sin(\alpha_2) - \sin(\alpha_1)} = g\tan(\frac{\alpha_1 + \alpha_2}{2}) \tag{1.19}$$

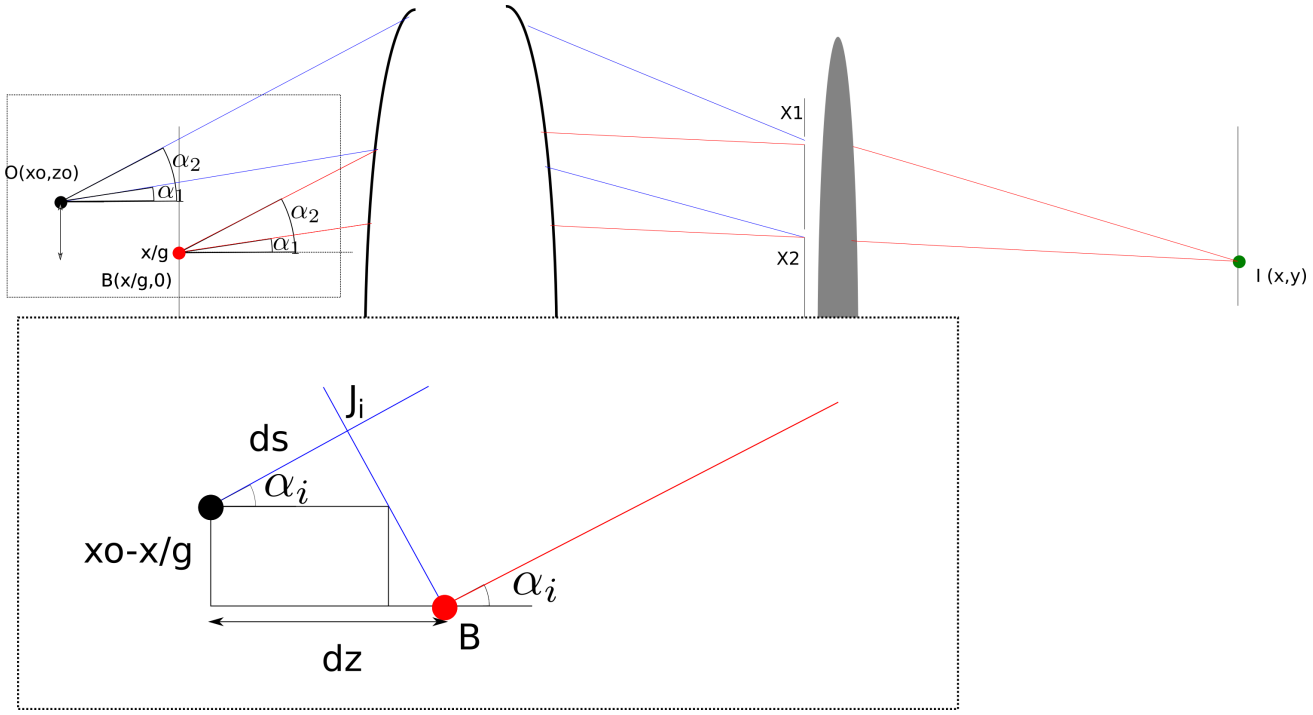

Figure 1-5: **Figure defining the notations used to calculate the axial magnification of the setup**. The object to be imaged is placed in O. The interferences are observed in I, located in the plane of the camera, and conjugated to the point B located in the front focal plane of the setup. α_i are the angles of the rays going through the slits at the position X_i. **Inset:** Definition of the construction point J_i. J_i belongs to the same wavefront as B with respect to the wave of angle α_i.

1.3.3 Characterization of the PSF of *Stereo Darkfield Interferometry*

Figure 1-6.b shows the experimental horizontal profile of the PSF ($f_x(x)$) obtained with *Stereo Darkfield Interferometry*. In this direction, we expect the profile intensity profile $f_x(x)$ to be the result of the multiplication of a sinc (due to the finite width of the slits) and of a cosine (due to finite distance between the slits) [Jackson et al., 2018, Hecht, 2002]. For the sake of simplicity, we fit the *sinc* envelope by a Gaussian since we are poorly interested in the secondary peaks.

Figure 1-6.c shows the experimental vertical profile of the PSF $f_y(y)$. In this direction, we expect the PSF to be a *sinc* function as it results from the diffraction by a simple slit. Again, it is here fitted to a Gaussian.

We expect the obtained PSF to be the combination of a diffraction pattern in the y-direction and of the diffraction pattern in the x-direction, and thus that the Y-profile is X-independent and vice-versa:

$$PSF(x,y) = f_x(x)f_y(y) = A\cos(k_x x)e^{-\frac{x^2}{2w_x^2}}e^{-\frac{y^2}{2W_y^2}}. \tag{1.20}$$

Again, the expected *sinc* functions have been replaced by Gaussians to simplify the analysis and the

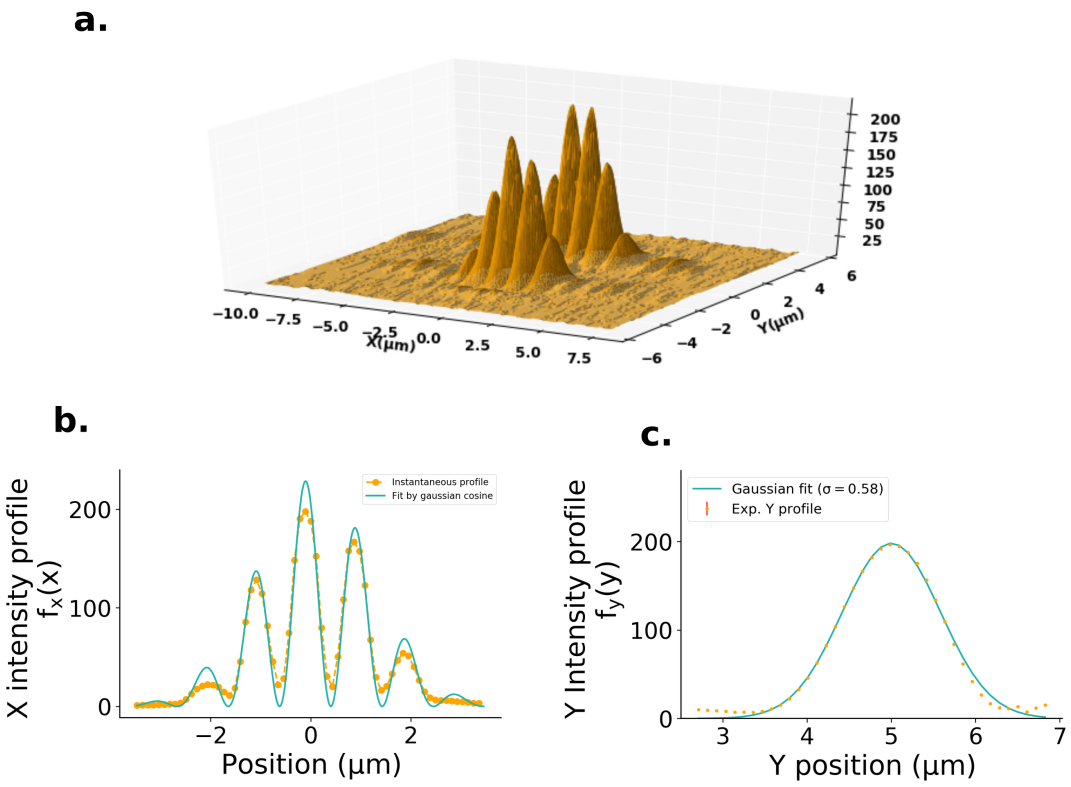

Figure 1-6: **Intensity profiles of the PSF of *Stereo Darkfield Interferometry*.** Spatial units are given in the object space. **a.** 3D surface plot of the PSF. **b.** Instantaneous X profile fitted by $f_x(x)$ as defined in equation 1.20. $k_x = 7$ μm^{-1}, $w_x = 1.2$ μm. **c.** Instantaneous Y profile fitted by $f_y(y)$ as defined in equation 1.20. $w_y = 0.58$ μm.

fitting procedure. This separability is qualitatively illustrated in figure 1-6.a. and justifies the formalism for the Fisher information shown in Equation 1.9.

1.3.4 Localization algorithm

The localization of the bead in the three directions is based on the precise sub-pixel localization of the interference fringes pattern along the two axes of the 2D image. The X direction is the structured direction and is particularly important for the determination of the axial position of the bead. Here we detail and compare two algorithms of localization. One is based on the phase shift in the Fourier space of the translated signal. Fourier decomposition appears indeed as a natural solution for two reasons. First, the pattern is localized in the frequency space since it results from double-slit interference. This is a nice feature because it can be easily filtered out using Fourier transform and deconvolved from low-frequency signals and PSF deformation. Second, translation of the signal results in a simple phase shift in the Fourier space and can thus be easily computed from Fourier decomposition. The second algorithm, based on the signal in the space of positions, is more empirical and allows avoiding two steps of Fourier analysis that can be annoying

in practice and introduce biases: phase unwrapping and windowing. Prior to the analysis, the camera image is cropped in small regions of interest (ROI) of 128 x 32 pixels around each fringe pattern. Then, their X-profile is averaged over the Y-axis, this is called the Y-averaged X-profile and serves as a base to compute the X translation of the fringe pattern. Similarly, the X-averaged y-profile serves to compute the Y translation of the fringe pattern.

Fringes X localization - Fourier's algorithm

The translation of a pattern in X is measured through the following steps:

1. A Blackmann-Nuttal [Nuttall, 1981] window of width 128 pixels is applied on the pattern. A window function is a function that converges continuously to zero (as well as its derivative) at the border of its range. It allows performing spectral analysis of non periodic signal with a finite support. However, a window affects the spectral estimate. The reader interested in optimal windowing is encouraged to consult the following course [Jeandet, 2018] and the following funding paper [Harris, 1978].

2. The windowed signal $f(x)$ is decomposed on the Fourier basis using discrete Fourier transform (DFT). Figure 1-7.b shows the amplitude $\mid \hat{f}_k \mid^2$ of the Fourier modes. The envelope corresponds to the slow modes while the oscillating part of the signal is contained in the second peak of the spectrum.

3. As the signal is shifted by δx, the phase of each mode k is shifted by a quantity $\frac{2\pi k \delta x}{L}$, where L is the length of the discrete signal. This property is used in order to infer δx. Using a fixed reference profile f_x^{ref}, we compute the phase shift of each mode between f^{ref} and f: $\delta\phi_k = \phi_k^{ref} - \phi_k$.

4. $\delta\phi_k$ is eventually unwrapped and its values at the modes of interest are fitted to a linear function (see figure 1-7.c). The value of the x-displacement of the pattern δx is inferred from the slope a of the fitted linear function: $\delta x = \frac{a}{2\pi}$.

Reference profile averaging

In order to obtain the phase of the reference profile ϕ^{ref} as accurately as possible, it needs to be averaged over several frames. However, between two successive frames, the images move slightly, because of slight mechanical drift or Brownian motion of the particle, and averaging the images over many frames might

result in blurring its shape (superposition of different images slightly translated from each other). We describe here an operation that allowed us to compute a reference profile while avoiding any blurring.

1. First, N images of length L pixels are windowed and decomposed on their Fourier bases consisting of the M modes of interest. This results in $M \times N$ variables $\phi_{i\in[0,N]}^{j\in[0,M]}$. Considering that the only transformation between two successive images is a translation of vector a_i, we have :

$$\phi_i^j = \phi_0^j + \frac{2\pi j a_i}{L} \tag{1.21}$$

2. The above expression results in $M \times N$ equations and $N+M$ unknown variables: N translation parameters a_i and M reference phases ϕ_0^j. This overdetermined linear problem can be written in matrix form :

$$\overbrace{\begin{bmatrix} \phi_1^1 \\ \phi_1^2 \\ \phi_1^3 \\ \cdots \\ \phi_2^1 \\ {\phi_2}^2 \\ {\phi_2}^3 \\ \cdots \end{bmatrix}}^{Y} = \overbrace{\begin{bmatrix} 1 & & & \frac{2\pi}{L} & & \\ & 1 & \cdots & \frac{4\pi}{L} & & \\ & & 1 & \frac{6\pi}{L} & & \\ & \cdots & & & \cdots & \cdots \\ 1 & & & & \frac{2\pi}{L} & \\ & 1 & \cdots & & \frac{4\pi}{L} & \\ & & 1 & & \frac{6\pi}{L} & \\ & \cdots & & & \cdots & \end{bmatrix}}^{X} \overbrace{\begin{bmatrix} \phi_0^1 \\ {\phi_0}^2 \\ {\phi_0}^3 \\ \cdots \\ a_0 \\ a_1 \\ a_2 \\ \cdots \end{bmatrix}}^{\beta} \tag{1.22}$$

3. We then perform a weighted linear regression in order to determine the reference profile and the translation parameters that minimize the least-square distance between the linear model and the successive recorded profiles. The weighted linear estimator $\hat{\beta}$ reads :

$$\hat{\beta} = (X^T W X)^{-1} X^T W Y,$$

where the matrices X, Y are defined in Equation 1.22. The matrix W is the matrix of weights. Assuming that errors on the phase are not correlated, it is diagonal and $W_{ii} = \frac{1}{\sigma_i}$, where σ_i is the estimated experimental error on the i-th measurement. Here we empirically choose $\sigma_i = \frac{1}{A_i}$, where A_i is the

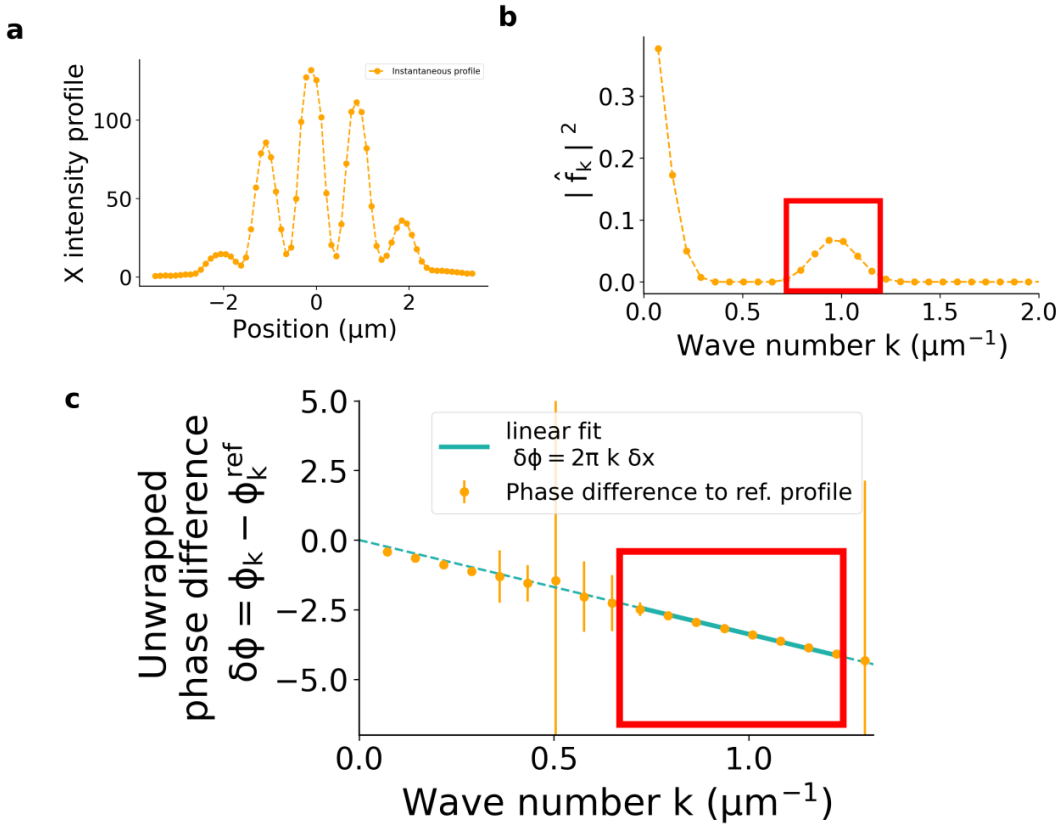

Figure 1-7: **X localization through discrete Fourier transform. a.** Instantaneous intensity X-profile of an interference pattern. **b.** Amplitude of the Fourier modes of the pattern showed in a. The sum is normalized to 1. The red square shows the modes that correspond to the oscillating part of the pattern. **c**. Unwrapped phase shift between the reference profile and the instantaneous profile showed in a. The phases of the modes inside the red square are fitted by a linear function. The displacement of the pattern in the direction x is inferred from the slope. Errors on the phase are taken as the inverse of the Fourier modulus shown in b.

amplitude of the Fourier mode whose phase is measured.

4. The first M lines of the vector $\hat{\beta}$ are the phases of the mode of the reference profile ϕ^j_{ref}.

X localization - The multiplication algorithm

As the particle moves in one of the three directions, the fringe pattern changes of position and the ROI must be adjusted to follow its center. Because the ROI is attached to the window, this implies discrete moves by one or several pixels of the window. These discrete moves affect the measured translation value. In order to avoid this artifact, we also used an alternative algorithm where no window is needed.

This empirical algorithm is based on the computation of the profile translation that minimizes the overlap between an experiment profile a theoretical profile. The theoretical profile corresponds to the analytical formula shown in 1.20, where the parameters w_x, w_y and k have been fitted to an experimental profile. The

Algorithm	Fourier	Multiplication
Localization error for fixed fringe	1.32 mpx	1.37 mpx
Computation time	60 μ s	140 μ s
Artifacts induced by a window	Yes	No

Table 1.1: **Comparison of the two algorithms described in this section for the estimation of the translation of the fringes.** The localization error corresponds to the spread of the distribution of the inferred localization of a fringe pattern over 800 frames. The computation time corresponds to a pair of fringe pattern (one per particle) analyzed with a single CPU core (Intel(R) Xeon(R) CPU E3-1270 v6 @ 3.80GHz).

best estimation of the translation parameter a_i is taken as the one that maximizes the score S defined by:

$$S(a) = \sum_{i}^{L} f_x(x_i) PSF(x_i - a) \tag{1.23}$$

S is thus the simple multiplication between the translated analytical profile and the instantaneous experiment profile f_x. The minimization is performed via Brent's method [Brent, 1971]. Because it is based on multiplication, the algorithm gives more weight the profile point with great intensity. The analytical profile converging to zero far away from the center of its center, it acts as a window. However, because this window moves at each iteration concomitantly with the parameter a of translation, there is no more artifact introduced by the windowing.

Interestingly, analysis made on the same movie with both algorithms show that the multiplication algorithm does not introduce measurement noise compared with the Fourier algorithm. However, it more than doubles the computation time (Table 1.1).

In the following, we will make use of the Fourier algorithm with a fixed ROI for the tracking of short substrates (< 100 nm) and use the multiplication algorithm for larger substrates or free particles, for which ROI update is necessary.

Y localization

Less effort has been dedicated to the algorithm of tracking in the Y direction as it does not contain information about the axial position of the particle and is thus less critical for us. Here, the center of the profile is simply obtained by computing the barycenter $\sum_{i=1}^{n} i f(x_i)$, where i stands for the pixel and f for the normalized light intensity.

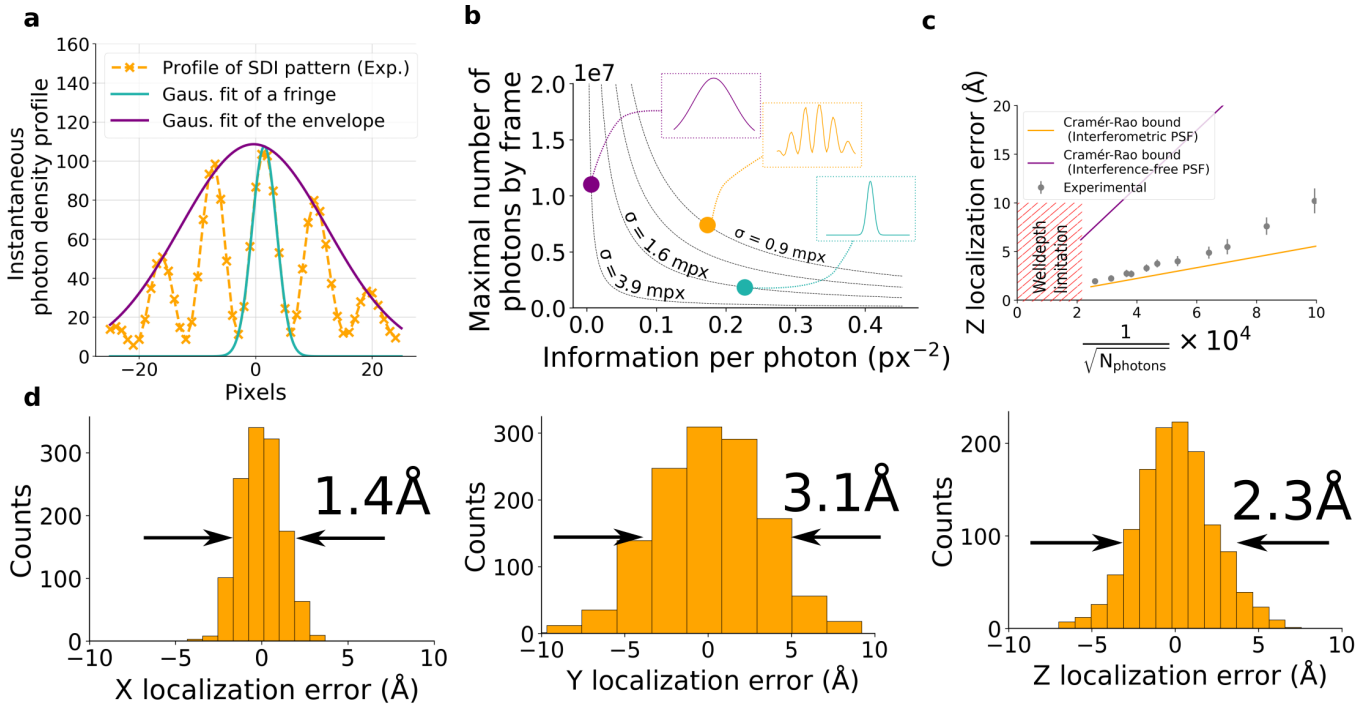

Figure 1-8: **Information content of the PSF of *Stereo Darkfield Interferometry* and experimental tracking precision. a.** Typical transverse density profile of a *SDI* pattern. One fringe and the envelope are being fitted by Gaussians. **b.** Theoretical number of photons by frame and information per photon for each profile shown in e. Interferences allow to increase the number of photons while keeping a good precision. Thin black lines join points with equal theoretical precision σ (values in millipixels). **c.** Standard deviation of the measured axial position of a microsphere as a function of light intensity (objective 100X). This is compared with the theoretical Cramér-Rao bounds computed from the experimental profile drawn in *d* and its envelope. The maximal light intensity is constrained by the camera's well depth (here 30.000 electrons per pixel). **d.** Distribution of the inferred position, at maximal light intensity, of the 3D position of stuck microspheres. 1280 frames are analyzed. No averaging is performed. The mechanical and thermal drift are subtracted in order to assess the optical noise of the setup (see Materials and Methods).

Imaging profile	Fisher Information ($px^{-2}.photon^{-1}$)	Maximal photon number per fringe and per frame	Theoretical localization precision (px)
SDI pattern (X)	$0,18$	7.4×10^6	0.9×10^{-3}
One fringe (X)	$0,23$	1.8×10^6	1.6×10^{-3}
Envelope (X)	$0,006$	11×10^6	3.9×10^{-3}
SDI pattern (Y)	$0,035$	7.4×10^6	2×10^{-3}

Table 1.2: Comparison of information related properties between the pattern of *Stereo Darkfield Interferometry*, the corresponding unstructured PSF, and a single peak of the pattern.

1.3.5 Subnanometer optical precision

In order to better understand the information theoretical content of this profile, we fit its envelope and a single peak to Gaussian functions. These fits are shown in figure 1-8.a. From these experimental profiles we deduce, using the discretized version of equation 1.9, the Fisher information that they contain with

respect to their translation as well as the maximum number of photons contained in one frame for a given camera well depth. Table 1.2 compares the number of photons and Fisher information that are contained in this PSF, as well as in a Gaussian fit of the envelope and in a single peak. Compared to these two cases, *SDI* permits to increase the number of photons contained in one frame without reducing drastically the information contained in one photon with regard to its horizontal translation (the direction that encodes for both the X and Z movement of the bead). Since the Y-profile is relatively well fitted by a Gaussian, the information contained in one photon concerning the translation along the axis Y can be computed from the Thomson-Webb formula (equation 1.10) and is also shown in table 1.2. It appears that it is smaller than in the X direction. This information could be increased by designing larger slits in the Y-direction (resulting in a thinner PSF at focus), but then, the PSF would be concentrated on a smaller camera area and the maximal number of photons received by frame would be smaller. Considering that the axial localization of the bead, whose information is contained in the X-direction of the PSF is the most critical for magnetic tweezers, we preferred to slightly sacrifice the precision in the Y-direction to optimize the frame-to-frame axial precision.

In order to measure accurately the optical noise of the setup and compare it to theory, it is necessary to uncouple it from the Brownian motion and from slow thermal or mechanical drifts that can affect the measurement. In order to do so, magnetic microbeads were melted on a glass surface. The position of 15 beads was then tracked for 5 seconds at 160 Hz at different light intensity. The average of the trajectory of the 15 beads was then subtracted from each individual trajectory in order to completely decouple the mechanical or thermal drifts from the setup. The spread of the distribution of the inferred positions of a particle was then compared to the theoretical Cramér-Rao lower bound (CRLB) computed from the x and y-profiles using the equation 1.9. The experiment was reproduced with different light intensities. The number of received photons N received at each intensity was computed by integrating the numerical level over the region of interest. The dependence of the localization error on the number of photons is shown on figure 1-8.c and figure 1-9, alongside the predicted localization error from the CRLB. The distributions of inferred position at maximum light intensity (well-depth saturation) are shown in figure 1-13.d. The x and z positions of the particles, that are deduced from the X translation of the fringe pattern almost reach the CRLB, showing that the inference algorithms are close to optimality. The Y position, while displaying a relatively small frame-to-frame localization error (3 ångströms), however, does not reach the CRLB, illustrating the sub-optimality of the naive algorithm used to measure the Y translation of the fringe pattern.

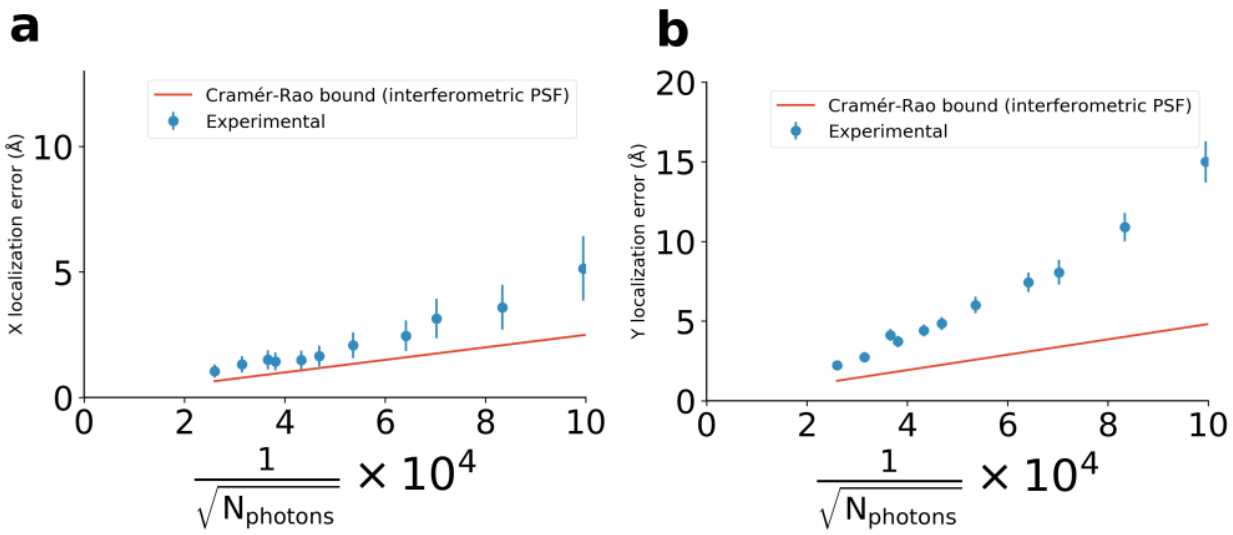

Figure 1-9: Experimental localization error in the X (**a**) and the Y (**b**) directions are compared to the Cramér-Rao lower bound.

1.3.6 Linearity and field dependence

Besides precision, linearity is another objective motivating the development of Stereo Darkfield Interferometry. Indeed, linearity would allow one to reach a good accuracy without the need of a calibration step. We briefly recall the difference between precision and accuracy: while a precision of σ consists in the ability to distinguish successive position p_1, $p_2 = p_1 + \sigma$ separated by a distance σ relatively from each other, accuracy consists in the ability to measure the position p from a given origin within a tolerance of σ. Exact linearity of the tracking technique would imply that the distance between the fringes is exactly proportional to the axial position of the bead z. Here we measure in what extent this is true.

In order to simulate experimentally a precise and controlled change of the position of the bead, we moved the objective (40X) using a piezoelectric device .

Figure 1-10.a shows the relation between the distance between the fringes and the focus position for a SDI setup with a 40X magnification. Figure 1-10.b shows the residues between the experimental points and the linear fit. The 40X setup displays nonlinearity up to 10 nm over an axial tracking range of 5 μm.

In order to reproduce the experiment with the 100X setup, which we did not equipped with a piezoelectric device, we used a 1 kb DNA hairpin as a proxy. The molecule was repetitively stretched at 18 pN and relaxed at 8 pN. Above 15 pN, the hairpin unzips and undergoes a sudden extension change of 1 μm (figure 1-10.e). During the opening, it also displays a blockage at a fixed position in the DNA sequence due

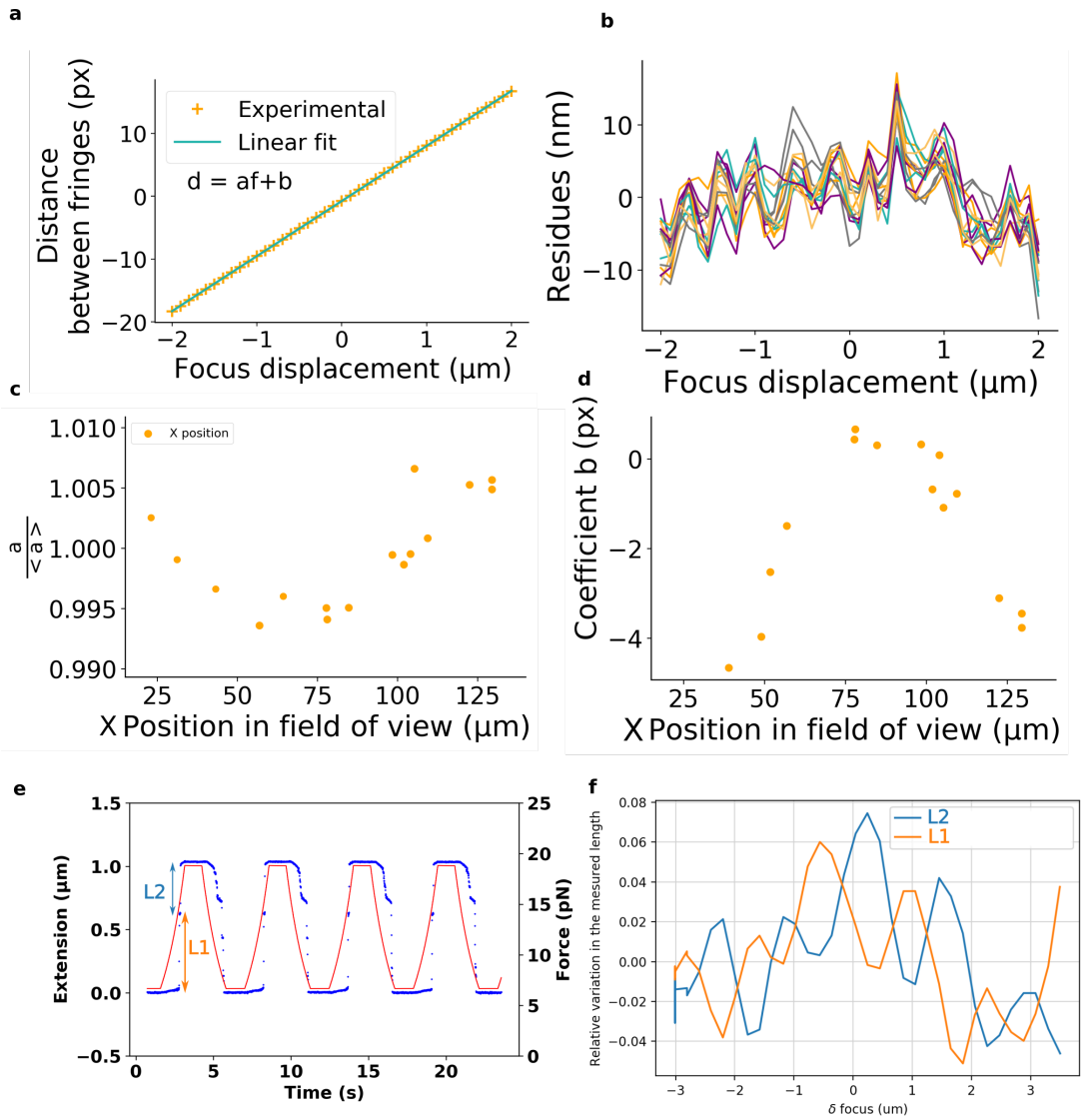

Figure 1-10: **Characterization of the linearity of *SDI* a.** Measured distance between the two fringes of one image as a function of the defocus (40X objective). **b.** Residues to linearity for 15 different beads. Pixels are converted to focus units, using the coefficient *a* of figure a., in order to clarify the extent of the error (15 different beads). **c**. Relative variation (compared to the average over all beads) of the slope of the linear relation shown in a. as a function of the bead position in the field of view (15 different beads). **d.** Variation of the intercept of the linear relation shown in a. as a function of the bead position in the field of view. **e.** Protocol for the measurement of non-linearity in the absence piezo devices (100X objective). A magnetic microbead is attached to a DNA molecule that undergoes transitions of fixed length when the force is changed. Red: applied force. Blue: measured extension. **f.** Variations of the measured transition length presented in e. when the focus is changed. 90 transitions are averaged for each focus position.

to the presence of a GC-rich region, which translates in a pause in the hairpin opening. We measured the position of the blockage compared to the closed state and to the open state as a function of focus position: if the system was perfectly linear, the measured value for these transitions should not depend on the focus position. We show in figure 1-10.f the result of this experiment. Over a focus sweep of 7 μm, the curves show non-negligible nonlinearity, with a measured extension that varies up to 10%.

While the causes of this nonlinearity were not identified with certainty during this work, three factors

might explain it:

- The first is the overlapping of the two vertically separated fringe patterns. Indeed, the second and third peaks of the vertical sinc pattern are responsible for a larger vertical spatial spread of the patterns (figure 1-11.a). This could be overcome by apodizing the slits in the y-direction in order to decrease the intensity of the secondary peaks.

- The second is the backscattering of the imaged particles, that probably causes a part of the light scattered from one of the incident light sources to reach the opposite fringe pattern. This effect will be stronger for small particles for which scattering is spatially more homogeneous. It will be discussed in more details in the next section.

- The third is the non-ideal translation of the fringe pattern with defocus. In equation 1.19, we calculated the translation of the interferometric pattern but not the translation of the envelope. Figure 1-11.b shows the movement of the position of a peak as a function of the one of the envelope when the focus is changed. The position of the envelope was computed by fitting the position of all bright peaks by a Gaussian while the position of the main peak was computed by fitting the signal by a Gaussian in its direct vicinity. It clearly appears that the envelope and the interferometric peaks do not translate at the same velocity, thus causing a slight deformation of the PSF with defocus.

.

Besides inducing non-linearity, the last point has another side effect: without the calibration of the envelope velocity, it becomes difficult to pair with certainty the peaks of the fringe pattern and of its translated version when the translation is too large. This uncertainty illustrated in figure 1-11.c might cause phase jumps in the signal: the translation of the fringe is only known modulo an interfringe. In practice, for the applications presented in this work, the problem could easily be solved, because we work at high-enough acquisition frequency so as to follow a given peak and avoid misidentifying it with its neighbors. However, this limits the absolute *calibration-free* characteristic of *Stereo Darkfield Interferometry*.

1.3.7 Impact of the size of the imaged particles

In this section, we explore the impact of the particle size on its imaging with *Stereo Darkfield Interferometry*. First, *Stereo Darkfield Interferometry* has been designed so that the size of the particle has a minimal impact on the shape of the PSF. Indeed, the PSF shape is primarily determined by the design of the slits. We show

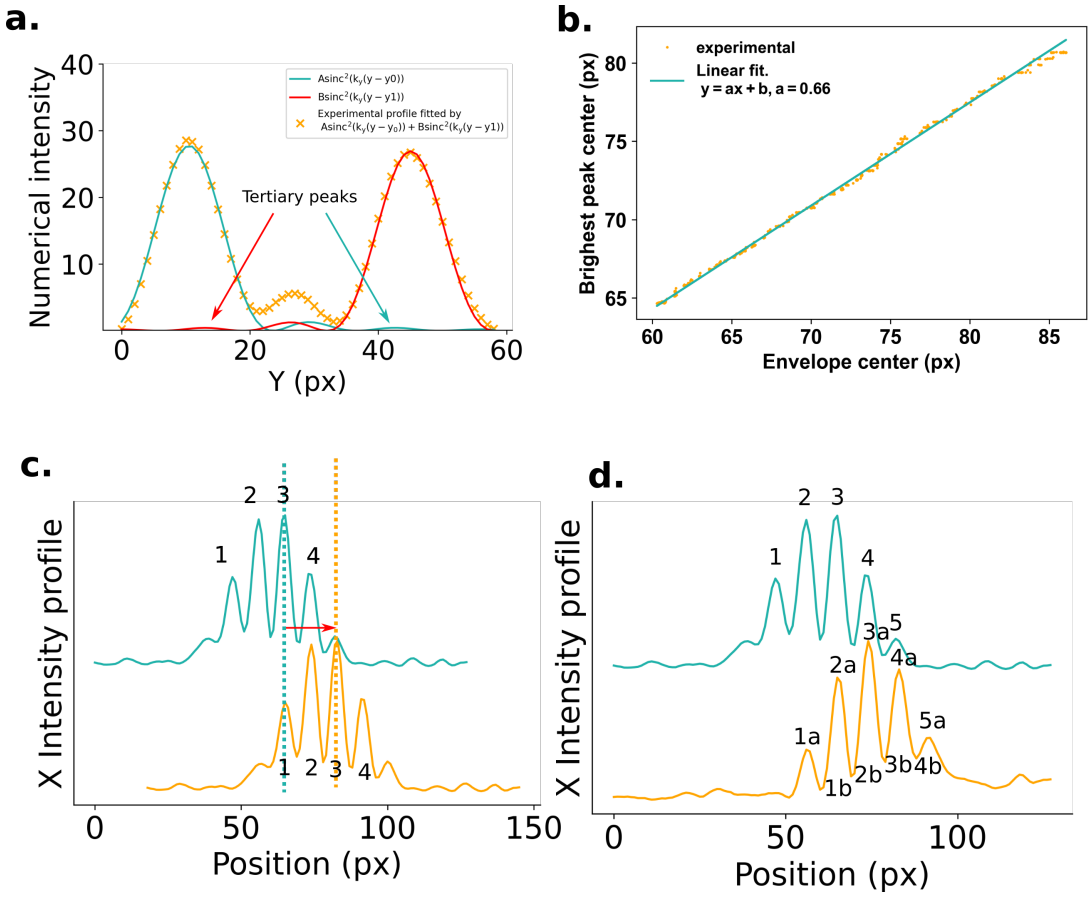

Figure 1-11: **Possible causes of non-linearity of *Stereo Darkfield Interferometry* a.** Experimental vertical profile of a whole SDI pattern (with the two-fringe pattern). Fitting this pattern by a sum of two sinc functions shows that the tertiary peak of each fringe pattern overlaps with the opposite fringe pattern. **b.** Experimentally determined position of the center of the envelope of a *SDI* profile as a function of the position of one peak *SDI*. These positions are inferred by applying two Gaussian fits as shown in figure 1-8.a. for the same image at different focus positions. The phase velocity is clearly smaller than the group velocity. This curve has been acquired for one bead. In practice, the dependence between both velocities is position-dependent. **c.** Representation of an ideal translation of the X-profile. The blue profile is experimental and the yellow one is the same as blue but translated. **d.** Real translation of the X-profile. The yellow profile has been captured from the same bead at a different focus position. Because of the deformation of the profile, measuring the translation is ambiguous without a calibration of the group velocity.

in figure 1-12 .a the image of particles of three different magnetic microspheres, whose diameters are respectively 0.5, 1 and 2.8 μm: they present very similar PSF. However, the brightness of the different beads are very different. The intensities of incident light I_i and the shutter times τ_s for the three images presented in figure 1-12.a are adjusted so that the image saturates the well depth of the camera. The ratio between the time-integrated light intensity for a given particle and the one for a reference particle of 1 μm is called E_c. We have : $E_c = \frac{I_i \tau_s}{I_i^{1\mu m} \tau_s^{1\mu m}}$. E_c for the three different sizes of particles is shown in figure 1-12.a. The microsphere of diameter 500 nm is roughly 7 times less bright than the bead of diameter 1 μm. This important difference is due to the dependence of the scattering cross-section on the particle diameter. For instance, for particles much smaller than the wavelength of the incident light ($d < 0.1\lambda$), which obey

Rayleigh scattering [Rayleigh, 1899], the coefficient Q_{scatt} that relates the incident light intensity and the scattered intensity evolves as d^4. In this Rayleigh case, the scattering is, furthermore, isotropic, while *SDI* only captures a small angular aperture defined by the width and position of the slits in the mask. With the slits used in this setup, we collect only 1.2% of the whole solid angles. We thus capture only 1.2% of the whole scattered light in the case of isotropic scattering.

However, magnetic microspheres used in magnetic tweezers have a micrometric size and do not fall under the Rayleigh regime. In particular, their scattering is not isotropic in space and is concentrated around $\theta = 0$, θ being the angle between the incident light and the scattering direction. In the far-field, the scattering properties only depend on θ and the so-called Mie scattering matrix S. For a unpolarized incident light, the scattered intensity in the direction θ is related to incident intensity I_{inc} as follows [Bohren and Huffman, 1983, Chapter 3, p.63]:

$$I_{scatt}(\theta) = \frac{I_{inc}}{2k^2d^2}(|S_{11}(\theta)|^2 + |S_{22}(\theta)|^2), \tag{1.24}$$

where k stands for the norm of the wave vector of the incident light, and d for the distance of the observer from the scatterer. For a layered or homogeneous sphere, the Mie scattering matrix can be computed as an infinite series. It depends on the complex refractive indices of the medium and of the particle, on the wavelength of the light and on the diameter of the particle. Here we used the Python PyMieScatt [Sumlin et al., 2018] module in order to compute these series. We then projected the obtained spherical intensity on the Fourier plane of the objective and integrated the scattered intensity that goes through the slits in our setup. Figure 1-12.b shows how the intensity scattered by a particle is distributed in the Fourier plane compared to the position of the slits. Figure 1-12.c shows the prediction of the scattered intensity captured by the slits and compares it to the experimental results.

In practice, it is difficult to observe magnetic particles (made out of iron oxide and polystyrene) of diameter smaller than 500 nm. Figure 1-12.d shows in the right bottom panel an image of a bead of diameter 300 nm. The top fringe is obtained with the same wavelength as the previous images for larger particles. Even by increasing the light power, distinguishing the particle becomes harder because of the larger relative intensity of the background scattering. A solution is to reduce the wavelength of the incoming light so as to increase the scattered intensity. For instance, the bottom fringe pattern of the same image was obtained with blue light (450 nm), and can be well distinguished from the background. However, this solution is

limited by the phototoxicity of small wavelengths.

As a consequence, it appears that *Stereo Darkfield Interferometry* is well suited to study microparticles. The light irradiance needed to track in real-time micro-beads with nanometer accuracy at 1 kHz is of the order of the W/cm^2, which is modest compared to the irradiance used for fluorescence-based 3D tracking $1kW/cm^2$. Observing particles of smaller sizes would, however, require advanced post-processing procedures in order to remove the background scattering [Möckl et al., 2020] or more powerful light sources with smaller temporal coherence, such as arc mercury lamps [Huhle et al., 2015].

1.4 Conclusion

We presented in this section *Stereo Darkfield Interferometry*, a PSF engineering method for 3D-tracking of microparticles. We showed that it allows a frame-to-frame optical precision of 2Å in the axial direction, This represents about one order of magnitude of improvement in the frame-to-frame optical precision of the widely-used ring-based methods. Compared to the most recently developed 3D-tracking methods, *SDI* performs well with respect to the information per photon contained in its PSF. Figure 1-13.a compares its information per photon with existing 3D-tracking methods for fluorescent imaging, where the information per photon is particularly important given the low photon yield. Interestingly, our method also answers two challenges that are stranger to researchers used to work with fluorescence. On one hand, it allows dark field (bright field is never an issue in fluorescence microscopy because of wavelength-based filtering). On the other hand, it allows to maximize of the photon-content of the PSF (fluorescence methods are usually not limited by the well depth of the cameras because of their low photon yield). Indeed, *SDI* performs particularly well regarding the maximum number of photons per frame (figure 1-13.b). That is mainly what allows such a good frame-to-frame resolution and the real-time tracking of a whole field of view (figure 1-14).

The intrinsic dark field characteristic of fluorescence also explains why fluorescence-based 3D tracking methods cannot be directly transposed to scattering-based techniques, where the incident light plays an important role and cannot be easily separated from the scattered light. It also explains why background scattering is less a problem in fluorescence: scattered light from non-fluorescent particles is simply filtered out. On the other hand, *SDI* would poorly perform in a single-molecule fluorescence context, because of its high photon cost: 99% of the light is lost in the case of particles much smaller than the wavelength.

Regarding particles of intermediary sizes (~100 nm), we showed that *SDI* is a limited solution and that optimization of the background treatment would still be necessary to permit such an application.

We also studied the linearity of *Stereo Darkfield Interferometry*. While it is at the core of the imaging concept, linearity is not ideal enough to permit, in the absence of calibration, an absolute localization with nanometer accuracy over a measurement range larger than the microns. Linearly fitting the response of the PSF to the defocus of the particle over such a range causes absolute measurement errors up to 10 nm. A few leads have been proposed in order to come closer to perfect linearity. However, at this stage, performing a calibration step with a piezoelectric device over the whole field of view seems the safest solution for applications that need an excellent accuracy. We showed that the evolution of residues with defocus was close to linear over defocus ranges of 100 nm: this would thus be the order of magnitude of the focus step size needed for calibration. In the following work, all applications of *SDI* to force spectroscopy involve substrate as short as 40 nm with a strong need for precision but not of accuracy. For such substrates (below 100 nm) and applications of that kind, a calibration step is not necessary and will not be performed.

Finally, we have not performed a thorough evaluation of the impact of the slits design during this work, essentially because their shape was already optimized for microbead tracking by Thibault Vieille[1] before the arrival of the author in the laboratory and the start of his research. Still, it is important to keep in mind that their width, length, position and separation are parameters that can be adapted to the application. In order to compensate for this lack of data, the reader will find in table 1.3 a qualitative assessment of the impact of these parameters on various optical properties of the setup, summarizing the considerations of this section.

[1] thibault.vieille@depixus.com

	Slits width	Slits height	Slits separation $x_2 - x_1$	Slits mean position $\frac{x_1+x_2}{2}$
Axial Fisher information per photon	—	—	↗ larger structure modes	↗ increased axial magnification
Max. photon numbers per frame	↘ thinner PS	↘ thinner PSF	—	—
Photon yield	↗ larger aperture	↗	—	↘ objective transmission at large angles
Depth of field	↘ smaller angular range	↘	—	—
Maximum particle density	↗ thinner PSF	↗ thinner PSF	—	—
Axial localization precision per frame	↘ less photons per frame	↘ less photons per frame	↗ better information per photon	↗ increased axial magnification
Transverse localization precision per frame (X-direction)	↘ less photons per frame	↘ less photons per frame	↗ better information per photon	—
Transverse localization precision per frame (Y-direction)	↘ less photons per frame	↗ thinner Gaussian in Y	—	—

Table 1.3: Impact of the slits design on the optical properties of SDI. The photon yield is the number of photons scattered by an object and received by the camera. The axial sensitivity is the axial magnification over the lateral magnification, as expressed in eq 1.19. ↗ indicates a positive effect, ↘ indicates a negative effect while — indicates a neutral effect.

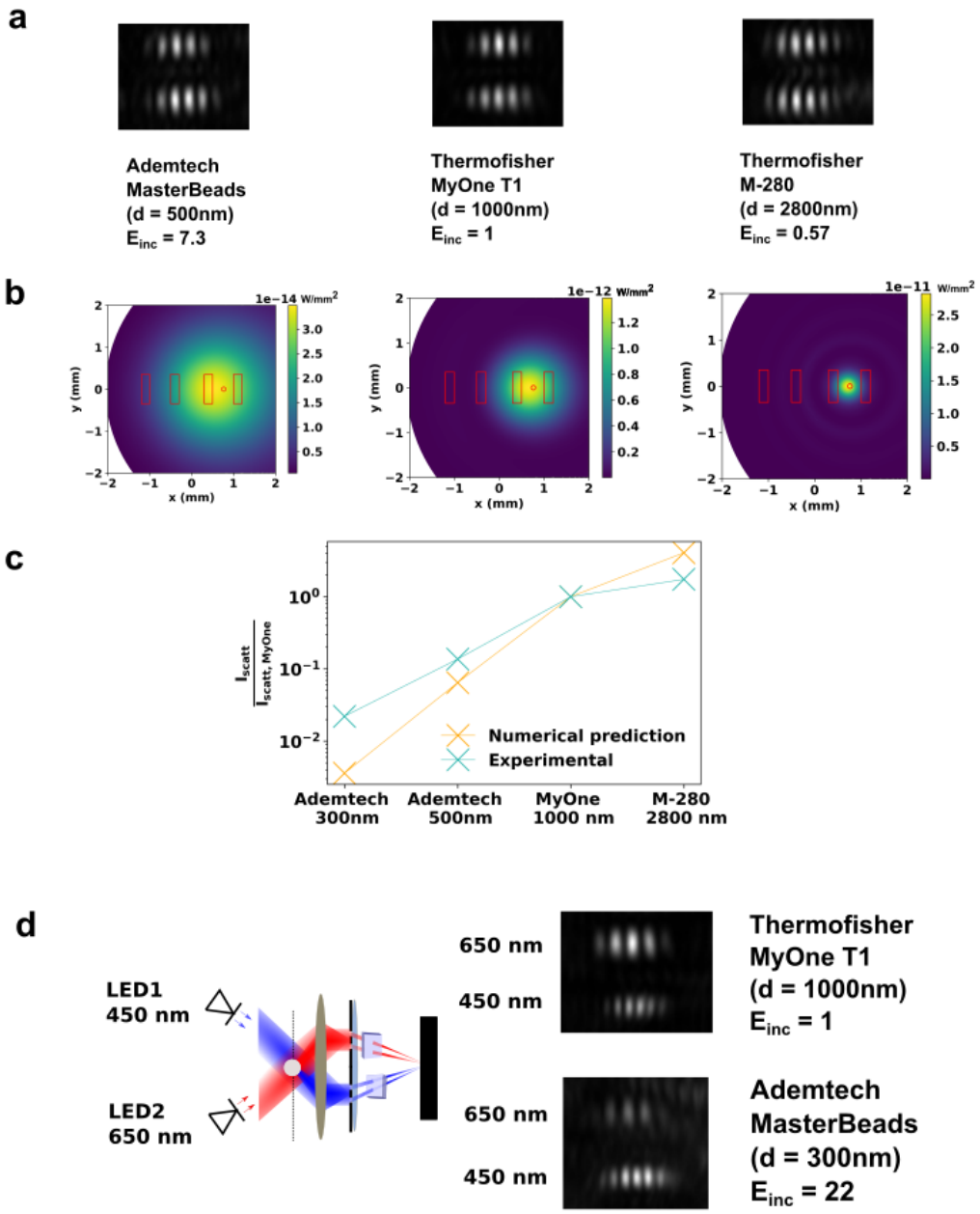

Figure 1-12: **Dependence of SDI images with particle sizes using a 100X objective. a**. Shape of the PSF for three different particle sizes. The intensity of the incident light and the shutter time are adjusted in order to acquire images close to pixel saturation condition. E_{inc} is the relative light power used for each imaged compared to the light power used to image the 1 μm bead (Thermofisher MyOne T1). It is computed as $(I_{bead} \times s_{bead})/(I_{MyOne} \times s_{MyOne})$, where I is the light power emitted by the LED and s the shutter time used to capture the images. **b.** Estimated distribution of the light intensity in the Fourier plane of the objective due to the scattering of one bead for a constant incident illumination of 1 W/m^2. Estimations are based on the computation of the Mie scattering matrix with the free software PyMieScatt [42]. The script is available at https//github.com/Mriv31/StereoDarkfieldInterferometry. Red rectangles represent the slits placed in the Fourier plane. The red circle represents the convergence point of the unscattered incident parallel light. For Ademtech beads, the refractive index of the beads is taken equal to 1.83. For Thermofisher beads, it is taken equal to 1.66. **c.** Comparison of the relative scattered light intensity (compared to MyOne beads) measured experimentally (blue) and computed (orange) by integrating the intensities shown in b. over the whole area of the slits. **d.** Effect of the wavelength on the SDI images. To facilitate comparison, one path is illuminated with a light of wavelength 450 nm while the other is illuminated with a light of wavelength 650 nm. The wavelength of the light changes the interfringe. More importantly, it strongly increases the brightness of particles of diameter 300 nm, allowing us to partially compensate the loss in scattering cross-section.

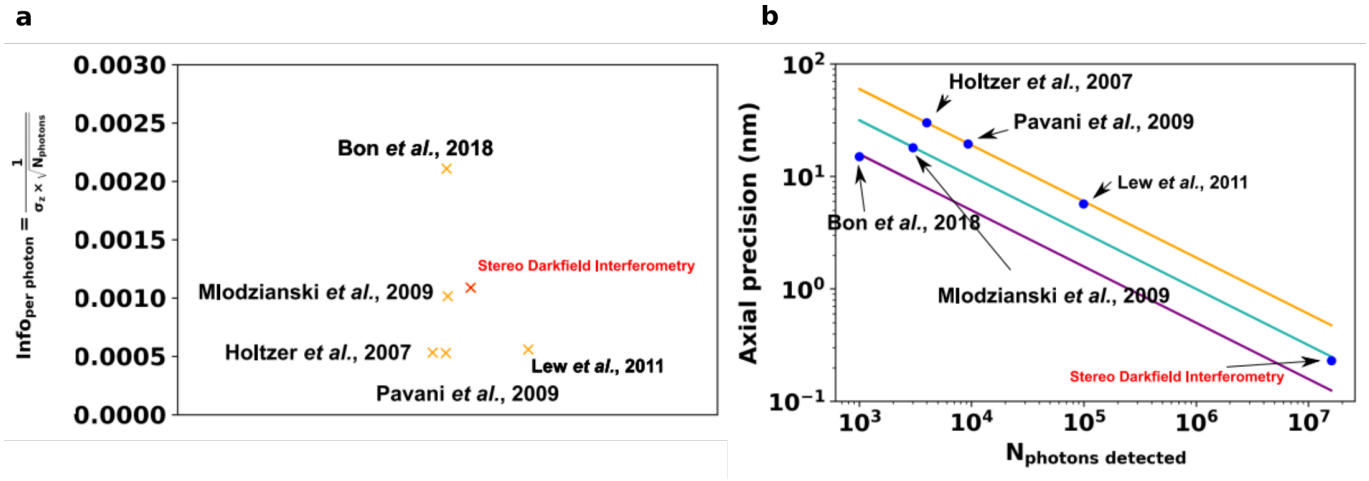

Figure 1-13: **Comparison of the performance of *Stereo Darkfield Interferometry* compared to other PSF engineering methods.** Selected methods are the one that mentioned the photon number and the associated axial localization σ_z **a.** Comparison of the information per photon $(\sigma_z \times \sqrt{N_{photons}})^{-1}$. **b.** Axial precision σ_z as a function $\sqrt{N_{photons}}$. Points belonging to the same lines have same information content per photon. *SDI* displays a remarkably high number of photons per frame.

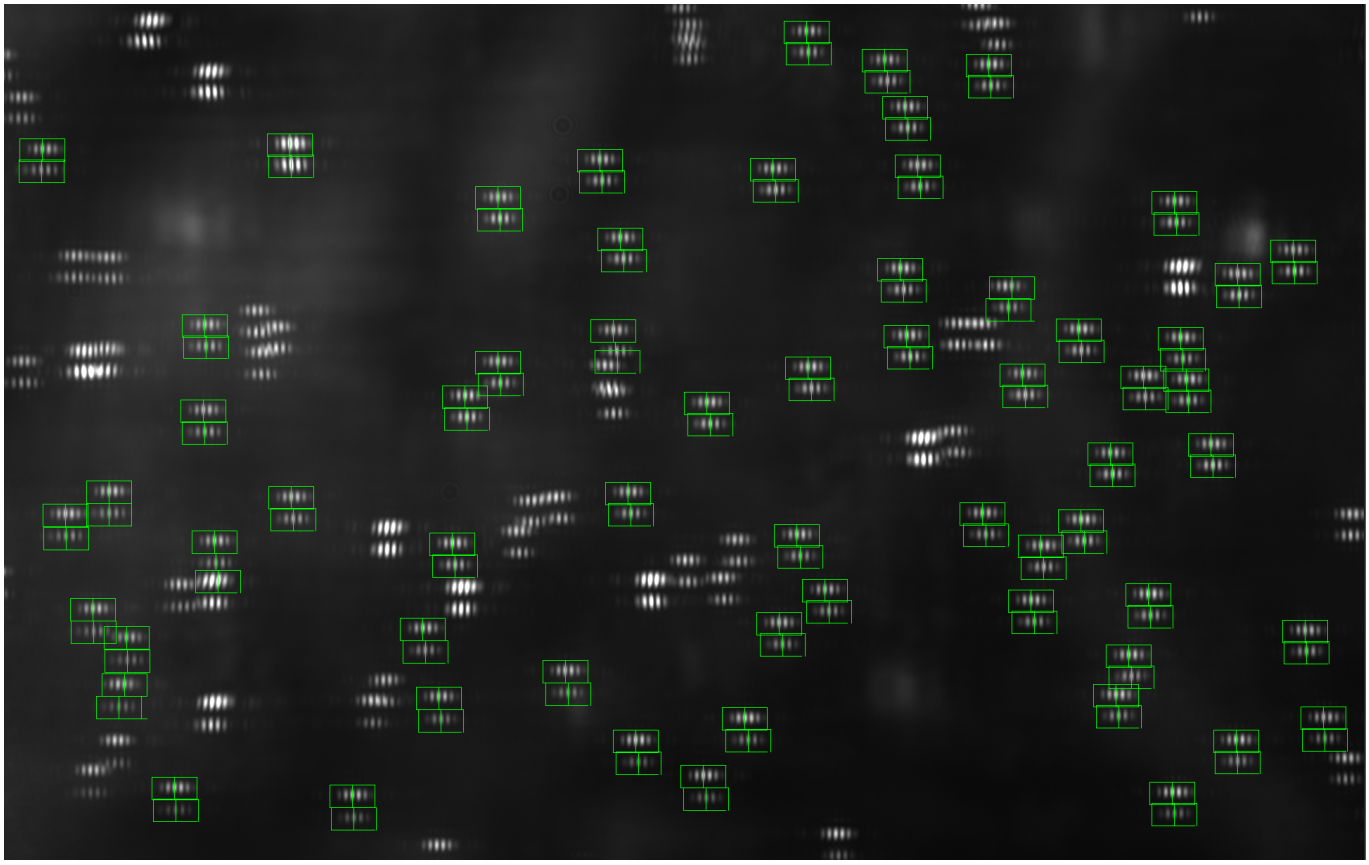

Figure 1-14: **A whole field of view tracked in real-time with *Stereo Darkfield Interferometry***. Each pair of fringes, materialized by two green boxes, corresponds to one magnetic bead. Scale bar, 10 μm. 100X objective.

Chapter 2

High-resolution magnetic tweezers

We described in the previous chapter a 3D-tracking optical method that allowed us to reach a subnanometer optical precision for the localization of a microparticle. This technique can be easily combined with force spectroscopy based on magnetic tweezers. As we explained in the introductory chapter of this work, typical magnetic tweezers use two antiparallel permanent magnets in order to create a strong and homogeneous magnetic gradient. The gap between the two magnets (typically 300 μm) is sufficiently wide to let the incoming incident light pass through. Contrarily to standard illumination techniques, *Stereo Darkfield Interferometry* makes use of two different light sources with important incident angles (~40°). This is not a problem as long as the direction of the gap of the magnet is aligned with the two opposite light sources (figure 2-1). *SDI* can thus be easily coupled to magnetic tweezers. However, the optical resolution is not the only limitation to the spatiotemporal resolutions of magnetic tweezers. Indeed, the ångströmic resolution that we described in the previous chapter only applied to fixed scatterers. For beads attached to biomolecules, the bead is not fixed and undergoes a Brownian motion that depends on the thermodynamical properties of the DNA and on the drag that is applied to the bead. This Brownian noise adds up to the optical localization noise. In this chapter, we will briefly describe the physics behind this noise. We will see that we cannot define a spatial resolution independently of a temporal resolution and will see how statistical mechanics allows predicting the spatiotemporal resolution of magnetic tweezers as a function of the size of the bead the biomolecule is tethered to. Then, we will demonstrate experipmentally that the gain in resolution allowed by the optical technique described in the previous chapter is sufficient to perform biophysical nanometric measurements that were not possible with magnetic tweezers so far. However, the characterization of the discrete helicase mechanism, which was an important motivation of this work,

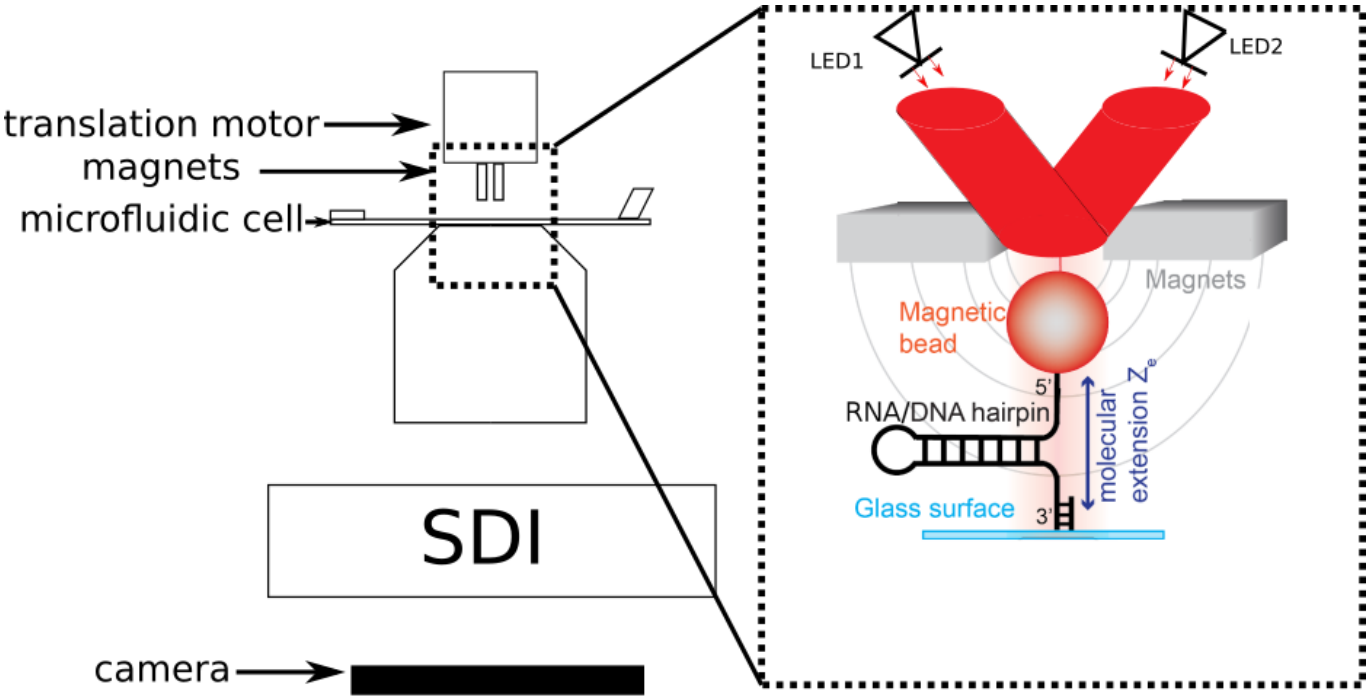

Figure 2-1: **Coupling of Stereo Darkfield Interferometry with magnetic tweezers.** The two light beams of the opposite incidence go through the gap between the magnets. The rotation of the magnets is still possible but only at discrete values (half-turns). The microbead is not displayed at the right scale. In the following work, we will use beads that are much larger ($d = 1\mu m$) than the DNA substrate ($l \simeq 40nm$).

remains, in spite of *Stereo Darkfield Interferometry*, partially unsatisfactory.

2.1 Physics of a tethered Brownian bead

2.1.1 Overdamped Langevin dynamics

The physics of a Brownian microsphere is classically described by the Langevin equation :

$$m\ddot{z} = -\gamma\dot{z} - k(z - z_0) + \Gamma_T(t), \tag{2.1}$$

where m is the mass of the particle, γ its friction coefficient, z_0 its equilibrium position, k the stiffness of the trap it is in, and Γ the random force applied on it by the thermal bath at temperature T, the so-called Langevin's force.

Usually, due to the small mass of the bead and the low Reynolds number the inertial term can be neglected in micromanipulation studies, and the corresponding equation is called the *overdamped* equation:

$$0 = -\gamma\dot{z} - k(z - z_0) + \Gamma_T(t), \tag{2.2}$$

The order of magnitude of the inertial term $m\ddot{z}$ in the whole Langevin equation is $\frac{mZ}{\tau^2}$ and the one of the friction term $\gamma\dot{z}$ is $\frac{\gamma}{\tau}$, where τ and Z are respectively the typical time and spatial amplitude of the bead's movement.

If the overdamped regime is valid, the typical time of motion reads $\tau = \frac{\gamma}{k}$. The overdamped approximation is thus self-consistent if :

$$\frac{m}{\tau^2} \ll \frac{\gamma}{k\tau},$$

which reduces in :

$$m \ll \frac{\gamma^2}{k}$$

For the micro-manipulation of a micrometric bead MyOne T1 (Thermofisher) in water,($\eta = 10^{-3}$), we have:

$$\gamma = 6\pi\eta R \simeq 10^{-8}\text{kg.s}^{-1} \tag{2.3}$$

$$k \in [10^{-5}, 10^{-2}]\ \text{N/m} \tag{2.4}$$

$$m = \frac{4}{3}\pi R^3 \rho \simeq 0.5 \times 10^{-15}\ \text{kg}, \tag{2.5}$$

the value of k depending on the tethered substrate and the applied force. We will give some examples later in this work.

For the extreme case $k = 10^{-2}$ N/m, we get:

$$\frac{mk}{\gamma^2} \simeq 0.05$$

For more common cases, where $k \approx 10^{-5} N/m$,

$$\frac{mk}{\gamma^2} \simeq 0.5 \times 10^{-4}$$

These orders of magnitudes justify the overdamped approximation.

Finally, we recall that the consistency of Langevin dynamics with statistical mechanics requires:

$$< \Gamma_T(t) >= 0 \tag{2.6}$$

$$< \Gamma_T(t)\Gamma_T(t') >= 2\gamma k_B T \delta(t-t') \tag{2.7}$$

2.1.2 Stiffness and thermodynamics of a tethered molecule at constant force

Here we recall some generalities concerning the thermodynamics of a single molecule tethered at force F. Indeed, the stiffness k of the energetic trap in which the bead is placed depends on the thermodynamics of the tethered molecule.

The probability density of a given polymer to have an end-to-end extension $\vec{l}$ when a force F_z is applied in the direction z reads:

$$\rho_F(\beta,\vec{l}) = C(\beta)e^{\beta(Fl_z - G(\beta,\vec{l}))}$$

$C(\beta)$ is a normalization constant and $G(\beta,\vec{l})$ is the partial free energy of the molecule:

$$G(\beta,\vec{l}) = k_B T \ln(\mathscr{Z}_{\vec{l}}),$$

where $\mathscr{Z}_{\vec{l}}$ is the partial partition function of the molecule that is the Boltzmann weight integrated over all microstates of the end-to-end extension $\vec{l}$:

$$\mathscr{Z}_{\vec{l}} = \int_{\{\sigma,\vec{l_\sigma}=\vec{l}\}} e^{-\beta E(\sigma)} d\sigma$$

In practice, if the molecule is tethered at large enough distance from the glass surface, its behavior is isotropic and only depends on l, the norm of $\vec{l}$. We thus write $G(\beta,l)$ instead of $G(\beta,\vec{l})$[1].

Let us call $\mathscr{G}$ the free energy of the molecule coupled to a magnetic bead at a magnetic force F.

$$\mathscr{G}(F,\vec{l}) = G(\beta,l) - Fl_z$$

The most probable value of $\vec{l}$ at constant force F is the one that minimizes $\mathscr{G}$:

[1] Let us note that $G(\beta,l)$ does not represent the probability for the end of the molecule to be at any point at a distance l from the other end but the probability that it is at one particular point in space separated by l from the other end.

$$\frac{\partial \mathscr{G}}{\partial l_z}\Big|_{\vec{l}=\vec{l^*}} = \frac{\partial G(\beta,l)}{\partial l}\frac{l_z^*}{l^*} - F = 0$$

$$\frac{\partial \mathscr{G}}{\partial l_x}\Big|_{\vec{l}=\vec{l^*}} = \frac{\partial G(\beta,l)}{\partial l}\frac{l_x^*}{l^*} = 0$$

$$\frac{\partial \mathscr{G}}{\partial l_y}\Big|_{\vec{l}=\vec{l^*}} = \frac{\partial G(\beta,l)}{\partial l}\frac{l_y^*}{l^*} = 0$$

If we make the standard hypothesis that $G(l)$ is strictly increasing and convex, this results in $l_x^* = 0, l_y^* = 0, l_z^* = l^*$ and $\frac{\partial G(\beta,l)}{\partial l}\Big|_{l^*} = F$.

By measuring the force $F(l)$ to be applied experimentally so that the most probable position of the molecule l^* is equal to l, one can thus reconstitute the dependence of its free energy:

$$G(\beta,l) = G(\beta,0) + \int_{l'=0}^{l'=l} F(l')\mathrm{d}l' \tag{2.8}$$

Let us note that the force extension curve $F(l)$ defines a bijective relation between l and F. Thus, most authors use indifferently both variables.

Let us now develop the free energy of the molecule in the vicinity of $\vec{l^*} = \begin{pmatrix} 0 \\ 0 \\ l^* \end{pmatrix}$

We first note that $l = \sqrt{l_x^2 + l_y^2 + l_z^2}$:

$$\left\{ \frac{\partial l}{\partial l_i} = \frac{l_i}{l} \right.$$

where i stands for x, y or z. It follows that:

$$\left\{ \frac{\partial G(l)}{\partial l_i} = \frac{\partial G(l)}{\partial l}\frac{l_i}{l} \right.$$

and:

$$\left\{ \frac{\partial G(l)}{\partial l_i \partial l_j} = \frac{\partial G(l)^2}{\partial^2 l}\frac{l_i}{l} + \frac{\partial G(l)}{\partial l}\frac{\delta_{ij}}{l} - \frac{\partial G(l)}{\partial l}\frac{l_i^2}{l^3} \right.$$

At the most probable position l^*, the Hessian of the free energy thus reads:

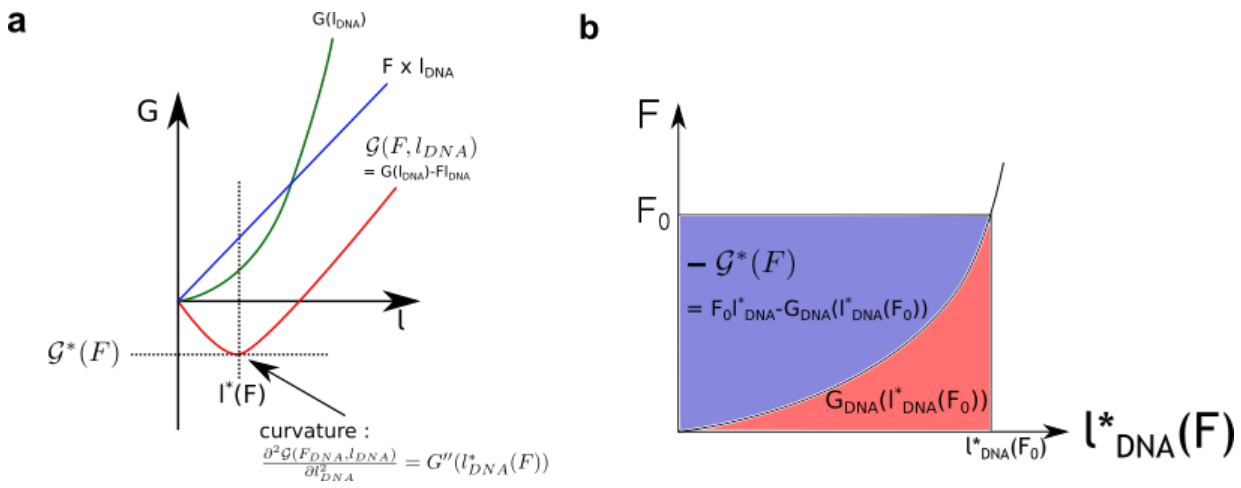

Figure 2-2: **Reminders of basic thermodynamics and definition of the notations. a.** The Gibbs free energy of the whole system (bead+molecule) at a force F, $\mathcal{G}^*(F)$, is the Legendre transform of the free energy of the molecule in the absence of force field $G(l)$. $\mathcal{G}^*(F)$ corresponds to the Gibbs free energy of the whole system at the molecule most probable position at force F, $l^*(F)$. The curvature of the red curve is the same as the one of the green curve and defines the fluctuations around the most probable length. **b.** A single-molecule experimentalist has access to the most probable length at force F, $l^*_{DNA}(F)$. From this force extension curve, we can easily reconstruct the molecule Gibbs energy as a function of its length l (red area). The energy of the whole system (bead + molecule) at force F is the opposite of the blue area.

$$\mathscr{H} = \begin{bmatrix} \frac{1}{l^*}F(l^*) & 0 & 0 \\ 0 & \frac{1}{l^*}F(l^*) & 0 \\ 0 & 0 & \frac{\mathrm{d}F}{\mathrm{d}l^*} \end{bmatrix} \tag{2.9}$$

where again $F(l^*)$is the force that verifies $\left.\frac{\partial G(\beta,l)}{\partial l}\right|_{l^*} = F$.

If we only consider the second-order derivatives and thus approximate locally the free energy of the molecule by a parabola, we get:

$$\rho_F(F,\vec{l}) = C(\beta)e^{\beta(Fl_z - G(\beta,l))} \simeq C(\beta)e^{\beta(Fl_z^* - G(\beta,l^*))}e^{\frac{-\beta}{2}\vec{l}^T\mathscr{H}\vec{l}} \simeq C_2(\beta,F)e^{\frac{-\beta}{2}\vec{l}^T\mathscr{H}\vec{l}}$$

As a consequence, the molecule behaves locally as a spring of stiffness

$$\begin{cases} k_x = \frac{F(l)}{l} \\ k_y = \frac{F(l)}{l} \\ k_z = \frac{\mathrm{d}F}{\mathrm{d}l} \end{cases} \tag{2.10}$$

Usually, the free energy of a polymer is extensive with regards to the number of monomers N. It is for example the case for the freely jointed chain model with extension (EFJC) or the worm-like chain

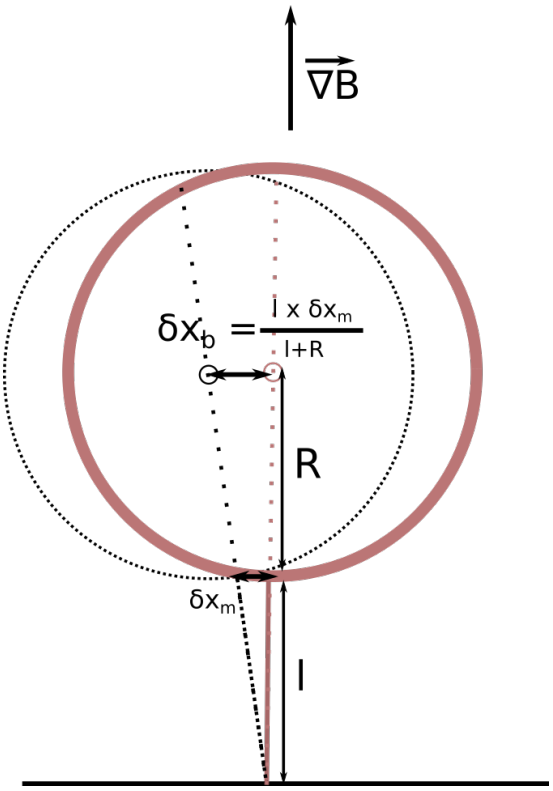

Figure 2-3: **How the bead affects the measurement of the stiffness of the tethered molecule.** Movement of the bead as described in [Allemand, 1997]. The bead moves proportionally to the molecule end and can freely rotate around its anchoring point. Its finite radius induces a movement of its center δx_b that displays a larger amplitude than the movement of the end of the molecule δx_m.

model (WLC) that describe well single-stranded and double-stranded DNA respectively. It follows that by multiplying the number of monomers by λ at constant force, the extension of the molecule is also multiplied by λ. It also follows that k_x, k_y, and k_z vary as $\frac{1}{N}$ at constant force[1]: the shorter the polymer, the more rigid.

When a micrometric bead is attached to a molecule, the amplitude of its fluctuation is larger than what is predicted by equation 2.10 because of its radius. This is explained in figure 2-3. As a consequence, the fluctuations of a bead of radius R tethered to a molecule need to be corrected and k_x becomes equal to $\frac{F(l)}{l+R}$ [Allemand, 1997, Daldrop et al., 2015, Ostrofet et al., 2018]. The direction x is here perpendicular to the magnetic field. In the parallel direction y, the fluctuations of the bead are made more complex by the magnetic anisotropy of the bead [Mosconi et al., 2011a]. In this direction, they depend on the distance of the anchoring point of the molecule on the bead with the main magnetic axis of the bead [Klaue and Seidel, 2009a].

[1]This dependence does not hold perfectly for short polymers. There are some finite-size effects that are for example well-described for double-stranded DNA [Seol et al., 2007]: while the force extension curve of long dsDNA is well-fitted by the worm-like chain [Bouchiat et al., 1999] with a persistence length of about 50 nm, shorter dsDNA polymers [Shon et al., 2019] (typically less than 10 kb) display spurious shorter persistence lengths that can be explained by the finite worm like chain model (FWLC).

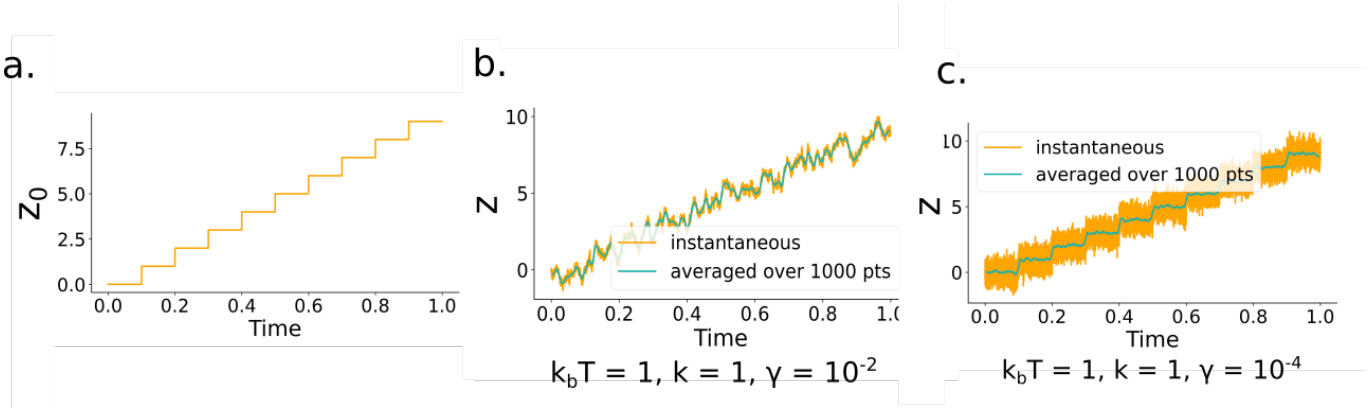

Figure 2-4: **Illustration of the impact of drag on the spatiotemporal resolution of steps in the movement of a Brownian bead.** Simulations of the overdamped Langevin equation with discrete changes of the equilibrium position z_0 **a**. Evolution of the equilibrium position z_0 with time. **b.** Brownian simulations with the time evolution of z_0 presented in a, $k = 1$, $k_BT = 1, \gamma = 10^{-2}$. **c.** Brownian simulation with the time evolution of z_0 presented in a, $k = 1$ $k_BT = 1, \gamma = 10^{-4}$.

2.1.3 Hydrodynamic drag, stiffness and spatio-temporal resolution

We describe here to what extent the Brownian motion of the bead limits the detection of discrete extension steps of a tethered molecule. We are thus interested in the minimum observable step size σ of the equilibrium position of the bead z_0 (*i.e* the extension of the tethered molecule).

The equipartition theorem states that the position of the bead $\delta_z = z - z_0$ verifies the following relation:

$$\sigma_{stat} = < \delta_z^2 > = \frac{k_BT}{k_z} \tag{2.11}$$

This indicates the amplitude of the Brownian motion of the bead, but time does not participate in this relation. However, imagine that the bead goes through all the possible positions allowed by 2.11 within $1\mu s$. Then, by averaging its position during 1ms, one could get a much better precision with regard to z_0. This effect is explained in figure 2-4. A Brownian motion is simulated while increasing the equilibrium position by regular steps. Both simulations are performed with the same stiffness, but the drag, and thus the timescale of the Brownian motion changes. In figure 2-4.b, it is not possible to distinguish the individual steps of the position of the Brownian particle because its velocity is too small compared to the time interval between two steps. However, in figure 2-4.c, individual steps can be easily distinguished by averaging the position of the fast-moving bead over many frames. This shows that the spatial resolution of a setup cannot be decoupled of its temporal resolution.

We will now formalize this intuition. The smallest averaging window that is necessary to get an error

on the mean position z_0 that is smaller than the step size σ will constitute a lower limit of the temporal precision T_{min} needed to distinguish the steps.

This temporal precision T_{min} thus must verify that:

$$< (\frac{1}{T_{min}} \int_0^{T_{min}} (z(t) - z_0)dt)^2 > \quad < \sigma^2$$

If such a relation holds, the error of estimation of z_0 through the averaging of the signal during T_{min} is small enough that the step can be observed when z_0 moves by a distance σ.

For the sake of simplicity but without losing generality, we will take $z_0 = 0$. We have, for any averaging window T_{av} :

$$< (\frac{1}{T_{av}} \int_0^{T_{av}} z(t)dt)^2 >= \frac{1}{T_{min^2}} \int_{t=0}^{T_{av}} \int_{t'=0}^{T_{av}} < z(t)z(t') > dtdt'$$

For an overdamped Brownian particle:

$$< z(t)z(t+u) >= \frac{k_B T}{k} e^{-\frac{k}{\gamma}|u|}$$

Considering the symmetry of the integration volume, the sub-volume where $t < t'$ is equal to the sub-volume where $t > t'$. Because of the absolute value, the integral of both of these subvolumes will also be equal and we thus have :

$$\begin{aligned}
\frac{1}{T_{min^2}} \int_{t=0}^{T_{av}} \int_{t'=0}^{T_{av}} < z(t)z(t') > dtdt' &= \frac{2}{T_{min^2}} \int_{t=0}^{T_{av}} \int_{t'=0}^{t} \frac{k_B T}{k} e^{-\frac{k}{\gamma}(t-t')} dtdt' \\
&= \frac{2}{T_{min^2}} \int_{t=0}^{T_{av}} \int_{u=0}^{t} \frac{k_B T}{k} e^{-\frac{k}{\gamma}u} dtdu \\
&= \frac{2k_B T}{T_{min^2} k} \int_{t=0}^{T_{av}} \frac{\gamma}{k}(1 - e^{-\frac{k}{\gamma}t}) dtdu \\
&= \frac{2\gamma k_B T}{T_{av}^2 k^2}(T_{av} - \frac{\gamma}{k}(1 - e^{-\frac{k}{\gamma}T_{av}}))
\end{aligned}$$

As stated above, this value corresponds to the square of the typical error made on the evaluation of the position of the trap after averaging during T_{av}. For $T_{av} \ll \frac{\gamma}{k}$, averaging does not increase the precision of the estimation of the bead position. This is due to the fact that the averaging window is shorter than the typical time of movement of the bead: at this time scale, the bead is almost motionless and the error with respect

to its position is given by the statistical error $\sigma_{stat} = \frac{k_B T}{k}$. For $T_{av} \gg \frac{\gamma}{k}$, the precision obtained as a function of the averaging verifies:

$$s^2 \simeq \frac{2\gamma k_B T}{T_{av} k^2} \tag{2.12}$$

Thus, we can deduce that the minimum averaging time $T_{\min}$ of the bead motion that allows distinguishing a step of amplitude σ. In order to distinguish such a step from a Gaussian of width s with a degree a certainty below 1 %, we should have $\sigma > 3s$:

$$T_{min} = \frac{18\gamma k_B T}{\sigma^2 k^2} \tag{2.13}$$

In particular, we obtain for this regime a relation between the spatial resolution of the steps $\Delta z = \sigma$ and the corresponding temporal resolution $\Delta T \simeq T_{min}$:

$$\Delta T (\Delta z)^2 = cte$$

This shows that, for a given couple of parameters of Brownian motion k and γ, the temporal resolution decreases as the square of the aimed spatial resolution. If we were able to distinguish nanometric steps every second, we would need to average the signal for at least $100s$ in order to distinguish steps at the ångström resolution. Finally, let us note that in practice, for the frame-to-frame noise, this averaging is performed by the acquisition procedure: an image of a bead is already averaged during the shutter time of the camera τ_s. Thus, we can replace T_{av} by the shutter time τ_s of the camera in order to predict the measured variance of the Brownian noise as the function of the acquisition frequency $f_{aq} = \frac{1}{\tau_s}$.[1]

In the last paragraph, we derived in the space of positions the theoretical limitation to spatiotemporal resolution due to the Brownian motion of the microbead. Because the goal is to observe extension steps localized in time, it seemed more intuitive. It is noteworthy that the proof is often performed in the Fourier space. Of course, the two approaches are equivalent and we recognize in equation 2.12 the level of noise density below the cut-off frequency $\omega_c = \frac{k}{\gamma}$ in the Fourier space: $P(\omega \ll \omega_c) = \frac{2\gamma k_B T}{k^2}$. The reader interested by the Fourier space derivation should refer to [Berg-Sørensen and Flyvbjerg, 2004]. Furthermore, [Lansdorp and Saleh, 2012] describes two accurate numerical methods (respectively in the frequency and in the

[1]The equivalence of τ_s and T_{av} presumes that the position inferred from an image of the bead acquired during τ_s is equal to the average of the positions inferred from N successive images acquired during $\frac{\tau_s}{N}$.

position space) allowing one to derive with high precision the parameters γ and k from an experimental Brownian motion. These methods are particularly critical for magnetic tweezers since the inference of $k_{x,y}$ allows calibrating the force created by the magnets 2.10. Interestingly, the work of [Berg-Sørensen and Flyvbjerg, 2004] also derives the corrections to the Brownian noise spectrum due to the discrete sampling (aliasing), due to the hydrodynamic inertia of the flow around the bead, and due to the increased *transverse* drag close to a surface (Faxén effect) [Faxén, 1922]. In the next paragraph, we describe the increased *axial* drag since in magnetic tweezers experiments, the molecule is perpendicular to the surface and its change of extension are thus related to the axial movement of the bead.

2.1.4 Hydrodynamic drag close to a surface

Equation 2.13 shows that two solutions can be considered to limit the effect of the Brownian motion. First, the drag coefficient can be reduced by decreasing the size of the bead. Second, the stiffness of the substrate can be increased, in particular by taking shorter substrates. If we approximate that k is proportional to the number of monomers, we expect, following equation 2.12, that the spatial resolution decreases as the number of monomers [1]. However, an antagonist effect takes place as the bead come closer to the surface. Indeed, the drag coefficient that opposes a bead movement close to plane surface increases as the bead comes closer to the surface. The correction to Stokes' law in this configuration has been derived analytically by Brenner [Brenner, 1961]. This correction depends on the distance between the center of the bead and the surface h and is contained in a function $\lambda(\frac{h}{R})$, where R is the radius of the bead. Thus, the corrected Stokes' law reads, with z the extension of the molecule, i.e. the distance between the attachment point on the bead and the surface:

$$\gamma(z) = 6\pi\eta R\lambda(\frac{z+R}{R}) \tag{2.14}$$

Figure 2-5.a shows $\lambda(\frac{z+R}{R})$ as a function of z for beads of radii 0.5 and 0.25 microns. Figure 2-5.b shows the whole drag coefficient in water for both radii. In this work, we will be mostly using dsDNA handles of a length of roughly 40 nm and beads of diameter 1 micron. Figure 2-5.a shows that at this distance, the Brenner correction adds a factor 14 to the drag coefficient. However, using longer dsDNA handles in order for the bead to be less close from the surface is not an interesting option. Indeed, as stated earlier, the stiffness of such handles decreases with the number of monomers and thus with their lengths: $k \propto \frac{1}{N} \propto \frac{1}{z}$.

[1] see footnote 1 page 55

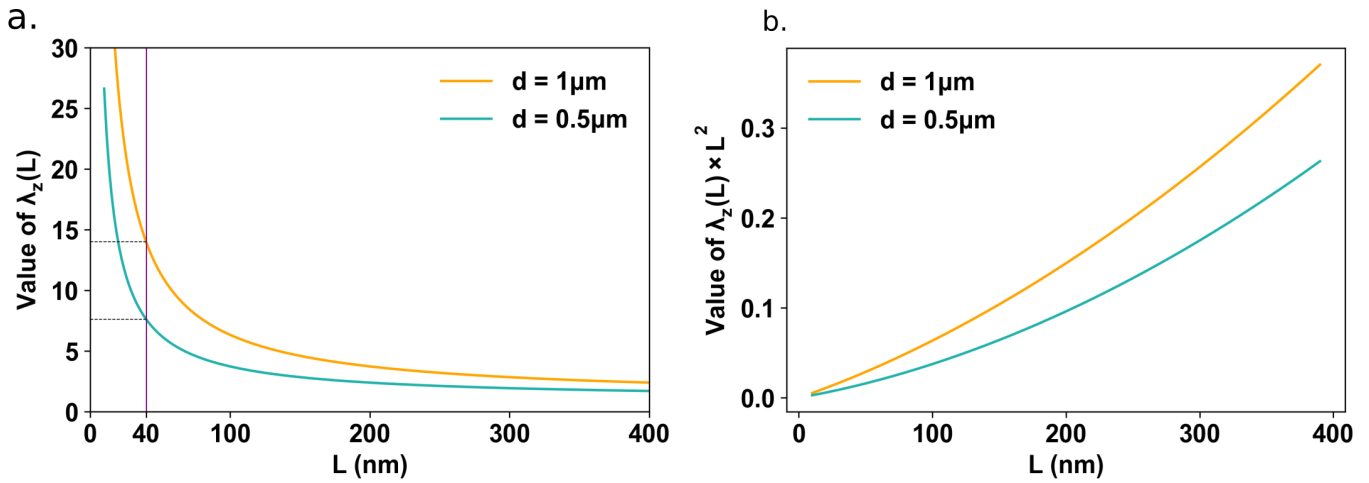

Figure 2-5: **Theoretical correction to Stoke's law for the hydrodynamic axial drag coefficient close to a surface. a.** Theoretical correction [Brenner, 1961] for the axial drag $\lambda_z(l)$ as a function of the distance between the bead and the surface for two different diameters of the bead. **b.** Function $\lambda_z(l)l^2$ for two different bead diameters.

Thus, the dependence of the spatiotemporal resolution with z verifies (equation 2.12):

$$\sigma^2 T_{av} \propto \frac{k_B T \lambda(\frac{z+R}{R})}{k(L)^2} \propto z^2 \lambda(\frac{z+R}{R}) \tag{2.15}$$

We draw this function as a function of z in figure 2-5.b. As can be seen, it is a growing function of z, thus showing that the increase of noise due to the decreased stiffness of the handles is stronger than the decrease of noise due to the decrease of the drag when the handles are taken longer. For this reason, this 1D-model of the behavior of the bead suggests that increasing the length of our dsDNA handles cannot help fighting against this surface effect. A solution would be to use stiffer handles than the DNA substrate whose change of extension we are measuring, in order to bring the bead further away from the surface without increasing significantly the stiffness of the construct. Such handles could be obtained with origami constructions and have been proposed in some optical tweezers studies, but will not be considered in this work.

2.1.5 Movement misalignment and post-correction

We realized during this work that an important source of noise could be avoided by using the information contained in the tracking of the X and Y directions. We can use these transverse tracking data in order to correct the measurement of the molecule extension normally contained in the Z direction.

Indeed, a slight misalignment of the optical axis (z_o) with the axis of the magnetic force (z) (determined by the position of the magnets) can cause a large increase of the measured noise in the z_o direction.

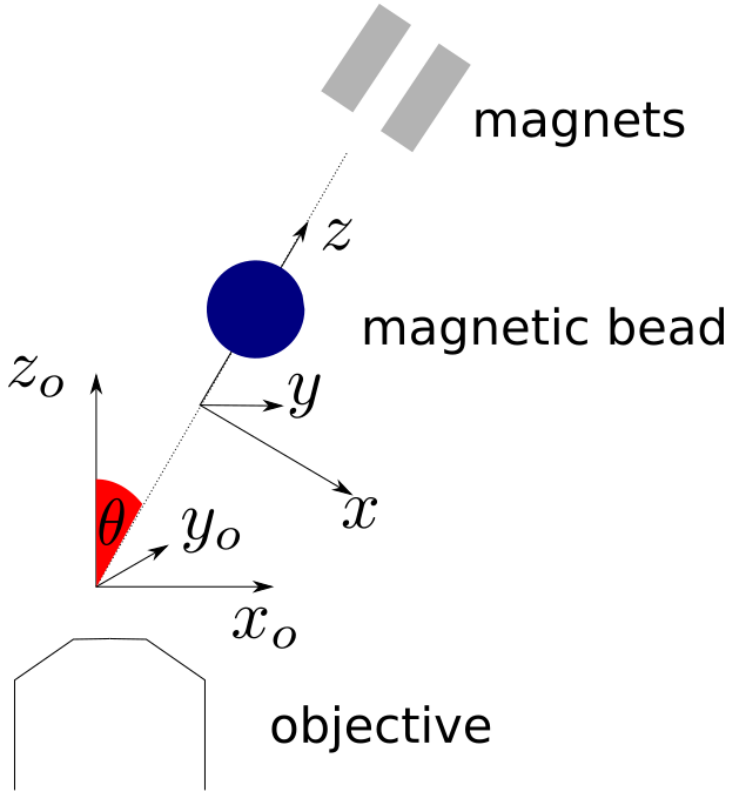

Figure 2-6: **Illustration of the misalignment between the optical axis and the magnet.** We claim that a slight misalignment between the magnetic axis, which is relevant for the thermodynamic understanding of the Brownian noise, and the optical axis, explains part of the noise in magnetic tweezers experiments and can be easily corrected by a post-processing rotation. On this picture, the angle is exaggerated on purpose, but even an angle as small as 1° can double the observed noise observed in the optical direction z_o.

Let's call θ the small angle between z_o and z and u the coordinate of the bead position along the axis of rotation (that belongs to the plane (x,y)) perpendicular to z. For small θ, z_o verifies:

$$z_o = z + \theta u \tag{2.16}$$

and the fluctuations verify (x,y and z being uncorrelated at the second order development of the molecule's free energy, equation 2.9):

$$\sigma_{z_o} = \sqrt{\sigma_z^2 + \theta^2 \sigma_u^2} \tag{2.17}$$

$$\sigma_{z_o} \simeq \sigma_z (1 + \frac{\theta^2}{2} \frac{\sigma_u^2}{\sigma_z^2}) \tag{2.18}$$

We saw earlier that (eq 2.12), at timescales below the $\tau = \frac{\gamma}{k}$, the noise due to the Brownian motion of

the bead is proportional to: $\frac{k_B T \gamma}{k^2}$.

Close to a surface, the corrections applied to the drag coefficient γ in the transverse directions x and y, $\lambda_{\parallel}(\frac{z}{R})$ are different from the corrections applied to γ in the axial direction z, $\lambda_{\perp}(\frac{z}{R})$. It is noteworthy that these correction coefficients were derived by Faxén [Faxén, 1922], O'Neill [O'Neill, 1964] and Brenner [Brenner, 1961, Goldman et al., 1967] in the case of a steady flow, and are thus only valid at very low Reynolds number. In our case, noting that the typical amplitude of the bead movement is $L = \sqrt{\frac{k_B T}{k}}$, its typical response time $\tau = \frac{\gamma}{k}$:

$$\mathrm{Re} = \frac{LR\rho}{\tau\eta} \tag{2.19}$$

$$= \sqrt{\frac{k_B T}{k}} \frac{k}{\gamma} \frac{R\rho}{\eta} \tag{2.20}$$

$$= \frac{\sqrt{k_B T k} R\rho}{\gamma\eta} \tag{2.21}$$

Using the order of magnitudes given in equation 2.5 that would result in the largest Reynold numbers *i.e.* $k = 10^{-2}$ N/m and $\gamma = 6\pi\eta R$ (no correction), we find $Re \simeq 3 \times 10^{-4}$, thus confirming the relevance of the use of the analytical methods cited above for the corrections of the drag close to a wall.

Here we will perform the numerical application for a micrometric bead ($R = 0.5\mu$m), in water, and attached to a 120-bp fragment of dsDNA and stretched at 13 pN. This is the configuration that will be used in the major part of the following work. At this force, the extension of double-stranded DNA is roughly z = 35 nm. Thus, the adimensional parameter for the position of the bead is equal to $\frac{R+z}{R} = 1.07$. At this distance, we have, for the tranversal [1] and axial [2] correction to the drag force:

$$\lambda_{\parallel}(1.08) = 2.5 \tag{2.22}$$

$$\lambda_{\perp}(1.08) = 15 \tag{2.23}$$

Furthermore, for such a dsDNA fragment, the worm-like chain (WLC) [3] model and the more accurate

[1] Linear extrapolation between the 5-th and 6-th values of Table 1 in [Goldman et al., 1967]
[2] Computed numerically at 30-th order with the infinite series derived in [Brenner, 1961]
[3] $L_p = 51.35$ nm, $L_0 = 0.34$ nm

finite worm-like chain model (FWLC) [1] respectively predict:

$$k_z = 0.01 \text{ or } 0.004 \text{ N/m} \tag{2.24}$$

$$k_x = 1.9 \times 10^{-5} \text{ N/m} \tag{2.25}$$

While the values for k_z are not critically different, we will use in the following the values provided by the FWLC model, since the model has been shown recently [Shon et al., 2019] to be in very good agreement with experimental data even for very short substrates.

The typical response times $\tau = \frac{\gamma}{k}$ read:

$$\tau_x = \frac{\gamma_\parallel}{k_x} = 1.3\text{ms} \tag{2.26}$$

$$\tau_\perp = \frac{\gamma_\perp}{k_\perp} = 33\mu\text{s}, \tag{2.27}$$

and the associated cut-off frequency:

$$f_c^x = \frac{1}{2\pi\tau_x} = 127\text{Hz} \tag{2.28}$$

$$f_c^z = \frac{1}{2\pi\tau_z} = 4.8 \times 10^3 Hz \tag{2.29}$$

For acquisition frequencies below this cut-off frequency, we thus get the following squared spatial resolution per time unit, or equivalently, noise density (equation 2.12):

$$P_x^2 = \sigma_x^2 T_{av} = \frac{2\gamma_\parallel k_B T}{k_x^2} = 0.54 \text{ nm}^2\text{Hz}^{-1} \tag{2.30}$$

$$P_z^2 = \sigma_z^2 T_{av} = \frac{2\gamma_\perp k_B T}{k_z^2} = 7 \times 10^{-5} \text{ nm}^2\text{Hz}^{-1} \tag{2.31}$$

Thus, the noise density below the cut-off frequency is expected to be larger in the lateral direction by a factor $\frac{\sigma_x T_{av}}{\sigma_z T_{av}} = 8600$, and thus the integrated noise at such an acquisition frequency is bigger in the lateral direction ($\sigma_\perp$) compared to the axial direction ($\sigma_\parallel$) by a factor $\sqrt{8600} \simeq 92$.

[1] See [Seol et al., 2007]. We use the WLC approximation of FWLC by adapting the persistence length with the empirical formula $L_p = \frac{L_{p\infty}}{1+\frac{aL_{p\infty}}{L_c}}$, $L_{p\infty} = 51.51$ nm, $a = 2.78$, $L_c = N \times 0.34$ nm

For this reason, given equation 2.17, an angle of 0.9° between the optical axis and the magnetic axis is large enough to double the measured noise in the optical axial position z_o compared to the noise in the magnetic direction z.

To overcome this issue, we post-rotated the experimental data in order to recover the magnetic direction z from the measurement in the optical referential (x_o,y_o,z_o). We look for the 3D rotation angles (α, β) that minimize the noise in the rotated z direction. Formally, we minimize σ_z with respect to α and β where :

$$\begin{bmatrix} x \\ y \\ z \end{bmatrix} = R(\alpha, \beta) \begin{bmatrix} x_o \\ y_o \\ z_o \end{bmatrix}$$

This minimization is obtained through standard gradient-descent algorithms. In figure 2-7.b, we show σ_{z_o} as a function of α and β and materialize the angles α^* and β^* that minimize the noise.

Figure 2-7.b shows the effect of the post-processing rotation on the spectrum of a tethered bead. Figures 2-7.a shows how the post-processing allows recovering signal of a much higher quality for a molecule undergoing extension steps of $1nm$, an experiment that will be described in the next section. Figure 2-7.d shows how the post-rotation allows a better distinction between the open and closed states of a 10-bp oscillating hairpin, an experiment that will be described in the next chapter. Finally, figure 2-8.a shows the noise density in the axial direction for 48 beads attached to a 120-bp dsDNA substrate before and after the post-rotation. The procedure reduces the noise density in the z-direction up to a factor 3.

2.1.6 Discrepancy between this simple model and experimental noise values

However, even with this procedure, we were not able to reach the expected value for the spatiotemporal resolution in the z-direction predicted in equation 2.31. We summarize in table 2.1 the noise density obtained in the three spatial directions for a 120-bp double-stranded DNA. For the X-direction, perpendicular to the magnetic field, the results are in relative agreement with what we expected, however, with a significantly higher drag coefficient. For the Y-direction, parallel to the magnetic field, experimental results are significantly different from the X-direction and show an important bead-to-bead spread. This is in accordance with previous results showing that this direction is constrained by the magnetic anisotropy and that the associated Brownian movement depends on the anchoring point of the molecule compared to the anisotropic axis, thus increasing the bead-to-bead variation.

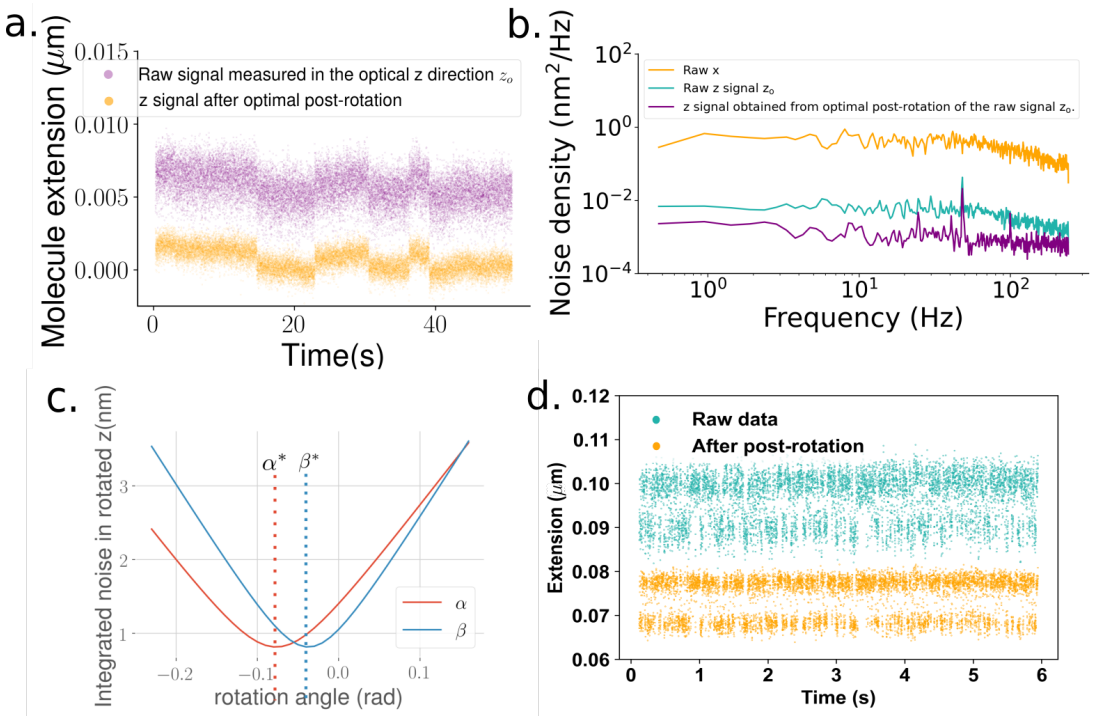

Figure 2-7: **Effect of post-rotation on the resulting signal. a.** Traces showing 1-nm steps as a consequence of oligonucleotide hybridization after and before post-rotation. The experience is described in the next section. The curves are vertically offset for clarity. **b.** Power spectrum comparison. The cutoff frequency of the X-signal is visible in the $z_o(t)$ trace, demonstrating that this axis is coupled with the x direction. The orange curve shows that rotating the signal allows decoupling the signals. **c.** Measured noise in the z-direction obtained through rotation of the measured data with angles (α,β) respectively around the x and the y-axis. The curve as a function of α is drawn for $\beta = \beta^*$. The curve as a function of β is drawn for $\alpha = \alpha^*$. **d.** Traces showing 10-nm steps resulting from the oscillation between the closed and open states of a 10-bp hairpin. The experience is described in the next chapter. The curves are vertically offset for clarity.

In the z-direction, the spatiotemporal resolution is much smaller than expected. To compare the values accurately with the theory presented in the last paragraphs, we subtracted the photon noise from the measured noise. Photon noise subtraction is performed by noting that $P^2_{z_{tot}} = P^2_{z_{phot}} + P^2_{z_{Brownian}}$. $P^2_{z_{phot}} = \frac{\sigma^2_{ff}}{f_{aq}}$, where σ_{ff} is the frame-to-frame localization error measured in chapter 1. The reader will note that $P_{z_{phot}}$ decreases with the increase of the acquisition frequency: this is due to the fact that the light intensity is adapted so as to always saturate the camera. Thus, at higher acquisition frequency, more photons are sampled. This subtraction, performed at $160Hz$, does not appear to significantly modify the noise density, showing that, with *Stereo Darkfield Interferometry*, the photon noise is not the limiting noise any more, but is the Brownian motion of the bead. After this subtraction, we measure that $P^2_{z_{Brownian}}$ is almost 8 times larger than expected (last row of table 2.1), with a value close to 6×10^{-2} nm.Hz^{-1}. We will now show how a more complete modeling of the bead dynamics can explain this discrepancy.

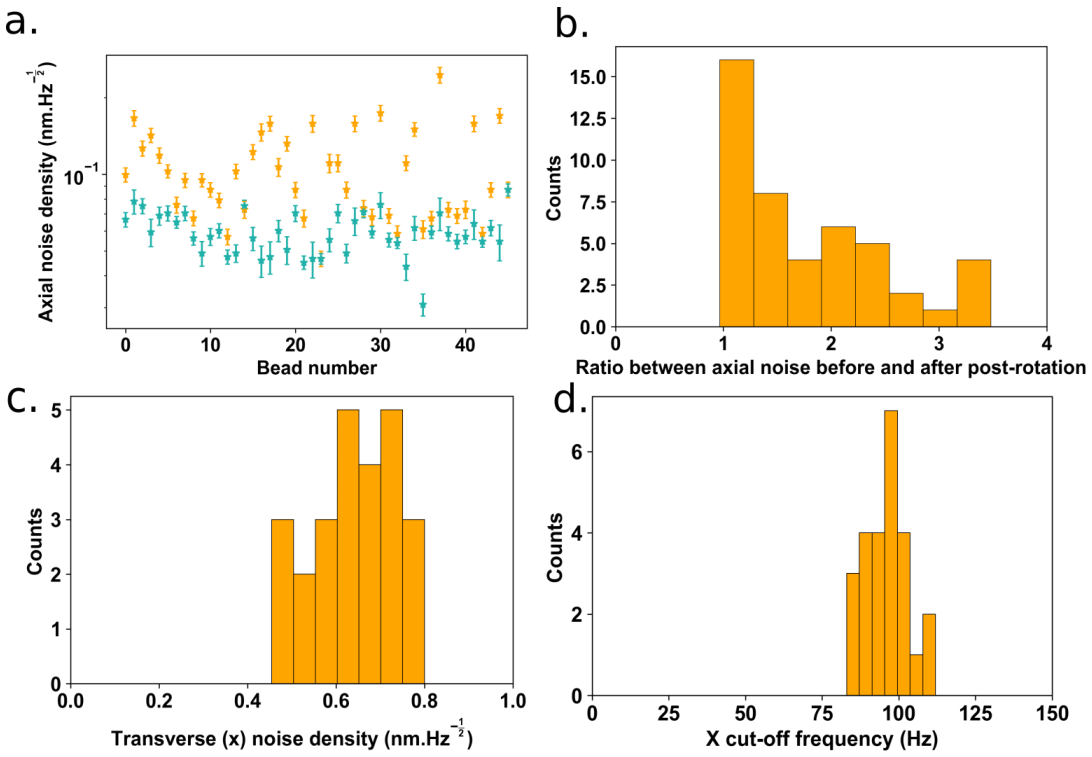

Figure 2-8: **Characterization of the Brownian motion of magnetic microbeads.** Characterization of the Z Brownian motion of magnetic microbeads (MyOne T1, Thermofisher) attached to a 10-bp hairpin and tethered by a 120-bp dsDNA, stretched at 13 pN. The hairpin opening ensures that the right DNA substrate is attached. It is then blocked in its open state by a complementary oligonucleotide. Data are derived from 48 beads tracked at 160 Hz. Orange: before post-rotation. Blue: same bead after post-rotation. **b.** Distribution of the ratio between the z noise density before and after the rotation. **c.** Distribution of the level of noise density at the plateau of the lorentzian spectrum, fitted from 29 beads, tracked at 1200 Hz. **d.** Distribution of the cut-off frequency in the X direction, fitted from 29 beads, tracked at 1200 Hz. Lorentzian spectra are fitted through MLE as described in [Lansdorp and Saleh, 2012]. Spectra are only fitted above 10Hz, in the flat region, of the spectrum, to separate the measurement of the Brownian motion of the bead from the slow experimental thermal drift.

2.1.7 Inclusion of hydrodynamic couplings and magnetic anisotropy

It appears that two crucial effects need to be incorporated in the simple model presented above in order to faithfully understand the measurement noise.

- First, superparamagnetic microbeads are **anisotropic** and present a preferred magnetic axis. When a magnetic field is applied, this consequently creates a torque that favors the alignment of the magnetic field with the anisotropy axis [Allemand, 1997, Mosconi et al., 2011b, Janssen et al., 2009]. If the molecule is attached close to the magnetic pole of the bead, this effect is known to increase the noise measured in the z-direction [Klaue and Seidel, 2009a] due to the rotational fluctuations of the bead (figure 2-9.a).

- Second, the proximity of the surface creates a coupling between the rotation and the translation of

	Expected	Measured
X cut-off frequency f_c^x (Hz)	127	96±8
Noise density below f_c^x $\sqrt{\sigma_x^2 T_{av}}$ (nm.Hz$^{-\frac{1}{2}}$)	0.73	$(8\pm0.6)\times10^{-1}$
k_x (N/m)	1.9×10^{-5}	$(2.13\pm0.34)\times10^{-5}$
λ_x	2.5	3.8±0.5
Y cut-off frequency f_c^y (Hz)	NR	352±90
Noise density below f_c^y $\sqrt{\sigma_y^2 T_{av}}$ (nm.Hz$^{-\frac{1}{2}}$)	NR	$(1.9\pm0.6)\times10^{-1}$
k_y (pN/nm)	NR	$(1.1\pm0.4)\times10^{-4}$
λ_y	NR	5.5±1
Noise density below f_c^z $P_z = \sqrt{\sigma_z^2 T_{av}}$ (nm.Hz$^{-\frac{1}{2}}$)	1.9×10^{-2}	$(5.9\pm1.2)\times10^{-2}$
Noise density below f_c^z $P_z = \sqrt{\sigma_z^2 T_{av}}$ (nm.Hz$^{-\frac{1}{2}}$) *Photon noise subtracted*	8.4×10^{-3}	$(5.6\pm1.2)\times10^{-2}$

Table 2.1: Characterization of the Brownian motion of magnetic microbeads (MyOne T1, Thermofisher) attached to a 10-bp hairpin and tethered by a 120-bp dsDNA, stretched at 13 pN and comparison with our simple model. The hairpin opening ensures that the right DNA substrate is attached. It is then blocked in its open state. X and Y data are derived from 29 beads, tracked at 1200 Hz. Z data are derived from 48 beads, tracked at 160 Hz. Data shown are the average of the measured values over all beads and errors correspond to the standard variation of the measured values over the beads. Lorentzian spectra are fitted through MLE as described in [Lansdorp and Saleh, 2012]. Spectra are only fitted above 10Hz, in the flat region, of the spectrum, to separate the measurement of the Brownian motion of the bead from the slow experimental thermal drift. $\lambda = \frac{\gamma}{6\pi\eta R}$. NR: not relevant. The cut-off frequencies in the y-direction can not be captured without taking in account the magnetic anisotropy of the bead.

the bead due to the asymmetric hydrodynamic flows. Thus, when the bead rotates around an axis, it creates a hydrodynamic force perpendicular to this axis and conversely, when the bead moves along an axis, it creates a torque along the perpendicular axis. The theory of these hydrodynamic effects has been extensively studied by Jeffery and later by Brenner and O'Neill in the late 60's [Jeffery, 1915, O'Neill, 1964, Goldman et al., 1967, O'Neill and Stewartson, 1967] .

If we take in account all these effects, the movement of the bead attached to the molecule can be modeled by the six following equations:

$$-\gamma_{xy}^{t}(z)v_x + \gamma_{xy}^{tr}(z)\Omega_y - F_x = F_x^{langevin} \tag{2.32}$$

$$-\gamma_{xy}^{r}(z)\Omega_y + \gamma_{xy}^{tr}(z)v_x - \tau_y = \tau_y^{langevin} \tag{2.33}$$

$$-\gamma_{xy}^{t}(z)v_y - \gamma_{xy}^{tr}(z)\Omega_x - F_y = F_y^{langevin} \tag{2.34}$$

$$-\gamma_{xy}^{r}(z)\Omega_x - \gamma_{xy}^{tr}(z)v_y - \tau_x = \tau_x^{langevin} \tag{2.35}$$

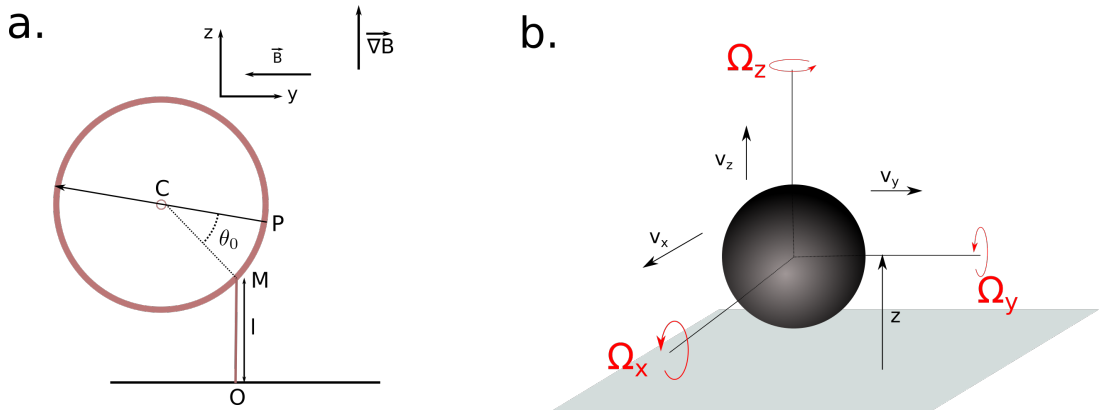

Figure 2-9: **A more refined view of the physics of the microbead. a.** The magnetic anisotropy of the bead induces a magnetic torque that favors the alignment of the anisotropy of the axis with the magnetic field. The physics of the bead depends on the angle θ_0 between the anchoring point of the molecule M and the magnetic pole P, as described in [Allemand, 1997] and [Klaue and Seidel, 2009b]. **b.** Close to a surface, the hydrodynamic torque and forces are modified and depend on z. Furthermore, transverse translation and rotation become coupled, as if the bead rolled.

$$-\gamma_z^t(z)v_z - F_z = F_z^{langevin} \tag{2.36}$$

$$-\gamma_z^r(z)\Omega_z - \tau_z = \tau_z^{langevin} \tag{2.37}$$

$\mathbf{v}$ is the velocity of the bead center C and Ω is the instantaneous rotation vector of the bead. $\mathbf{F}$ is the sum of the force applied by the molecule on the bead F_{mol} and the magnetic force $\mathbf{F}$. The direction of $\mathbf{F}_{mol}$ is defined by the position of the attaching points of the molecule on the bead M and the surface O. Its norm is equal to $G'(l)$, where G is the free energy of the molecule and l its instantaneous length. τ is the sum of the torque applied by the molecule on the bead τ_{mol} and of the magnetic torque due to the bead anisotropy τ_{mag}. τ_{mol} is equal to $\vec{CM} \times \mathbf{F}$, where C is the position of the center of the bead. τ_{mag} is equal to $\alpha\vec{M} \times \vec{B}$, where $\vec{M}$ is the magnetization of the bead, aligned along its anisotropy axis, and α is the anisotropy coefficient, measuring the degree of anisotropy of the bead. While it varies from bead to bead, we will take it equal to 0.005, as it corresponds to previously measured values [Mosconi et al., 2011b] and because it allows our simulation to fit reasonably the measured cut-off frequency in the direction y of the magnetic field (350 Hz, table 2.1).

It is noteworthy that with our magnet configuration (Material and Methods C.1.11), the magnetic field varies exponentially with the distance of the magnets from the surface and verifies $B(z) = \lambda \frac{dB(z)}{dz}$, where λ is the distance between both magnets. This exponential dependence is valid for forces larger than the picoNewton (figure C-12 in Material and Methods). Because the magnetic force is proportional to $\frac{dB(z)}{dz}$ and the magnetic torque to $B(z)$, this results in the fact that torque and forces vary proportionally in this force range. Thus, the equilibrium angle of the bead compared to the magnetic field should not depend on the

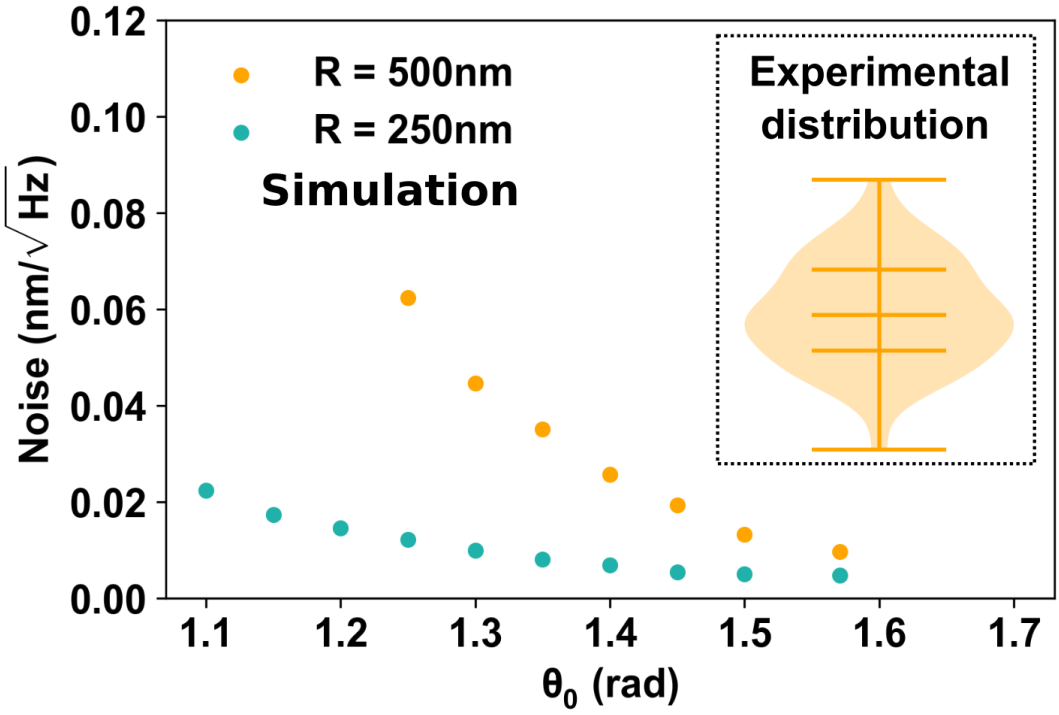

Figure 2-10: **Simulation of the 3D-movement of a tethered bead close to a surface.** The physics model described in this part, taking into account the full hydrodynamic coupling with the surface and the magnetic anisotropy of the bead is simulated at 25°C, for a double-stranded molecule DNA of 120 bp tethered at 13 pN, and a magnetic anisotropy coefficient of 0.005. We represent the simulated z noise density averaged 0 and 160 Hz as a function of the tethering angle θ_0. The violin plot on the right represents the post-processed experimental axial noise for the beads represented in figure 2-8.a. Horizontal bars represent extrema, medians, and quartiles.

applied magnetic force. Furthermore, the norm of the magnetic torque can be simply written as $\alpha\lambda|F_{mag}|$. We also note that the dynamics of the bead depends on the angle between the magnetic pole of the bead and the anchoring point of the molecule on the bead, which is random, given that we do not control where the molecule attaches on the bead. This angle is called θ_0.

γ_{xy} and γ_z are respectively the hydrodynamic drags in the directions transverse to the surface and in the direction perpendicular to the surface. γ^r, γ^t and γ^{tr} denote respectively the rotational, translational drags and the rotation-translation coupling. Infinitely far from the surface, γ^r equals $8\pi\eta R^3$, γ^t is equal to $6\pi\eta R$ and γ^{tr} is equal to 0. Their values as a function of the distance z of the bead from the surface and the bead radius R are summarized in [Perkins and Jones, 1992]. Given that the amplitude of the Brownian motion in z is of the order of the nanometer, which is relatively small compared to the distance of the bead from the surface (typically 40 nm), we will neglect the dependence of γ to z during the dynamics. We write $\gamma(z) = \gamma(z_0)$, where z_0 is the average position of the bead for a given set of parameters.

v_z and Ω_z are not coupled, and thus their Langevin torque and force verify the fluctuation dissipation relations $< F_z^{Langevin}(t)F_z^{Langevin}(t') >= 2k_BT\gamma_z^t(z_0)\delta(t-t')$ and $< \tau_z^{Langevin}(t)\tau_z^{Langevin}(t') >= 2k_BT\gamma_z^r(z_0)\delta(t-$

t'). However, v_x is coupled to Ω_y and v_y to Ω_x through the coefficient $\gamma_{xy}^{tr} > 0$. This imposes a reduction of the system in order to compute the Langevin force and torque. For example, the hydrodynamic tensor defining the frictional torque and force can be written in the x and y directions, (equation 2.32 and equation 2.33):

$$\begin{bmatrix} f_x \\ \tau_y^{fr} \end{bmatrix} = \overbrace{\begin{bmatrix} -\gamma_{xy}^{t}(z) & \gamma_{xy}^{tr}(z) \\ \gamma_{xy}^{tr}(z) & -\gamma_{xy}^{r}(z) \end{bmatrix}}^{\Gamma} \begin{bmatrix} v_x \\ \Omega_y \end{bmatrix}$$

We can decompose $\Gamma = PDP^{-1}$, then $P^{-1}V$ defines a linear combination of Ω_y and v_x that follow 1D Langevin equations, of effective viscosity parameters D_{00} and D_{11} and thus with effective Langevin forces that verify $< F_i(t)F_i(t') >= 2k_BTD_{ii}\delta(t-t')$.

We were not able to derive analytically the dynamics the 3D-motion of the bead test follows this set of six coupled equations. However, since the diagonalization of P provides the intensity of the Langevin forces, we were able to simulate the system (Appendix B).

The simulated z-noise density below 160 Hz obtained from these simulations are shown in figure 2-10. Interestingly, their values for small tethering angles ($\theta_0 < 1.3$) fit much better with the experimental results than our previous simplistic model, showing that the hydrodynamic couplings and the magnetic anisotropy of the bead constitute an important source of noise. Still, it is not clear why we do not observe more beads with lower noise density. Indeed, figure 2-10 shows that the noise critically depends on the anchoring point of the molecule compared to the anisotropy axis. However, if the molecule was randomly attached to the bead, we expect that θ_0 should be distributed as $\sin\theta_0$. In the accessible angle range for a short molecule of 40 nm ($1.2 < \theta_0 < \frac{\pi}{2}$), the sinus is almost constant. Thus, we would expect that the noise density represented in figure 2-10 should be equally distributed, which is not the case. A possibility would be that the superparamagnetic beads have one or several secondary anisotropy axis. This would explain why there is always an axis verifying that θ_0 is relatively small. However, no data permit to infirm or confirm this hypothesis.

While the noise is substantially larger than what was expected at the start of the project, it is important to note that the noise-density value in the z-direction, 0.06nm $/\sqrt{\text{Hz}}$ should theoretically allow the detection of nanometric steps in the data down to a time scale of $\simeq 0.06$ s (equation 2.13), prediction that we are going to test experimentally in the next section. Finally, figure 2-10 suggests that the radius of the bead plays a critical role in the noise density at low frequencies. Without taking the hydrodynamic effects of the

surface, this noise should scale as $\sqrt{R}$. However, since the effect of the wall on the hydrodynamic coefficient depends strongly on $\frac{z}{R}$, this increases the impact of the bead's radius. However, we could not test the noise with beads of smaller radii in this work since we were lacking sufficiently small magnetic microbeads. Indeed, the saturation magnetization, and thus the maximum applied force, scales as the volume of the bead, that is R^3.

2.2 Two biophysical applications

2.2.1 Force spectroscopic measurement of the hybridization of short oligonucleotides with nanometric resolution.

We now illustrate the spatiotemporal resolution of our magnetic tweezers based on *Stereo Darkfield Interferometry* through various single-molecule force spectroscopy measurements.

Figure 2-11 shows the kinetics of hybridization of short oligonucleotides that were obtained by using the nanometric precision of *SDI*. A DNA molecule with a short single stranded (ss) segment is attached between a magnetic microsphere (MyOne^{TM}) and the surface and pulled at a force of $\sim$ 13 pN. A free 8-bp oligonucleotide complementary to the ssDNA segment of the tethered molecule is injected in the solution. As the oligonucleotide hybridizes to the molecule, 8 bases of the latter are converted from ssDNA to dsDNA, causing a shortening of the molecule of $\approx$ 1.5 Å per base at 13 pN, that is a total 1.2 nm extension difference (Figure 2-11.b). When the oligonucleotide unbinds, the molecule recovers its original length. The resulting two-state dynamics allow characterizing the kinetics of the hybridization process (figure 2-11.c-e). As expected from previous studies, the binding constant k_{on} is almost constant in this force range, while the unbinding constant k_{off} is strongly dependent of the force (figure 2-12.b-c).

Besides demonstrating the precision of our magnetic tweezers, this experiment can be slightly modified in order to provide an accurate single-molecule measurement of the energy of base-stacking. Base stacking is an interaction between the aromatic rings of successive nucleic acids and is a major contributor, alongside the hydrogen bonds between complementary bases, to the stability of the duplex structure [Yakovchuk et al., 2006]. We used the precision of *Stereo Darkfield Interferometry*-based magnetic tweezers in order to investigate the effect of the stacking of the oligonucleotide with the neighbour dsDNA. For this purpose, we reproduced the experiment on two different substrates (figure 2-12.a). On one of them, the fully stacked configuration, the oligonucleotide hybridizes with a single-stranded gap whose size is exactly 8 bp. On

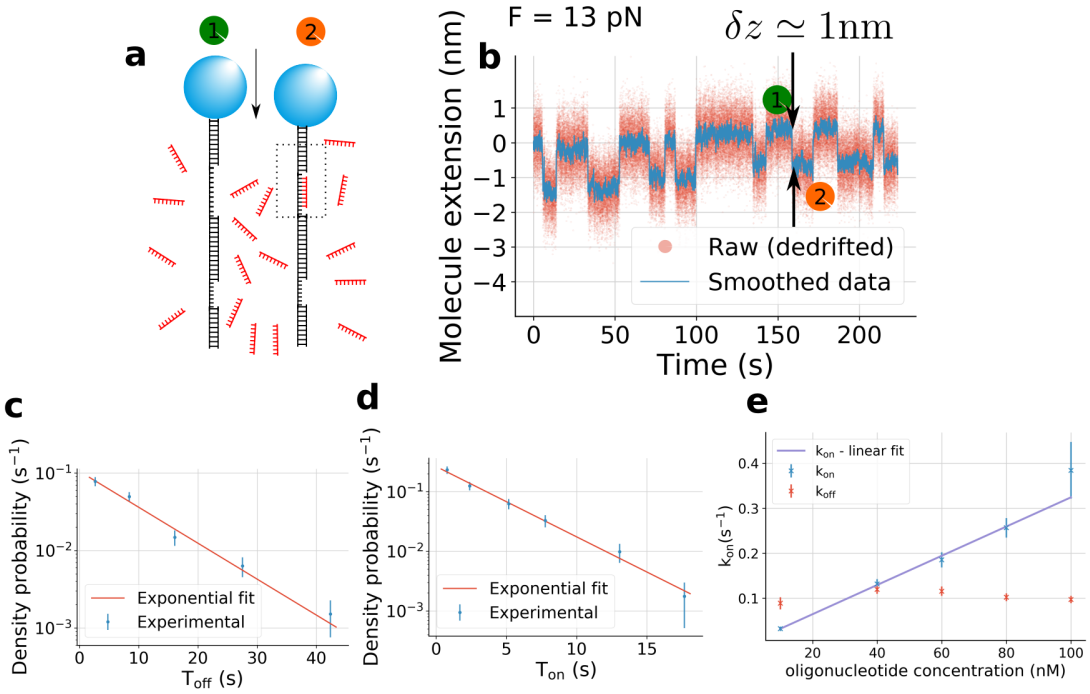

Figure 2-11: **Measurement of the hybridization of a 8-base oligonucleotide. a.** Illustration of the experiment: above 5 pN, dsDNA is longer than ssDNA and thus the hybridization of an oligonucleotide induces a shortening of the molecule. **b.** Trace showing several cycles of hybridization and deshybridization of the oligonucleotide at F = 13 pN and at a concentration of oligonucleotide of . **c.** Corresponding distribution of times spent in the hybridized state. **d.** Corresponding distribution of times spent in the de-hybridized state. **e.** Binding rate as a function of oligonucleotide concentration. T = 298.15 K

the other, the half-stacked configuration, the single-stranded gap is larger (14 bp) than the oligonucleotide, thus preventing stacking interaction on one of the free ends of the ss fragment. While a similar experiment was pioneered by Whitley *et al.* in [Whitley et al., 2017] using FRET, we here are able to perform it in a fluorescence-free setup, thus avoiding an eventual bias that could be introduced by the interaction between the fluorescent label and the DNA. From the difference in the measured hybridization kinetics between the two substrates (figure 2-12.b), we notably extract the free energy of stacking (see figure 2-12.d) and find $\Delta G_{stacking,AG} = 2.0 \pm 0.2$ kcal/mol. The free energy does not depend on the force in the considered range (12-18 pN). This is coherent with the fact that the elongation of dsDNA is almost constant in this force range. The method could be easily expanded to a more complete characterization of the energetics of such short segments of nucleic acids.

2.2.2 Helicase stepping: some preliminary results

Helicases are essential enzymes that unwind dsDNA to separate the two DNA strands. They are key elements of DNA replication and repair. As an helicase unwinds a DNA hairpin pulled at 8 pN and tethered

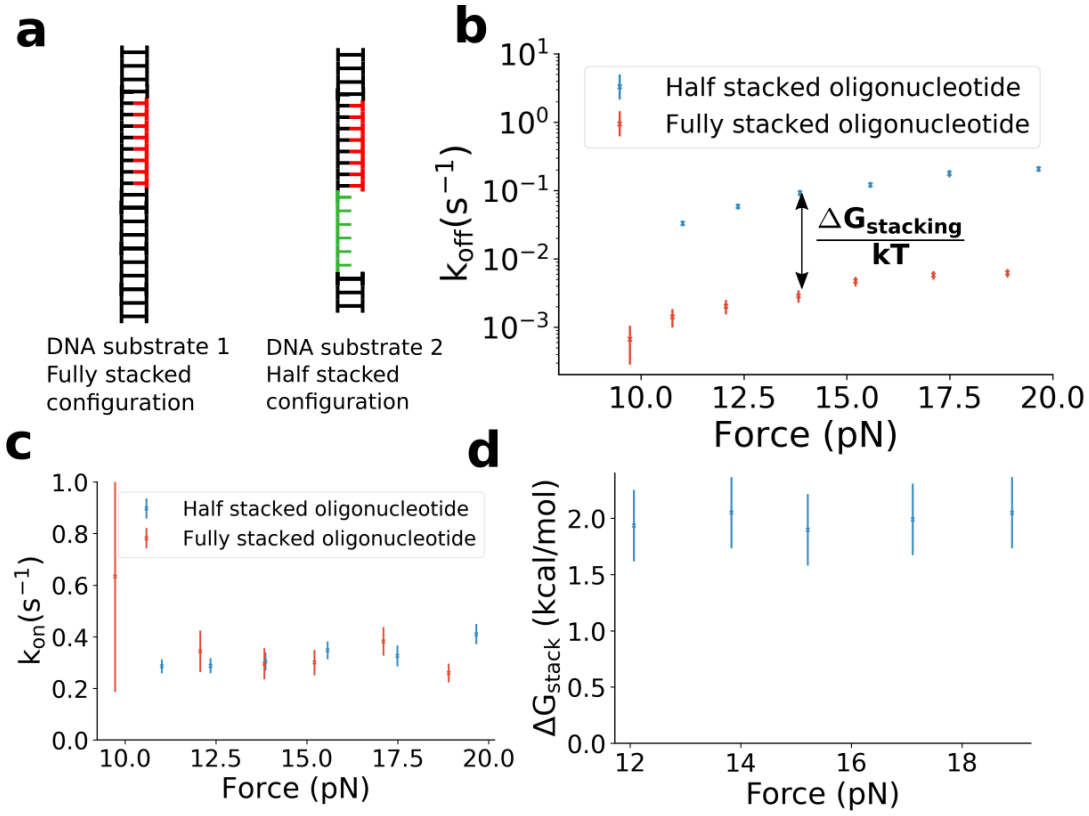

Figure 2-12: **Measurement of the stacking energy between 3'-A and 5'-G. a.** Illustration of the experiment. The hybridization presented earlier is reproduced in a fully stacked configuration that allows the stacking of both ends of the oligonucleotide with the tethered substrate. **b.** Comparison of the de-hybridization rate of the oligonucleotide between the fully and half-stacked substrate. **c.** Comparison of the binding rate of the oligonucleotide between the fully and half-stacked substrate. **d.** $\Delta G_{stacking} = kT \log \frac{k_{\text{off,FS}} k_{\text{on,HS}}}{k_{\text{off,HS}} k_{\text{on,FS}}}$, where FS and HS stand respectively for fully-stacked and half-stacked configuration. T = 298.15 K

between a surface and a magnetic bead, the measured elongation increases by twice the length of a ssDNA base for each base pair unwound, that is roughly 0.8 nm (see Figure 2-13.a). Distinguishing individual steps of an helicase with magnetic tweezers thus requires tracking the bead with subnanometric resolution and was one of the main motivations of the present work.

Upf1 is an helicase belonging to the Super-Family 1 that were studied in previous works of this team using magnetic tweezers [Fiorini et al., 2015, Fiorini et al., 2015]. However, we were so far not able to measure its discrete unwinding events. On Figure 2-13.b, we show that the resolution enhancement provided by *SDI* allows resolving its individual steps, provided that the ATP concentration is low enough (500 nM) in order to reduce the involved kinetic rates. The 30-bp hairpin is open step-by-step until the remaining unwound part becomes too short and starts to oscillate spontaneously between its open and closed states under the influence of the applied force and of the thermal fluctuations (starting from 272s).

Detecting steps in noisy data can prove a tricky exercise in practice, in particular for a signal presenting low-frequency drifts that forbid long-time averaging. Furthermore, the observer does not know *a priori*

when steps take place, while the spatiotemporal resolution predicted by equation 2.12 only holds if the averaging is performed separately before and after the jump, and not over the jump position. In order to test possible jump positions, we use the algorithm *Moving Step Fit* (MSF) described in [Opfer and Gottschalk, 2012], fitting the signal by horizontal lines instead of fitting it by any linear function. A window w is defined. For each point in the data x_i, the mean of the signal m_i^l between $i-w/2$ and i is computed along with the residues of the fit, called left residues RSS_l:

$$RSS_i^l = \sum_{j=i-w/2}^{i} (x_j - m_i^l)^2 \tag{2.38}$$

Equivalently, the mean of the signal m_i^r between i and $i+w/2$ is computed along with the residues of the fit, called right residues RSS_r:

$$RSS_i^r = \sum_{j=i}^{i+w/2} (x_j - m_i^r)^2 \tag{2.39}$$

Finally, the mean of the signal m_i over the whole window w is computed, along with the whole residues RSS:

$$RSS_i = \sum_{j=i-w/2}^{i+w/2} (x_j - m_i)^2 \tag{2.40}$$

The MSF score is defined as :

$$MSF_i = \mid m_i^r - m_i^l \mid (RSS_i - RSS_i^r - RSS_i^l) \tag{2.41}$$

A step is detected at the position x_i if the following conditions are true :

- The step is larger than a given threshold t_s :

$$\mid m_i^r - m_i^l \mid > t_s \tag{2.42}$$

- The score MFS_i is larger than a score threshold t_{MFS}.

We set the score threshold t_{MFS} by computing the distribution of scores on a signal that precedes the injection of the helicase, *i.e.* where no step is expected. The threshold is defined as the score value where the cumulative probability of scores on such a step-free trace equals 99.99%. For such a threshold, a false positive detection every 10000 points (62.5 seconds at 160 Hz) is expected.

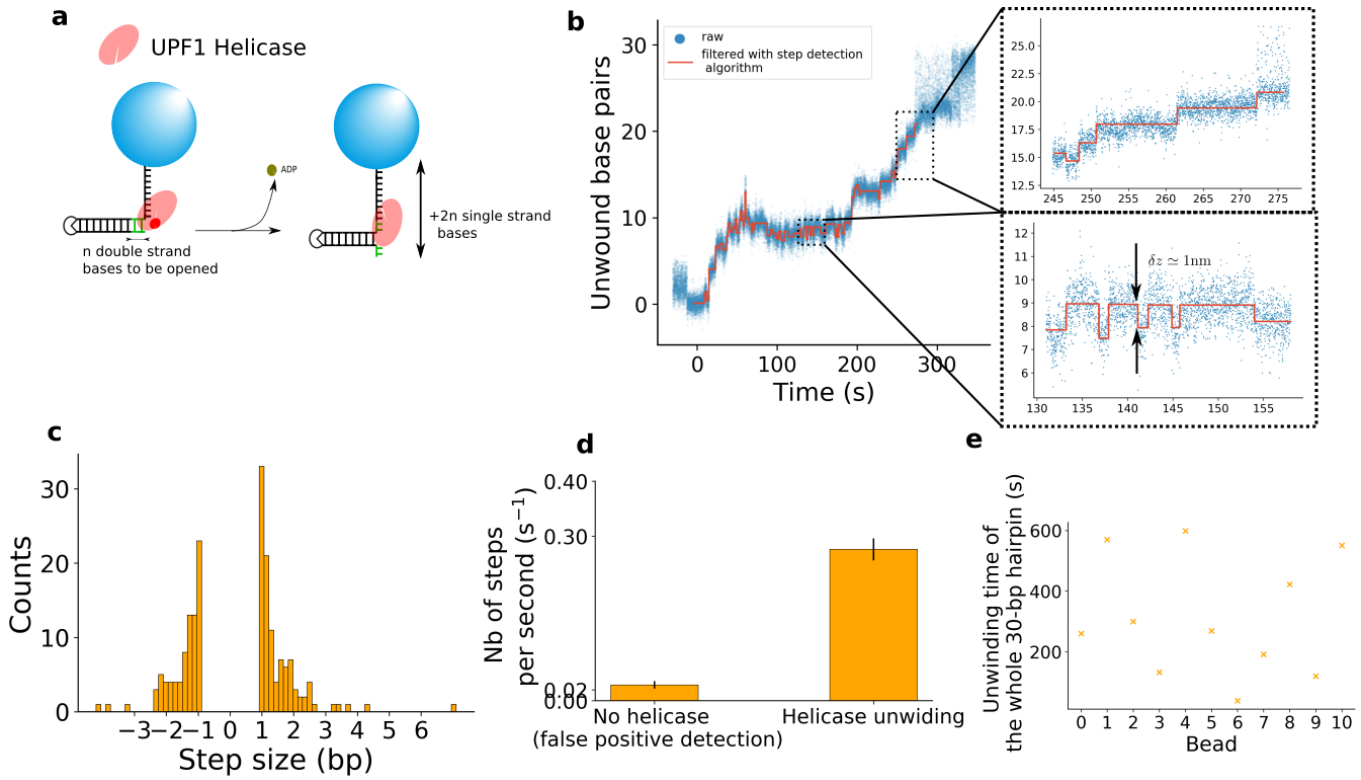

Figure 2-13: **Towards the characterization of the discrete stepping mechanism of helicases. a.** Illustration of the experiment (represented numbers of bases are not accurate). As the helicase Upf1 unwind a base pair of DNA, the extension of the tethered molecule increases by the extension of two bases, that is roughly 0.8 nm. **b.** A typical trace showing the unwinding of a 30-bp DNA hairpin by the Upf1 helicase at 9 pN, with 500 nM ATP **c.** Distribution of detected step sizes during the unwinding of a unique hairpin (bead 2) (190 events). **d.** Rates of false positive detection (steps detected without helicase). Nsteps=18, T = 628s. **e.** Rates of step detection for bead 2. (steps detected during helicase unwiding). Nsteps = 190, T = 689s. **f.** Average time between two successive steps over 11 beads studied in this work.

Figure 2-13.d shows the number of false positive per unit of time obtained by analyzing, with the algorithm described above, 628s seconds of signals before the helicase injection, compared to the number of stepping events per unit of time during helicase unwinding at 500 nM ATP. The distribution of step sizes detected when the enzyme is added in solution is shown in figure 2-13.c. The shape of this distribution displays a spurious lower bound, around 1 bp (0.9 nm). This is due to the score threshold chosen above. However, decreasing this threshold strongly increases the detection of false positive step detection, such as shorter steps cannot be measured with high fidelity.

While we clearly observe discrete steps during helicase unwinding, only a few experiments allowed us to clearly distinguish the discrete opening of the whole hairpin. Furthermore, the unwinding time of the whole hairpin varied significantly from one experiment to the other (figure 2-13.e). We suspect this is due to a bad control of ATP concentration during the experiment. Indeed, the helicase is introduced at a concentration of 120 nM while we must work at ATP concentration of roughly 500 nM. Furthermore, maintaining a constant

flux in order to renew the buffer is impossible since it induces an important noise of measurement which origin remains unclear. In these conditions, a small residual ATPase activity of Upf1 would consume the ATP present in solution. As a consequence, and considering that several months of experiments only led to 11 traces allowing to distinguish the individual steps of the helicase during hairpin opening, it appears, that, at this stage, our tool will not permit to revolutionize the quantitative understanding of the discrete mechanisms of helicases. Further work is needed either to reduce experimental noise and/or to stabilize a low ATP concentration.

2.3 Conclusion

We presented in this chapter how the Brownian motion of the magnetic bead alters the spatiotemporal resolution of magnetic tweezers. Other sources of noise were fought against during this work but were not mentioned in this chapter as they are of lesser physical interest. Solutions against these sources of noise are described in the material and methods section. They mainly include the stable thermalization of the objective, the damping of the mechanical noise of the building, the stabilization of the intensity of the light sources and the disconnection of the camera from the computer power-supply. At the level of long time scales (> 1s), these sources of noise are still present and prevent the accurate measurement of slow extension changes or the averaging of slow Brownian motions. However, at the shorter time scales needed to measure fast extension steps, they are not a problem. With the optical precision of *Stereo Darkfield Interferometry*, the photon noise is now negligible compared to the Brownian motion of the bead. However, it appeared that the Brownian motion is much larger than what we predicted with naive arguments. We understood that this was due to the vicinity of the surface, that causes a dramatic increase of the drag coefficients, and to the magnetic anisotropy of the bead. This suggests that future research should focus on reducing these hydrodynamic effects. First, the synthesis of smaller magnetic beads would allow us to reduce the effect of the increased drag close to the surface. This could for example be achieved by using materials with a higher saturation magnetization than iron oxides, such as cobalt [Li et al., 2009]. Second, the patterning of the surface with regularly spaced posts [Ybert et al., 2007] would allow decreasing the effective hydrodynamic *no-slip* lengths close to the surface and thus the surface-induced drag.

In spite of these limitations, we were able to reach with magnetic tweezers the precision of some of the best optical tweezers (figure 2-14). We illustrated this precision with the model measurement of the

thermodynamics of base stacking. However, we were not able to surpass this spatiotemporal resolution. In particular, our observations of helicase stepping are not precise nor reproducible enough in order to draw interesting conclusions regarding their kinetics. Our method presents the same limitations as the data from optical tweezers (continuous step size distributions, low-ATP constraint) but also adds additional experimental difficulties. One one hand, the concentration of the enzyme is hard to master due to the proximity of the surface. On the other hand, the ATP concentration cannot be stabilized since a permanent hydrodynamic flow in the microfluidic cell induces a strong noise. As a consequence, it appears that gaining insight into helicase mechanisms cannot escape a more radical increase of the spatiotemporal resolution of magnetic tweezers down do the ångström at the timescale of a few milliseconds. Regarding this question, it is interesting to note that recent progress with nanopores allowed an extremely precise characterization of the microsecond discrete dynamics of helicases [Craig et al., 2019, Laszlo et al., 2017, Caldwell and Spies, 2017], suggesting that the technique is better suited for this type of application than micro-manipulation.

Nevertheless, while the motivations of this work were not completely fulfilled, an unexpected consequence of our gain in spatiotemporal resolution is the possibility to design extremely stable fluctuating probes out of nucleic acids, allowing very precise thermodynamic and kinetic measurements. This possibility, that is inherently linked to the force and temperature stability of magnetic tweezers, will be the object of the next chapter.

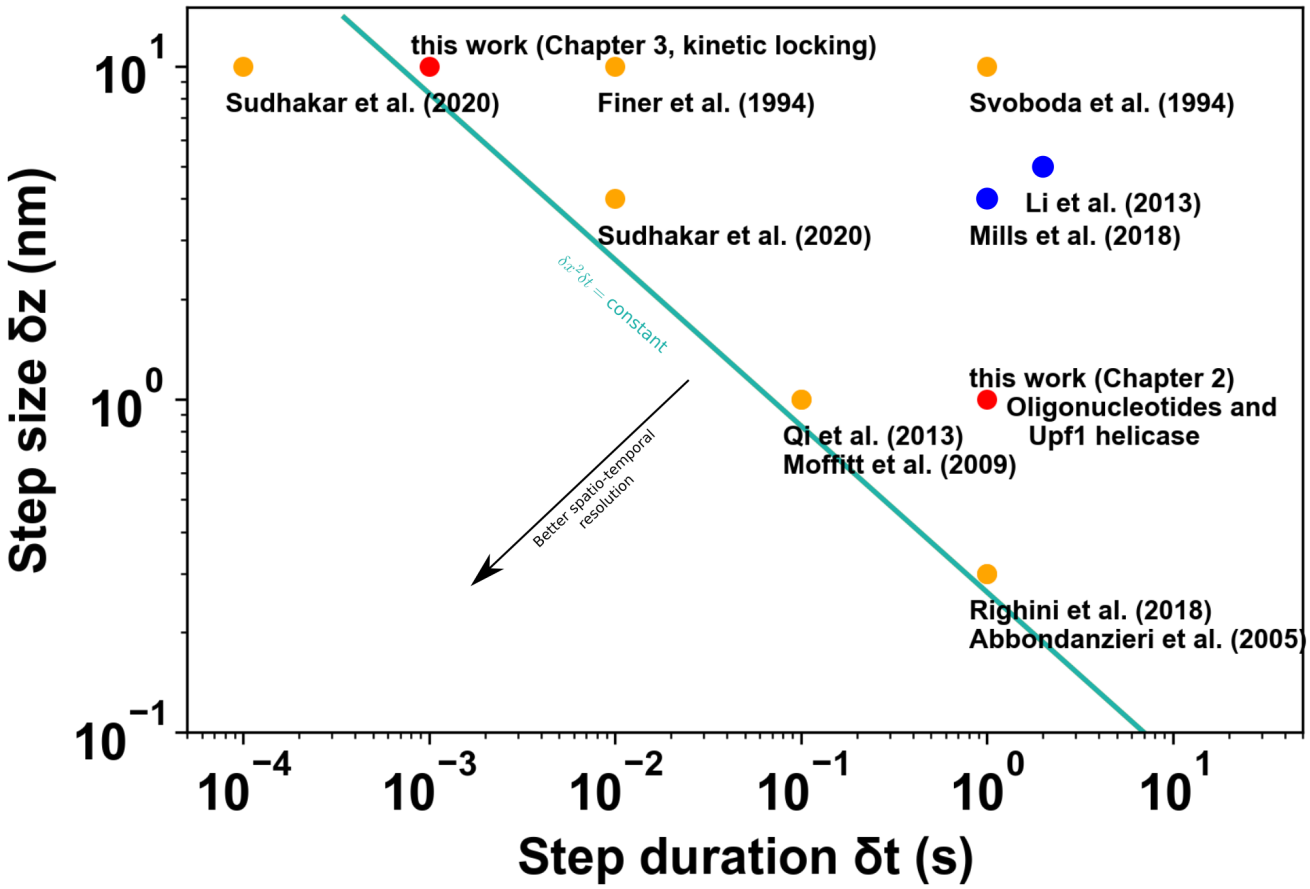

Figure 2-14: **Spatiotemporal resolution of our magnetic tweezers compared to previous single-molecule measurement.** We compare the spatio-temporal resolution demonstrated in our work with magnetic tweezers (in red) with some of the best single-molecule micro-manipulation experiments related to discrete extension steps (orange: optical tweezers, blue: magnetic tweezers). Most of them concern molecular motors except [Li et al., 2013], which describes successive folding and unfolding of G-quadruplexes. The blue line represents points of equal spatio-temporal resolution. Our work allowed us to approach the resolution of the best optical tweezers, however without outperforming them. Interestingly, optical tweezers made little progress during the last decade, except recently with the work of [Sudhakar et al., 2020], thanks to the use of significantly smaller beads. This bolsters our ambition to develop smaller magnetic beads out of more magnetic materials.

Chapter 3

Kinetic locking: a method to measure biomolecular interactions involving nucleic acids

We characterized in the previous chapter the spatiotemporal resolution of magnetic tweezers equipped with *Stereo Darkfield Interferometry* and demonstrated this resolution by resolving nanometric steps at the timescale of a few hundreds of milliseconds. Here we show that they allow the accurate measurements of the kinetic of a fluctuating DNA hairpin with a few milliseconds time resolution. We use this property, associated with the force and temperature stability of magnetic tweezers, to design a fast DNA fluctuating probe, whose kinetic rates are sensitive to its environment. The presence of a DNA-binding enzyme or of an oligonucleotide complementary to the probe affect its fluctuation rates and allows measuring the kinetic and thermodynamic constants of binding of these molecules with the probe. Contrarily to the existing detection methods based on single-molecule force spectroscopy, this sensitive technique, that we called *kinetic locking* does not rely on measuring spatial extension changes caused by binding but on the changes of the temporal properties of the probe. This technique complements bulk assays to measure binding kinetics and binding affinities.

3.1 An extremely stable DNA Fluctuating probe

3.1.1 The fluctuations of a 10-bp hairpin in the millisecond range

A DNA or RNA hairpin (HP) is a molecule of nucleic acid (NA) that contains a self-complementary portion. When pulled at a force F, such a hairpin can be found either in its open or closed state. In the open state, the self-complementary portion is linearized, the Watson-Crick interaction between the complementary bases is broken. In the closed state, the self-complementary portion is folded into a duplex structure. Both states can be differentiated with single-molecule force spectroscopy as they result in different extensions, separated by the length of the single-stranded DNA that appears unfolded. This length consists of the sum of the length of the loop and of twice the number of base pairs contained in the hairpin. For example, a 10-bp hairpin with a loop of 4 bases will unfold in 24 bases of single-stranded DNA, and the difference of extension between the closed and the open state at a force F will be $24 \times l_{ssDNA}(F)$, where $l_{ssDNA}(F)$ is the extension of a single DNA base at the force F. The difference of free energy between the open and the closed state of the system comprised of the magnetic bead and of the molecule $\mathscr{G}^*(F)$ reads:

$$\Delta\mathscr{G}^*(F) = \mathscr{G}^*_{open}(F) - \mathscr{G}^*_{closed}(F) = \overbrace{(N_{HP}+N_{loop})G_{ssDNA}(l_{ssDNA}(F)) - \frac{N_{HP}}{2}G_{dsDNA}(0) - G_{loop,constrained} - \underbrace{F(N_{loop}+N_{HP})l_{ssDNA}(F)}_{\text{energy of the microbead}}}^{\text{energy of the molecule}} \quad (3.1)$$

The second term is directly due to the applied force on the bead, it favors the states of longer extension. The first term mainly contains the free energy of hybridization of the nucleic acid $N_{HP}G_{ssDNA}(0) - \frac{N_{HP}}{2}G_{dsDNA}(0)$. This term favors the closed (hybridized) state of short extension. The other contributions appearing in this first term are a bit more subtle. First, there is the contribution of the elastic energy contained in single-stranded DNA, which results in the difference between $G_{ssDNA}(0)$ and $G_{ssDNA}(F)$. This part will be discussed later, when we consider how the hybridization energy varies with force. The other contribution $N_{loop}G_{ssDNA}(F) - G_{loop,constrained}$ contains the thermodynamics of a loop whose ends are constrained by the duplex. This term contains the impact of the loop on the stability of an open hairpin [Woodside et al., 2006b] in general, the loop favors the open state of the hairpin as it is energetically unfavorable to constrain its ends close to each other. The important point here is that the force-dependent term

$(N_{HP}+N_{loop})G_{ssDNA}(F)-F(N_{loop}+N_{HP})l_{ssDNA}(F)$ decreases with the force, as shown in figure 2-2.b., for any molecule whose force extension curve increases monotonously. Thus, equation 3.1 is in agreement with the intuition that larger force favors the open state by decreasing its free energy compared to the closed state.

We expect the probability of finding the hairpin in its closed state to be equal to:

$$p_{open}(F)=\frac{e^{-\frac{\mathcal{G}^*_{open}(F)}{k_BT}}}{e^{-\frac{\mathcal{G}_{open}(F)}{k_BT}}+e^{-\frac{\mathcal{G}^*_{closed}(F)}{k_BT}}}=\frac{1}{1+e^{\frac{\Delta\mathcal{G}^*(F)}{k_BT}}} \tag{3.2}$$

This probability can be rigorously measured only if it is possible to observe both states at constant force. However, the transition between the states is only possible at a force where the energy difference of both states with the transition state is small compared to the thermal energy. For long hairpins (typically > 50 bp), fluctuations between the open and the closed state cannot be observed since the activation energy of the transition is too large at the force where both states should coexist: this results in a phenomenon of hysteresis. The force must be increased far above the coexistence force in order to observe the opening of the hairpin. On the contrary, the force must be decreased below the coexistence force in order to observe the opening of the hairpin. This effect is shown in figure 3-1 that displays repetitive force extension curves of a $1.1kb$ hairpin.

Nevertheless, for a short hairpin with a short loop, the transitions between the open and the closed states can be observed at constant force [Woodside et al., 2006a]. We illustrate this by pulling at 9.5 pN on a 10-bp DNA hairpin with a loop of 4 bases (figure 3-2.a). The sequence of this hairpin will be used through all this chapter. Figure 3-2.b shows the hairpin fluctuating between its open and closed state. With our magnetic tweezers equipped with *Stereo Darkfield Interferometry*, both states are clearly distinguishable from one another down to milliseconds time scales. This allows us to sample the distribution of times spent in the open state T_{open} and in the closed state T_{closed} with high precision: several tens of thousands of times can be sampled in a few hundreds of seconds of measurements. We show in figure 3-2.e the distributions of T_{open} and T_{close} at various forces. They display very clear exponential distributions, showing that we can model the dynamics by two simple kinetic rates k_f (fold) a,d k_u (unfold), such as the probability ρ to observe both

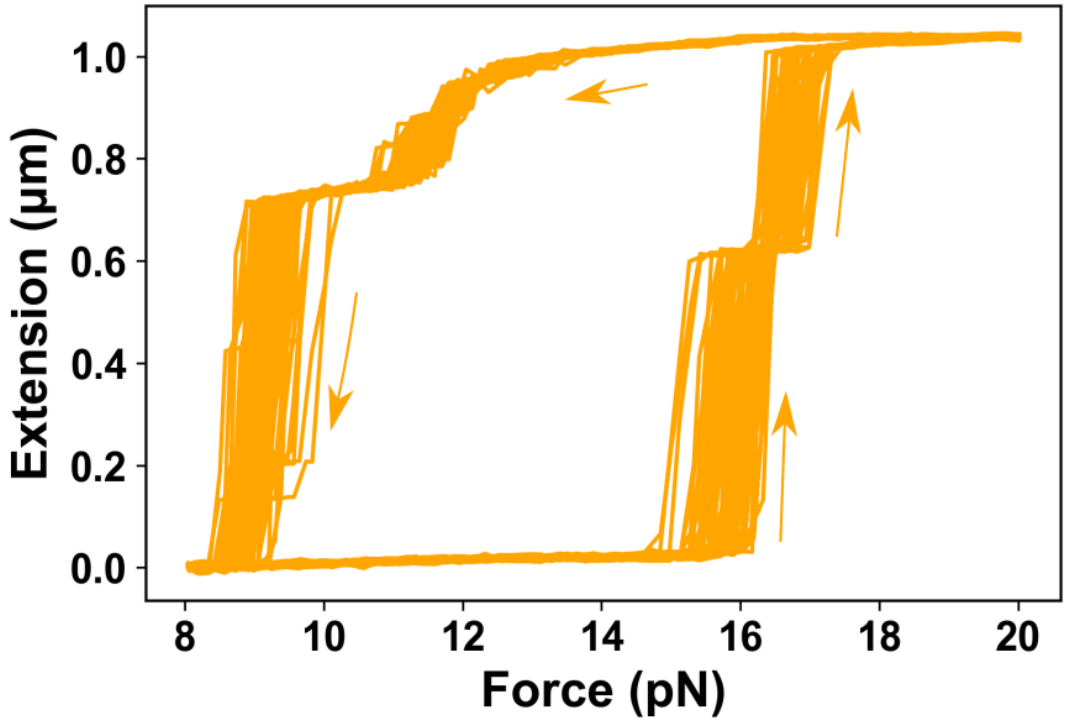

Figure 3-1: **Force extension curve of a DNA hairpin of 1.1 kb over 100 cycles.** For such a long molecule, the curve displays hysteresis and reproducible pauses during the opening and the closing that can be attributed to a complex sequence-dependent energy landscape.

times read:

$$\rho(T_{open}) = k_f e^{-k_f T_{open}} \tag{3.3}$$

$$\rho(T_{closed}) = k_u e^{-k_u T_{closed}} \tag{3.4}$$

Figure 3-2 shows the measured k_f and k_u as the function of the force obtained by fitting the time distribution by an exponential function. We will now explain shortly how to correct this curve in order to take into account the limited time resolution of the setup.

3.1.2 Correction of the impact of the acquisition frequency for rapid kinetic rates

When the acquisition frequency is slow compared to the dynamics of oscillation, we miss some events. For example, if k_u approaches $10^3 s^{-1}$ at a kHz acquisition frequency (figure 3-2.c above 11 pN), we miss events in the closed state when their lifetime is smaller than a millisecond. $\tau_s = \frac{1}{f_{aq}}$ is the minimal observable lifetime. Fitting the exponential distribution of lifetimes above τ_s instead of averaging all individual lifetimes is a simple way to capture k_u in this case without being biased by τ_s. However, most authors do not note

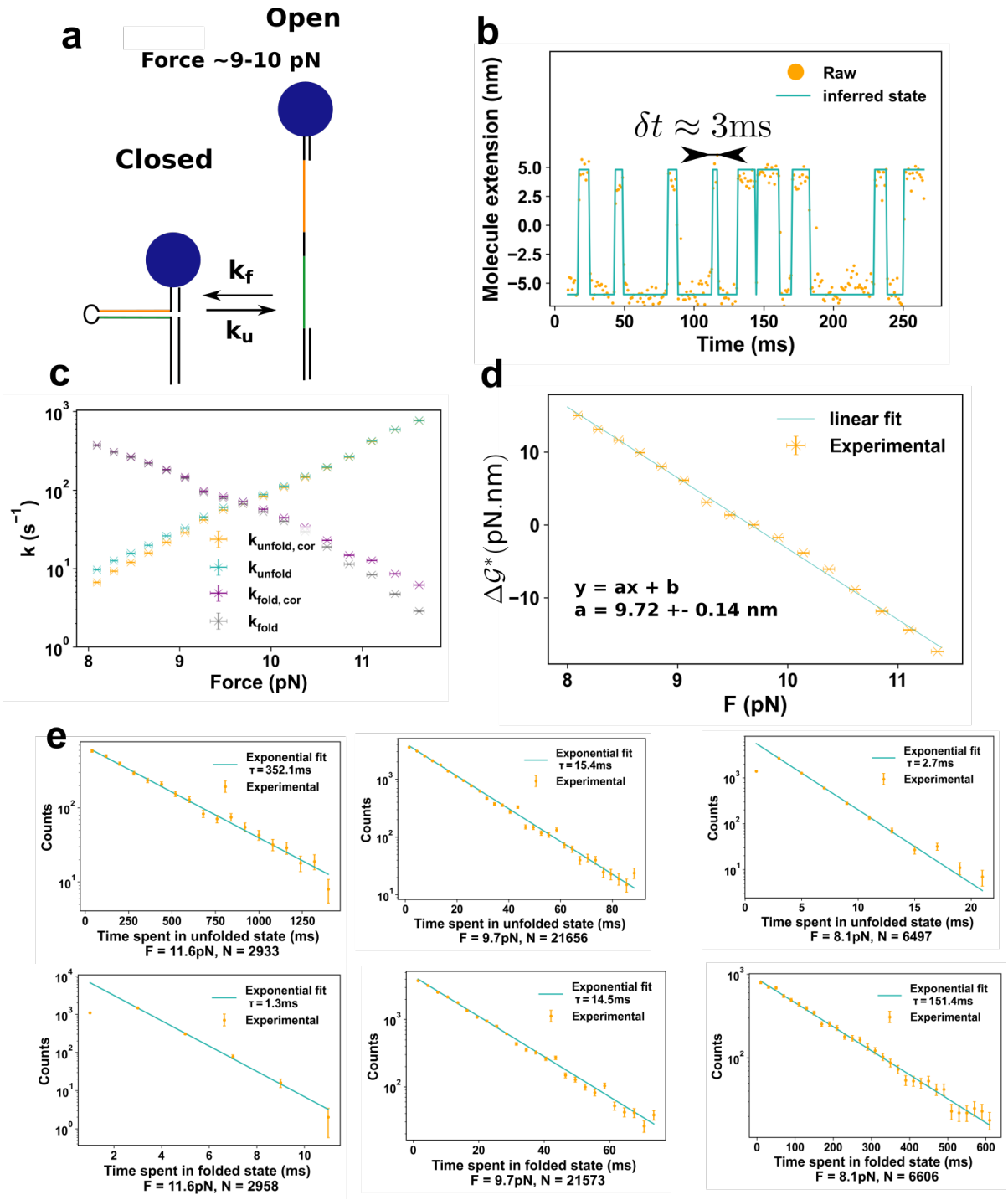

Figure 3-2: **Kinetics of folding/unfolding of a 10 bp hairpin a.** Illustration and definition of the kinetic constant. **b**: Trace representing the closing and the opening of a 10bp-hairpin at a acquisition frequency of 1500 Hz. The high optical resolution of SDI allows a frame-by-frame determination of the state of the hairpin and thus a millisecond time resolution. **c.** Kinetics of opening/closing of the HP as a function of the applied force. The subscript *cor* stands for the correction of hidden events as explained in the main text. The $\sim 0.5\%$ variability on the force is deduced from the error given by the constructor of the motor controlling the magnets. There is, furthermore, a $\sim 5\%$ systematic error on the force due to the bead magnetization. This curve being treated as the standard force curve throughout all this work, this systematic error is present in the same way in the whole chapter. **d.** $\mathcal{G}^*(F) = k_B T \ln(k_f/k_u)$ and corresponding linear fit. **e** Distribution of folding/unfolding times at three different forces. Exponential fitting of the distribution allows for the determination of the kinetic parameters represented in b. Error bars represent a relative error of $1/\sqrt{N}$, where N is the number of samples used to estimate a particular data point.

that this low cut-off also has an impact on the estimation of the opposite kinetic rate k_f, even if the latter is slow compared to the acquisition frequency. Indeed, if a significant number of events spent in the closed state is missed, then the time spent in the open state is overestimated. When unbiased, the probability of observing a time T_{open} reads $\rho(T_{open}) = k_f e^{-k_f T_{open}}$. If we now take into account the probability p_0 that we do not observe an event of closing, this relation becomes:

$$\rho(T_{open}) = k_f(1-p_0)\sum_{k=0}^{\infty} \overbrace{\frac{k_f T_{open}}{k!} e^{-k_f T_{open}}}^{\text{Probability that k folding events happen during } T_{open}} \times \underbrace{p_0^k}_{\text{Probability that these k events are hidden}}, \quad (3.5)$$

which reduces in:

$$\rho(T_{open}) = k_f(1-p_0)e^{-k_f T_{open}(1-p_0)}. \quad (3.6)$$

Thus, k_f is underestimated by a factor $1-p_0$. p_0 being the probability that a closing event is not observed, it takes the simple expression:

$$p_0 = \int_{T_{closed}=0}^{T=\tau_s} k_u e^{-k_u T_{closed}} \mathrm{d}T_{closed} = 1 - e^{-k_u \tau_s} \quad (3.7)$$

Let us illustrate this effect with the point at F = 11.6 pN in figure 3-2.e. At this point, we measure that $k_u = 770\mathrm{s}^{-1}$. Thus, at 1000 Hz, $p_0 = 0.54$: we miss half of the events in the closed state. As a consequence, the opposite kinetic rate k_f is underestimated by a factor $\simeq 2$. Figure 3-2.c shows the corrected kinetic rates as a function of force as well as the estimated $\Delta\mathscr{G}^*(F)$ computed from equation 3.2.

3.1.3 Temporal stability

A very sensitive validity check of the following work is given by the stability of the transition rates of the hairpin system versus time: it must display a strong temporal stability and must be measured with a high statistical precision. For the 10-bp DNA hairpin presented here, at 9.5 pN, the time between two transitions is of the order of 10 ms, allowing us to measure $N = 10^4$ transitions during a typical acquisition time of 100s and thus to reduce the relative error made on the estimation of the kinetic rates to $\sqrt{N} \simeq 1\%$. Figure 3-3 shows the temporal stability of these rates at the scale of a single hairpin pulled at a constant force during several hours. 7000 s of acquisition are separated into 20 chunks of 350 s. The kinetic rates inferred from

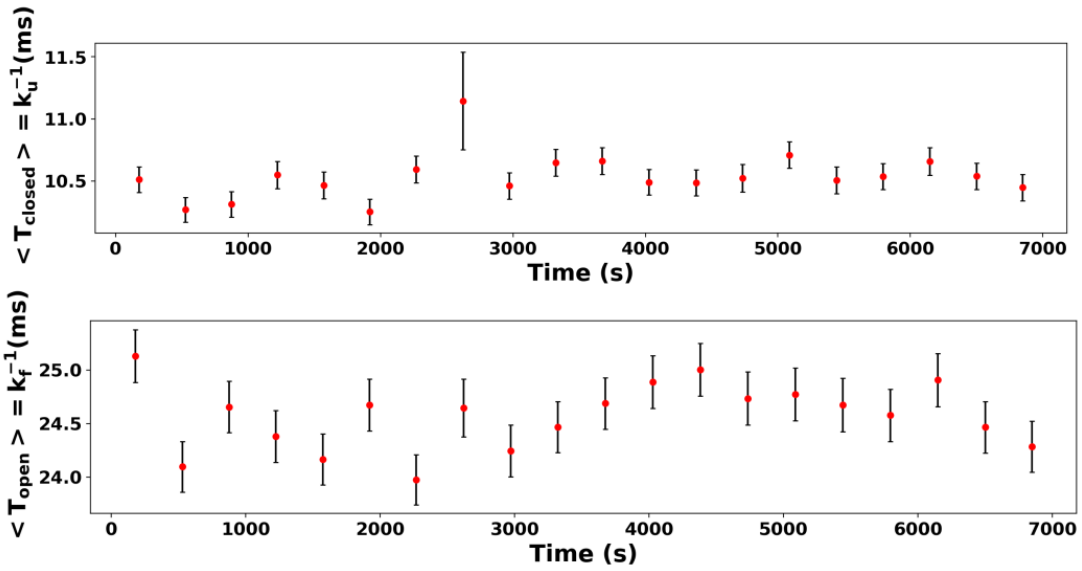

Figure 3-3: **Time course measurement of the average times spent in the closed and open states by the probe.** Times are measured during 7000s of acquisition of the extension a single molecule. The average is performed over time bins of 350s. Error bars are calculated through bootstrap resampling.

each of them are all equal within a tolerance of 1 ms[1].

3.2 Kinetic locking

3.2.1 Kinetic model

Kinetic locking consists in detecting perturbations to the kinetics of the hairpin described above. For example, a molecule binding to ssDNA prevents the closing of the hairpin and will thus increase the time spent in this opened state. On the other hand, a molecule binding to dsDNA prevents the opening of the hairpin and will consequently increase the time spent in its closed state. Therefore, these altered fluctuations can be used to detect binding events. The kinetic scheme of this procedure is illustrated in figure 3-4.

Let us formalize this effect, calling k_{on} the binding rate of the molecule to the DNA hairpin and k_{off} the dissociation rate of the molecule from the DNA. We will suppose here that the external molecule binds to the hairpin in its open state (thus to single-stranded DNA), but the exact same computation could be done for a molecule binding to the hairpin in its closed state by replacing k_u and k_f.

Calling $P_f(t)$ the probability for the hairpin to be in the open free state (no molecule bound), $P_l(t)$ the probability to be in the open locked state (molecule bound), and $P_c(t)$ the probability to be in the closed

[1] *i.e* 5-10% of variation compared to their typical value. While very small, this variation of the kinetic rates is larger than the 1% statistical error expected for more than 10000 independent points. If it is due to a force fluctuation, figure 3-2.c shows that the latter should be smaller than 0.1 pN in order to account for the 1 ms variation at $F_{1/2}$.

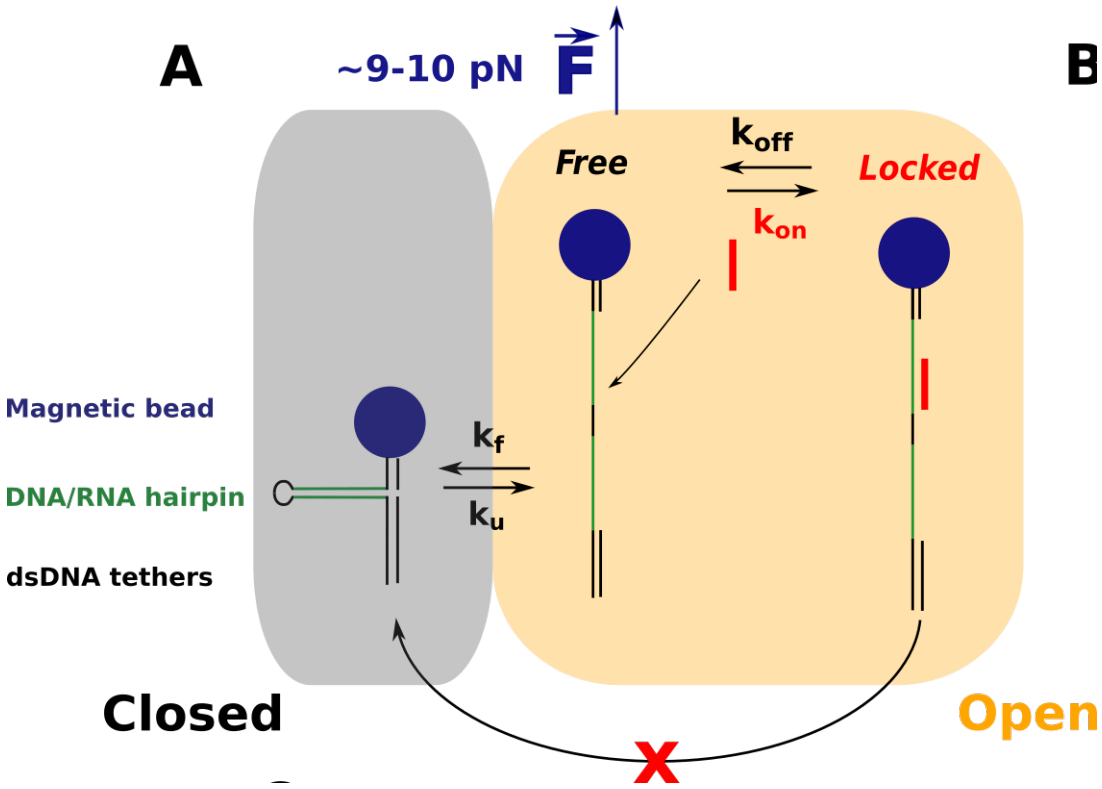

Figure 3-4: **Description of the kinetic locking assay.** When a molecule binds to the probe, it blocks it transiently in the open state.

state, the systems follows the dynamics :

$$\begin{bmatrix} \frac{dP_f}{dt} \\ \frac{dP_l}{dt} \\ \frac{dP_c}{dt} \end{bmatrix} = \begin{bmatrix} -(k_f + k_{\text{on}}) & k_{\text{off}} & k_u \\ k_{\text{on}} & -k_{\text{off}} & 0 \\ k_f & 0 & -k_u \end{bmatrix} \begin{bmatrix} P_f \\ P_l \\ P_c \end{bmatrix}. \tag{3.8}$$

The free (f) and locked (l) open states are indistinguishable. The probability to be in one of these open states is called $P_o(t) = P_f(t) + P_l(t)$. Given a hairpin that just moved to the open free state ($P_f(0) = 1, P_l(0) = 0, P_c(0) = 0$),we are interested in $\rho_o(T)$, the distribution of times spent in the open states before a closing event $(l \to c)$ happens. Such a closing event being observable, we are not interested in the subsequent dynamics of the hairpin. Thus, the dynamics of interest is limited to the system

$$\begin{bmatrix} \frac{dP_f}{dt} \\ \frac{dP_l}{dt} \end{bmatrix} = \underbrace{\begin{bmatrix} -(k_f + k_{\text{on}}) & k_{\text{off}} \\ k_{\text{on}} & -k_{\text{off}} \end{bmatrix}}_{A} \underbrace{\begin{bmatrix} P_f \\ P_l \end{bmatrix}}_{P}, \tag{3.9}$$

with $\rho_o(T) = \frac{dP_f}{dt} + \frac{dP_l}{dt} = -k_f P_f$

The matrix A has two negative eigenvalues λ_{+-}that verify:

$$\lambda_{+-} = \frac{-1}{2}\left[(k_f + k_{\text{on}} + k_{\text{off}}) \pm \sqrt{(k_f + k_{\text{on}} + k_{\text{off}})^2 - 4k_{\text{off}}k_f}\right]. \tag{3.10}$$

Two corresponding eigenvectors are:

$$V_\pm = \begin{bmatrix} \alpha_\pm \\ 1 \end{bmatrix}, \tag{3.11}$$

with

$$\alpha_\pm = \frac{\lambda_\pm + k_{\text{off}}}{k_{\text{on}}}. \tag{3.12}$$

We deduce the two combinations of $P_f$and P_l whose decay is exponential :

$$\alpha_\pm P_f + P_l = C_\pm e^{\lambda_\pm t}. \tag{3.13}$$

The integration constants $\alpha_\pm$ can be deduced from the initial conditions $(P_f(0) = 1, P_l(0) = 0)$, resulting in :

$$C_\pm = \alpha_\pm. \tag{3.14}$$

We deduce the expression for $P_f(t)$:

$$P_f(t) = \frac{\alpha_+ e^{\lambda_+ t} - \alpha_- e^{\lambda_- t}}{\alpha_+ - \alpha_-}. \tag{3.15}$$

And the expression for the distribution of times spent in the open state :

$$\rho(T) = k_f P_f(t) = k_f \frac{\alpha_+ e^{\lambda_+ t} - \alpha_- e^{\lambda_- t}}{\alpha_+ - \alpha_-}. \tag{3.16}$$

Thus, the distribution of times spent in the open state should be double exponential distribution, from which we can extract the kinetic parameters of binding k_{on} and k_{off}.

3.2.2 Measurement of the binding kinetics in the case $k_{\text{off}} \ll k_f$ and $k_{\text{on}} \ll k_f$

Here we show the effect of introducing an oligonucleotide of 7 bases that is complementary to the hairpin. Upon injection of an oligonucleotide complementary to the hairpin sequence, the hairpin stays locked in the open state during ~ 250 ms (figure 3-5.a). Since this time is much larger than the time spent by the probe in its open state, we can interpret this time at the typical binding time of the oligonucleotide. This intuition is backed by the solution of the above model when the typical times of the probe are much smaller than the times of binding of the oligonucleotide. Indeed, developing equation 3.10 at the order 2 in $\frac{k_{\text{off}}}{k_f}$ and $\frac{k_{\text{on}}}{k_f}$, we have:

$$\lambda_{\pm} = -\frac{k_f}{2}(1 + \frac{k_{\text{on}} + k_{\text{off}}}{k_f} \pm (1 + \frac{k_{\text{on}} - k_{\text{off}}}{k_f} + 2\frac{k_{\text{off}} k_{\text{on}}}{{k_f}^2})) \tag{3.17}$$

The first order is sufficient to deduce the limit of $\lambda_{\pm}$. We find:

$$\begin{aligned} \lambda_{+} &= -k_f(1 + O(\tfrac{k_{\text{off}}+k_{\text{on}}}{k_f})) \\ \lambda_{-} &= -k_{\text{off}}\big(1 + O(\tfrac{k_{\text{off}}+k_{\text{on}}}{k_f})\big) \end{aligned} \tag{3.18}$$

In this limit, the distribution of times is thus a double exponential with very separated times that can be resolved. The long times correspond to $\frac{1}{k_{\text{off}}}$ and the short times to $\frac{1}{k_f}$. We can unequivocally associate the long binding times to the presence of the oligonucleotide and the short binding times to the spontaneous binding of the probe.

This conclusion is confirmed by the change of the distribution of the open times as a function of the concentration of oligonucleotide (figure 3-5.b), and allows us to calculate the kinetic rates of binding of the 7-mer at $F \sim 9.5$ pN. We find $k_{\text{on}}(F) = 6.90 \pm 0.2 \mu\text{M}^{-1}\text{s}^{-1}$ and $k_{\text{off}}(F) = 4.35 \pm 0.14\text{s}^{-1}$.

3.2.3 Binding thermodynamics of very short oligonucleotides.

In the previous chapter (figure 2-12.b), we had measured that an oligonucleotide of 8 bases stayed hybridized longer than 5 seconds at 10 pN. In the previous subsection, we measured that the oligonucleotide of 7 bases stayed hybridized 250 ms. In spite of the sequence difference between both experiments, it shows that one unique base changes the hybridization time of several orders of magnitudes. It comes from the fact that the binding time evolves exponentially with the energy of hybridization while this energy depends linearly with the length of the oligonucleotide. For this reason, it is expected that oligonucleotides shorter than

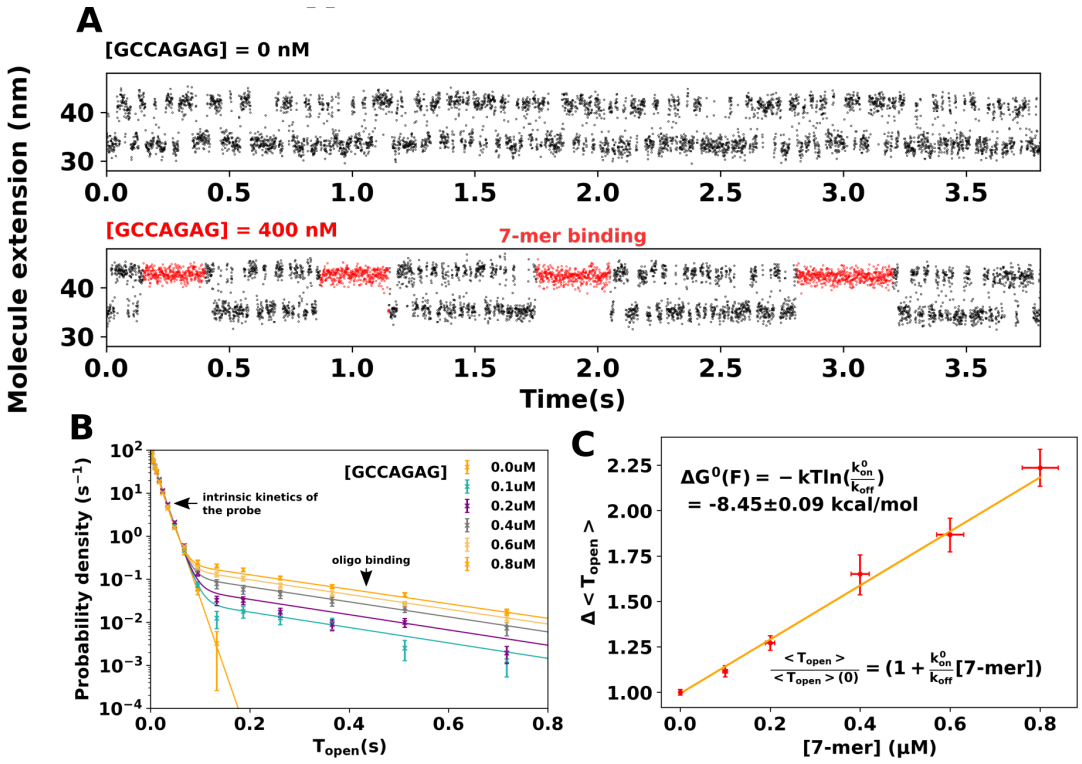

Figure 3-5: **Kinetic locking of the fluctuating probe by an oligonucleotide of 7 bases. a.** Evolution of the extension of the hairpin in the absence of oligonucleotide in solution (top) and in the presence of the complementary 7-mer (bottom). **b.** Distribution of the times spent by the DNA probe in its open state as a function of the concentration of 7-mer. The clear double exponential distribution allows us to deduce the binding rates k_{on} and k_{off}. **c.** Relative evolution of the mean time spent by the DNA probe in the open state $\overline{T_{\text{open}}}$ as a function of the concentration of 7-mer. The slope allows us to compute the energy of binding. Y-errors are computed through bootstrap resampling. X-errors are based on a putative error of 5% on the concentration. Each data point consists in the averaging of at least 7000 events.

7 bases will bind during times shorter than tens of milliseconds, and thus that their hybridization cannot be unequivocally distinguished from the spontaneous closing of the fluctuating hairpin.

However, our model predicts that the average time spent in the open state by the fluctuating probe should increase linearly with the concentration of oligonucleotides, the slope depending on the free energy of hybridization $\Delta\mathscr{G}_{\text{binding}}$. Indeed, the mean time spent in the open states $\overline{\text{T}_{\text{open}}}$ reads:

$$\begin{aligned}
\overline{\mathrm{T_{open}}} &= \int_0^{+\infty} T\rho(T)dT = \frac{k_f}{\alpha_+ - \alpha_-}\left(\frac{\alpha_+}{{\lambda_+}^2} - \frac{\alpha_-}{{\lambda_-}^2}\right) \\
&= \frac{k_f}{\lambda_+ - \lambda_-}\left(\frac{\lambda_+ + k_{\mathrm{off}}}{{\lambda_+}^2} - \frac{\lambda_- + k_{\mathrm{off}}}{{\lambda_-}^2}\right) \\
&= k_f \frac{(\lambda_+ + k_{\mathrm{off}})\lambda_-^2 - (\lambda_- + k_{\mathrm{off}})\lambda_+^2}{{\lambda_+}^2{\lambda_-}^2(\lambda_+ - \lambda_-)} \\
&= \frac{k_f k_{\mathrm{off}}({\lambda_-}^2 - {\lambda_+}^2 + k_f\lambda_+\lambda_-(\lambda_- - \lambda_+)}{{\lambda_+}^2{\lambda_-}^2(\lambda_+ - \lambda_-)} \\
&= \frac{-(\lambda_- + \lambda_+) + k_f}{\lambda_+\lambda_-} \\
&= \frac{k_{\mathrm{on}} + k_{\mathrm{off}}}{k_f k_{\mathrm{off}}},
\end{aligned}$$

where we used that $\lambda_+ + \lambda_- = -(k_{\mathrm{on}} + k_{\mathrm{off}})$ and $\lambda_+\lambda_- = k_f k_{\mathrm{off}}$

k_{on} is proportional to the concentration of oligonucleotides : $k_{\mathrm{on}} = k^0_{\mathrm{on}}C$. Considering that the energy of hybridization verifies : $\Delta G^0 = kT\ln(\frac{k^0_{\mathrm{on}}}{k_{\mathrm{off}}})$, we get:

$$\overline{\mathrm{T_{open}}} = \frac{1}{k_f}(1 + Ce^{\frac{\Delta G^0}{kT}}). \tag{3.19}$$

Fitting $\overline{\mathrm{T_{open}}} = aC + b$ as a linear function of the concentration thus should allow us to retrieve $\Delta G^0 = kT\ln(\frac{a}{b})$.

Interestingly, this dependence is also valid for the fast hybridization of 5-mer, even if their typical association and dissociation times are smaller than the typical fluctuating times of the probe.

We verify that our experiments confirm the linear dependence of $\overline{\mathrm{T_{open}}}$ with the concentration of oligomers (figure 3-6.a). The oligonucleotides are inserted in the solution at concentrations from the micromolar to the millimolar range in order to observe a measurable signal on T_{open}. All external parameters are fixed during injection. In particular, the magnets are kept fixed (and thus the force), during the whole sweep of oligonucleotide concentrations. This allows us to exclude any effect of a force change on the kinetics of the probe. We check that this force does not change substantially by drawing the time spent in the closed state, that should not depend on the concentration of oligonucleotide (figure 3-6.c). Indeed, the closed state is not affected by the oligonucleotide presence, within the precision (1 ms) of our experiments.

The reader will have noted that the oligonucleotides are introduced in unusual large concentrations, compared to the standards of single molecules experiments (typically the nanomolar, or roughly one molecule

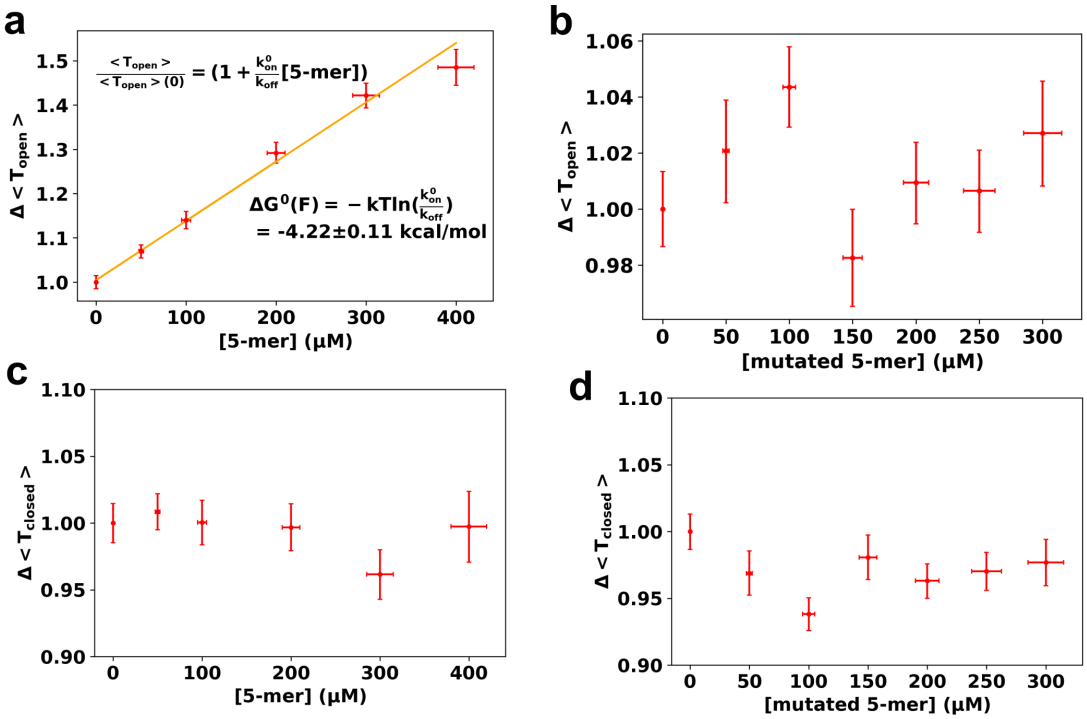

Figure 3-6: **Kinetic locking of the fluctuating probe by an oligonucleotide of 5 bases. a.** Relative evolution of the mean time spent by the DNA probe in the open state $\overline{T_{\text{open}}}$ as a function of the concentration of a 5-mer complementary to the probe (CAGAG). **b.** Relative evolution of the mean time spent by the DNA probe in the open state $\overline{T_{\text{open}}}$ as a function of the concentration of a 5-mer that is not complementary to the probe (CACAG). **c.** Relative evolution of the mean time spent by the DNA probe in the closed state $\overline{T_{\text{closed}}}$ as a function of the concentration of a 5-mer complementary to the probe (CAGAG). **d.** Relative evolution of the mean time spent by the DNA probe in the closed state $\overline{T_{\text{closed}}}$ as a function of the concentration of a 5-mer that is not complementary to the probe (CACAG).

per micron cube). For this reason, we have to control that the effect on the opening time of the presence of oligonucleotide is not due to an increase of ionic strength due to the presence of charged nucleic acids in high concentrations. We thus introduced oligonucleotides of the same length that are not complementary to the sequence of the fluctuating hairpin. Here again, the presence of such oligonucleotides results in the absence of measurable change of the time spent in the open state (figure 3-6.b-d). We can thus assert that the increase of time spent in the open state is due to the locking effect of the oligonucleotide complementary to the sequence of the probe, validating our protocol for the measurement of the thermodynamics of binding.

For such short oligonucleotides, the distribution of time spent in the open state looks is a single exponential and not a double exponential, contrarily to what we claimed above. This is due to the fact that when k_{on} and k_{off} are much larger than k_f, the fastest time of the double exponential is not observable given the time resolution of our experiment.

Indeed, in this case, the first eigenvalue in 3.10 reads, at the first order in $\frac{k_f}{k_{\text{on}}+k_{\text{off}}}$:

$$\lambda_+ = (k_{\text{off}} + k_{\text{on}}) \tag{3.20}$$

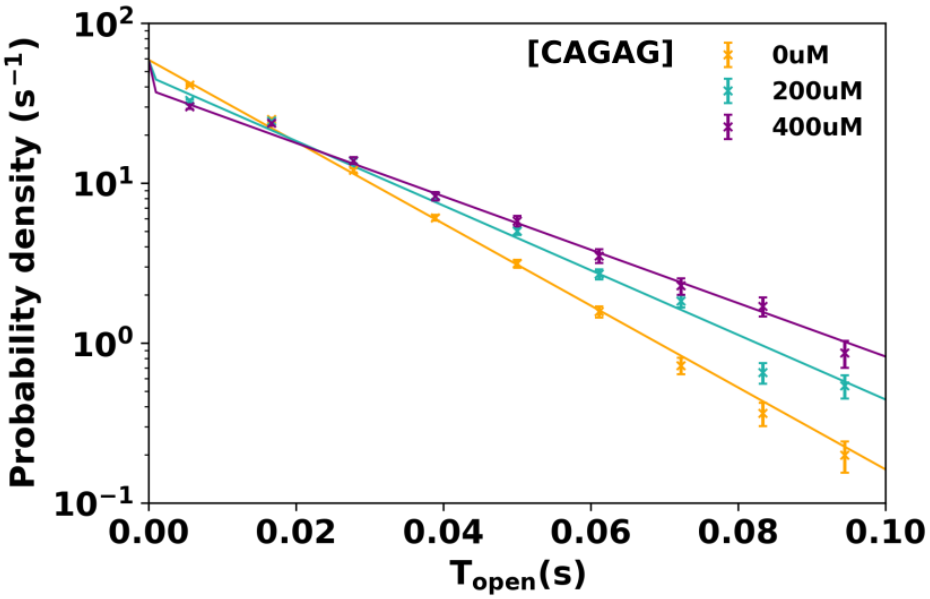

Figure 3-7: **Distribution of the times spent by the DNA probe in its open state as a function of the concentration of 5-mer.** The kinetics of hybridization of the oligonucleotide being much faster than the kinetics of the probe, all distributions follow single exponential laws. k_{on} and k_{off} cannot be inferred.

This corresponds to short times that cannot be observed.

The second value reads, still, at the first order in $\frac{k_f}{k_{\text{on}}+k_{\text{off}}}$:

$$\lambda_- = -\frac{1}{2}\left[(k_f+k_{\text{on}}+k_{\text{off}}) - (k_{\text{on}}+k_{\text{off}})(1+\frac{k_f}{k_{\text{on}}+k_{\text{off}}} - \frac{2k_f k_{\text{off}}}{(k_{\text{on}}+k_{\text{off}})^2}\right] \tag{3.21}$$

$$= -\frac{k_{\text{off}}k_f}{k_{\text{off}}+k_{\text{on}}} \tag{3.22}$$

$$= -\frac{k_f}{1+\frac{k_{\text{on}}}{k_{\text{off}}}} \tag{3.23}$$

This eigenvalue corresponds to a time that evolves in the same way that the average time $\overline{T_{open}}$, increasing linearly with the concentration. Thus, in this regime, the observable distribution follows a simple exponential distribution that does not allow measuring k_{on} and k_{off}. Only their ratio, and thus ΔG, can be measured.

This limiting case is actually an illustration of the classical kinetic approximation of *quasi-equilibrium*. It states that, for a simple kinetic reaction such as:

$$\text{closed} \xleftarrow{k_f} \text{free} \underset{k_{\text{on}}}{\overset{k_{\text{off}}}{\leftrightarrows}} \text{locked}, \tag{3.24}$$

if k_f is slow compared to the other rates, one can make the approximation that $\frac{[\text{free}]}{[\text{locked}]} = \frac{k_{\text{off}}}{k_{\text{on}}}$. Thus, with $[\text{free}] + [\text{locked}] = 1$ as initial condition, we have that the apparent rate of folding is $k_f[F] = \frac{k_f}{1+\frac{k_{\text{on}}}{k_{\text{off}}}}$, recalling our relation 3.23.

As a consequence, the interpretation of our experimental results for very short oligonucleotides with millisecond binding rates is all contained in the *quasi-equilibrium* hypothesis: the oligonucleotides in solution are constantly binding and unbinding to the probe, decreasing the time it spends in the open free state FF where it can close and thus decreasing the probability of closing per unit of time. It is substantially different from what we observed earlier with the oligonucleotide of 7 bases, where one long event spent in the open state could be attributed to a single oligonucleotide binding to the probe. Here, in the high concentration conditions used to observe the thermodynamics of 5- and 6-mers, many different oligonucleotides bind and unbind during a single opening event.

3.2.4 Influence of standard chemical modifiers and comparison with the nearest-neighbour model

We briefly studied the influence of standard chemical modifiers to the hybridization energy of oligonucleotides. First, we measured the effect of adding an acridine group at the 5'-position of the 5-mer, an intercalator that is often used to stabilize the hybridization of short nucleotides. Then, we measured the effect of adding a Cy3 group at the 5' position of the 5-mer. Cy3 is a common fluorophore, that is for example used in FRET experiments to detect the hybridization of two complementary DNA oligonucleotides. Interestingly, the modified oligonucleotides displayed a larger or equal hybridization energy than the 6-mer, 6-mer that has one additional cytosine compared to the 5-mer. Thus, these experiments confirm and quantify the strong interaction of these modifiers with DNA. This interaction might be strongly sequence dependent, so that a more thorough tabulation will be necessary. Still, the result shows that using fluorophores such as Cy3 for single-molecule characterization of binding energies requires extra caution.

We also compare in table 3.1 the ΔG obtained with our measurements with the widely used nearest-neighbor (NN) tables [SantaLucia Jr and Hicks, 2004]. Usual salt corrections were used [Schildkraut and Lifson, 1965, von Ahsen et al., 2001]. The nearest-neighbor model consists in capturing the thermodynamic properties of DNA in a table containing all the energies of the di-base NN where N can be any of the four bases [Allawi and SantaLucia, 1997]. Interestingly, our results are in very good agreement with the prediction of the model. This is rather surprising since our measurements are performed at $\simeq 9.5pN$ whereas

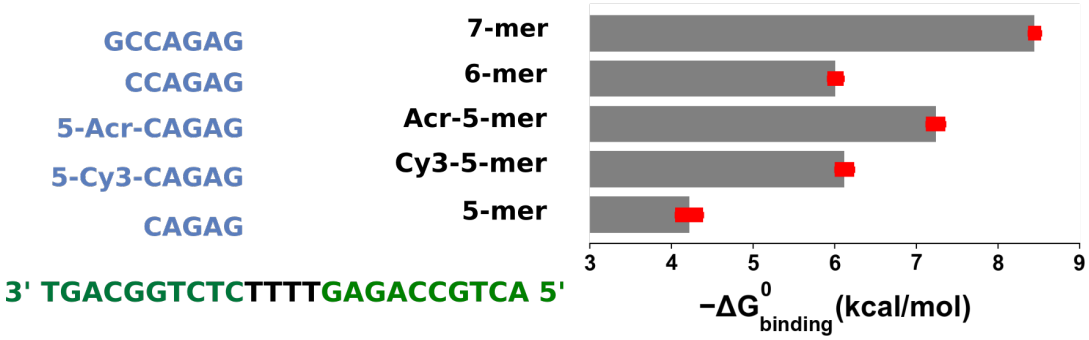

Figure 3-8: **Free energies of binding of five different oligonucleotides measured with kinetic locking.** The sequence of the probe is shown in green and the sequences of the oligonucleotides in blue. Cy3 and acridine modifications increase substantially the binding energy.

Oligomer	CAGAG	CCAGAG	GCCAGAG	5'-MeO-Cl-Acr CAGAG	5'-Cy3 CAGAG
ΔG - kinetic lock	-4.26 ± 0.08	-6.01 ± 0.09	-8.45 ± 0.09	-7.24 ± 0.06	-6.12 ± 0.09
ΔG - SantaLucia & Hicks	-4.05	-6.01	-8.42	N/A	-5.57*

Table 3.1: **Comparison of the experimental binding energies (in kcal/mol) obtained by *kinetic locking* with standard predictions by the nearest-neighbor model at 25°C.** NN-computations were made with the freely available software Biopython [Cock et al., 2009] after correction of two misreproduced values from the cited thermodynamic tables. Displayed errors are statistical errors. The application of a force of 9.5 pN induces a systematic correction that lies between -0.015 and 0.040 kcal/mol/nucleotide (see next subsection). All curves used to infer these values are shown in figure 3-9. *The effect of the Cy3 group is estimated using the sequence dependent estimations provided by Moreira *et al.* in [Moreira et al., 2015].

the NN-model is calibrated with bulk experiments performed at $0pN$.

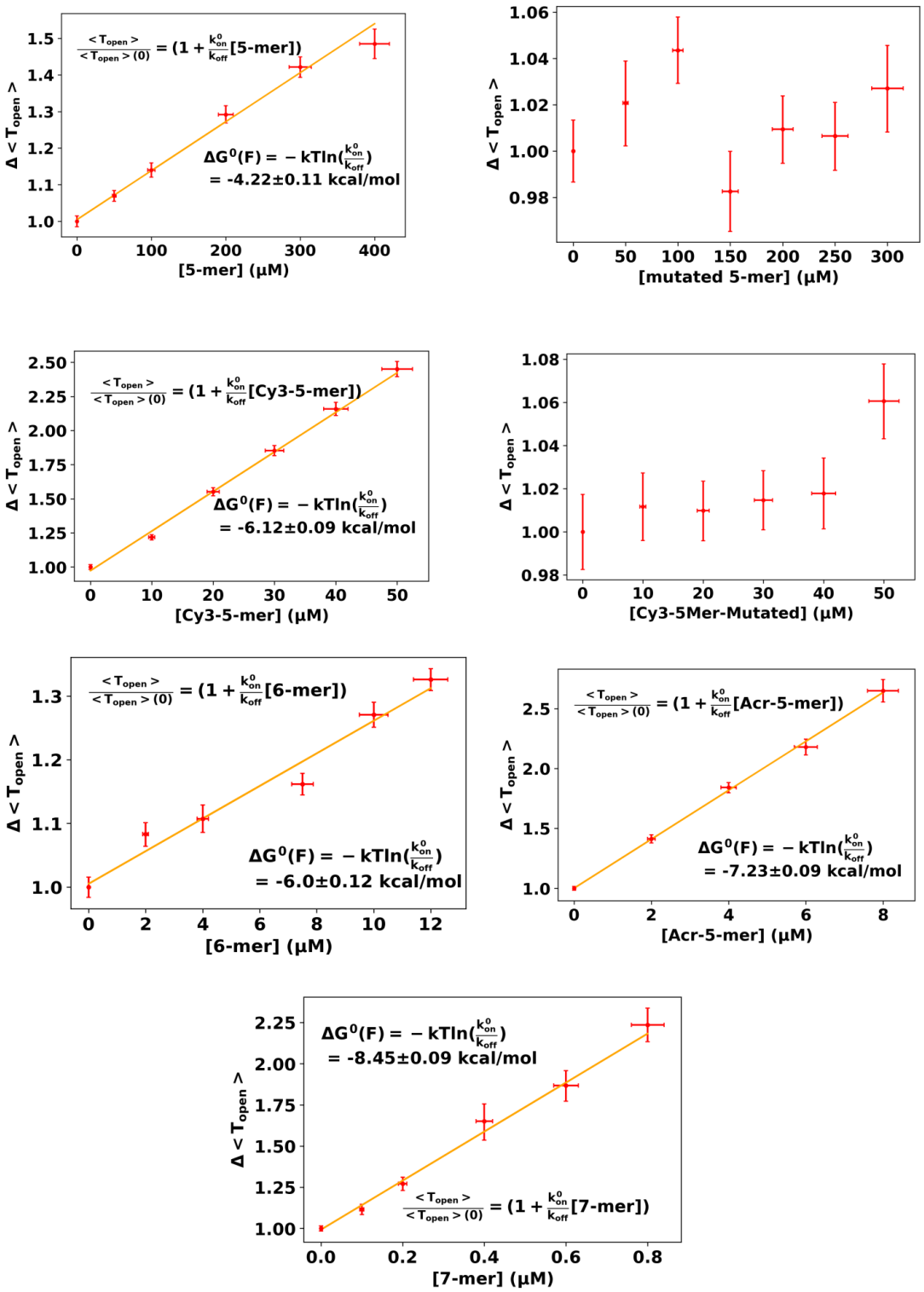

Figure 3-9: **Average times spent by the fluctuating probe in its open state $< T_{\text{open}} >$ as a function of oligonucleotide nature and concentration.** Error bars are computed by bootstrap resampling. Errors on the fit are computed using the covariance matrix. Averages are performed on samples containing at least 4000 independent times. Mutated 5-mers (CACAG) have a mismatch at the third position compared to the oligonucleotides (CAGAG) that are complementary to the hairpin sequence.

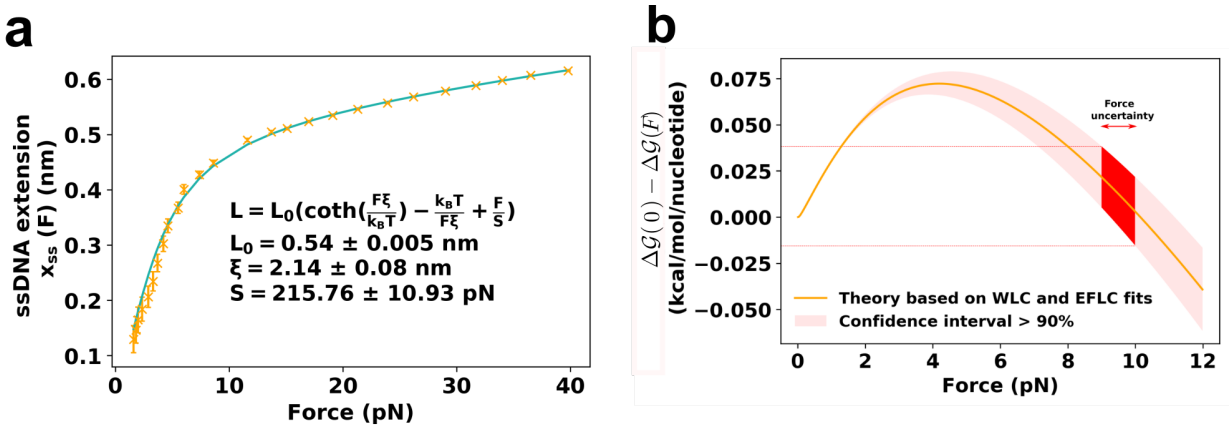

Figure 3-10: **Impact of the pulling force on the measurement of the binding energy. a.** Experimental force-extension curve of a single-stranded DNA molecule and corresponding fit to the freely jointed chain model with extension (EFJC). Data from [Manosas et al., 2012b] **b.** Contribution of the force to $\Delta G_{\text{binding}}$ computed using the worm-like chain model for double-stranded DNA (persistence length of 50 nm and maximum length per nucleotide of 0.34 nm), and the freely jointed chain model with extension for single-stranded DNA.

3.2.5 Comment on the influence of the force on the thermodynamic measurements

Here we explain why the influence of the force is negligible in the force range we are considering.

First, we remind how the force-extension curves allow computing the free energy of DNA at various extensions $G_{\text{ss/ds}}(l_{\text{ss/ds}})$.

From the experimental force extension curve, one can compute $G_{\text{ss/ds}}(F)$ by integrating the observed extension curve with respect to l (red area in figure 2-2) :

$$G_{\text{ss/ds}}(F) = G_{\text{ss/ds}}(l_{\text{ss/ds}}(F)) = G_{\text{ss/ds}}(0) + \int_{l'=0}^{l'=l_{\text{ss/ds}}(F)} f(l')\mathrm{d}l' \tag{3.25}$$

$\Delta\mathcal{G}_{\text{binding}}(F)$ is the difference of free energy of the whole system (molecule + bead) pulled at force F when the DNA goes to its double-stranded state (final state, hybridized) from its dissociated state, consisting of two single-stranded DNA, the first being pulled at force F, and the other, free in solution, on which no force is applied :

$$\Delta\mathcal{G}_{\text{binding}}(F) = \underbrace{G_{\text{ds}}(F) - Fl_{\text{ds}}(F)}_{\textbf{bead + dsDNA pulled at F}} - \underbrace{(G_{\text{ss}}(F) - Fl_{\text{ss}}(F))}_{\textbf{bead +ssDNA pulled at F}} - \underbrace{G_{\text{ss}}(0)}_{\textbf{free oligo}} \tag{3.26}$$

Thus, using the equation just above :

$$\Delta\mathscr{G}_{\text{binding}}(F) = \left(G_{\text{ds}}(0) + \int_{l'=0}^{l'=l_{\text{ds}}(F)} f(l')\mathrm{d}l' - Fl_{\text{ds}}(F)\right) - \left(G_{\text{ss}}(0) + \int_{l'=0}^{l'=l_{\text{ss}}(F)} f(l')\mathrm{d}l' - Fl_{\text{ss}}(F)\right) - G_{\text{ss}}(0) \tag{3.27}$$

In the two parentheses, we recognize an integration by part, and thus:

$$\Delta\mathscr{G}_{\text{binding}}(F) = \left(G_{\text{ds}}(0) + \int_{f=0}^{f=F} l_{\text{ds}}(f)\mathrm{d}f\right) - \left(G_{\text{ss}}(0) + \int_{f=0}^{f=F} l_{\text{ss}}(f)\mathrm{d}f\right) - G_{\text{ss}}(0) \tag{3.28}$$

$$= \Delta\mathscr{G}_{\text{binding}}(0) + \int_{f=0}^{f=F} l_{\text{ds}}(f)\mathrm{d}f - \int_{f=0}^{f=F} l_{\text{ss}}(f)\mathrm{d}f \tag{3.29}$$

The force-extension curve of double-stranded DNA $x_{ds}(f)$ is well established (the worm-like chain model fits it well for forces < 15 pN). The force-extension curve of single-stranded DNA $x_{ss}(f)$ is derived from the fit of a long ssDNA by the freely jointed chain model with extension (EFJC, Figure 3-10.a). The corresponding estimation of $\Delta\mathscr{G}_{\text{binding}}$ as a function of the force is shown on Figure 3-10.b. The confidence interval is based on the errors made on the fit of the ssDNA by the EFJC model. The figure shows that the contribution of the force to $\Delta\mathscr{G}_{\text{binding}}$ is smaller than 0.04 kcal/mol/nucleotide in the force range of our experiments. This explains *a posteriori* why our results are close from the model based on 0-force measurements.

3.3 An application of kinetic locking to the measurement of NA/protein interactions

Helicases of the RecQ family are thought to play an important role in the stabilization of stalled replication forks [Bachrati and Hickson, 2008]. RecQ homologues have for example been proved to be essential for RF restart [Davies et al., 2007] and to accumulate at genomic *loci* known to be fragile replication sites [Lu et al., 2013]. While our team studied in previous work the way it unwinds DNA using magnetic tweezers [Bagchi et al., 2018], they were not able to properly measure its affinity to replication fork compared to pure ssDNA, as we were lacking a means to detect its individual bindings independently from its DNA unwinding activity. Other micromanipulation studies [Klaue et al., 2013] suggested a stronger residence time of RecQ close to a replication fork but without providing quantitative binding rates. Finally, bulk experiments showed that RecQ displays a stronger affinity for substrates containing a replication fork with a gap on the leading strand

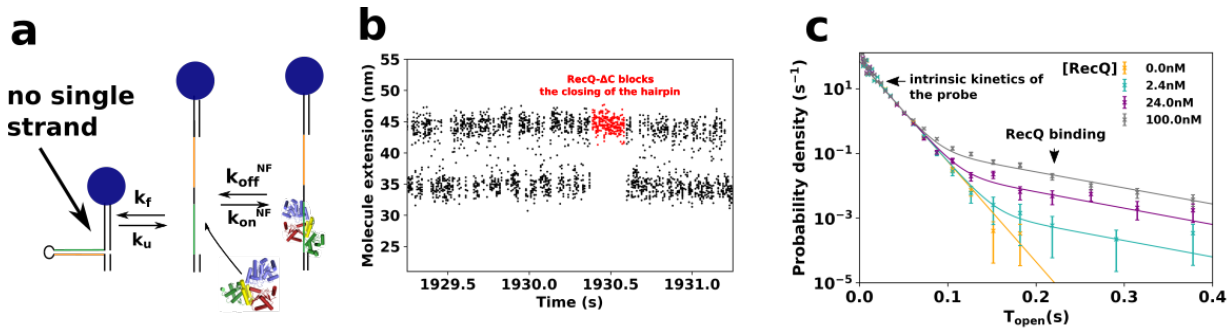

Figure 3-11: **Detection and quantification of the binding of RecQ-ΔC using kinetic locking. a.** 10-bp hairpin without ssDNA gap is used as a fluctuating probe. **b.** Binding of RecQ-ΔC can be observed through the transient blocking of the hairpin (HP) in its open state. c. **d.** Distribution of times spent by the hairpin in its open state as a function of RecQ-ΔC concentration, fitted by the double exponential law predicted by the kinetic model. Relative errors of a given bin are taken as $1/\sqrt{N}$ where N is the number of points in the bin. F=9.5 pN. T=25°*C*.

(LeGF) [Hishida et al., 2004].

Here we propose to use kinetic locking in order to investigate the associated binding rates of E. coli RecQ with a nucleic acid in the absence of ATP. We limit our study to the catalytic core domain, conserved among all enzymes belonging to the RecQ family and essential for their unwinding activity . This portion of the protein consists of the RecA-like helicase domain and the RecQ-Δ*C* domain, comprising a Zn^{2+}-binding site and a winged-helix. Our construct thus lacks the HRDC domain, absent in two human RecQ helicases [Kitao et al., 1998, Croteau et al., 2012], that is thought to be involved in the substrate specificity of the various enzymes of the RecQ family [Bernstein and Keck, 2005] and that partially impairs unwinding activity in E.Coli RecQ [Bagchi et al., 2018, Harami et al., 2015].

3.3.1 RecQ detection through the kinetic locking of a fluctuating hairpin

The same scheme of kinetic locking as for the detection of oligonucleotides was used. We injected the enzyme in the cell containing the fluctuating probe. As RecQ-Δ*C* bound the open ssDNA, it blocked the probe in its open state. Because its residence time on ssDNA was one order of magnitude larger than the typical time spent by the probe in its open state in the absence of RecQ-Δ*C* ($\frac{1}{k_f}$), both times were clearly distinguishable, giving rise to a well-defined double-exponential distribution (figure 3-11.c). This is similar to the binding of the oligonucleotide of length 7 illustrated earlier. Similarly, we can thus interpret the long time of the double exponential as $\frac{1}{k_{\text{off}}}$, *i.e* the dissociation time of RecQ-Δ*C*.

3.3.2 Kinetic locking unveils the stabilization of the replication fork by RecQ.

In order to test the affinity of RecQ for a nascent replication fork, we designed a slight variation of the above substrate, now leaving a single stranded gap of 14 nucleotides on the leading strand strand to allow the binding of RecQ-ΔC in the vicinity of the fork (figure 3-12).

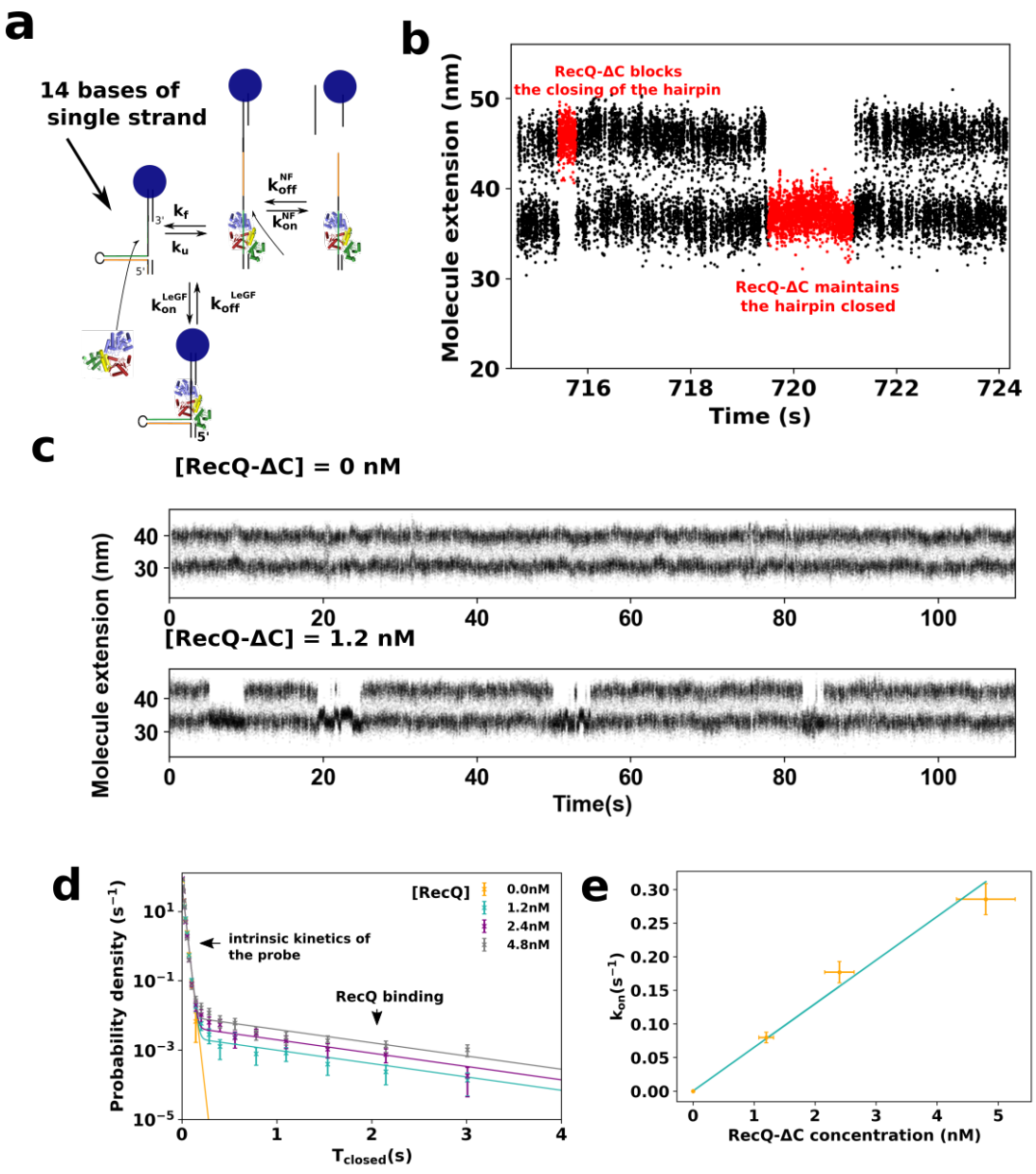

Figure 3-12: **RecQ-ΔC stabilizes a fraying replication fork. a.** 10-bp hairpin with a 14-nt ssDNA gap (Left) is used as a fluctuating probe, simulating a leading-gapped replication fork, LeGF. **b.** Binding of RecQ-ΔC on the ssDNA gap results in the transient stabilization of the hybridized state of the HP or in the transient blocking of the hairpin refolding. **c.** Larger time view of b., with and without RecQ-ΔC. **d.** Distribution of times spent by the hairpin in its closed state as a function of RecQ-ΔC concentration, fitted by a double exponential law. F=9.5 pN. T=25°*C*. **e.** Binding rate k_{on} in the closed state for configuration as a function of RecQ-ΔC concentration. Y relative errors correspond to the inverse of the squareroots of the number of observed events. X-relative errors are based on a 10% relative error on the concentration.

We hypothesize that this stabilization mechanism of a fraying hairpin is used by helicases of the RecQ family helping polymerases to reload [Cobb et al., 2003] and allowing the restart of stalled replication

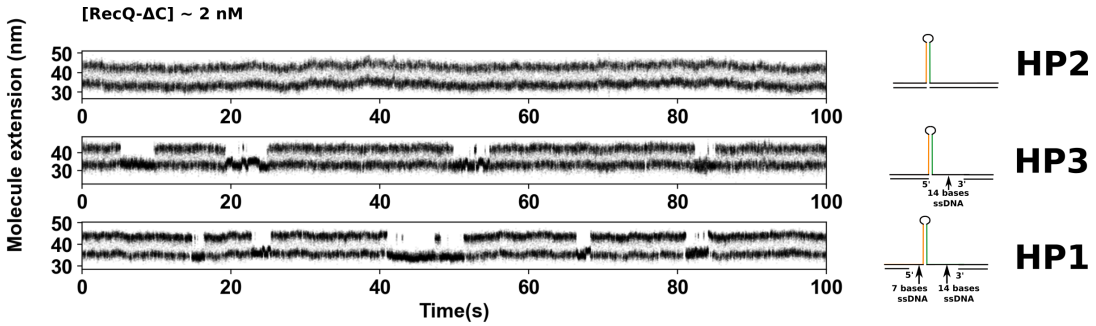

Figure 3-13: **RecQ-ΔC stabilizes a fraying replication fork independently of the presence of a close 5' end on the lagging strand.** Time-course experiments showing the extension changes of the fluctuating probe in presence of RecQ-ΔC at 2 ± 1 nM for different probes (right) whose sequence can be found in Table C.6. The stabilization of the closed state only happen when there is a single-stranded gap on the leading strand (HP1 and HP3), and is happening regardless of the presence of a single-stranded gap on the lagging strand (HP1).

forks [Davies et al., 2007].

3.4 Conclusion

We described a single-molecule micro-manipulation method that uses a stable fluctuating hairpin in order to perform kinetic and thermodynamic measurements of interactions involving nucleic acids. Kinetic measurements are limited to binding rates larger or of the order of the fluctuations of the probe. In this work, this limits the time resolution to 10 ms. However, it could be increased by using a high-speed camera to track the molecule extension (10 kHz) while concomitantly increase the folding rate of the probe by slightly decreasing the applied force. On the other hand, thermodynamic measurements do not suffer this limit in time resolution.

We showed that the method was able to provide precise data regarding the thermodynamics of oligonucleotides shorter than 7 nucleotides. It opens the way to a thorough tabulation of the interaction of various chemical modifiers with DNA as a function of sequence context. In particular, the method will help identify chemical modifications that stabilize short duplexes strongly enough so as to allow mechanical sequencing [Ding et al., 2012]. The precision of the technique is made possible by the high force stability of magnetic tweezers and by the low statistical error. The latter arises from the large number of independent events that can be observed in a few hundreds of seconds.

Consequently, *kinetic locking* complements the recent progress of the single-molecule community in characterizing the binding of shorter and shorter oligonucleotides. Among bulk experiments, temperature-jump infrared spectroscopy is to our knowledge the only technique that was able to provide data [Menssen

and Tokmakoff, 2019] on the thermodynamics of such short oligonucleotides. It consists of changing within a few microseconds the temperature of the sample containing the oligonucleotides. By monitoring with infrared (IR) spectroscopy the evolution of the proportion of the duplex state compared to the free single-stranded state, the technique allows one to measure sub-millisecond kinetics of association and dissociation. However, it still suffers from two biases. First, hydrogen must be replaced by deuterium in order to obtain a clear IR signal. However, deuterium is known to affect significantly the thermodynamics of hydrogen bonds, the core of Watson-Crick interaction between complementary bases [Singh and Rao, 2011]. Second, unrealistic salt conditions must be used ([Na] $\sim$ 200 mM and [Mg] $\sim$ 40 mM) so as to keep the association times smaller than the thermalization time of the sample which limits the observation time.

Through the observation of RecQ binding events, we also showed a proof-of-concept of the application of kinetic locking to the characterization of the NA/proteins-binding kinetics. The technique presents the advantage to enable the fluorescence-free detection of discrete protein/NA binding events, alleviating the need of protein labeling while avoiding the disturbance of the measured interaction by an external probe. The time-resolution presented here exceeds label-free single-molecule methods based on periodic force changes [Kostrz et al., 2019, Koch et al., 2002] that are well suited to study long dissociation times but not short and repetitive bindings. Compared to stopped-flow bulk assays, such as the one based on tryptophan fluorescence [Kocsis et al., 2014], it avoids photo-bleaching, hidden binding events [Li et al., 2007], and the need to introduce chemical competitors to evaluate dissociation kinetics. More importantly, the single-molecule nature of the experiment gives important insights about the nature of the interaction between the protein and its substrate, as was shown by the unexpected stabilization of the probe by RecQ catalytic core.

The main limitation is the narrow force range (8-15 pN) of applications, since the NA substrate needs to be stretched in order to induce its fluctuations. This limits the comparison of the results with bulk experiments performed at zero force. However, this force range corresponds to the typical forces felt by NA during transcription, translation or replication and is thus consistent with physiological conditions.

Our assay could be expanded to the study of a broad spectrum of DNA/RNA-binding proteins (notably transcription and translation factors, polymerases, helicases, primases, exon junction complexes), and of their sequence and substrate specificity. While proteins binding to dsNA will very probably stabilize the probe in its closed state, proteins that bind to ssDNA will stabilize the probe in its open state. It will certainly be necessary to adapt the length of the probing hairpin to the footprint of the protein.

Conclusion

In this work, we characterized a 3D-tracking method for microparticles, called *Stereo Darkfield Interferometry*. We showed that it enabled an ångström frame-to-frame precision, allowing high-resolution, low-frequency and real-time localization of microbeads. Interestingly, its linearity avoids the need of a lookup table, but with two reservations. First, the deviations from linearity only permit nanometer accuracy over a focus range of 100 nanometers. For a focus range of 4 microns, the accuracy goes to 10 nanometers, showing the need for a calibration for applications that need strong accuracy in addition to strong precision. Second, the deviations from aplanetism require a calibration over the field of view in order to track particles free to move transversely. However, this requirement is relieved for lower-magnification objectives (20X), enabling the calibration-free tracking of single cells (Appendix A).

We then applied this technique to magnetic tweezers via the tracking of short, and thus stiff, DNA molecules. Strikingly, this allowed to observe nanometric steps in the extension of biophysical systems that were so far out of reach for magnetic tweezers in spite of many precedent attempts. This opens up the possibility to couple the best spatiotemporal resolution of micro-manipulation with the parallelism of magnetic tweezers. However, significant progress in surface passivation is still required, given that working close to the surface results in numerous non-specific attachments of beads and thus in the decrease of the number of molecules observed simultaneously. The proximity with the surface also affects the spatiotemporal resolution of the method, due to the dramatic increase of hydrodynamic drag. We mentioned possible future research that would contribute to overcome this difficulty. Among them, the use of materials with higher magnetic saturation, such as cobalt, would enable to develop smaller microbeads while keeping the maximum force above 15 pN. On the other hand, no-slip surfaces, for example consisting of spaced micrometric posts, would also reduce the effects of the confined hydrodynamic flows close to the surface.

Finally, we presented a method, kinetic locking, based on the enhanced spatio-temporal resolution of our magnetic tweezers and on their force stability. Using a fast fluctuating hairpin as a probe, we were able

to measure precisely the thermodynamics of binding of oligonucleotides as short as five nucleotides. Most interestingly, we presented a proof-of-concept of an accurate measurement of sub-second binding kinetics of proteins with their nucleic acid substrates. We envision that this label-free technique will prove a valuable tool for enzymologists, since NA-binding proteins are numerous and involved in many critical biological processes.

Our work shows that magnetic tweezers, that are by far the most simple and democratic micro-manipulation method, can reach spatio-temporal resolutions close to the best optical tweezers. Because magnetic tweezers are simple to take in hand, we hope that it will convince numerous teams of biochemists to adopt micro-manipulation, and thus participate in spreading methods, that, in spite of their undeniable standardization, still frightens some researchers outside of the physics community. Our simple and calibration-free 3D-tracking method will also offer new possibilities to biologists studying the motility of single cells. However, we were not able to significantly disrupt the resolution limits of single-molecule micro-manipulation. In particular, we were not able to comply with our first objective, that is to capture precisely and in a reproducible manner the discrete dynamics of molecular motors in the presence of physiological nucleotide concentrations. Other competing techniques, in particular nanopores-based detection are making impressive progress in the field, and maybe, they will allow in the next years the emergence of an accurate physical theory of the dynamics of these motors at the microsecond time scale.

Appendix A

Embedded *SDI* objective

Stereo Darkfield Intereferometry can be directly embedded into an objective and thus can be commercially distributed as a 3D-tracking module for any preexisting microscope. Due to the technical complexity of planar high magnification objectives, such an embedding would need to be performed by the objective supplier. However, in order to demonstrate this possibility, we disassembled a simpler X20 objective and added the SDI slits directly in the back focal plane of the objective. We brought two prisms of opposite angles directly in contact with the slits (figure A-1.a-c). These prisms produce a phase shift in the Fourier space that translates into a position shift in the real image space, preventing the superimposition of the two interferometric patterns. They play the same role as the parallel slides presented above. In this low magnification configuration, the precision is micrometric, while the axial depth of view is greatly enhanced with a conserved linear response: the distance between the interferometric fringes depends linearly on the z position over ranges of the order of 150 μm (figure A-1.i). Residues to linearity over such a range lay are of the order of the micron and are shown in figure A-1.h. Concerning illumination, the angles corresponding to the slits being smaller, one parallel light source is in this case sufficient to perform the measurement.

The parameters of this configuration are perfectly suited for the 3D-tracking of microorganisms. In particular, contrarily to the case of high-magnification objectives, these systems show a very good aplanetism and a strong linearity, allowing the tracking of free micro-swimmers without calibrations. *Isabelle Eisenmann*[1] characterized more thoroughly this aplanetism for the X8 objective (figure A-2). She showed that it is possible to 3D-track micro-objects with an accuracy of 6 μm over a long axial depth of field (~1mm) and large transverse field of view (~1 cm).

As an example of application, we show in figure A-1.e the image of the model micro-swimmer *Chlamy-*

[1] isabelle.eisenmann@ens.psl.eu

domonas reinhardtii acquired with the modified objective of magnification 20X. We studied the dynamics of freely swimming algae confined in a microfluidic Hele-Shaw cell (i.e. width and length $\gg$ height) of thickness $\approx 150\mu$m. Filtering out short trajectories ($<$ 1.5s spent in the field of view) and cells with deficient vertical swimming (spanning less than 110 um in the axial direction), we analysed the statistics of 117 independent trajectories and found that the dynamic is largely dominated by the presence of confining walls. As illustrated by the typical track in figure A-1.i, most of the cells performed back and forth movements between the upper and lower boundaries. The distribution of their axial position displays peaks at $20-30\mu m$ from the cell limit (figure A-1.k), in accordance with previous 2D horizontal measurements [Brun-Cosme-Bruny, 2019]. Measuring the vertical angle α_z of each of the 117 trajectories within the middle of the chip (for z between 60 and 90 μm) we found that it is symmetrically distributed around 0 (figure A-1.k) with a clear peak at $\approx \pm 25^\circ$. This value compares reasonably well with the most probable outgoing angle following wall scattering as measured in [Kantsler et al., 2013], which shows that after interacting with either wall the cells keep swimming in the same direction until colliding with the opposite boundary. This is consistent with the long $\approx$ 10s run time extracted from the run-and-tumble dynamics performed by the algae in bulk [Polin et al., 2009], since in our case it takes on average $\approx$ 2.5s to cross the height of the channel. Finally, the symmetry observed in the distribution of angles indicates that gravity axis [Kam et al., 1999] does not play any role in this confined configuration, simply because the gravitational torque [Pedley and Kessler, 1992] felt by the algae is too small to bias the cell swimming direction over such a short vertical distance.

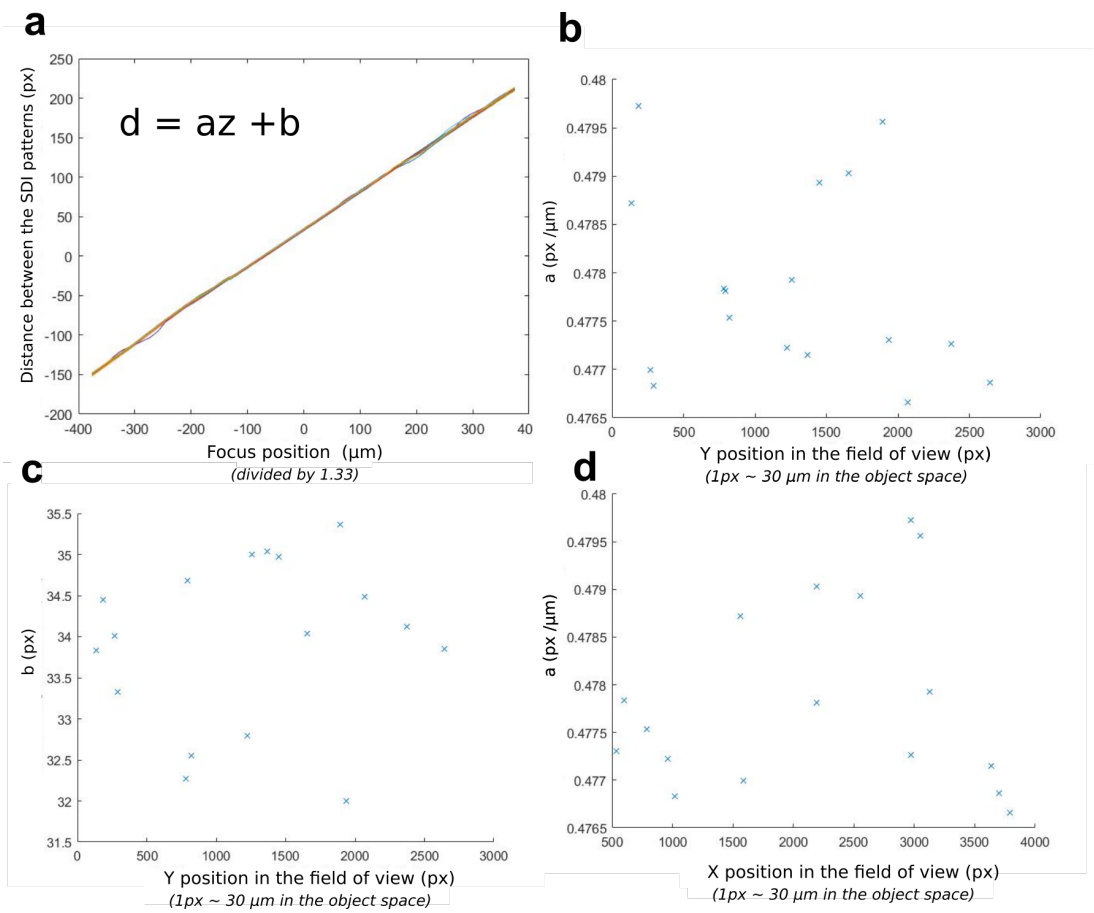

Figure A-2: **Linearity and aplanetism of the SDI system implemented on a 8X objective. a.** Distance between the SDI patterns as a function of the focus position for 17 beads spread randomly in a field of view (~1x1.3cm). All curved are linearly fitted, $d = az + b$. **b.** Dependence of the slope of the signal of a. on the Y position of the beads. **c.** Dependence of the the intercept of the signal of a. on the Y position of the beads. **d.** Dependence of the the slope of the signal of a. on the X position of the beads.

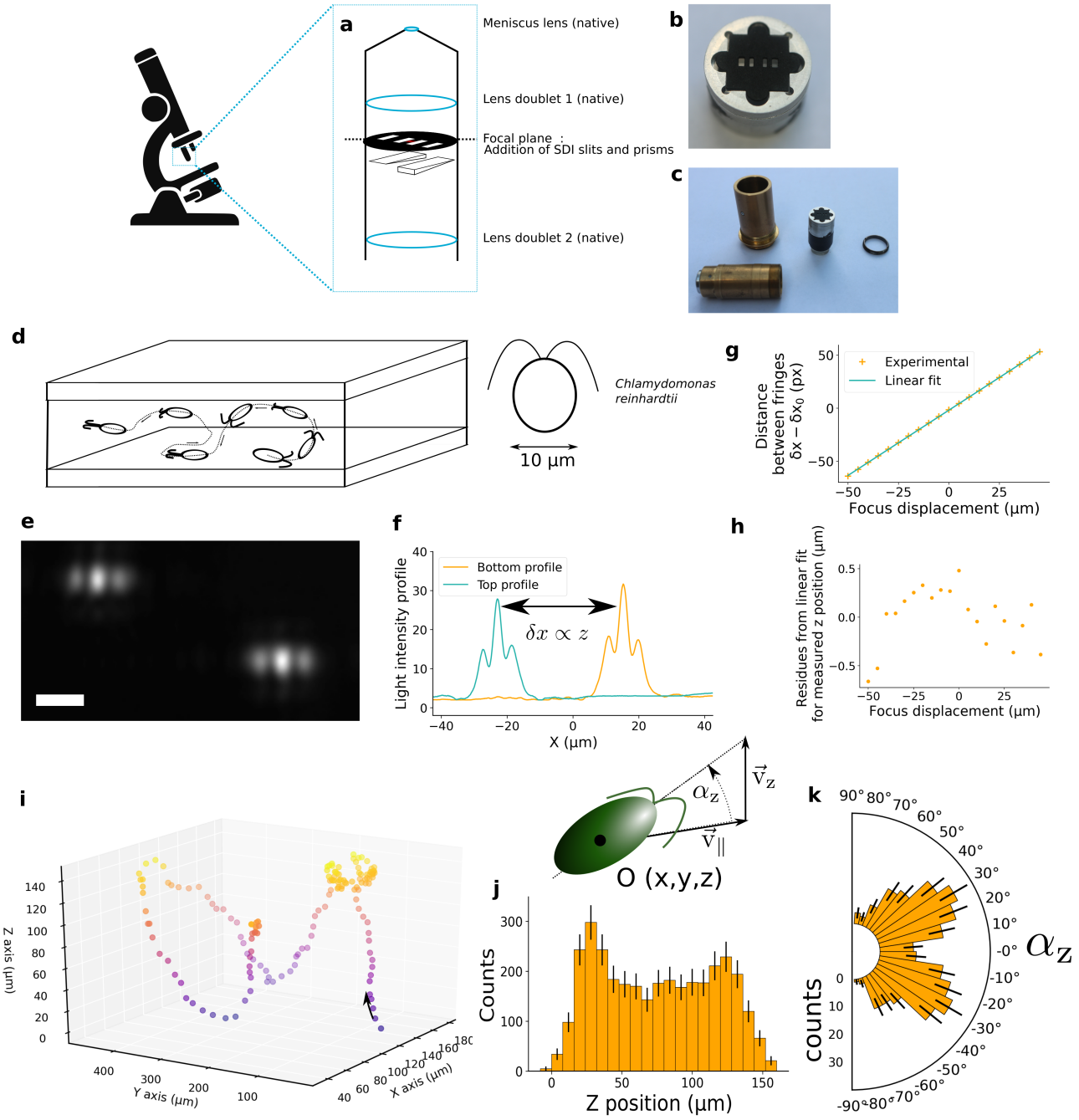

Figure A-1: **Application of *Stereo Darkfield Interferometry* to single-cell tracking and direct embedding in a commercial objective. a.** Schematic description of the modified objective (Olympus, achromatic 20X). The *SDI* slits brought in contact with two prisms of opposite angles are added in the Fourier plane of the objective. **b.** Picture of the slits and of the mechanics allowing their insertion in the objective. Photo credit: Vincent Croquette, Laboratoire de Physique de l'Ecole Normale Supérieure. **c.** Picture of the disassembled objective. Photo credit: Vincent Croquette, Laboratoire de Physique de l'Ecole Normale Supérieure. **d.** Schematic representation of the tracking experiment: algae *Chlamydonomonas reinhardtii* are inserted in a flow cell containing TAP buffer and their movement is tracked. **e.** An image of an *alga* obtained with the integrated objective. White bar: 10 μm **f.** Horizontal profile of light intensity corresponding to the image f. The lateral shift between the two interference profile allows measuring the axial position z. **g.** Dependency of the distance between the interference fringes on the position of the focus for an alga fixed on the surface. **h.** Residues from the linear fit of the dependence between the bead-to-objective axial (z) distance and the distance between the interference fringes. **i.** A 3D trajectory obtained thanks to the *SDI* modified objective. Acquisition frequency: 10 Hz. Each point corresponds to one frame. Colors represent z. **j.** Distribution of the Z position of the algae over 3314 positions taken from 117 individual trajectories. **k.** Distribution of the vertical angles while an alga crosses the middle of the flow cell (z between 60 and 90 μm). 332 crossing events. 117 trajectories.

Appendix B

Brownian simulation of a tethered bead close to a surface

We detail the numerical scheme used in section 2.1.7 to simulate the more detailed physics of a tethered Brownian bead subject to hydrodynamic interactions with the surface. The corresponding C++ code is available online at https://github.com/Mriv31/BrownianBead.

Parameters

- Γ contains the hydrodynamic coupling coefficient in the transverse direction.
- γ_z^t contains the axial translational drag
- γ_z^r contains the axial rotational drag
- R is the radius of the bead
- θ_0 is the angle between the anchoring point of the molecule on the bead and the anisotropy axis.
- α is the the anisotropy coefficient.
- λ is the gap between the magnets.
- F_{mag} is the magnetic force applied on the bead along the direction z.
- δt is the time step (0.1 microsecond).

Variables

- The origin O of the coordinate system is taken as the anchoring point of the molecule on the surface.
- C contains the position of the center of the bead.
- M contains the position of the molecule anchoring point on the bead surface relatively to the center of the bead
- P_m contains the position of the magnetic pole relatively to the center of the bead
- l contains the length of the molecule

Initialization

- l is taken equal to the length of the molecule at force F as predicted by the worm-like chain model.
- M is set at $(0, R\cos(\theta_0), -R\sin(\theta_0)$, where θ_0 is the tethering angle.
- C is set at $(0, -R\cos(\theta_0), l + R\sin(\theta_0)$
- P_m is set $(0, R, 0)$, along the magnetic field.
- The hydrodynamic coefficients are computed at the initial position C_z of the bead of radius R using the series summarized in the equations 5.1, 5.3 and 5.10 of [Perkins and Jones, 1992]. The number 1 of the second line of equation 5.10 is an error and should be removed.
- The matrix Γ of the hydrodynamic coupling is diagonalized and decomposed as PDP^{-1}.

Iteration

1. The force applied by the molecule $\mathbf{F}_{mol}$ on the bead is computed. It has the direction $\vec{MO}$ and the norm $WLC(l)$.
2. The torque applied by the molecule $\tau_{mol} = \vec{CM} \times \mathbf{F}_{mol}$.
3. $\tau_{mag} = \vec{CP_m} \times \vec{B}$ and has the norm $\alpha F_{mag} \lambda$.
4. $F = F_{mag} + F_{mol}$
5. $\tau = \tau_{mol} + \tau_{mag}$
6. The coupled variables Ω_x and v_y are decoupled by applying the matrix P^{-1} into $v^0_{y\Omega}$ and $v^1_{y\Omega}$. The same transformation is applied to τ_x and F_y to obtain $F^0_{y\Omega}$ and $F^1_{y\Omega}$.
7. Same for Ω_x and v_y but with the matrix P.
8. $v_z = \frac{F_z + \frac{\sigma_z}{\sqrt{dt}}}{\gamma^t_z}$, where σ_z is random normal variable of mean 0 and variance $2k_BT\gamma^t_z$
9. The same procedure is applied for Ω_z but replacing F_z by τ_z and γ^t_z by γ^r_z.
10. The same procedure is applied for $v^i_{y\Omega}$,$v^i_{x\Omega}$, but replacing F_z by $F^i_{y\Omega}$ and γ^t_z by D_{ii}.
11. P is applied to $v^i_{y\Omega}$ to obtain v_y and Ω_x.
12. P^{-1} is applied to $v^i_{x\Omega}$ to obtain v_x and Ω_y
13. $C_x = C_x + dtv_x$, $C_y = C_y + dtv_y$, $C_z = C_z + dtv_z$
14. $P_m = P_m + dt\Omega \times P_m$
15. $M = M + dt\Omega \times M$
16. $\theta = \arccos(P_m \cdot M)$
17. θ should be equal to θ_0. In order to avoid the accumulation of numerical drifts, small numerical errors are corrected in order to ensure the respect of this constraint. Rodrigue's rotation formula around the axis perpendicular to the plane formed by P_m and M is used to restore the exact angle between the anisotropy axis and the molecule anchoring point.

$$P_m = P_m\cos(\theta_0 - \theta) + \frac{sin(\theta_0 - \theta)}{sin(\theta_0)}M - \sin(\theta_0 - \theta)\frac{\cos(\theta_0)}{\sin(\theta_0)}P_m; \tag{B.1}$$

18. The length of the molecule is updated $l = |\vec{OM}|$.

Appendix C

Material and methods

C.1 Optics

C.1.1 Out-of-the-objective setup (40x and 100x objectives)

Superluminescent LEDs (Exalos, EXS210030-03, 650 nm, 10 mW) are placed in the object focal plane of a diode collimation package (Thorlabs, LTN330A) and the outcoming parallel beams are directed to the pupil of the oil objectives (respectively UPLSAPO100X and UPLSAPO40X) with opposite incident angles. Their intensity is regulated through a feedback loop based on the signal of the monitor photodiode included in the chip. The optical axis is then switched from vertical to horizontal using a mirror (BBEA1-E0Z, Thorlabs). The 4f setup, used to access the Fourier plane, is made of two lenses of focal 100mm (AC254, Thorlabs). A sheet of black paper (Canson, 160 g/m2) is then cut with a laser cutting machine in order to get the pair of slits needed for the SDI technique. Slits consist of four identical rectangles (200μmx700μm) whose centers are placed at the following positions with respect to the optical axis: ([-1.5mm,0],[-0.4mm,0],[0.4mm,0],[1.5mm,0]). The slits are brought in contact with a thin lens of focal 100mm (Thorlabs, LBF254-100-A). Then, a pair of optically clear glass slides (4mmx8mm) of thickness 1mm is placed in contact with this lens. Both are tilted in the y-direction with opposite angles of ± 17 degrees in order to shift the beams stemming from both pair of slits in opposite y-directions. Finally, the resulting pattern is imaged on a monochromatic CMOS camera (UI-3060-CP-M, IDS Ueye), placed at 100mm from the titled glass slides. The camera is linked through USB3.1 to a computer that processes the images in real-time. The protocol of the alignment is described further in the document.

C.1.2 Holder for the tilted glass slides

C.1.3 SLEDS stabilization

The superluminescent LEDs (Exalos, EXS210030-03, 650 nm, 10 mW) contain a native photodiode, that allows stabilizing their light intensity. We use our own electronic driver. It consists in a comparator (figure C-1: an operation amplifier (TLV2461) controls the transistor 2n2222 such as the voltage created by the current emitted by the MPD creates a tension at the negative entry of the operation amplifier that is equal to the set value V_{ref}.

C.1.4 Camera alimentation

We observed that the noise of the signal was correlated with the CPU-usage. A sudden high CPU-usage could be observed in the tracking signal. This could be resolved by decoupling the alimentation of the camera from the computer. The mass (black) and the alimentation (red) cable of the camera were extracted.

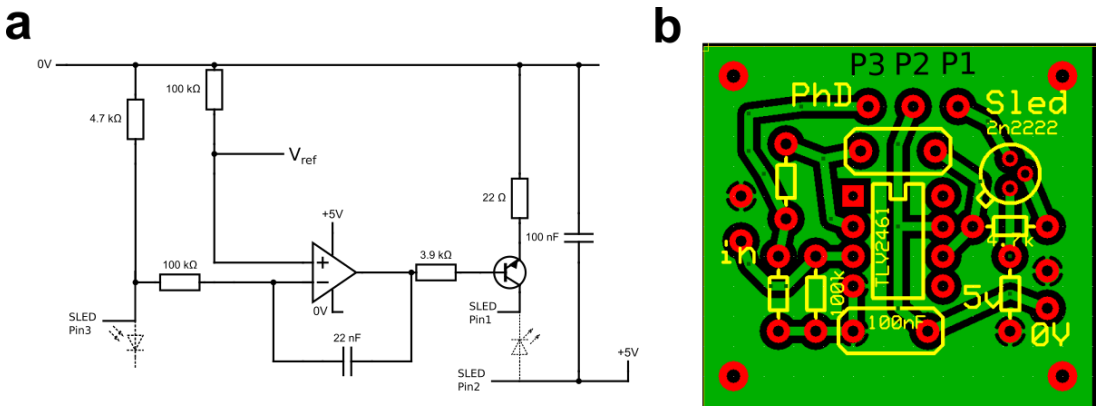

Figure C-1: **Electronics for the stablilization of the SLED EXS210030-03 a**. Electronic circuit. **b**. Corresponding PCB.

The black was connected to the mass of the computer and to the mass of a stabilized power supply (5V). The alimentation cable was connected to the output of the power supply.

C.1.5 Temperature control

In order to minimize optical drifts that are due to temperature changes, the objective is inserted into a box made of duralumin. The box temperature is controlled through 6 Peltier moduli placed in parallel (ET-063-08-15, Adaptive). The PID feedback loop then allows to reach a temperature stabilization with the precision of 0.0001K. The temperature is read in the following way: thermistors (TDK, B57703M0103) are connected to Wheastone bridges converting the resistance difference into a voltage. The voltage is then read with a 32-bit Sigma-Delta analog to digital converter (ADC).

C.1.6 Micro-controller

Temperature, light and focus are controlled through a Teensy USB development card, version 3.5. The C code run on the Teensy has been written by Gaël Radou[1] and then adapted to control the SLEDS. It is available at https://tig.phys.ens.fr/ABCDLab/SDITeensy/.

C.1.7 Focus adjustment

For the linearity test of the setup with 40x or 100x magnification, the objective is moved with a piezo nanofocusing device (P-725.2CL, Physik Instrumente). For the other measurements on this setup, the piezo nanofocusing device is replaced by a deformable stage to avoid any noise inherent to the piezoelectric device. The position of the screw controlling the stage is measured with a rotational magnetic sensor (AMS,AS5048A). For the linearity test of the 20x setup used for algae tracking, the objective is moved by the stepper motor driving the microscope focus (IX81, Olympus).

C.1.8 SDI alignment procedure

This protocol has been written by Thibault Vieille[2] and reproduced here with his permission.

We develop the following alignment method with the goal of positioning the amplitude mask 1) in the Fourier plane with a sub-millimetric accuracy and 2) centered on the optical axis of the system with the accuracy of ten microns. As the Fourier plane is located inside the microscope objective, a 4f line is

[1] gael.radou@depixus.com
[2] thibault.vieille@depixus.com

installed to provide a mechanical access on its image plane (pair of 1" achromatic doublet lens of 100mm, the focal length has been chosen to avoid 1) vignetting effect and 2) off-axis aberrations of more powerful doublet lens).

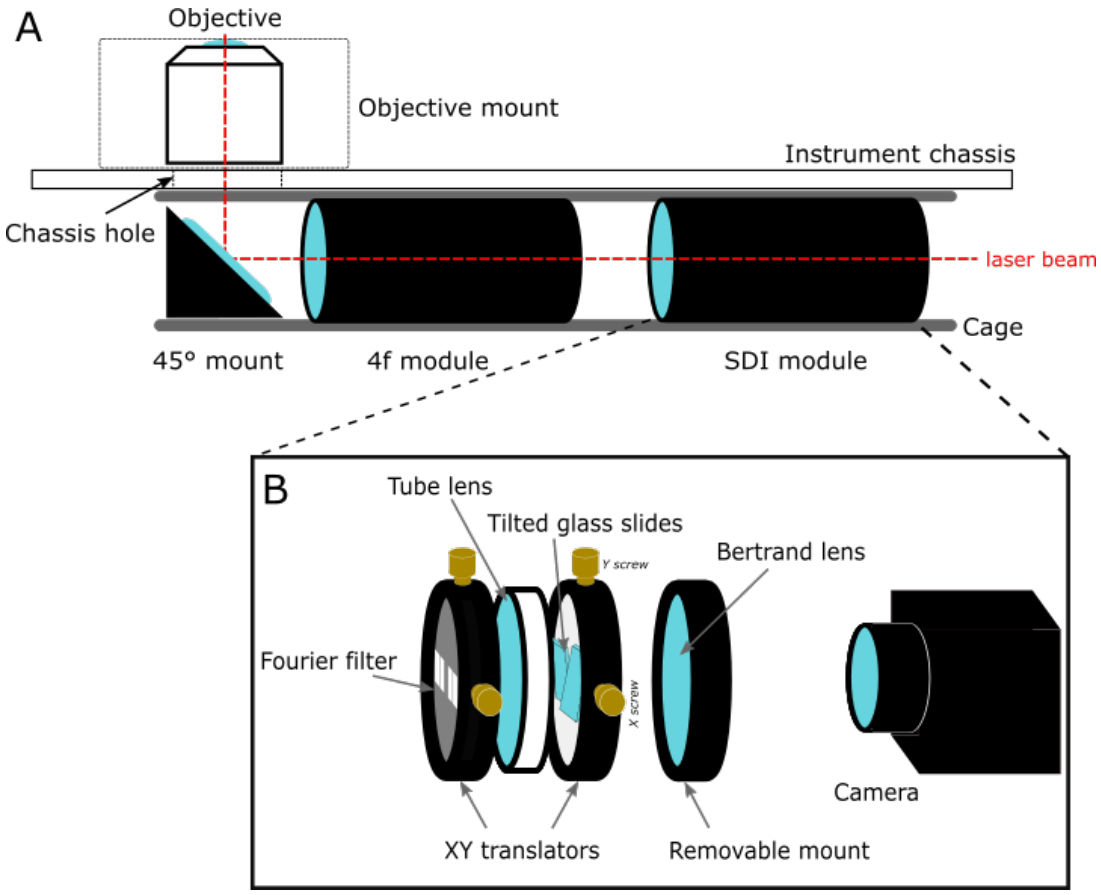

Figure C-2: **[Assembly of the external SDI module] A**. A folded 4f line (elliptic mirror + 2 100mm Thorlabs) is positioned below the objective to provide mechanical access to its Fourier plane. **B**. The SDI module comprises 1) a compact assembly of amplitude mask-tube lens-tilted glass windows, 2) a removable Bertrand lens and 3) a camera.

Phase 1: Assembly and Installation of the 4f line

1. The distance between the two lenses of the 4f line is locked (SM1 tubes from Thorlabs) once obtained sharp images of objects at the infinity. To do so, a temporary cage system assembles the 4f line and a module composed by a 50mm achromatic lens and a camera at its focal plane.

2. The 4f line is installed in the cage system, attention is paid to align it along the optical axis:

   (a) First, a temporary module composed by SM1 tubes and a camera are assembled such that once brought in contact with the 4f-module, the camera is placed at the focal plane of the second lens of the 4f-module.

   (b) The whole module (4f line + a temporary module) is then moved along the optical axis until one gets a sharp image of the pupil (see Figure C-3).

The assembly and integration of the SDI module itself employ a Bertrand lens, used to simultaneously obtain a sharp image of the mask containing the slits and of the back focal plane of the microscope objective (typically an object attached on the ceiling of the room).

Phase 2: assembly of the SDI module.

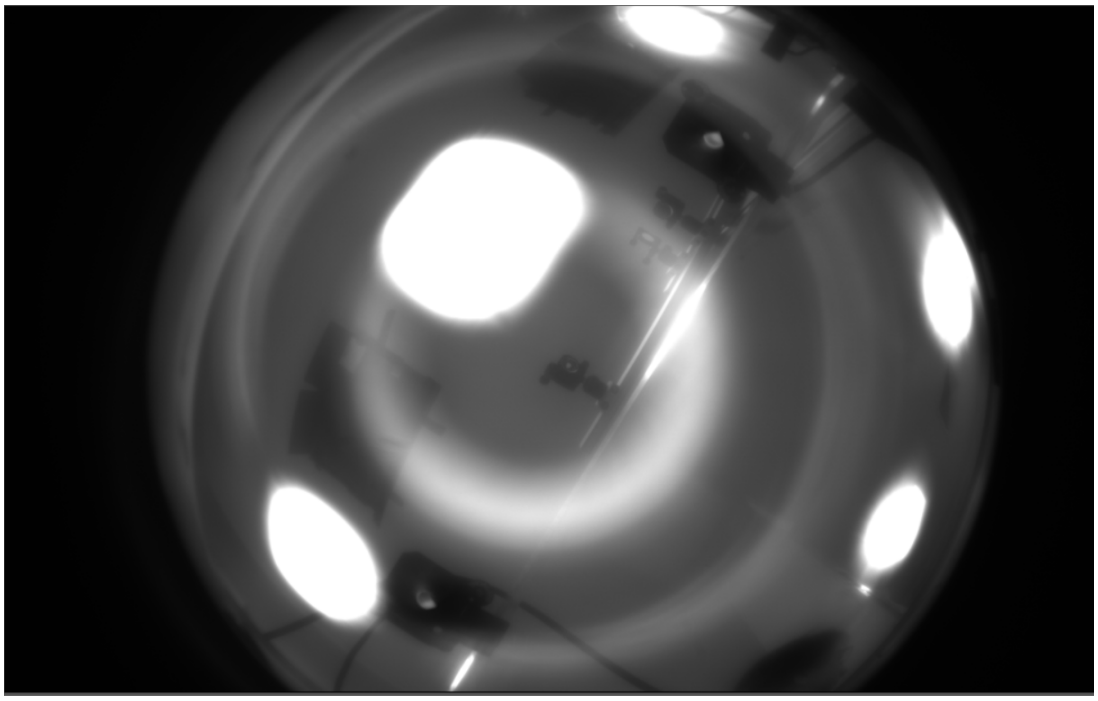

Figure C-3: Image of the entrance pupil (telecentric objective) observed on a camera temporarily placed at the focal plane of the second lens of the 4f line, after proper positioning of the 4f line in the system: the large black squares pieces of cardboard positioned on the ceiling of the room.

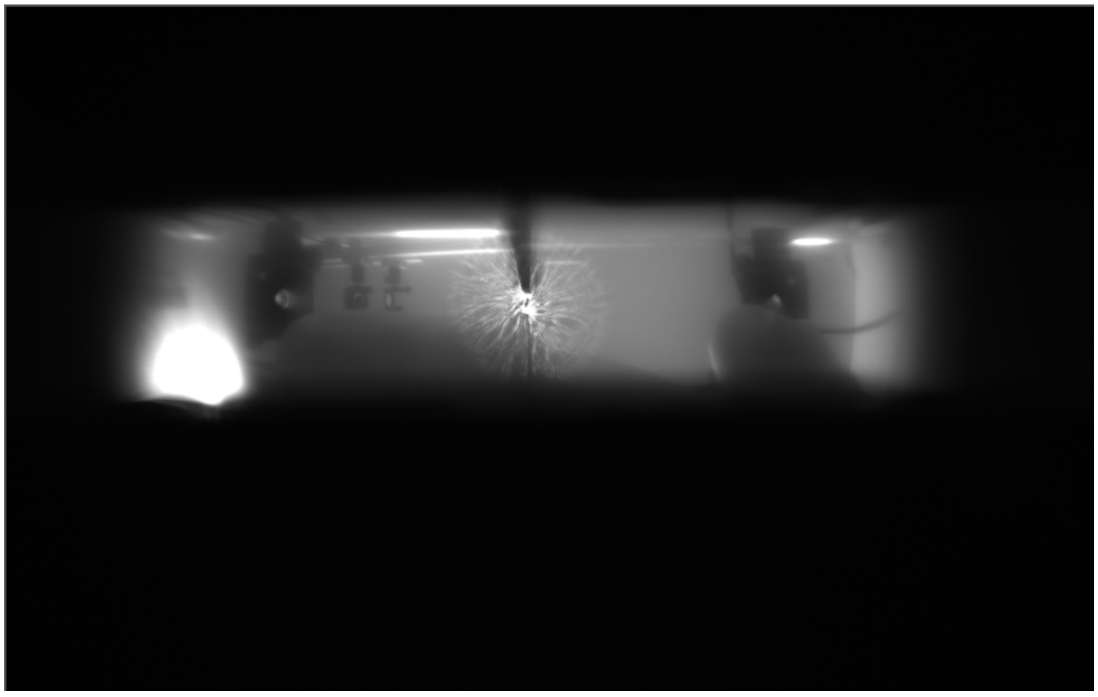

Figure C-4: Image of the Fourier plane of the objective, here observed through the Bertrand lens of the SDI module. Slits have been removed, and the glass slits have been centered such that the spot of a HeNe alignment laser is shown split and largely cut by the line between the glass windows.

1. 3 optical components (mask containing the slits - tube lens - pair of tilted glass slides, see Figure C-2) are assembled in a cage system such that the tube lens is sandwiched tightly between the mask and the tilted glass slides.

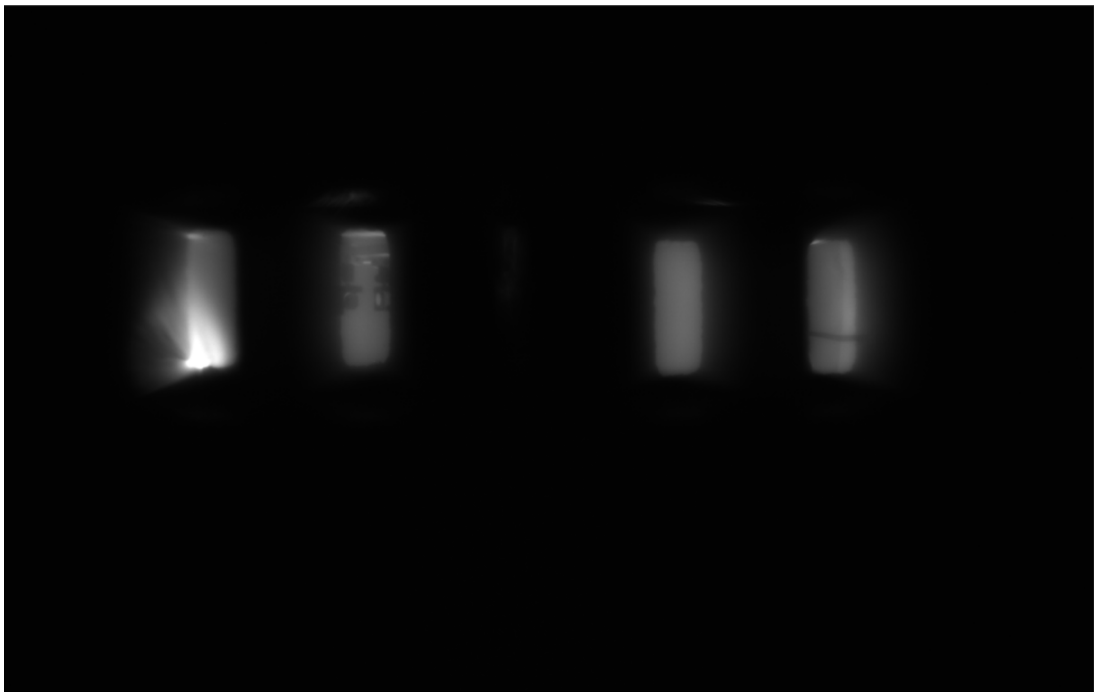

Figure C-5: Same type of image, but with a mask added: slits of the mask and objects placed at an infinite distance of the objective are simultaneously sharp.

2. Once this module is assembled, the camera is added at the focal point of the tube lens (the tilted glass slides must be in place during this tuning).

3. A Bertrand lens (25mm of focal length, to perform 1:1 imaging between the place containing the slits and the camera plane) is added in the assembly, by the means of a magnetic mount (CPF90, Thorlabs), the position of which along the optical axis being tuned along the cage system axis until one gets a sharp image of the slits.

Phase 3: coarse implementation of the SDI module on the system

1. With Bertrand lens on position, the SDI module is inserted on the main cage system of the instrument and its position along the optical axis is manually tuned until one gets a sharp image of the back focal plane through the mask (Figure C-7).

2. The lateral position of the mask containing the slits and the glass slides are then adjusted to be centered onto the central of the pupil image (an alignment laser on top of the system can help).

3. At that point, the illumination angles of the two light sources are optimized by ensuring that they converge in the center of each pair of slits.

This protocol typically results in good quality SDI images. However:

- Residual error in the transverse positioning of the mask in the Fourier plane may result in the selection of slightly different angles for the left and right pairs of slits: this leads to a common differential sensitivity (variation of phase vs. defocus) between the two sets of fringes on the field of view. For example, all top fringes share the same offset of sensitivity compared to their corresponding bottom fringes.

- Residual error in the positioning of the mask along the optical axis (i.e., not truly in the Fourier plane) involves that the selected averaged angles may according to the position in the field of view.

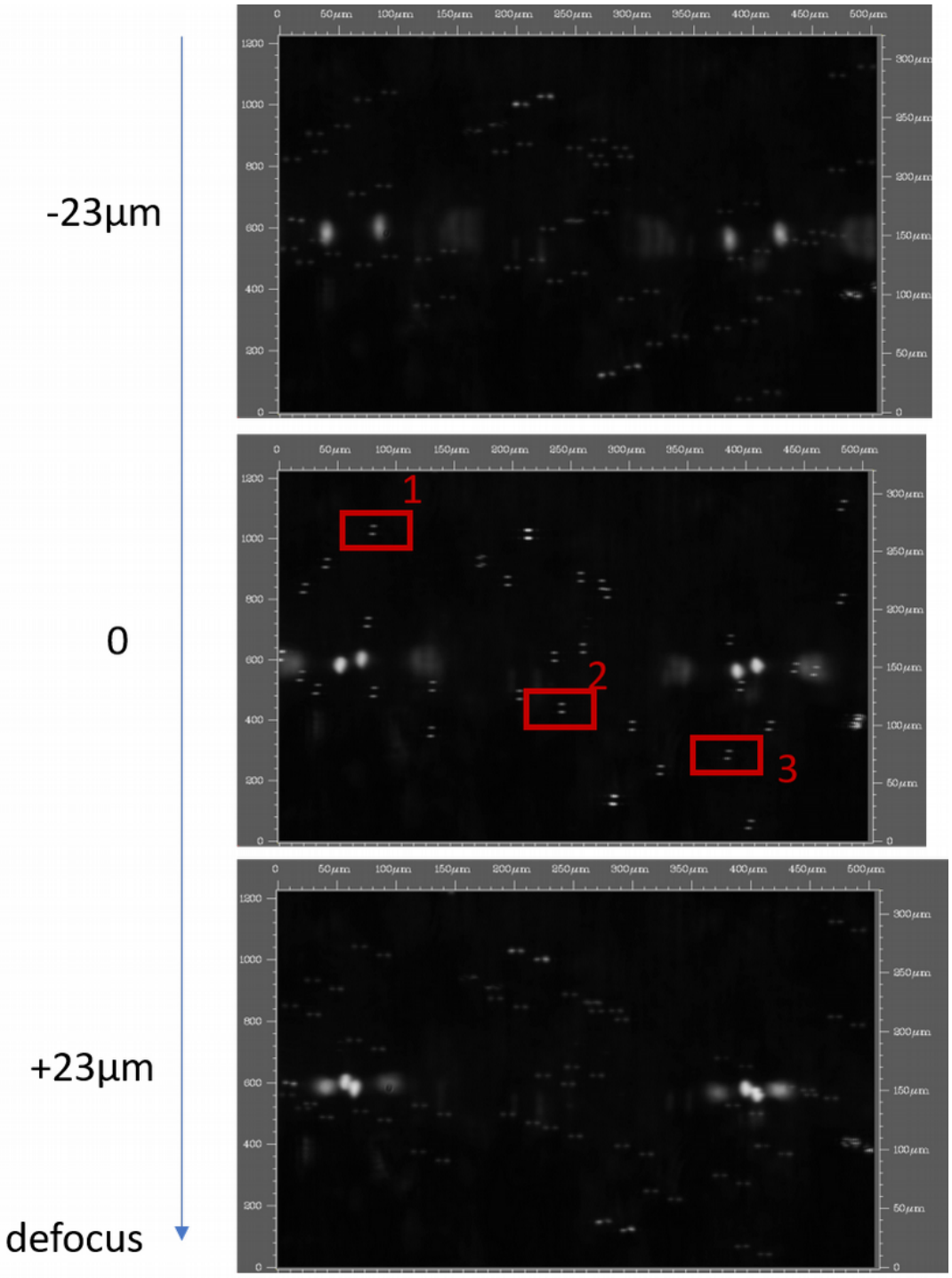

Figure C-6: Images recorded for -23,0,+23 μm of defocus at the final position of the mask. Three objects are selected (see associated text). The large white spots are caused by the edges of a thermalization box present in the light path and are not related to the SDI imaging itself.

Consequently, a final alignment step is performed directly on the signals generated by fixed objects in the field of view of the microscope.

Phase 4: fine adjustment of the SDI module.

1. 3 images obtained at focus are recorded, as well as images taken at large and symmetrical values of defocus (above the depth of field allowed by the setup, i.e. until the two optical rays for each fringe are separated).

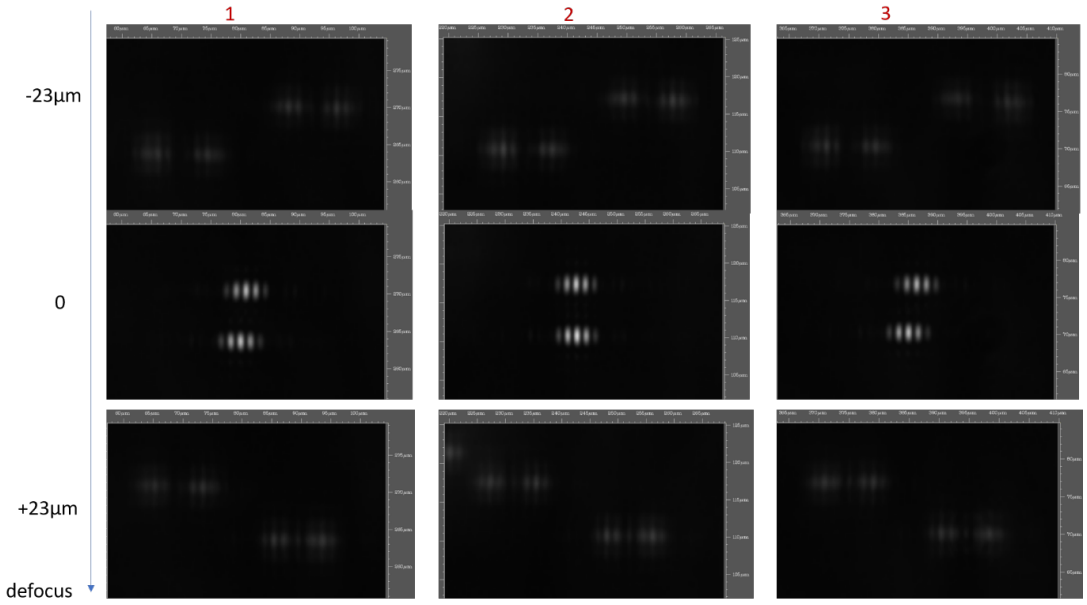

Figure C-7: Images obtained for the 3 objects selected on the field of view and for the 3 focus positions.

2. 3 objects are selected, located on the center and on both sides (along the mask axis) of the field of view.

3. The transverse position of the mask is corrected (using micrometric screws), until on-axis image shows no differential sensitivity between both sets of fringes.

4. Longitudinal position of the complete SDI module (sliding along the optical axis on the cage system) is corrected until one sees no different sensitivities between on-axis image and off-axis images (symmetric).

5. Steps 1-3-4 are iterated until convergence.

A typical set of images corresponding to one iteration of this process is shown on Figure C-6 and Figure C-7. They have been recorded during the alignment of an SDI instrument featuring a 40X oil-immersion system.

C.1.9 Measurement of the transfer function of the 100X objective

The transfer function of the 100X objective was measured in the following way. The camera was placed in the back-focal plane of the objective, re-imaged with a 4f setup. Immersion oil was added on the objective, then a coverslip of width 170 microns. The angle of the incident light was incremented by moving the light on a circular support placed above the objective. The setup was photographed. The precise incidence angle (~1 degree precision) was measured numerically on the resulting picture. The position of the focusing point in the back-focal plane was measured directly using the image of the back-focal plane taken with the camera.

C.1.10 Modified 20x objective

An achromatic objective 20X from Olympus was dismantled. We have replaced a cylindrical spacer 14 mm wide and 10 mm long just after the front lens component of the objective by a holder supporting a black paper with slits followed by prisms and a spacer so that this system also spans 10 mm. A round glass slide of

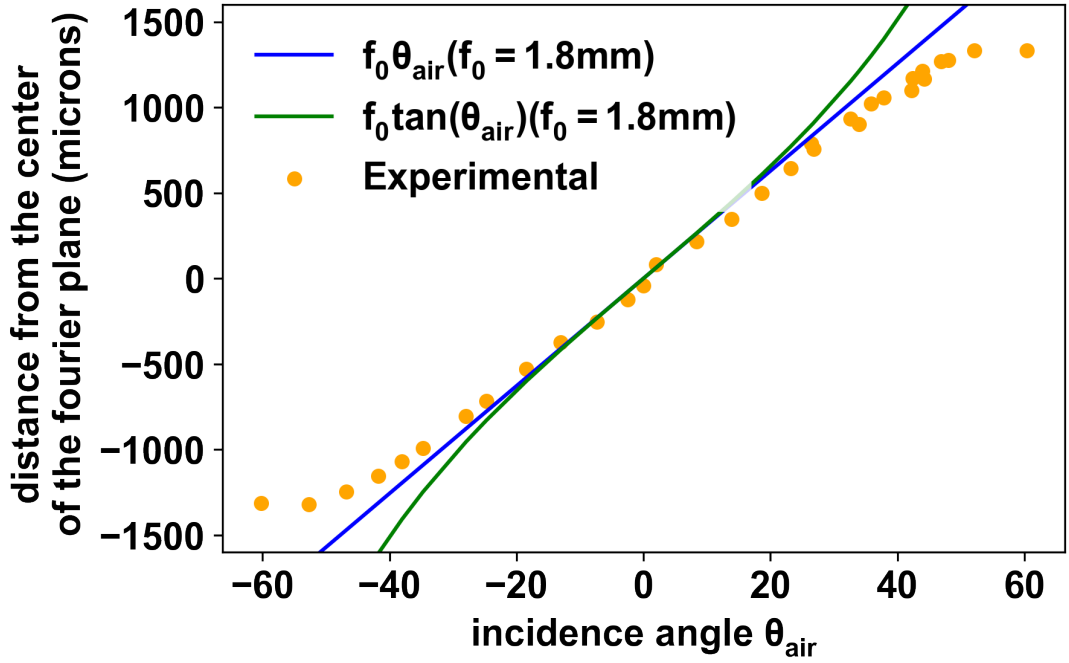

Figure C-8: **Transfer function of the 100X objective used in this work (UPLSAPO100X, Olympus).** Position of the PSF in the back-focal plane of the objective as a function of the incidence angle (measured in the air) of the parallel incoming light.

radius 13 mm was inserted in the holder to hold the prisms. We have machined a (8 mm x 8 mm) rectangle slit in the holder allowing us to introduce two optically clear glass slides (4 mm x 8 mm) of thickness 1 mm in contact with the round one. One of the rectangular glass slides was slightly titled by introducing a thin sheet of paper of thickness $\approx 10\mu m$ (cigarette paper) between it and the round slide. The other rectangular glass slide was tilted in the opposite direction by introducing an identical sheet of paper on the opposite side. The space left between the round slide and the tiled rectangular slides was filled by capillarity with a drop of Olympus immersion oil, in order to create two prisms of opposite angles. The shape of the holder avoids the displacement of the slides by the meniscus of the oil. It also features two holes on the side in order to introduce the immersion oil (figure C-9). A sheet of black paper in which the *SDI* slits were cut was then added on top of the prisms. Slits consist in four rectangles which centers are placed at the following positions with respect to the optical axis: ([-2.2mm,0],[-0.9mm,0],[0.9mm,0],[2.2mm,0]). Outer slits (width: 0.85 mm, height: 1.25 mm) are wider than inner slits (width: 0.55 mm, height: 1.25 mm) in order to compensate for the smaller light intensity at large scattering angles. The height of the cylindrical spacer was adjusted so that, once the objective is reassembled, the slits are located at the back focal plane of the objective. Lateral centering of the slits-containing mask is permitted by the interlocking shapes of the mask and its support.

Remark: *Isabelle Eisenmann* performed a similar operation with a 8X objective.

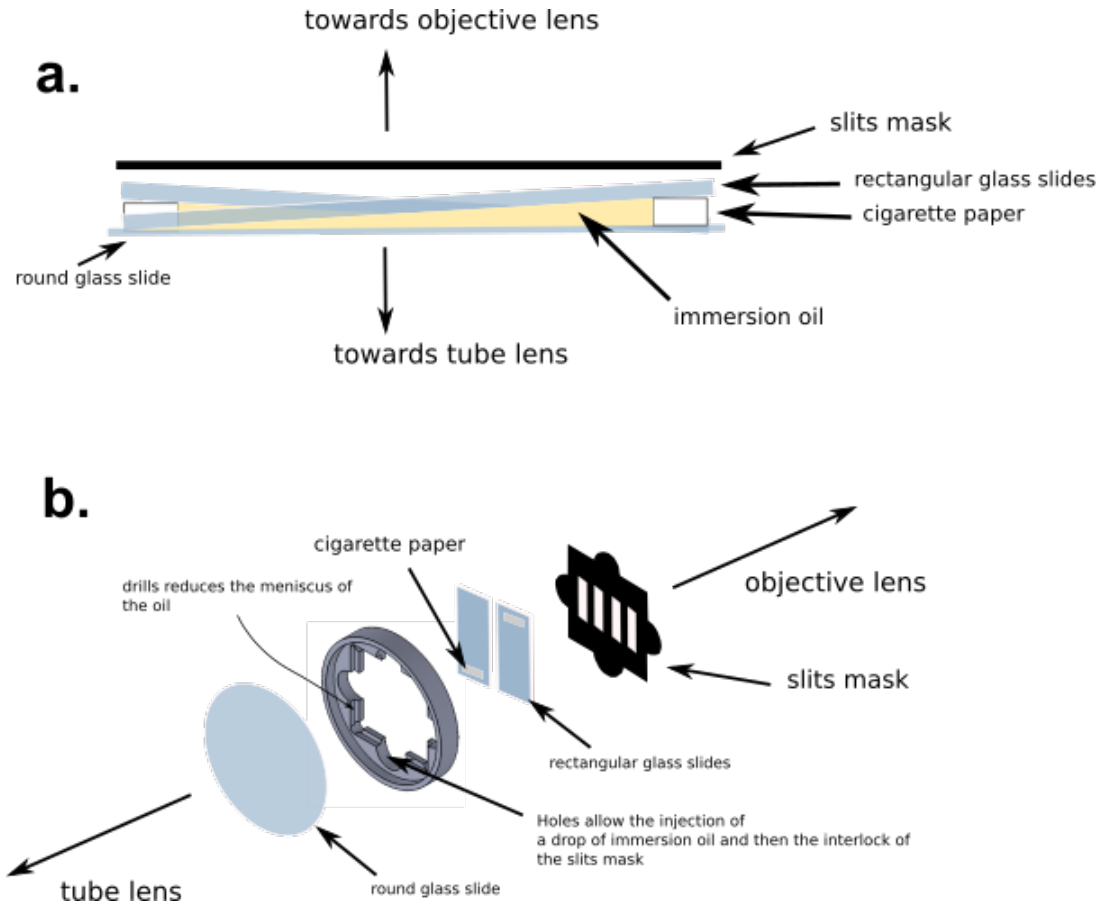

Figure C-9: **Design of prisms of small angles for the embedded SDI objective. a**. Prisms with small angle of incidences are realized by tilting rectangular slides with a sheet of cigarette paper. Not-to-scale drawing. In reality, the cigarette paper is much thinner (10μm than the length of the slides (8mm). The space between the rectangular slides and the round support glass slide is filled with immersion oil. **b**. Holder allowing to keep together the pieces shown in a. inside the objective (in the Fourier plane).

C.1.11 Magnets

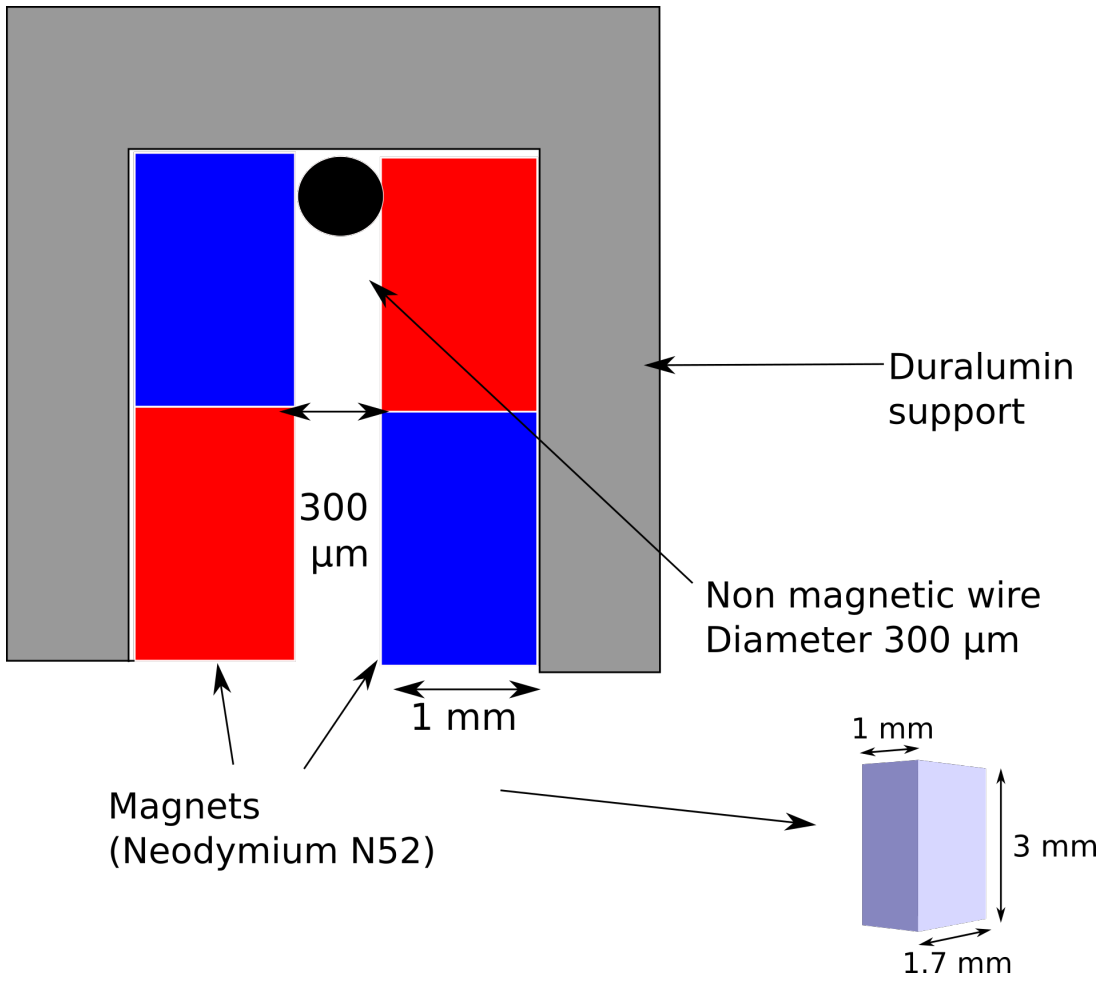

Figure C-10: **Magnets configuration used in this work.** The magnetic field is created by two magnets (HKCM, 9964-71786, Q01.7x01x03Ni-N52) of opposite polarity separated by a small amagnetic wire of diameter 300 microns. Magnets are chosen coated with black epoxy in order to avoid reflections.

C.1.12 Magnets alignment

The position of the magnets is adjusted with micrometric screws. In order to ensure that the magnetic field is centered with regard to the field of view, the following procedure is performed:

1. Inject 1 uL of magnetic bead in the flow-cell.
2. When they appear in the field of view, bring the magnets at a distance of 300 um from the surface.
3. stop the injection and wait for the flow to stop.
4. release the magnets and wait for the beads to form an homogeneous cloud.
5. Approach the magnets down to 125 um from the surface. At this distance, the magnetic field buckles and the beads are attracted preferentially by one of the two permanent magnets.
6. Move the magnets in the direction of the gap and repeat the previous steps until half of the beads are attracted towards one of the magnets and half of the beads are attracted towards the other magnet (figure C-11).

7. Move the magnets in the perpendicular direction until the beads only move in the direction of the gap and that no lateral movement can be observed upon approaching the magnets.

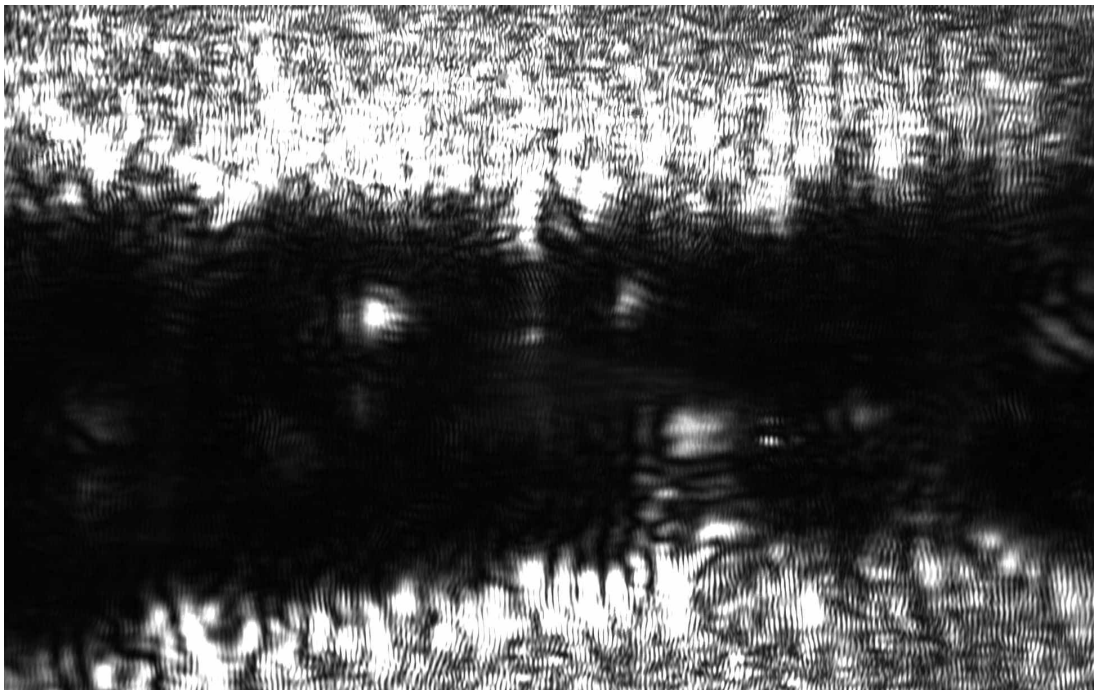

Figure C-11: **The buckling instability of the magnetic field close to the surface allows centering the magnets.** When the magnets are approached at 125 um from the glass surface, the magnetic field buckles. When the magnets are centered with regard to the field of view, half of the beads are attracted by the top magnet and half of the beads are attracted by the bottom magnet.

C.1.13 Force calibration

At each experiment, the magnets are brought closer and closer from the surface by steps of 5 microns until they touch the mylar (the plastic sheet forming the *roof* of the flow-cell). Given that the mylar has a thickness of 50 um as well as the double-sided tape forming the flow cell, we consider that the magnets are at 100 microns from the surface.

The magnetic field exerted by the magnets as the function of their distance from the glass surface is calibrated using long dsDNA λ molecules as already described in previous work (figure C-12).

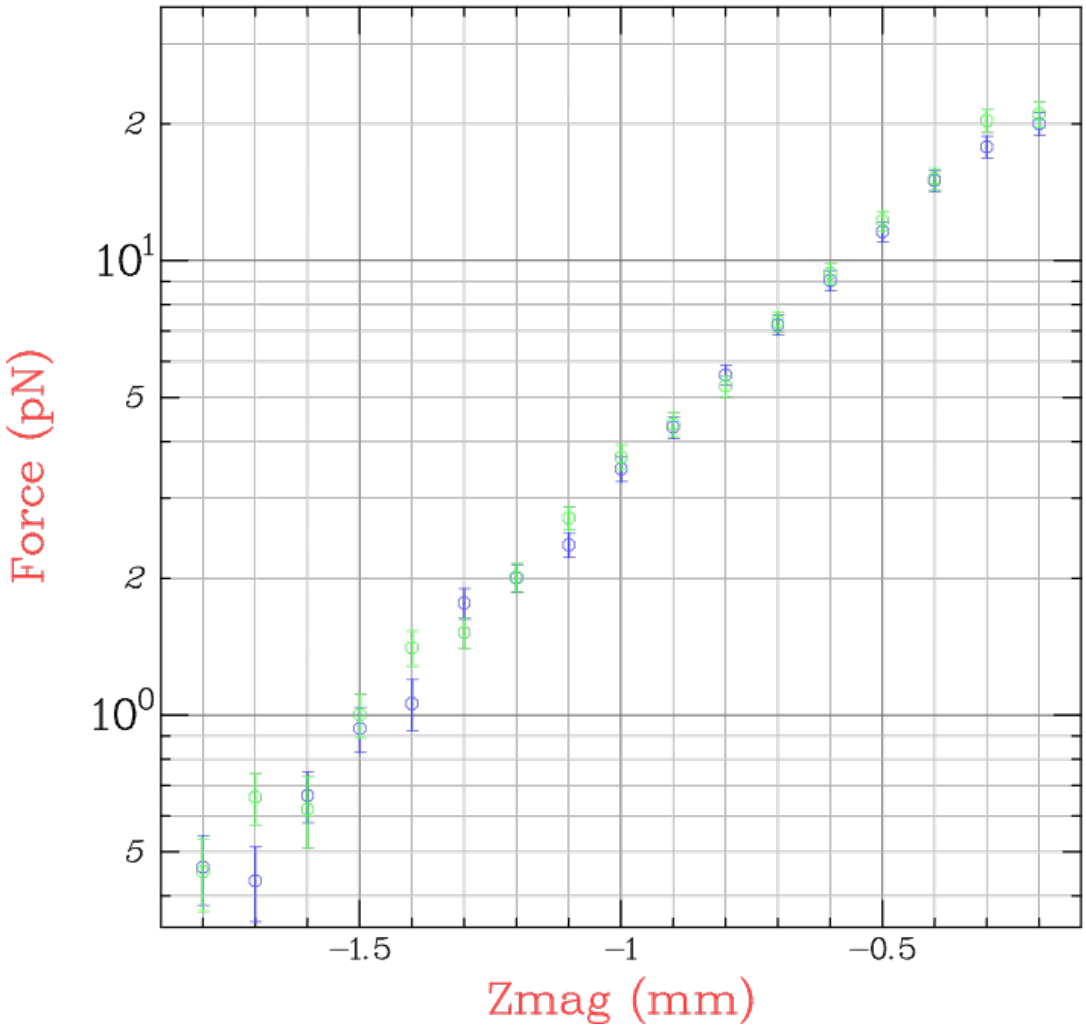

Figure C-12: **Calibration force curve used as a reference during this work.** A λ-DNA molecule is attached between the suface and a microbead and the fluctuations in the x and y directions are measured as a function of the distance of the magnets from the surface. From these fluctuations one can deduce the force applied on the bead as described in the main text. Blue: X-direction (perpendicular to the magnetic field). Green: Y-direction (parallel to the magnetic field).

C.2 Single-molecule sample preparation

C.2.1 Surface attachment procedures

During this work, two methods were used to attach single molecules to the surface (figure C-13).

Click-chemistry attachment:

A surface coated with azide is incubated with an oligonucleotide containing DBCO. It results in a surface coated with oligonucleotide to which one can hybridize other nucleic acids.

- 👍 Covalent and strong attachment (allows performing measurements during several days without losing beads).
- 👍 Long lifetimes of the coated glass, even dry. In the absence of the use of proteins in high concentrations, can be used during several weeks without losing in attachment efficiency.
- 👍 Hybridized molecules can be washed out by rincing with NaOH 15mM. It allows resetting the surface for new experiments.

- DNA binding proteins might attach to the oligonucleotides coated on the glass surface. Protein concentration in solution will consequently be affected. The lifetime of the cell will also be decreased.
- Relatively expensive ($\sim$ 30 euros per cell).
- Molecules are attached by hybridization and might be detached by helicases. However, the problem can be overcome at low helicase concentration by using longer hybridized section (more than 60 bases). Then the substrate can re-hybridize after the passage of the helicase. (*In theory, one could perform ligation in the flow-cell between the red and orange oligonucleotide on figure C-13.c. However, I was not able to get good yields*).

Dig-antidig attachment:

A glass surface is coated with anti-digoxigenin antibodies. DNA molecules are either hybridized to adaptor containing dig groups or directly dig-tailed.

- The flow-cell is not coated with DNA/RNA, avoiding unwanted interaction with proteins.
- The molecule of interest can be attached without hybridization (figure C-13.d).
- Less expensive.
- High probability of detachment. Impossible to work with the same molecule during several hours.
- Smaller lifetime. At each experiment, the attachment efficiency decreases.

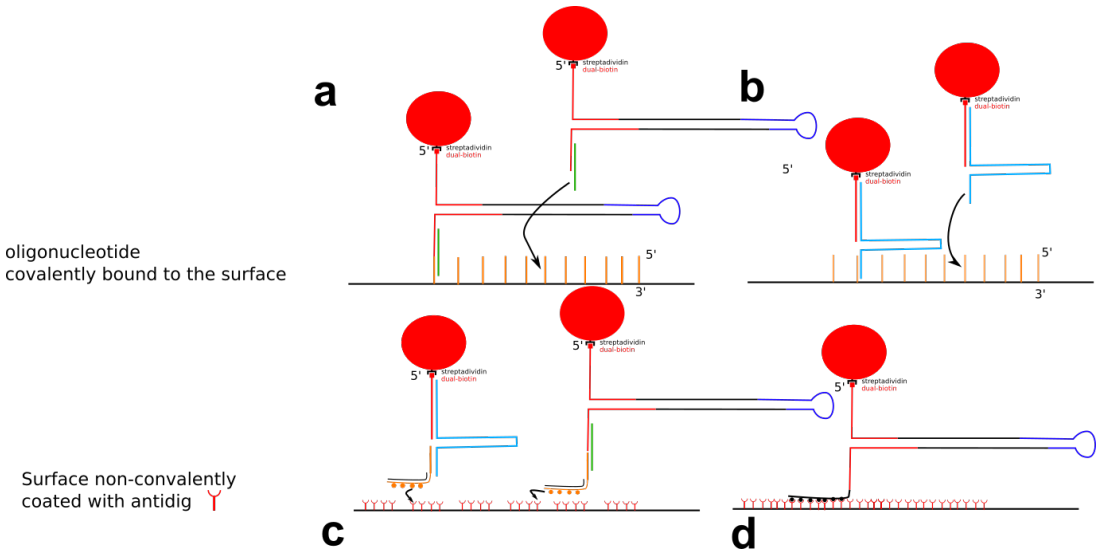

Figure C-13: **Surface attachments methods used in this work. a**. First, an oligonucleotide with 3'DBCO modification is covalently bound everywhere on a azide-treated surface. Beads attached to single-hairpin via biotin/streptavidin interaction and hybridized to an adaptor (green) is then introduced in the cell and attached by hybridization to the oligo on the surface. **b**. Same as a. but the hairpin is complementary to the surface (no need of an adaptor) and is attached to the bead by hybridization to an oligonucleotide containing a biotin. **c.** Glass surfaces are coated with anti-digoxigenin antibodies either by adsorption or covalently by using epoxy-treated surface. Then, the same beads and molecules as in a. and b. can be used by pre-attaching them to an oligonucleotide containing a dig tail. **d.** Here, the dig-tail is directly incorporated into the hairpin. No hybridization is necessary for the attachment.

C.2.2 Preparation of coverslips for click-chemistry attachment of DNA/RNA

1. Take an azide-coated surface (PolyAn 2D Azide). Use a freshly opened package (less than a week). If some surfaces of the package are not used, put them back at 4°C, protected from light.
2. Remove the protection on one side of the channel-containing double side tape (ARcare 92712, Adhesive Research).
3. Attach the tape on the azide-coated surface and apply a pressure on the tape to ensure proper adhesion.
4. Add 20 uL (a drop) of (100 nM DBCO-containing oligonucleotide, 500 mM NaCl, 10 mM PBS) in the channel.
5. Wait two hours or until the surface is dry.
6. Remove the remaining solution with distilled water.
7. Dry with dry air.
8. Remove the second protection of the double side tape.
9. Attach a sheet of mylar (50 um thick, 48-2F-OC, CSHyde) with two holes of diameter 2 mm. Apply a pressure on the tape to ensure proper adhesion.
10. Add inlets and outlets so as to complete the microfluidic cell.
11. Flow passivation buffer in the flow cell. The cell can be used immediately or stored at 4°C.

C.2.3 Preparation of coverslips for dig/anti-dig attachment of DNA/RNA

1. Take a clean glass surface (Schott, NEXTERION® Coverslip custom, #1.5H) or an epoxy-coated surface (Schott, NEXTERION® Coverslip E #1.5H). A plasma cleaner can also be used to clean standard slides.
2. Remove the protection on one side of the channel-containing double side tape (ARcare 92712, Adhesive Research).
3. Attach the tape on the glass surface and apply a pressure on the tape to ensure proper adhesion.
4. Remove the second protection of the double side tape.
5. Attach a sheet of mylar (50 um thick, 48-2F-OC, CSHyde) with two holes of diameter 2 mm. Apply a pressure on the tape to ensure proper adhesion.
6. Add inlets and outlets so as to complete the microfluidic cell.
7. Flow 40 uL of pure antidig in the flow cell.(Jackson Immuno Research, IgG Fraction Monoclonal Mouse Anti-Digoxin, 200-002-156). No air should remain in the flow-cell. Incubate two hours.
8. Remove the antidig from the flow cell and flow passivation buffer in the flow cell. Passivate overnight.

C.2.4 Bead preparation

Molecules to be tethered are first hybridized to the possible adaptors needed for their attachment. This hybridization is performed in passivation buffer at 100 nM. Biotin adaptors are inserted at the same concentration as they cannot be rinsed after attachment to the beads. Other adaptor can be put in excess to maximize the hybridization efficiency.

Hybridized molecules are then diluted in passivation puffer. Synthetic hairpins, whose concentration are well known are diluted down to 2 pM.

Hairpin	Source plasmid	PCR Primer 1	PCR Primer 2	Oligo-yshape	Yshape-biotine	loop	Length of HP (bp)
HP179	PS006	P1-005	P2-005	MR100	PS179	MR000	1053
HP005	PS005	P1-005	P2-005	PS866	PSTreble	PS124	1072
HP006	PS006	P1-005	P2-005	MR-YSHAPE1	MR-YSHAPE2	MR000	1053
HP4kb	Lambda-DNA	P4K1	P4K2	MR-YSHAPE1	MR-YSHAPE2	MR000	3931

Table C.1: **Oligonucleotides for hairpin construction.**

Purified hairpin are typically diluted down to 0.2 ng/uL. However, this dilution needs to be adjusted in order to maximize surface attachment. If too many beads attach and do not extend upon force application, DNA/RNA was not diluted enough: several molecules are attached per bead. If the efficiency of attachment is too low, DNA/RNA was too diluted.

5uL of streptatividin coated Dynabeads MyOne T1 (Thermofisher) are washed three times in 200 uL of passivation buffer. The diluted substrate is then incubated with the beads in a total volume of 20uL of passivation buffer. The beads are then rinsed three times with passivation buffer in order to remove unbound DNA and excess adaptors.

C.3 Biochemistry

Some methods of this section are related to side projects that are not presented in this work. They are presented here in order to ensure a smooth handover with the students taking over these projects and to ensure the reproducibility of the preliminary results.

C.3.1 DNA hairpin construction and purification

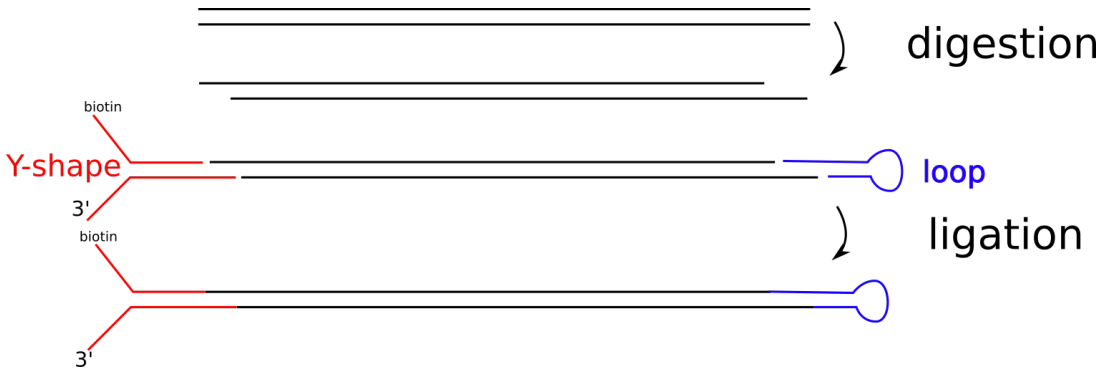

Figure C-14: **Hairpin construction.** A linear or circular dsDNA is molecule is digested. Then, it is ligated with a loop and two partially complementary oligonucleotides.

1. Primers are chosen so as to (i) have a melting temperature close to 60°C (computed with the software Snapgene) (ii) to avoid the possibility of multimers (iii) contain a BsmBI restriction site that leaves overhangs compatible to the loop (AAGC) and the Y-shape (GATT).
2. PCR is performed with Q5 high-fidelity polymerase (NEB) in multiple PCR tubes of final volume of 25 uL.
    - Final concentrations: 1X Q5 buffer, 1uM of each primer, 10-15 ng of template DNA, 0.02 U/uL Q5 polymerase
    - 30 s denaturation at 98°C
    - 30 cycles of 10 s at 98°C, 30 s at 61°C, 45 s/kb at 72°C

- 5 min of final extension at 72°C
- keep at 4°C

3. The PCR product is run on a 1.5% agarose gel during 30 minutes at 100V in TAE. The band corresponding to the desired product is cut out from the gel.

4. The gel portion is purified with a nucleospin (M&N) column (two washing steps, 2 min at 70°C to remove remaining ethanol, two elutions of 1 min in water, 15 uL at 70°C).

5. The PCR product is digested by Esp3I one hour at 37°C and purified as in the previous step (no agarose gel and elution in 20uL of water).

6. The product is mixed at 100nM with the Y-shape oligonucleotide (1uM) and the loop oligonucleotide (2uM). See table C.1.

7. Ligation is performed with T4 Dna ligase in a final volume of 20uL during 1 hour at 25°C.

8. The product is run through an agarose gel and a purification column. Its concentration is measured with a Nanodrop machine.

9. *Remark: to obtain a good yield, the 4kb hairpin was purified from the gel by electro-elution in a dialysis bag (Slide-A-Lyzer, 30kDa) instead of using a column. The bag was filled with TAE. It was placed in a electrophoresis chamber and the DNA was migrated out of the gel at 100V during 2 minutes. Then, a reversed voltage was applied during 10 seconds to detach the DNA from the dialysis tube. The dialysis bag was then placed in TE buffer and dialysed during 2 hours. The dialysis bag was opened and the DNA-containing solution (200 uL) was evaporated down to 20 uL.*

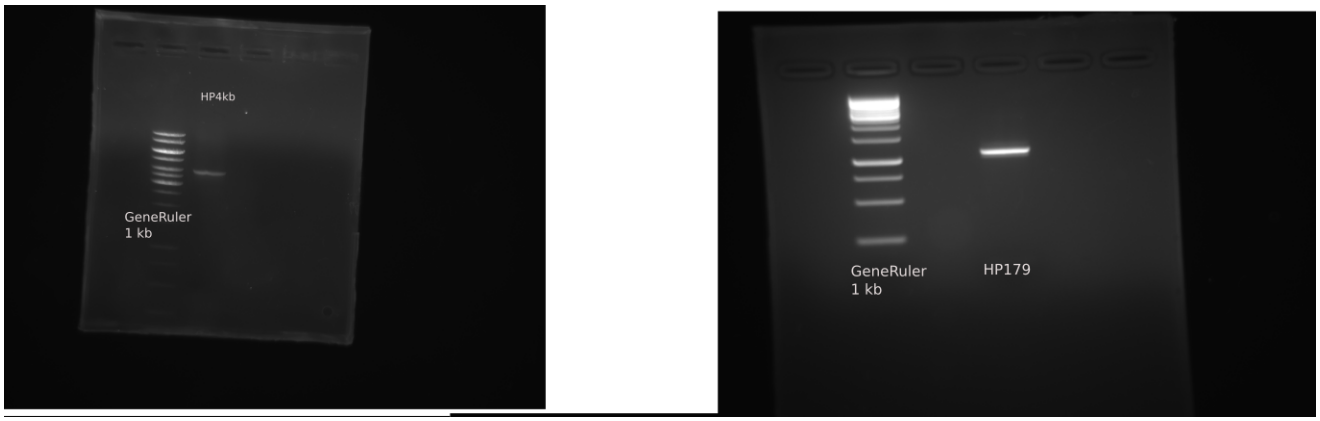

Figure C-15: Agarose gels of two constructed DNA hairpins. Left: HP4kb. Right: HP179

C.3.2 Dig tailing of DNA substrates

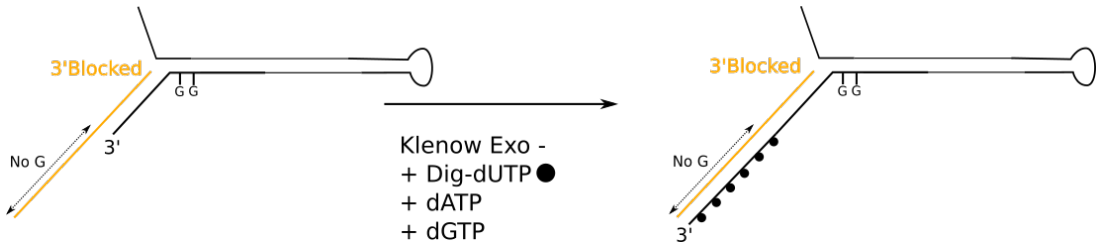

Figure C-16: **Dig tailing.** Dig tailing is obtained by hybridizing at the 3' end of a molecule an oligonucleotide with a long flap that contains no G. The 3' of this oligonucleotide can be protected. The flap is polymerized with Dig-dUTP instead of dTTP, with a polymerase that lacks strand-displacement activity. The absence of dCTP, the absence of strand-displacement activity, and the blockage of the 3' of the oligonucleotide are three redundant measures that prevent the polymerization from the 3'-end of the oligonucleotide.

Dig tailing is performed by hybridizing an oligonucleotide with the molecule to be tailed. The oligonucleotide has a long ssDNA tail on the 5' side that contains regularly spaced adenines but no guanine. The hybridized substrate is polymerized with Klenow Exo - in the absence of desoxycytidine triphosphate (dCTP) in order to ensure a one-way polymerization.

1. 10 - 100 ng HP click substrate (with part complementary to PS867) Max 10 uL
2. 1 uL oligo *Fill-in-Dig-No-G* (100 nM)
3. 0.5 uL dATP 10 mM
4. 0.5 uL dGTP 10 mM
5. NO dCTP
6. 5 uL 1mM dUTP-Digoxigenin (Roche)
7. 2 uL NEB 2 Buffer
8. 1 uL Klenow Exo - (NEB)
9. Water -> 20 uL total volume
10. Mix well and incubate 1 hour at 37°C
11. Purify the DNA (nucleospin column, M&N)

C.3.3 Insertion of bases of reversed polarity

Gibson assembly can not be performed to insert modified bases in the hairpin. It was thus performed by successive ligation.

A segment of 600 bases of dsDNA was obtained by performing a PCR on PS005 with the primers P1-005 and P2-005-600. A segment of 400 bases of dsDNA was obtained by performing a PCR on PS005 with the primers P2-005 and P1-005-400 (figure C-17, left panel). Both segments were digested with BsaI and Esp3I. The insert (1uM) and the loop MR000 (2 uM) were ligated with the segment of 400 bp (400 ng/uL) during 4 hours at 25°C. Y-shape (PS179+MR100, 1 uM) was ligated with the segment of 600 bp (200 ng/uL) during during 3 hours at 25°C. Both products were gel-purified ((figure C-17, middle panel), followed by a purification on column. Both products were then ligated at 25°C during two hours. The final product was gel-purified (figure C-17, right panel), followed by a purification on column.

Remark: In order to design overhangs for successive ligation, it is important to choose compatible overhangs in order to reduce non-specific ligations. Recently, a comprehensive list of compatible overhangs of length 4 has been published [Potapov et al., 2018].

Figure C-17: Agarose gels illustrating the construction of hairpins with modified bases. Left: Preliminar PCR. Middle: Intermediary ligations. Right: Final ligations of theintermediary products.

C.3.4 180-bp RNA hairpin construction

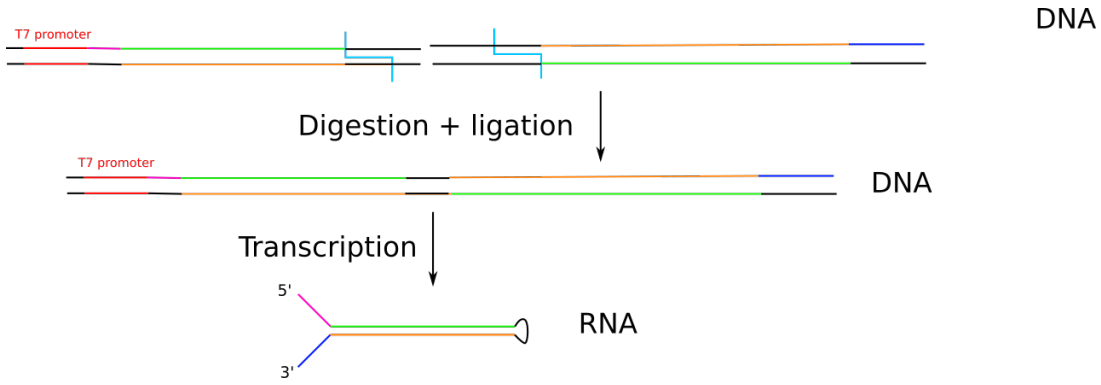

Figure C-18: **Synthesis of RNA hairpins** First, two DNA geneblocks are digested and ligated so as to form a long palindromic DNA molecule. Then, transcription is performed with T7 polymerase so as to form a RNA hairpin. Biotin and surface-attachment are then performed by hybridization.

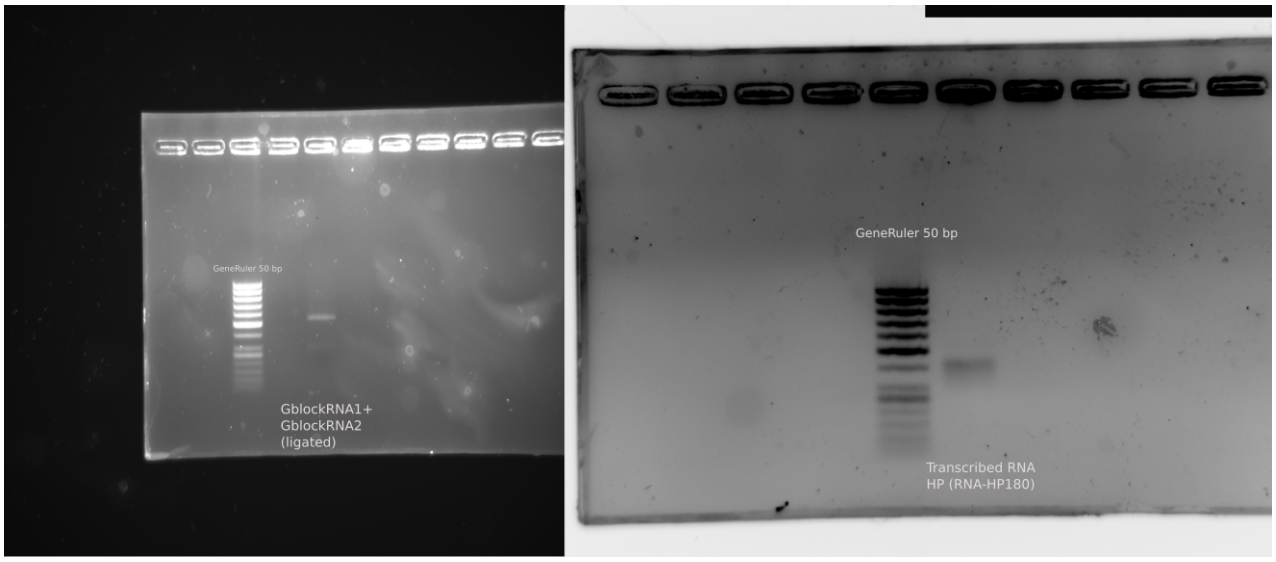

Figure C-19: Agarose gels of the construction of a RNA hairpin. Left: Palindromic dsDNA (534 bp). Right: RNA hairpin (180 bp of dsRNA + 138 ssRNA)

First, a dsDNA containing a 360bp palindromic region (2x180bp) is constructed from two gene blocks. Then, the long palindromic DNA is transcribed with T7 RNA polymerase.

Palindromic DNA

The two gene blocks *Gblock1_RNA-HP* (500 ng) and *Gblock2_RNA-HP* (500 ng) are diluted in 5 uL of RNAse free water. They are then digested and ligated in one step.

1. Gblock1 3 uL
2. Gblock2 3 uL
3. BSAI-HF (NEB) 0.5 uL
4. Dna ligase T4 (NEB, 400 units/uL) 0.5 uL
5. ATP 10mM (Roche) : 1.2 uL
6. Cutsmart buffer (NEB) 10X: 1.2 uL
7. RNAse free water: 2.5 uL
8. Incubate at 37°C 2 hours

The tube now contains roughly 600 ng of ligated product in 12 uL. 2 uL are run on a agarose gel 1.5% (figure C-19, left panel). The remaining 10 uL are not purified. Enzymes are not heat deactivated in order to avoid spontaneous migration of a HJ junction is the ligated product.

T7 transcription

The palindromic substrate is transcribed with the mMESSAGE mMACHINE^{TM} T7 Transcription Kit (ThermoFisher).

1. 2 uL RNAse free water
2. 10 uL NTP-CAP (Kit)
3. 2 uL GTP (Kit)

4. 2 uL reaction buffer (Kit)
5. 2 uL palindromic DNA ($\sim$ 100ng)
6. 2 uL Enzyme mix (Kit)
7. Incubate two hours at 37°C.

1 uL of product is run on a agarose gel, 2%, ((figure C-19, right panel). The product is purified with a Monarch RNA purification kit (NEB,T2040L) and eluted into 20 uL of RNAse fre water. The RNA concentration is measured with Nanodrop: $\sim 900nM$. 1 uL of murine Rnase inhibitor (M0314L, NEB), is added to the product, which is then stored at -80°C.

C.3.5 Preparation of lambda DNA for click chemistry

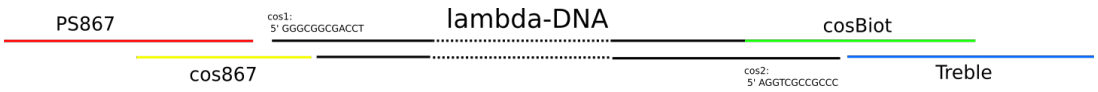

Figure C-20: Functionalization of λ-DNA for single-molecule experiments. PS867 is complementary to the DBCO oligonucleotide on the surface and the treble oligocucleotide contains three biotins.

In order to perform a force calibration, a commercial λ molecule (SD0021, Thermofisher, Dam-, Dcm-, $\sim$ 100nM) was used. The ligation presented in figure C-20 was performed in two steps. **Be careful when pipeting λ-DNA. Long DNA molecules can break !**

First, the biotinylated oligonucleotide is ligated:

1. Mix cosBiot (1uM final), Treble (1uM final), λ-DNA (50 nM final), 2uL Ligase T4 buffer 10X in a final volume of 17 uL.
2. Heat at 85°C in order to melt the cohesive ends of λ-DNA and allow the rehybridization with the biotinylated oligonucleotide.
3. Let cool down to room tempetature.
4. add 2uL of ATP 10 mM and 1 uL of T4 DNA ligase.
5. ligate at 37°C during one hour.

Then, the excess of biotinylated oligonucleotide is removed by centrifugation through a porous membrane (Microcon DNA fastflow). The ligated producted is diluted in 500uL of water and centrifugated 20 minutes at 500g. The operation is repeated once. Then, 150 uL of NaCl (20 mM, 10 mM Tris HCl, pH7.6) is added to the centrifugation tube and centrifugated during 7 minutes at 500g. The remaining volume above the porous membrane (10 uL) is pipeted and put into a 1.5mL tube.

Second, the oligonucleotide complementary to the surface is ligated to the other end of the λ molecule.

1. Mix cosBiot (1uM final), Treble (1uM final), ligated product, 2uL Ligase T4 buffer 10X in a final volume of 17 uL.
2. Heat at 85°C
3. Let cool down at room tempetature.
4. add 2uL of ATP 10 mM and 1 uL of T4 DNA ligase.
5. ligate at 37°C during two hours.

Then, the excess of PS867 oligonucleotide is removed by centrifugation through a porous membrane (Microcon DNA fastflow). The ligated product is diluted in 500uL of water and centrifuged 20 minutes at 500g. The operation is repeated 1 time. Then, 150 uL of NaCl (20 mM, 10 mM Tris HCl, pH7.6) is added to the centrifugation tube and centrifuged during 7 minutes at 500g. The remaining volume is kept at $-20°C$.

C.3.6 RecQ-ΔC purification

RecQ-ΔC was purified by *Bertrand Ducos*[1] as described in [Bagchi et al., 2018].

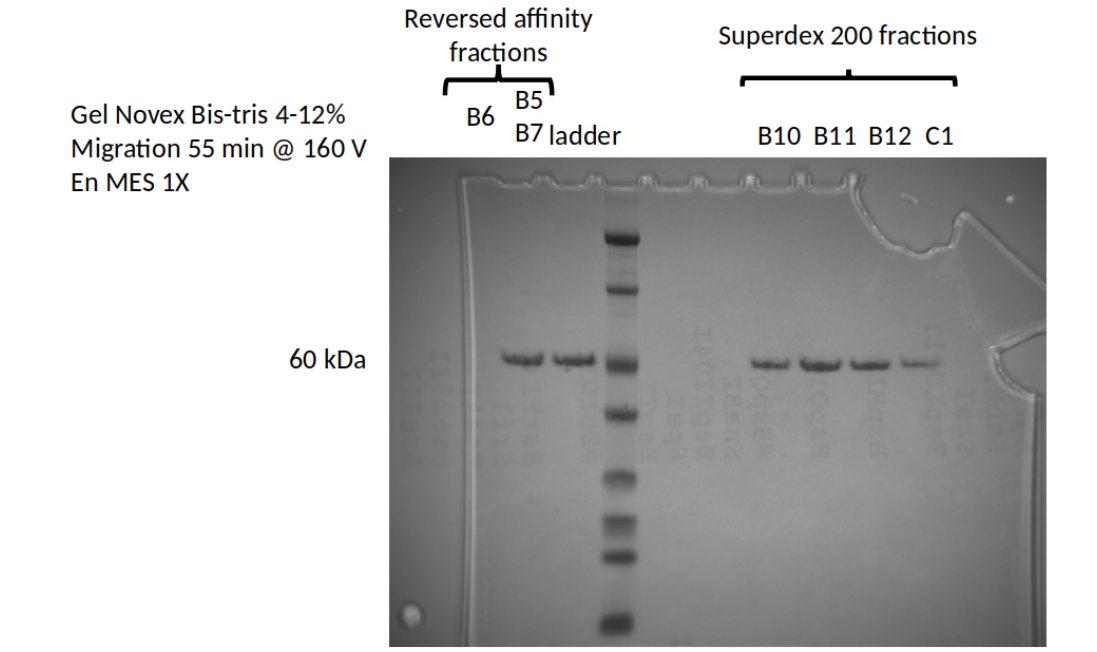

Figure C-21: **Purified RecQ-ΔC** *(from Bertrand Ducos)*

C.3.7 yUpf1-HD purification

The helicase domain of yeast-Upf1 was purified by *Nadia Ruiz-Gutierrez*[2] as described in [Kanaan et al., 2018].

[1] bertrand.ducos@phys.ens.fr
[2] ruiz@biologie.ens.fr

C.3.8 Fast assembly of long three-way junctions.

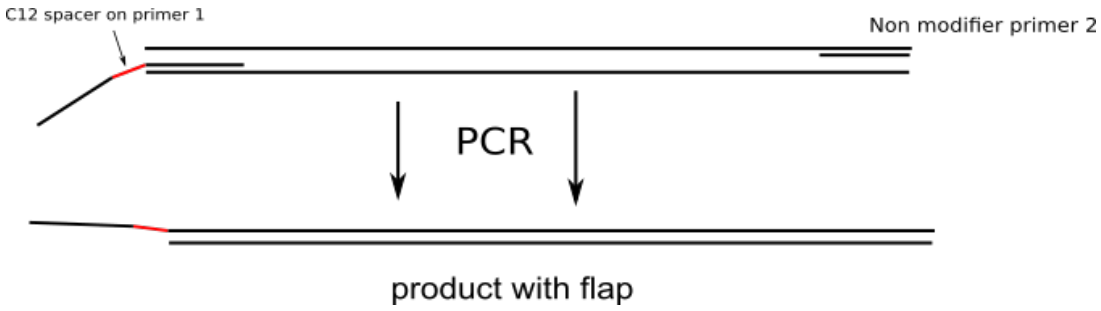

Figure C-22: **Production of dsDNA with ssDNA flap** Double-stranded DNA with flaps are made by PCR, using a primer with a C12 spacer that causes polymerase stalling (at least of Q5® and Phusion® HF polymerases).

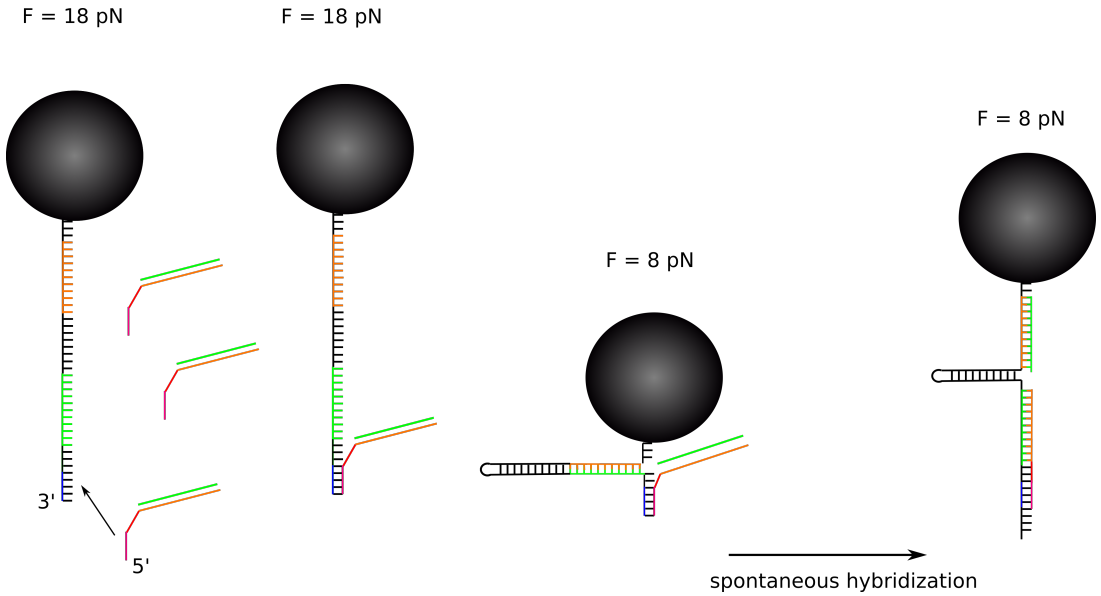

Figure C-23: **Assembly of long three-way junctions by dsDNA invasion.** Long single-stranded DNA (>200 bases) are difficult to synthesize or amplify. However, a three way-junction can simply be obtained by invasion of a double-stranded DNA as described above. The last step is thermodynamically favored be cause the number of hybridized bases in unchanged while the position of the bead in the force field is energetically advantageous. In practice, several opening/closing cycles must be performed before observing the invasion.

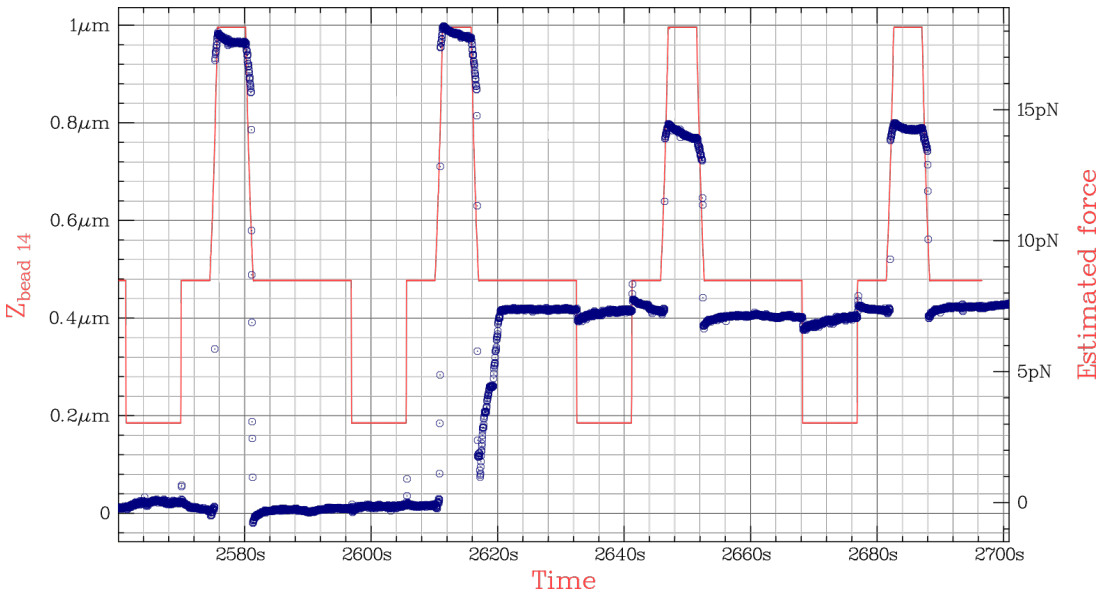

Figure C-24: **Evolution of the extension of a hairpin during invasion.** The invasion process is described in figure C-23. A 600-bp DNA complementary to the hairpin (HP179) with 20 bases ssDNA flap is injected at 10nM. Red:applied force. Blue: molecule extension. Invasion occurs at 2620s.

C.3.9 ssDNA amplification

In order to synthetize long single-stranded DNA, linear amplification with a unique primer was performed. First, a classical PCR was performed (Primer1: P1-005 Primer2: P2-005-600) in order to obtain a large quantity of dsDNA (same protocol as in section C.3.1. Primers were then removed on a column. The resulting PCR product was then amplified with both primers independently during 15 cycles in 8 different tubes of 25 uL, in order to only obtain the ssDNA corresponding to the primer that was used. The single-stranded DNA was then gel purified in order to separate it from the double-stranded product (figure C-25).

The yield of the experiment is low (< 100 ng of ssDNA) and one amplification had to be performed for ∼5 single-molecule experiments. Some publications seem to suggest that the yield can be made better [Heiat et al., 2017, Wooddell and Burgess, 1996, Veneziano et al., 2018]. Other methods that were not tested here include the selective degradation of the phosphorylated strand by λ-exonuclease [Avci-Adali et al., 2010] and the capture of one of the strand (biotinylated) by streptavidin beads [Espelund et al., 1990].

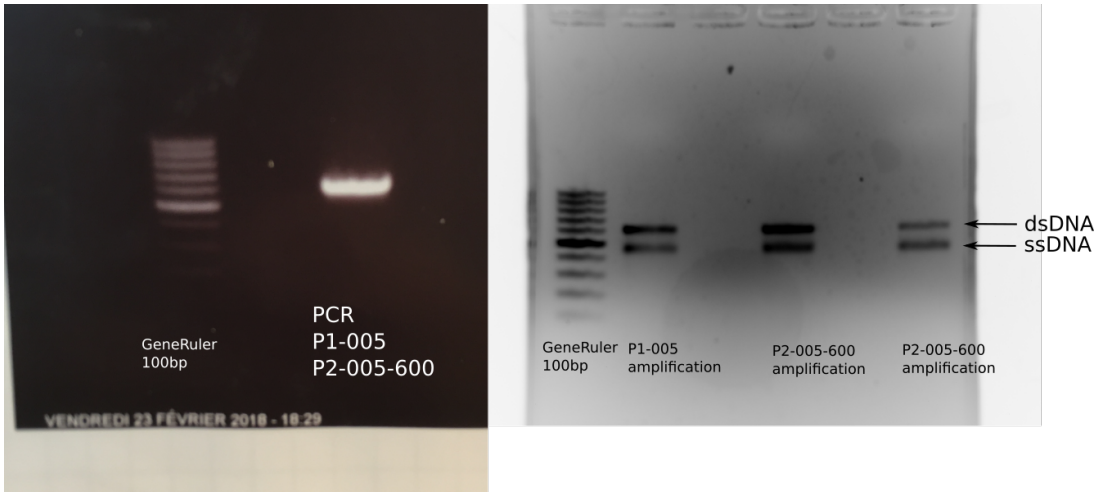

Figure C-25: **1.5% agarose gels resulting from ssDNA amplification.** Left: dsDNA PCR-amplified from PS006 with the primers P1-005 and P2-005-600. Right: Result of assymetric amplification of the PCR-product (using only one of both primers.) The second lower band corresponds to the single-stranded DNA product.

C.4 Single-molecule experiments

C.4.1 Direct visualization of the hybridization of a 8-bases oligonucleotide (Chapter 2).

The substrate used in these assays (HP3) is a 153-bases ssDNA strand. Once hybridized to MR-YSHAPE1 and VC625, the size of the remaining single-stranded DNA reduces to 38 bp. 24 of these bases fold into a 10 bp hairpin with a 4-base apex loop. This hairpin is used to test that only one DNA molecule is bound to the beads by testing the fluctuation between the open and closed state at 10 pN. Once this is checked, the hairpin is blocked by a 16bp oligonucleotide (OliBlock-half-stack) for the half-stack configuration or by a 22bp oligonucleotide (Oliblock-full-stack) for the fully stacked configuration. The remaining bases of single-stranded DNA contain the 8-base sequence that is complementary to the oligonucleotide whose hybridization kinetics is measured. The assay is realized in hybridization Buffer 1 (HB1).

C.4.2 Upf1 stepping

The substrate used in these assays (HP30) is a 153-base ssDNA strand. Once hybridized to MR-YSHAPE1 and VC625, the size of the single-stranded DNA reduces to 78 bases. Among them, a 30-bp is included with a loop of 4 bases. It is flanked by two handles of 7 successive thymines. Once the beads are attached to the surface of the cell, the buffer is changed to Upf1 buffer (200uL of buffer are flowed twice). A force scan going from 20 to 8 pN is performed. Beads that display spontaneous oscillations between the closed and the open stare are selected. The force is then fixed to 8 pN on average and the helicase domain of yeast-Upf1 purified as described in [Kanaan et al., 2018] is injected with ATP (500 nM) in Upf1 buffer at a concentration of 10 nM unless otherwise mentioned.

C.4.3 Kinetic locking: oligonucleotides

The fluctuating probe used to measure oligonucleotide binding is HP1. Once the hairpin is hybridized to MR-YSHAPE1 and VC625, 7 ss bases are left on the 5' side and 14 on the 3' side. Measurements are performed in hybridization buffer 2 (HB2). The oligonucleotides are ordered dry (Eurogentec) and diluted in the same buffer preparation as the one used during the hybridization assay in order to avoid any change in salinity upon injection. Concentrations are calculated based on the quantity indicated by the provider. Upon change of oligonucleotide concentration, the inlet of the flow cell is washed two times with 200 uL of new solution. Extra care must be taken to remove any remaining solution in the inlet between two washing steps. Then, 200 uL of the new solution are injected in the inlet and 160 uL of solutions are flowed in at 10 uL/min. Rarely ($\simeq 15\%$ of the cases), some oscillating hairpins showed abrupt changes of their kinetic rates upon flowing new solution while the position of the magnet was not changed. These beads were discarded. More often ($\simeq 30\%$ of the cases), the temperature of the sample changed by more than 0.05°C during the whole experiment. In this case, data were discarded.

C.4.4 Kinetic locking: RecQ-ΔC

RecQ - ΔC is stored at 4°C. RecQ-ΔC from the B11 fraction was taken from the fridge before each acquisition and was diluted without ATP in RecQ Buffer at a concentration specified in the main text. The fluctuating probes HP1 (7-bases ssDNA gap on lagging strand and 14-bases ssDNA gap on leading strand) HP2 (14-bases ssDNA gap on leading strand), HP3 (no gap) are used. Measurements are performed in RecQ buffer. The concentration of the enzyme is assessed through UV absorbance (210-340 nm) with a Nanodrop (Thermofisher) spectrophotometer ($\varepsilon = 45840 \mathrm{M}^{-1}\mathrm{cm}^{-1}$).

C.4.5 Measurement of the optical noise of the setup

In order to measure accurately the optical noise of the setup and compare it to theory, it is necessary to uncouple it from the Brownian motion and from slow thermal or mechanical drifts that can affect the measurement. In order to do so, we melt MyOne T1 beads (ThermoFisher) on a glass surface. The stock solution was diluted 10000 times and then spread on a glass slide. The slide was then heated at 110°C for 5 minutes following the evaporation of the solution. A standard flow cell was then assembled with this slide and water was injected. The position of 15 beads was then tracked for 5 seconds at 160 Hz at different light intensity. The average of the trajectory of the 15 beads was then subtracted from each individual trajectory in order to get rid of mechanical or thermal drifts.

C.5 Data treatment

C.5.1 Data acquisition

The extensions of the molecule is acquired in real-time and imaged by treating using the home-made C/C++ acquisition program *Xvin* can be found at https://tig.phys.ens.fr/ABCDLab/xvin/.

C.5.2 Treatment of *SDI* images

The code allowing to treat the *SDI* images can be found in the Xvin folder plug-ins-src/trackBead/, in the files SDI_2_functions.c and SDI_2_utils.c

C.5.3 Step detection algorithm

The code allowing to find steps in data can be found in the Xvin folder plug-ins-src/FindSteps/FindSteps.c. Parameters used in this work are indicated in the main text.

C.5.4 Noise as a function of photon numbers

The optical noise as a function of photon numbers was analyzed from raw images using the Xvin code that can be found in plug-ins-src/NoiseInImage/NoiseInImage.c

C.5.5 Post-rotation

The post-rotation of the data is performed by calling the function mod_bead_angles that can be found in the file plug-ins-src/trackBead/record.c. In the graphical interface, the function is called by the menu "Record menu/Oligo functions/Modify bead angles". The angles should be computed on a window of ~ 1 second where the signal does not display large drifts.

C.5.6 Detection of hybridization events for direct visualization of 8-bp oligonucleotide hybridization

In order to detect the events:

1. Call the function "Select events/Find NHN or NRN events".
2. Select "Non linear"
3. minimum δZ: 0.0007 um

4. Filter min length: 8, filter max length:32
5. sigma: adjust as a function of the high-frequency noise in your signal (typically between 0.0008 and 0.001 um).
6. select "click here if you expect only two states"
7. If no event was recorded previously, select "Click here to not check existing events".

The code for the corresponding functions can be found in the file plug-ins-src/trackBead/record.c

C.5.7 Detection of closing/opening events for kinetic locking

The changes of states (open/close) of the fluctuating probe are detected automatically with the program *Xvin*, when the summed change of extension over a monotonous section of the extension curve is larger than 8 nm. In order to detect the events:

1. Call the function "Select events/Find NHN or NRN events".
2. Select "Naive"
3. minimum δZ: 0.008 um
4. Averaging length before/after: 2
5. select "click here if you expect only two states"
6. If no event was recorded previously, select "Click here to not check existing events".

In order to draw all times spent in the open and closed states:

1. Call the function "Select events/Statistics on discrete events".
2. Select "Draw distribution of times between successive steps of opposite signs only (two level)"
3. Select "Average time between the two events"
4. Unselect "Do I have to sort the events by starting time ?"

C.5.8 Parameter inference from kinetic locking experiments

Times spent in the open state T_{open} correspond to the difference between the detected times of two successive opening and closing events. Times spent in the closed state T_{closed} correspond to the difference between the detected times of two successive closing and opening events. Average times $\overline{T_{open/closed}}$ correspond to naive mean values. Errors are computed using bootstrap resampling. All averages of the hairpin closing and opening times are performed on samples containing at least 4000 independent events. In the case of concentration-dependent double-exponential distributions, the times are fitted to the exact formula provided in the main text with the SciPy [Virtanen et al., 2020] curvefit function. A single fit is used for all concentrations. Errors on the fit are computed based on bootstrap resampling : 100 samples of the same size as the original data sample are generated by resampling the original data with replacement. The fitting procedure is then applied to all samples, returning a distribution of inferred kinetic parameters. The values shown in the article correspond to the averages of these distributions while the errors correspond to their standard deviations. The proportion of long times in the double-exponential distribution is then verified with a binning-free expectation maximization (EM) algorithm based on the Pomegranate [Schreiber, 2017] Python module. All data analysis procedures can be found at https://github.com/Mriv31/kineticlocking.

C.5.9 Noise density computation

The spectral density of the noise presented in this paper are computed with the following normalization. A signal consisting of N points acquired x_j at f_{aq} is decomposed by Discrete Fourier Transform:

$$\hat{X}_k = \sum_{j=0}^{N-1} x_j e^{\frac{-i2\pi jk}{N}}$$

We recall that the DFT verifies the Plancherel theorem:

$$\sum_{j=0}^{N-1} x_j^2 = \frac{1}{N} \sum_{j=0}^{N-1} |\hat{X}_j|^2$$

The power spectrum is then computed as

$$P_k = \frac{|\hat{X}_k|^2}{N f_{aq}}$$

Let us note that the integral of this density over all frequencies, reads:

$$\int_0^{f_{aq}} P(f)\mathrm{d}f \sim \frac{f_{aq}}{N} \sum_{k=0}^{N-1} P_k \tag{C.1}$$

$$= \frac{f_{aq}}{N} \sum_{k=0}^{N-1} \frac{|\hat{X}_k|^2}{N f_{aq}} \tag{C.2}$$

$$= \frac{1}{N^2} \sum_{k=0}^{N-1} |\hat{X}_k|^2 \tag{C.3}$$

$$= \frac{1}{N} \sum_{k=0}^{N-1} x_k^2 \tag{C.4}$$

$$= \sigma_x^2 \tag{C.5}$$

This normalization is common [Berg-Sørensen and Flyvbjerg, 2004] but it is important to note that an other common normalization is:

$$P'_k = \mathbf{2}\frac{|\hat{X}_k|^2}{N f_{aq}}$$

, such as

$$\int_0^{\frac{f_{aq}}{\mathbf{2}}} P(f)\mathrm{d}f = \sigma_x^2$$

With **our** normalization, the spectrum of a Brownian bead reads [Berg-Sørensen and Flyvbjerg, 2004]:

$$P(f) = \frac{k_B T}{2\pi^2 \gamma (f^2 + f_c^2)},$$

where $f_c = \frac{k}{2\pi\gamma}$.

C.6 DNA sequences

DNA sequences that are relevant for the main results of this work are presented here. DNA constructs and other sequences can be found at http://www.normalesup.org/~mrieu/images/All_seq_MR.xls.

DNA name (cf. Material and methods)	Sequence
HP3 (stacking assay)	5' GTCTTCTTCTGTCTAATCCTTCACCGTGTCTTTTGGTCTTTCTGGTGCTCTTCGAATACTGCCAGAGTTTTCTCTGGC AGTGCGTGCTCGCAGTGACCGGCGCTATTAGCTTCCATACCAGCTGGCAACATCCATCATGATCCGCTACTCCCA 3'
Oliblock-half-stack	5' ACTGCCAGAGAAAACT 3'
Oliblock-full-stack	5' GCACGCACTGCCAGAGAAAACT 3'
HP1 (fluctuation assay)	5' GTCTTCTTCTGTCTAATCCTTCACCGTGTCTTTTGGTCTTTCTGGTGCTCTTCGAATTTTTTTTACTGCCAGAGTTT TCTCTGGCAGTGCGTGCTCGCAGTGACCGGCGCTATTAGCTTCCATACCAGCTGGCAACATCCATCATGATCCGCTACTCCCA 3'
HP 2 : Probe without SS PAD (fluctuation assay)	5' GTCTTCTTCTGTCTAATCCTTCACCGTGTCTTTTGGTCTTTCTGGTGCTCTTCGAATACTGCCAGAGTTT TCTCTGGCAGTACCGGCGCTATTAGCTTCCATACCAGCTGGCAACATCCATCATGATCCGCTACTCCCA 3'
HP30 (UPF1)	5' GTCTTCTTCTGTCTAATCCTTCACCGTGTCTTTTGGTCTTTCTGGTGCTCTTCGAATTTTTTTTCGTAGTGAGACCTGTGAGCTACTGCCAGAGTTTTC TCTGGCAGTAGCTCACAGGTCTCACTACGTTTTTTTTTTTTTTACCGGCGCTATTAGCTTCCATACCAGCTGGCAACATCCATCATGATCCGCTACTCCCA 3'
SDI-oligo-8bp	CACTGCGA

C.7 Buffers

Passivation buffer: 140 mM NaCl, 3 mM KCl, 10 mM Na2HPO4, 1.76 mM KH2PO4, BSA 2%, Pluronic F-127 2%, 5mM EDTA, 10 mM NaN3, pH 7.4
Hybridization Buffer 1 (HB1): 100mM Nacl, 40mM Tris-Hcl pH 7.6
Hybridization buffer 2 (HB2): 20 mM Tris-Hcl pH 7.6, 3mM MgCl2, 100 mM KCl
RecQ buffer: 20 mM Tris-Hcl pH 7.6, 3mM MgCl2, 50 mM NaCl
Upf1 buffer: 100mM KCl, 3mM MgCl2, 40 mM Tris-Hcl pH 7.6
SMARCAL buffer: 40mM HEPES pH 7.6, 20mM KCl, 5mM MgCl2, 1mM ATP, 1mM TCEP, 100 ug/mL BSA
ZranB3 buffer: 40mM Tris pH 7.5, 100 KCl, 5mM MgCl2, 1mM ATP, 100 ug/mL BSA
HLTF buffer: 40mM Tris pH 7.6, 50mM NaCl, 5mM MgCl2, 1mM ATP, 1mM TCEP, 100 ug/mL BSA

Appendix D

Bibliography

[Abbondanzieri et al., 2005] Abbondanzieri, E., Greenleaf, W., Shaevitz, J., Landick, R., and Block, S. (2005). Direct observation of base-pair stepping by RNA polymerase. *Nature*, 438(7067):460–465.

[Adachi et al., 2007] Adachi, K., Oiwa, K., Nishizaka, T., Furuike, S., Noji, H., Itoh, H., Yoshida, M., and Kinosita Jr, K. (2007). Coupling of rotation and catalysis in F1-ATPase revealed by single-molecule imaging and manipulation. *Cell*, 130(2):309–321.

[Adachi et al., 2000] Adachi, K., Yasuda, R., Noji, H., Itoh, H., Harada, Y., Yoshida, M., and Kinosita, K. (2000). Stepping rotation of F1-ATPase visualized through angle-resolved single-fluorophore imaging. *Proceedings of the National Academy of Sciences*, 97(13):7243–7247.

[Allawi and SantaLucia, 1997] Allawi, H. T. and SantaLucia, J. (1997). Thermodynamics and NMR of internal G T mismatches in DNA. *Biochemistry*, 36(34):10581–10594.

[Allemand, 1997] Allemand, J.-F. (1997). *Micro-manipulations de molécules d'adn isolées*. PhD thesis, Paris 6.

[Andrecka et al., 2016] Andrecka, J., Takagi, Y., Mickolajczyk, K., Lippert, L., Sellers, J., Hancock, W., Goldman, Y., and Kukura, P. (2016). Interferometric scattering microscopy for the study of molecular motors. In *Methods in enzymology*, volume 581, pages 517–539. Elsevier.

[Ashkin, 1997] Ashkin, A. (1997). Optical trapping and manipulation of neutral particles using lasers. *Proceedings of the National Academy of Sciences*, 94(10):4853–4860.

[Avci-Adali et al., 2010] Avci-Adali, M., Paul, A., Wilhelm, N., Ziemer, G., and Wendel, H. P. (2010). Upgrading SELEX Technology by Using Lambda Exonuclease Digestion for Single-Stranded DNA Generation. *Molecules*, 15(1):1. Publisher: Multidisciplinary Digital Publishing Institute (MDPI).

[Bachrati and Hickson, 2008] Bachrati, C. Z. and Hickson, I. D. (2008). RecQ helicases: guardian angels of the DNA replication fork. *Chromosoma*, 117(3):219–233.

[Baddeley et al., 2011] Baddeley, D., Cannell, M. B., and Soeller, C. (2011). Three-dimensional sub-100 nm super-resolution imaging of biological samples using a phase ramp in the objective pupil. *Nano Research*, 4(6):589–598.

[Bagchi et al., 2018] Bagchi, D., Manosas, M., Zhang, W., Manthei, K. A., Hodeib, S., Ducos, B., Keck, J. L., and Croquette, V. (2018). Single molecule kinetics uncover roles for E. coli RecQ DNA helicase domains and interaction with SSB. *Nucleic Acids Research*, 46(16):8500–8515.

[Berg-Sørensen and Flyvbjerg, 2004] Berg-Sørensen, K. and Flyvbjerg, H. (2004). Power spectrum analysis for optical tweezers. *Review of Scientific Instruments*, 75(3):594–612. Publisher: American Institute of Physics.

[Bernstein and Keck, 2005] Bernstein, D. A. and Keck, J. L. (2005). Conferring substrate specificity to DNA helicases: role of the RecQ HRDC domain. *Structure*, 13(8):1173–1182. Publisher: Elsevier.

[Bernstein et al., 2010] Bernstein, K. A., Gangloff, S., and Rothstein, R. (2010). The RecQ DNA helicases in DNA repair. *Annual review of genetics*, 44:393–417.

[Betzig et al., 2006] Betzig, E., Patterson, G. H., Sougrat, R., Lindwasser, O. W., Olenych, S., Bonifacino, J. S., Davidson, M. W., Lippincott-Schwartz, J., and Hess, H. F. (2006). Imaging intracellular fluorescent proteins at nanometer resolution. *Science*, 313(5793):1642–1645.

[Block et al., 1990] Block, S. M., Goldstein, L. S., and Schnapp, B. J. (1990). Bead movement by single kinesin molecules studied with optical tweezers. *Nature*, 348(6299):348–352.

[Bohren and Huffman, 1983] Bohren, C. F. and Huffman, D. R. (1983). *Absorption and scattering of light by small particles*. John Wiley & Sons.

[Bon et al., 2018] Bon, P., Linares-Loyez, J., Feyeux, M., Alessandri, K., Lounis, B., Nassoy, P., and Cognet, L. (2018). Self-interference 3D super-resolution microscopy for deep tissue investigations. *Nature methods*, 15(6):449–454. Publisher: Nature Publishing Group.

[Bouchiat et al., 1999] Bouchiat, C., Wang, M. D., Allemand, J.-F., Strick, T., Block, S., and Croquette, V. (1999). Estimating the persistence length of a worm-like chain molecule from force-extension measurements. *Biophysical journal*, 76(1):409–413.

[Brennan et al., 1987] Brennan, C. A., Dombroski, A. J., and Platt, T. (1987). Transcription termination factor rho is an RNA-dna helicase. *Cell*, 48(6):945–952.

[Brenner, 1961] Brenner, H. (1961). The slow motion of a sphere through a viscous fluid towards a plane surface. *Chemical engineering science*, 16(3-4):242–251. Publisher: Pergamon.

[Brent, 1971] Brent, R. P. (1971). An algorithm with guaranteed convergence for finding a zero of a function. *The Computer Journal*, 14(4):422–425.

[Brown and Twiss, 1956] Brown, R. H. and Twiss, R. Q. (1956). Correlation between photons in two coherent beams of light. *Nature*, 177(4497):27–29.

[Brun-Cosme-Bruny, 2019] Brun-Cosme-Bruny, M. (2019). *Swimming of active suspensions in a crowded environment*. Theses, Université Grenoble Alpes. Issue: 2019GREAY045.

[Caldwell and Spies, 2017] Caldwell, C. C. and Spies, M. (2017). Helicase SPRNTing through the nanopore. *Proceedings of the National Academy of Sciences*, 114(45):11809–11811.

[Charvin et al., 2005] Charvin, G., Strick, T., Bensimon, D., and Croquette, V. (2005). Tracking topoisomerase activity at the single-molecule level. *Annu. Rev. Biophys. Biomol. Struct.*, 34:201–219.

[Cheng et al., 2011] Cheng, W., Arunajadai, S. G., Moffitt, J. R., Tinoco, I., and Bustamante, C. (2011). Single-Base Pair Unwinding and Asynchronous RNA Release by the Hepatitis C Virus NS3 Helicase. *Science*, 333(6050):1746–1749.

[Clarke et al., 2009] Clarke, J., Wu, H.-C., Jayasinghe, L., Patel, A., Reid, S., and Bayley, H. (2009). Continuous base identification for single-molecule nanopore DNA sequencing. *Nature nanotechnology*, 4(4):265–270.

[Cobb et al., 2003] Cobb, J. A., Bjergbaek, L., Shimada, K., Frei, C., and Gasser, S. M. (2003). DNA polymerase stabilization at stalled replication forks requires Mec1 and the RecQ helicase Sgs1. *The EMBO journal*, 22(16):4325–4336.

[Cock et al., 2009] Cock, P. J., Antao, T., Chang, J. T., Chapman, B. A., Cox, C. J., Dalke, A., Friedberg, I., Hamelryck, T., Kauff, F., and Wilczynski, B. (2009). Biopython: freely available Python tools for computational molecular biology and bioinformatics. *Bioinformatics*, 25(11):1422–1423.

[Cognet et al., 2008] Cognet, L., Tsyboulski, D. A., and Weisman, R. B. (2008). Subdiffraction far-field imaging of luminescent single-walled carbon nanotubes. *Nano letters*, 8(2):749–753.

[Comstock et al., 2015] Comstock, M. J., Whitley, K. D., Jia, H., Sokoloski, J., Lohman, T. M., Ha, T., and Chemla, Y. R. (2015). Direct observation of structure-function relationship in a nucleic acid–processing enzyme. *Science*, 348(6232):352–354.

[Cordin and Beggs, 2013] Cordin, O. and Beggs, J. D. (2013). RNA helicases in splicing. *RNA biology*, 10(1):83–95.

[Craig et al., 2017] Craig, J. M., Laszlo, A. H., Brinkerhoff, H. D., Derrington, I. M., Noakes, M., Nova, I. C., Doering, K. M., Tickman, B. I., Leeuw, N. F. D., and Gundlach, J. H. (2017). Direct Single Molecule Measurement of ATP Hydrolysis Substates in Hel308 DNA Helicase using Nanopore Tweezers. *Biophysical Journal*, 112(3):169a.

[Craig et al., 2019] Craig, J. M., Laszlo, A. H., Nova, I. C., Brinkerhoff, H., Noakes, M. T., Baker, K. S., Bowman, J. L., Higinbotham, H. R., Mount, J. W., and Gundlach, J. H. (2019). Determining the effects of DNA sequence on Hel308 helicase translocation along single-stranded DNA using nanopore tweezers. *Nucleic acids research*, 47(5):2506–2513. Publisher: Oxford University Press.

[Croteau et al., 2012] Croteau, D. L., Singh, D. K., Ferrarelli, L. H., Lu, H., and Bohr, V. A. (2012). RECQL4 in genomic instability and aging. *Trends in Genetics*, 28(12):624–631. Publisher: Elsevier.

[Daldrop et al., 2015] Daldrop, P., Brutzer, H., Huhle, A., Kauert, D. J., and Seidel, R. (2015). Extending the range for force calibration in magnetic tweezers. *Biophysical journal*, 108(10):2550–2561.

[Davies et al., 2007] Davies, S. L., North, P. S., and Hickson, I. D. (2007). Role for BLM in replication-fork restart and suppression of origin firing after replicative stress. *Nature Structural & Molecular Biology*, 14(7):677–679.

[De Vlaminck and Dekker, 2012] De Vlaminck, I. and Dekker, C. (2012). Recent advances in magnetic tweezers. *Annual review of biophysics*, 41:453–472.

[Dekker, 2007] Dekker, C. (2007). Solid-state nanopores. *Nature nanotechnology*, 2(4):209–215.

[Dekker et al., 2002] Dekker, N., Rybenkov, V., Duguet, M., Crisona, N., Cozzarelli, N., Bensimon, D., and Croquette, V. (2002). The mechanism of type ia topoisomerases. *Proceedings of the National Academy of Sciences*, 99(19):12126–12131.

[Dessinges et al., 2004] Dessinges, M.-N., Lionnet, T., Xi, X. G., Bensimon, D., and Croquette, V. (2004). Single-molecule assay reveals strand switching and enhanced processivity of uvrd. *Proceedings of the National Academy of Sciences*, 101(17):6439–6444.

[Ding et al., 2012] Ding, F., Manosas, M., Spiering, M. M., Benkovic, S. J., Bensimon, D., Allemand, J.-F., and Croquette, V. (2012). Single-molecule mechanical identification and sequencing. *Nature Methods*, 9(4):367–372.

[Dulin et al., 2017] Dulin, D., Arnold, J. J., van Laar, T., Oh, H.-S., Lee, C., Perkins, A. L., Harki, D. A., Depken, M., Cameron, C. E., and Dekker, N. H. (2017). Signatures of nucleotide analog incorporation by an RNA-dependent RNA polymerase revealed using high-throughput magnetic tweezers. *Cell reports*, 21(4):1063–1076.

[Dulin et al., 2015a] Dulin, D., Cui, T. J., Cnossen, J., Docter, M. W., Lipfert, J., and Dekker, N. H. (2015a). High Spatiotemporal-Resolution Magnetic Tweezers: Calibration and Applications for DNA Dynamics. *Biophysical Journal*, 109(10):2113–2125.

[Dulin et al., 2015b] Dulin, D., Vilfan, I. D., Berghuis, B. A., Hage, S., Bamford, D. H., Poranen, M. M., Depken, M., and Dekker, N. H. (2015b). Elongation-competent pauses govern the fidelity of a viral RNA-dependent RNA polymerase. *Cell reports*, 10(6):983–992.

[Dulin et al., 2015c] Dulin, D., Vilfan, I. D., Berghuis, B. A., Poranen, M. M., Depken, M., and Dekker, N. H. (2015c). Backtracking behavior in viral RNA-dependent RNA polymerase provides the basis for a second initiation site. *Nucleic acids research*, 43(21):10421–10429.

[Eaton and West, 2010] Eaton, P. and West, P. (2010). *Atomic force microscopy*. Oxford university press.

[Edwards et al., 2017] Edwards, D. T., Faulk, J. K., LeBlanc, M.-A., and Perkins, T. T. (2017). Force Spectroscopy with 9-μs Resolution and Sub-pN Stability by Tailoring AFM Cantilever Geometry. *Biophysical Journal*, 113(12):2595–2600. Publisher: Elsevier.

[Edwards et al., 2015] Edwards, D. T., Faulk, J. K., Sanders, A. W., Bull, M. S., Walder, R., LeBlanc, M.-A., Sousa, M. C., and Perkins, T. T. (2015). Optimizing 1-μs-Resolution Single-Molecule Force Spectroscopy on a Commercial Atomic Force Microscope. *Nano Letters*, 15(10):7091–7098. Publisher: American Chemical Society.

[Espelund et al., 1990] Espelund, M., Stacy, R. A., and Jakobsen, K. S. (1990). A simple method for generating single-stranded DNA probes labeled to high activities. *Nucleic Acids Research*, 18(20):6157. Publisher: Oxford University Press.

[Faxén, 1922] Faxén, H. (1922). Der Widerstand gegen die Bewegung einer starren Kugel in einer zähen Flüssigkeit, die zwischen zwei parallelen ebenen Wänden eingeschlossen ist. *Annalen der Physik*, 373(10):89–119. _eprint: https://onlinelibrary.wiley.com/doi/pdf/10.1002/andp.19223731003.

[Fazal and Block, 2011] Fazal, F. M. and Block, S. M. (2011). Optical tweezers study life under tension. *Nature photonics*, 5(6):318–321.

[Finer et al., 1994] Finer, J. T., Simmons, R. M., and Spudich, J. A. (1994). Single myosin molecule mechanics: piconewton forces and nanometre steps. *Nature*, 368(6467):113–119.

[Fiorini et al., 2015] Fiorini, F., Bagchi, D., Le Hir, H., and Croquette, V. (2015). Human Upf1 is a highly processive RNA helicase and translocase with RNP remodelling activities. *Nature communications*, 6(1):1–10. Publisher: Nature Publishing Group.

[Förster, 1948] Förster, T. (1948). Zwischenmolekulare energiewanderung und fluoreszenz. *Annalen der physik*, 437(1-2):55–75.

[Förster, 1982] Förster, T. (1982). *Fluoreszenz organischer verbindungen*. Vandenhoeck & Ruprecht.

[Giannone et al., 2013] Giannone, G., Hosy, E., Sibarita, J.-B., Choquet, D., and Cognet, L. (2013). High-content super-resolution imaging of live cell by upaint. In *Nanoimaging*, pages 95–110. Springer.

[Godin et al., 2014] Godin, A. G., Lounis, B., and Cognet, L. (2014). Super-resolution microscopy approaches for live cell imaging. *Biophysical journal*, 107(8):1777–1784.

[Goldman et al., 1967] Goldman, A. J., Cox, R. G., and Brenner, H. (1967). Slow viscous motion of a sphere parallel to a plane wall—I Motion through a quiescent fluid. *Chemical Engineering Science*, 22(4):637–651.

[Gopich and Szabo, 2007] Gopich, I. V. and Szabo, A. (2007). Single-molecule FRET with diffusion and conformational dynamics. *The Journal of Physical Chemistry B*, 111(44):12925–12932. Publisher: ACS Publications.

[Gosse and Croquette, 2002] Gosse, C. and Croquette, V. (2002). Magnetic Tweezers: Micromanipulation and Force Measurement at the Molecular Level. *Biophysical Journal*, 82(6):3314–3329.

[Ha, 2001] Ha, T. (2001). Single-molecule fluorescence resonance energy transfer. *Methods*, 25(1):78–86.

[Haber, 1999] Haber, J. E. (1999). DNA recombination: the replication connection. *Trends in biochemical sciences*, 24(7):271–275.

[Harami et al., 2015] Harami, G. M., Nagy, N. T., Martina, M., Neuman, K. C., and Kovács, M. (2015). The HRDC domain of E. coli RecQ helicase controls single-stranded DNA translocation and double-stranded DNA unwinding rates without affecting mechanoenzymatic coupling. *Scientific Reports*, 5(1):11091.

[Harms et al., 2001] Harms, G. S., Cognet, L., Lommerse, P. H., Blab, G. A., and Schmidt, T. (2001). Autofluorescent proteins in single-molecule research: applications to live cell imaging microscopy. *Biophysical journal*, 80(5):2396–2408.

[Harris, 1978] Harris, F. J. (1978). On the use of windows for harmonic analysis with the discrete fourier transform. *Proceedings of the IEEE*, 66(1):51–83.

[Hecht, 2002] Hecht, E. (2002). *Optics*. Addison-Wesley. Google-Books-ID: 7aG6QgAACAAJ.

[Heiat et al., 2017] Heiat, M., Ranjbar, R., Latifi, A. M., Rasaee, M. J., and Farnoosh, G. (2017). Essential strategies to optimize asymmetric PCR conditions as a reliable method to generate large amount of ssdna aptamers. *Biotechnology and applied biochemistry*, 64(4):541–548.

[Hinterdorfer and Dufrêne, 2006] Hinterdorfer, P. and Dufrêne, Y. F. (2006). Detection and localization of single molecular recognition events using atomic force microscopy. *Nature methods*, 3(5):347–355.

[Hirono-Hara et al., 2001] Hirono-Hara, Y., Noji, H., Nishiura, M., Muneyuki, E., Hara, K. Y., Yasuda, R., Kinosita, K., and Yoshida, M. (2001). Pause and rotation of F1-ATPase during catalysis. *Proceedings of the National Academy of Sciences*, 98(24):13649–13654.

[Hishida et al., 2004] Hishida, T., Han, Y.-W., Shibata, T., Kubota, Y., Ishino, Y., Iwasaki, H., and Shinagawa, H. (2004). Role of the Escherichia coli RecQ DNA helicase in SOS signaling and genome stabilization at stalled replication forks. *Genes & development*, 18(15):1886–1897. Publisher: Cold Spring Harbor Lab.

[Hodeib, 2017] Hodeib, S. (2017). *Real-time unfolding of DNA G-quadruplexes by helicases and polymerases*. PhD thesis.

[Hodeib et al., 2016] Hodeib, S., Raj, S., Manosas, M., Zhang, W., Bagchi, D., Ducos, B., Allemand, J.-F., Bensimon, D., and Croquette, V. (2016). Single molecule studies of helicases with magnetic tweezers. *Methods*, 105:3–15. Publisher: Elsevier.

[Huang et al., 2008] Huang, B., Wang, W., Bates, M., and Zhuang, X. (2008). Three-dimensional super-resolution imaging by stochastic optical reconstruction microscopy. *Science (New York, N.Y.)*, 319(5864):810–813.

[Huhle et al., 2015] Huhle, A., Klaue, D., Brutzer, H., Daldrop, P., Joo, S., Otto, O., Keyser, U. F., and Seidel, R. (2015). Camera-based three-dimensional real-time particle tracking at kHz rates and Ångström accuracy. *Nature communications*, 6(1):1–8. Publisher: Nature Publishing Group.

[Itoh et al., 2004] Itoh, H., Takahashi, A., Adachi, K., Noji, H., Yasuda, R., Yoshida, M., and Kinosita, K. (2004). Mechanically driven ATP synthesis by F1-ATPase. *Nature*, 427(6973):465–468.

[Jackson et al., 2018] Jackson, D. P., Ferris, N., Strauss, R., Li, H., and Pearson, B. J. (2018). Subtleties with Young's double-slit experiment: Investigation of spatial coherence and fringe visibility. *American Journal of Physics*, 86(9):683–689. Publisher: American Association of Physics Teachers.

[Jacobson et al., 2020] Jacobson, D. R., Uyetake, L., and Perkins, T. T. (2020). Membrane-Protein Unfolding Intermediates Detected with Enhanced Precision Using a Zigzag Force Ramp. *Biophysical Journal*, 118(3):667–675.

[Janssen et al., 2009] Janssen, X., Schellekens, A., van Ommering, K., van IJzendoorn, L., and Prins, M. (2009). Controlled torque on superparamagnetic beads for functional biosensors. *Biosensors and Bioelectronics*, 24(7):1937 – 1941.

[Jeandet, 2018] Jeandet, A. (2018). Window function. `ftp://ftp.lpp.polytechnique.fr/jeandet/keep/sync/fftw/Window%20function.pdf`. Accessed: 2020-12-10.

[Jeffery, 1915] Jeffery, G. B. (1915). On the Steady Rotation of a Solid of Revolution in a Viscous Fluid. *Proceedings of the London Mathematical Society*, s2_14(1):327–338. _eprint: https://londmathsoc.onlinelibrary.wiley.com/doi/pdf/10.1112/plms/s2_14.1.327.

[Jia et al., 2014] Jia, S., Vaughan, J. C., and Zhuang, X. (2014). Isotropic 3D Super-resolution Imaging with a Self-bending Point Spread Function. *Nature Photonics*, 8:302–306.

[Jia et al., 1996] Jia, Y., Kumar, A., and Patel, S. S. (1996). Equilibrium and stopped-flow kinetic studies of interaction between T7 RNA polymerase and its promoters measured by protein and 2-aminopurine fluorescence changes. *The Journal of Biological Chemistry*, 271(48):30451–30458.

[Johnson et al., 2007] Johnson, D. S., Bai, L., Smith, B. Y., Patel, S. S., and Wang, M. D. (2007). Single-molecule studies reveal dynamics of DNA unwinding by the ring-shaped t7 helicase. *Cell*, 129(7):1299–1309.

[Kam et al., 1999] Kam, V., Moseyko, N., Nemson, J., and Feldman, L. J. (1999). Gravitaxis in Chlamydomonas reinhardtii: Characterization using Video Microscopy and Computer Analysis. *International Journal of Plant Sciences*, 160(6):1093–1098. Publisher: The University of Chicago Press.

[Kanaan et al., 2018] Kanaan, J., Raj, S., Decourty, L., Saveanu, C., Croquette, V., and Le Hir, H. (2018). UPF1-like helicase grip on nucleic acids dictates processivity. *Nature communications*, 9(1):1–9. Publisher: Nature Publishing Group.

[Kantsler et al., 2013] Kantsler, V., Dunkel, J., Polin, M., and Goldstein, R. E. (2013). Ciliary contact interactions dominate surface scattering of swimming eukaryotes. *Proceedings of the National Academy of Sciences*, 110(4):1187–1192. Publisher: National Acad Sciences.

[Kao and Verkman, 1994] Kao, H. P. and Verkman, A. S. (1994). Tracking of single fluorescent particles in three dimensions: use of cylindrical optics to encode particle position. *Biophysical Journal*, 67(3):1291–1300.

[Kato-Yamada et al., 1998] Kato-Yamada, Y., Noji, H., Yasuda, R., Kinosita, K., and Yoshida, M. (1998). Direct observation of the rotation of ε subunit in F1-ATPase. *Journal of Biological Chemistry*, 273(31):19375–19377.

[Kim and Saleh, 2009] Kim, K. and Saleh, O. A. (2009). A high-resolution magnetic tweezer for single-molecule measurements. *Nucleic Acids Research*, 37(20):e136–e136.

[King et al., 2019] King, G. A., Burla, F., Peterman, E. J., and Wuite, G. J. (2019). Supercoiling DNA optically. *Proceedings of the National Academy of Sciences*, 116(52):26534–26539.

[Kitao et al., 1998] Kitao, S., Ohsugi, I., Ichikawa, K., Goto, M., Furuichi, Y., and Shimamoto, A. (1998). Cloning of two new human helicase genes of the RecQ family: biological significance of multiple species in higher eukaryotes. *Genomics*, 54(3):443–452. Publisher: Elsevier.

[Klaue et al., 2013] Klaue, D., Kobbe, D., Kemmerich, F., Kozikowska, A., Puchta, H., and Seidel, R. (2013). Fork sensing and strand switching control antagonistic activities of RecQ helicases. *Nature Communications*, 4(1):2024.

[Klaue and Seidel, 2009a] Klaue, D. and Seidel, R. (2009a). Torsional stiffness of single superparamagnetic microspheres in an external magnetic field. *Physical review letters*, 102(2):028302. Publisher: APS.

[Klaue and Seidel, 2009b] Klaue, D. and Seidel, R. (2009b). Torsional stiffness of single superparamagnetic microspheres in an external magnetic field. *Physical review letters*, 102(2):028302.

[Koch et al., 2002] Koch, S. J., Shundrovsky, A., Jantzen, B. C., and Wang, M. D. (2002). Probing protein-DNA interactions by unzipping a single DNA double helix. *Biophysical journal*, 83(2):1098–1105. Publisher: Elsevier.

[Kocsis et al., 2014] Kocsis, Z. S., Sarlós, K., Harami, G. M., Martina, M., and Kovács, M. (2014). A Nucleotide-dependent and HRDC Domain-dependent Structural Transition in DNA-bound RecQ Helicase. *The Journal of Biological Chemistry*, 289(9):5938–5949.

[Kornberg and Baker, 2005] Kornberg, A. and Baker, T. A. (2005). *DNA Replication*. University Science Books.

[Koster et al., 2005] Koster, D. A., Croquette, V., Dekker, C., Shuman, S., and Dekker, N. H. (2005). Friction and torque govern the relaxation of DNA supercoils by eukaryotic topoisomerase ib. *Nature*, 434(7033):671–674.

[Kostrz et al., 2019] Kostrz, D., Wayment-Steele, H. K., Wang, J. L., Follenfant, M., Pande, V. S., Strick, T. R., and Gosse, C. (2019). A modular DNA scaffold to study protein–protein interactions at single-molecule resolution. *Nature nanotechnology*, 14(10):988–993. Publisher: Nature Publishing Group.

[Kowalczykowski, 2015] Kowalczykowski, S. C. (2015). An overview of the molecular mechanisms of recombinational DNA repair. *Cold Spring Harbor Perspectives in Biology*, 7(11):a016410.

[Lansdorp and Saleh, 2012] Lansdorp, B. M. and Saleh, O. A. (2012). Power spectrum and Allan variance methods for calibrating single-molecule video-tracking instruments. *The Review of Scientific Instruments*, 83(2).

[Lansdorp et al., 2013] Lansdorp, B. M., Tabrizi, S. J., Dittmore, A., and Saleh, O. A. (2013). A high-speed magnetic tweezer beyond 10,000 frames per second. *Review of Scientific Instruments*, 84(4):044301.

[Laszlo et al., 2016] Laszlo, A. H., Derrington, I. M., and Gundlach, J. H. (2016). MspA nanopore as a single-molecule tool: From sequencing to SPRNT. *Methods (San Diego, Calif.)*, 105:75–89.

[Laszlo et al., 2017] Laszlo, A. H., Derrrington, I. M., and Gundlach, J. H. (2017). Subangstrom measurements of enzyme function using a biological nanopore, SPRNT. In *Methods in enzymology*, volume 582, pages 387–414. Elsevier.

[Li, 2008] Li, G.-M. (2008). Mechanisms and functions of DNA mismatch repair. *Cell research*, 18(1):85–98.

[Li et al., 2013] Li, W., Hou, X.-M., Wang, P.-Y., Xi, X.-G., and Li, M. (2013). Direct measurement of sequential folding pathway and energy landscape of human telomeric g-quadruplex structures. *Journal of the American Chemical Society*, 135(17):6423–6426.

[Li et al., 2007] Li, Y., Augustine, G. J., and Weninger, K. (2007). Kinetics of complexin binding to the SNARE complex: correcting single molecule FRET measurements for hidden events. *Biophysical journal*, 93(6):2178–2187. Publisher: Elsevier.

[Li et al., 2009] Li, Y., Zhao, J., Su, X., Zhu, Y., Wang, Y., Tang, L., and Wang, Z. (2009). A facile aqueous phase synthesis of cobalt microspheres at room temperature. *Colloids and Surfaces A: Physicochemical and Engineering Aspects*, 336(1-3):41–45.

[Lin et al., 2017] Lin, W., Ma, J., Nong, D., Xu, C., Zhang, B., Li, J., Jia, Q., Dou, S., Ye, F., Xi, X., et al. (2017). Helicase stepping investigated with one-nucleotide resolution fluorescence resonance energy transfer. *Physical review letters*, 119(13):138102.

[Lionnet et al., 2007] Lionnet, T., Spiering, M. M., Benkovic, S. J., Bensimon, D., and Croquette, V. (2007). Real-time observation of bacteriophage T4 gp41 helicase reveals an unwinding mechanism. *Proceedings of the National Academy of Sciences*, 104(50):19790–19795.

[Lipfert et al., 2009] Lipfert, J., Koster, D. A., Vilfan, I. D., Hage, S., and Dekker, N. H. (2009). Single-molecule magnetic tweezers studies of type ib topoisomerases. In *DNA Topoisomerases*, pages 71–89. Springer.

[Liu et al., 2020] Liu, N.-N., Ji, L., Guo, Q., Dai, Y.-X., Wu, W.-Q., Guo, H.-L., Lu, K.-Y., Li, X.-M., and Xi, X.-G. (2020). Quantitative and real-time measurement of helicase-mediated intra-stranded G4 unfolding in bulk fluorescence stopped-flow assays. *Analytical and Bioanalytical Chemistry*.

[Lu et al., 2013] Lu, X., Parvathaneni, S., Hara, T., Lal, A., and Sharma, S. (2013). Replication stress induces specific enrichment of RECQ1 at common fragile sites FRA3B and FRA16D. *Molecular Cancer*, 12(1):29.

[Maier et al., 2000] Maier, B., Bensimon, D., and Croquette, V. (2000). Replication by a single DNA polymerase of a stretched single-stranded dna. *Proceedings of the National Academy of Sciences*, 97(22):12002–12007.

[Manosas et al., 2010] Manosas, M., Meglio, A., Spiering, M. M., Ding, F., Benkovic, S. J., Barre, F.-X., Saleh, O. A., Allemand, J. F., Bensimon, D., and Croquette, V. (2010). Magnetic tweezers for the study of DNA tracking motors. In *Methods in enzymology*, volume 475, pages 297–320. Elsevier.

[Manosas et al., 2013] Manosas, M., Perumal, S. K., Bianco, P. R., Ritort, F., Benkovic, S. J., and Croquette, V. (2013). RecG and UvsW catalyse robust DNA rewinding critical for stalled DNA replication fork rescue. *Nature communications*, 4(1):1–12.

[Manosas et al., 2012a] Manosas, M., Spiering, M. M., Ding, F., Bensimon, D., Allemand, J.-F., Benkovic, S. J., and Croquette, V. (2012a). Mechanism of strand displacement synthesis by DNA replicative polymerases. *Nucleic acids research*, 40(13):6174–6186.

[Manosas et al., 2012b] Manosas, M., Spiering, M. M., Ding, F., Croquette, V., and Benkovic, S. J. (2012b). Collaborative coupling between polymerase and helicase for leading-strand synthesis. *Nucleic acids research*, 40(13):6187–6198.

[Manrao et al., 2012] Manrao, E. A., Derrington, I. M., Laszlo, A. H., Langford, K. W., Hopper, M. K., Gillgren, N., Pavlenok, M., Niederweis, M., and Gundlach, J. H. (2012). Reading DNA at single-nucleotide resolution with a mutant MspA nanopore and phi29 DNA polymerase. *Nature Biotechnology*, 30(4):349–353. Number: 4 Publisher: Nature Publishing Group.

[Marko and Siggia, 1995] Marko, J. F. and Siggia, E. D. (1995). Stretching dna. *Macromolecules*, 28(26):8759–8770.

[Menssen and Tokmakoff, 2019] Menssen, R. J. and Tokmakoff, A. (2019). Length-dependent melting kinetics of short DNA oligonucleotides using Temperature-Jump IR spectroscopy. *The Journal of Physical Chemistry B*, 123(4):756–767. Publisher: ACS Publications.

[Mickolajczyk et al., 2020] Mickolajczyk, K. J., Shelton, P. M., Grasso, M., Cao, X., Warrington, S. R., Aher, A., Liu, S., and Kapoor, T. M. (2020). Force-dependent stimulation of RNA unwinding by SARS-CoV-2 nsp13 helicase. *bioRxiv*.

[Miller et al., 2017] Miller, H., Zhou, Z., Shepherd, J., Wollman, A. J., and Leake, M. C. (2017). Single-molecule techniques in biophysics: a review of the progress in methods and applications. *Reports on Progress in Physics*, 81(2):024601.

[Miller et al., 2018] Miller, H., Zhou, Z., Shepherd, J., Wollman, A. J. M., and Leake, M. C. (2018). Single-molecule techniques in biophysics: a review of the progress in methods and applications. *Reports on Progress in Physics. Physical Society (Great Britain)*, 81(2):024601.

[Mills et al., 2018] Mills, M., Tse-Dinh, Y.-C., and Neuman, K. C. (2018). Direct observation of topoisomerase ia gate dynamics. *Nature structural & molecular biology*, 25(12):1111–1118.

[Möckl et al., 2020] Möckl, L., Roy, A. R., Petrov, P. N., and Moerner, W. (2020). Accurate and rapid background estimation in single-molecule localization microscopy using the deep neural network bgnet. *Proceedings of the National Academy of Sciences*, 117(1):60–67.

[Moerner and Fromm, 2003] Moerner, W. and Fromm, D. P. (2003). Methods of single-molecule fluorescence spectroscopy and microscopy. *Review of Scientific instruments*, 74(8):3597–3619.

[Moffitt et al., 2009] Moffitt, J. R., Chemla, Y. R., Aathavan, K., Grimes, S., Jardine, P. J., Anderson, D. L., and Bustamante, C. (2009). Intersubunit coordination in a homomeric ring ATPase. *Nature*, 457(7228):446–450.

[Moffitt et al., 2006] Moffitt, J. R., Chemla, Y. R., Izhaky, D., and Bustamante, C. (2006). Differential detection of dual traps improves the spatial resolution of optical tweezers. *Proceedings of the National Academy of Sciences*, 103(24):9006–9011. Publisher: National Acad Sciences.

[Moreira et al., 2015] Moreira, B. G., You, Y., and Owczarzy, R. (2015). Cy3 and Cy5 dyes attached to oligonucleotide terminus stabilize DNA duplexes: predictive thermodynamic model. *Biophysical chemistry*, 198:36–44.

[Morin et al., 2018] Morin, T. J., McKenna, W. L., Shropshire, T. D., Wride, D. A., Deschamps, J. D., Liu, X., Stamm, R., Wang, H., and Dunbar, W. B. (2018). A handheld platform for target protein detection and quantification using disposable nanopore strips. *Scientific reports*, 8(1):1–12.

[Mosconi et al., 2011a] Mosconi, F., Allemand, J. F., and Croquette, V. (2011a). Soft magnetic tweezers: a proof of principle. *Review of scientific instruments*, 82(3):034302.

[Mosconi et al., 2011b] Mosconi, F., Allemand, J. F., and Croquette, V. (2011b). Soft magnetic tweezers: a proof of principle. *Review of scientific instruments*, 82(3):034302. Publisher: American Institute of Physics.

[Neuman and Nagy, 2008] Neuman, K. C. and Nagy, A. (2008). Single-molecule force spectroscopy: optical tweezers, magnetic tweezers and atomic force microscopy. *Nature Methods*, 5(6):491–505.

[Noller, 1991] Noller, H. F. (1991). Ribosomal RNA and translation. *Annual review of biochemistry*, 60(1):191–227.

[Nuttall, 1981] Nuttall, A. (1981). Some windows with very good sidelobe behavior. *IEEE Transactions on Acoustics, Speech, and Signal Processing*, 29(1):84–91. Conference Name: IEEE Transactions on Acoustics, Speech, and Signal Processing.

[O'Neill and Stewartson, 1967] O'Neill, M. and Stewartson, K. (1967). On the slow motion of a sphere parallel to a nearby plane wall. *Journal of Fluid Mechanics*, 27(4):705–724.

[O'Neill, 1964] O'Neill, M. E. (1964). A Slow motion of viscous liquid caused by a slowly moving solid sphere. *Mathematika*, 11(1):67–74. Publisher: London Mathematical Society.

[Opfer and Gottschalk, 2012] Opfer, J. and Gottschalk, K.-E. (2012). Identifying discrete states of a biological system using a novel step detection algorithm. *PLoS One*, 7(11). Publisher: Public Library of Science.

[Ortega Arroyo et al., 2014] Ortega Arroyo, J., Andrecka, J., Spillane, K., Billington, N., Takagi, Y., Sellers, J., and Kukura, P. (2014). Label-free, all-optical detection, imaging, and tracking of a single protein. *Nano letters*, 14(4):2065–2070.

[Ortega-Arroyo and Kukura, 2012] Ortega-Arroyo, J. and Kukura, P. (2012). Interferometric scattering microscopy (iSCAT): new frontiers in ultrafast and ultrasensitive optical microscopy. *Physical Chemistry Chemical Physics*, 14(45):15625–15636.

[Ostrofet et al., 2018] Ostrofet, E., Papini, F. S., and Dulin, D. (2018). Correction-free force calibration for magnetic tweezers experiments. *Scientific reports*, 8(1):1–10.

[Oukhaled et al., 2007] Oukhaled, G., Mathe, J., Biance, A.-L., Bacri, L., Betton, J.-M., Lairez, D., Pelta, J., and Auvray, L. (2007). Unfolding of proteins and long transient conformations detected by single nanopore recording. *Physical review letters*, 98(15):158101.

[Pabo and Sauer, 1992] Pabo, C. O. and Sauer, R. T. (1992). Transcription factors: structural families and principles of DNA recognition. *Annual review of biochemistry*, 61(1):1053–1095.

[Paul et al.,] Paul, T., Voter, A. F., Cueny, R. R., Gavrilov, M., Ha, T., Keck, J. L., and Myong, S. E. coli Rep helicase and RecA recombinase unwind G4 DNA and are important for resistance to g4-stabilizing ligands. *Nucleic Acids Research*.

[Pavani et al., 2009] Pavani, S. R. P., Thompson, M. A., Biteen, J. S., Lord, S. J., Liu, N., Twieg, R. J., Piestun, R., and Moerner, W. E. (2009). Three-dimensional, single-molecule fluorescence imaging beyond the diffraction limit by using a double-helix point spread function. *Proceedings of the National Academy of Sciences of the United States of America*, 106(9):2995–2999.

[Pedaci et al., 2011] Pedaci, F., Huang, Z., Van Oene, M., Barland, S., and Dekker, N. H. (2011). Excitable particles in an optical torque wrench. *Nature Physics*, 7(3):259–264.

[Pedaci et al., 2012] Pedaci, F., Huang, Z., van Oene, M., and Dekker, N. H. (2012). Calibration of the optical torque wrench. *Optics express*, 20(4):3787–3802.

[Pedley and Kessler, 1992] Pedley, T. J. and Kessler, J. O. (1992). Hydrodynamic Phenomena In Suspensions Of Swimming Microorganisms. *Annual Review of Fluid Mechanics*, 24(1):313–358.

[Perkins and Jones, 1992] Perkins, G. S. and Jones, R. B. (1992). Hydrodynamic interaction of a spherical particle with a planar boundary: II. Hard wall. *Physica A: Statistical Mechanics and its Applications*, 189(3):447–477.

[Perkins, 2014] Perkins, T. T. (2014). Ångström-precision optical traps and applications.

[Poisson, 1837] Poisson, S. D. (1837). *Recherches sur la probabilité des jugements en matière criminelle et en matière civile*. Bachelier.

[Polin et al., 2009] Polin, M., Tuval, I., Drescher, K., Gollub, J. P., and Goldstein, R. E. (2009). Chlamydomonas Swims with Two "Gears" ina eukaryotic version of run-and-tumble locomotion. *Science*, 325(July):487.

[Potapov et al., 2018] Potapov, V., Ong, J. L., Kucera, R. B., Langhorst, B. W., Bilotti, K., Pryor, J. M., Cantor, E. J., Canton, B., Knight, T. F., Evans, T. C., and Lohman, G. J. S. (2018). Comprehensive Profiling of Four Base Overhang Ligation Fidelity by T4 DNA Ligase and Application to DNA Assembly. *ACS Synthetic Biology*, 7(11):2665–2674. Publisher: American Chemical Society.

[Qi et al., 2013] Qi, Z., Pugh, R. A., Spies, M., and Chemla, Y. R. (2013). Sequence-dependent base pair stepping dynamics in XPD helicase unwinding. *eLife*, 2:e00334.

[Rao, 1992] Rao, C. R. (1992). Information and the accuracy attainable in the estimation of statistical parameters. In *Breakthroughs in statistics*, pages 235–247. Springer.

[Rayleigh, 1899] Rayleigh, L. (1899). Xxxiv. on the transmission of light through an atmosphere containing small particles in suspension, and on the origin of the blue of the sky. *The London, Edinburgh, and Dublin Philosophical Magazine and Journal of Science*, 47(287):375–384.

[Ribeck and Saleh, 2008] Ribeck, N. and Saleh, O. A. (2008). Multiplexed single-molecule measurements with magnetic tweezers. *Review of Scientific Instruments*, 79(9):094301.

[Rief et al., 1997] Rief, M., Oesterhelt, F., Heymann, B., and Gaub, H. E. (1997). Single molecule force spectroscopy on polysaccharides by atomic force microscopy. *Science*, 275(5304):1295–1297.

[Righini et al., 2018] Righini, M., Lee, A., Cañari-Chumpitaz, C., Lionberger, T., Gabizon, R., Coello, Y., Tinoco, I., and Bustamante, C. (2018). Full molecular trajectories of RNA polymerase at single base-pair resolution. *Proceedings of the National Academy of Sciences*, 115(6):1286–1291. Publisher: National Academy of Sciences Section: Biological Sciences.

[Rodriguez-Larrea and Bayley, 2013] Rodriguez-Larrea, D. and Bayley, H. (2013). Multistep protein unfolding during nanopore translocation. *Nature nanotechnology*, 8(4):288–295.

[Rotem et al., 2012] Rotem, D., Jayasinghe, L., Salichou, M., and Bayley, H. (2012). Protein detection by nanopores equipped with aptamers. *Journal of the American Chemical Society*, 134(5):2781–2787.

[Roy et al., 2008] Roy, R., Hohng, S., and Ha, T. (2008). A practical guide to single-molecule fret. *Nature methods*, 5(6):507–516.

[Rust et al., 2006] Rust, M. J., Bates, M., and Zhuang, X. (2006). Sub-diffraction-limit imaging by stochastic optical reconstruction microscopy (storm). *Nature methods*, 3(10):793–796.

[Sancataldo et al., 2017] Sancataldo, G., Scipioni, L., Ravasenga, T., Lanzanò, L., Diaspro, A., Barberis, A., and Duocastella, M. (2017). Three-dimensional multiple-particle tracking with nanometric precision over tunable axial ranges. *Optica*, 4(3):367–373. Publisher: Optical Society of America.

[SantaLucia Jr and Hicks, 2004] SantaLucia Jr, J. and Hicks, D. (2004). The thermodynamics of DNA structural motifs. *Annu. Rev. Biophys. Biomol. Struct.*, 33:415–440.

[Santoso et al., 2010] Santoso, Y., Joyce, C. M., Potapova, O., Le Reste, L., Hohlbein, J., Torella, J. P., Grindley, N. D., and Kapanidis, A. N. (2010). Conformational transitions in DNA polymerase i revealed by single-molecule fret. *Proceedings of the National Academy of Sciences*, 107(2):715–720.

[Schildkraut and Lifson, 1965] Schildkraut, C. and Lifson, S. (1965). Dependence of the melting temperature of DNA on salt concentration. *Biopolymers: Original Research on Biomolecules*, 3(2):195–208.

[Schottky, 1918] Schottky, W. (1918). Über spontane stromschwankungen in verschiedenen elektrizitätsleitern. *Annalen der physik*, 362(23):541–567.

[Schreiber, 2017] Schreiber, J. (2017). Pomegranate: fast and flexible probabilistic modeling in python. *The Journal of Machine Learning Research*, 18(1):5992–5997. Publisher: JMLR. org.

[Schuler and Eaton, 2008] Schuler, B. and Eaton, W. A. (2008). Protein folding studied by single-molecule FRET. *Current opinion in structural biology*, 18(1):16–26. Publisher: Elsevier.

[Seol et al., 2007] Seol, Y., Li, J., Nelson, P. C., Perkins, T. T., and Betterton, M. D. (2007). Elasticity of Short DNA Molecules: Theory and Experiment for Contour Lengths of 0.6–7μm. *Biophysical Journal*, 93(12):4360–4373.

[Seol and Neuman, 2011] Seol, Y. and Neuman, K. C. (2011). Single-molecule measurements of topoisomerase activity with magnetic tweezers. In *Single molecule enzymology*, pages 229–241. Springer.

[Sharonov and Hochstrasser, 2006] Sharonov, A. and Hochstrasser, R. M. (2006). Wide-field subdiffraction imaging by accumulated binding of diffusing probes. *Proceedings of the National Academy of Sciences*, 103(50):18911–18916.

[Shechtman et al., 2014] Shechtman, Y., Sahl, S. J., Backer, A. S., and Moerner, W. E. (2014). Optimal point spread function design for 3D imaging. *Physical Review Letters*, 113(13):133902.

[Shon et al., 2019] Shon, M. J., Rah, S.-H., and Yoon, T.-Y. (2019). Submicrometer elasticity of double-stranded DNA revealed by precision force-extension measurements with magnetic tweezers. *Science Advances*, 5(6):eaav1697. Publisher: American Association for the Advancement of Science Section: Research Article.

[Short and Mandel, 1983] Short, R. and Mandel, L. (1983). Observation of sub-poissonian photon statistics. *Physical review letters*, 51(5):384.

[Siddhanta and Narayana, 2012] Siddhanta, S. and Narayana, C. (2012). Surface Enhanced Raman Spectroscopy of Proteins: Implications for Drug Designing. *Nanomaterials and Nanotechnology*, 2:1. Publisher: SAGE Publications Ltd STM.

[Singh et al., 2016] Singh, D., Sternberg, S. H., Fei, J., Doudna, J. A., and Ha, T. (2016). Real-time observation of DNA recognition and rejection by the RNA-guided endonuclease cas9. *Nature communications*, 7(1):1–8.

[Singh et al., 2018] Singh, D., Wang, Y., Mallon, J., Yang, O., Fei, J., Poddar, A., Ceylan, D., Bailey, S., and Ha, T. (2018). Mechanisms of improved specificity of engineered cas9s revealed by single-molecule fret analysis. *Nature structural & molecular biology*, 25(4):347–354.

[Singh and Rao, 2011] Singh, S. and Rao, C. N. R. (2011). Deuterium isotope effects on hydrogen bonding. *Canadian Journal of Chemistry*. Publisher: NRC Research Press Ottawa, Canada.

[Smith et al., 1992] Smith, S. B., Finzi, L., and Bustamante, C. (1992). Direct mechanical measurements of the elasticity of single DNA molecules by using magnetic beads. *Science*, 258(5085):1122–1126.

[Spies, 2012] Spies, M. (2012). *DNA helicases and DNA motor proteins*, volume 767. Springer Science & Business Media.

[Spies, 2014] Spies, M. (2014). Two steps forward, one step back: determining XPD helicase mechanism by single-molecule fluorescence and high-resolution optical tweezers. *DNA repair*, 20:58–70.

[Spindler et al., 2016] Spindler, S., Ehrig, J., König, K., Nowak, T., Piliarik, M., Stein, H. E., Taylor, R. W., Garanger, E., Lecommandoux, S., Alves, I. D., et al. (2016). Visualization of lipids and proteins at high spatial and temporal resolution via interferometric scattering (iSCAT) microscopy. *Journal of Physics D: Applied Physics*, 49(27):274002.

[Stanley et al., 2006] Stanley, L. K., Seidel, R., Van Der Scheer, C., Dekker, N. H., Szczelkun, M. D., and Dekker, C. (2006). When a helicase is not a helicase: dsDNA tracking by the motor protein ecor124i. *The EMBO Journal*, 25(10):2230–2239.

[Strick et al., 1996] Strick, T. R., Allemand, J.-F., Bensimon, D., Bensimon, A., and Croquette, V. (1996). The elasticity of a single supercoiled DNA molecule. *Science*, 271(5257):1835–1837.

[Strick et al., 2000] Strick, T. R., Croquette, V., and Bensimon, D. (2000). Single-molecule analysis of DNA uncoiling by a type ii topoisomerase. *Nature*, 404(6780):901–904.

[Sudhakar et al., 2020] Sudhakar, S., Abdosamadi, M. K., Jachowski, T. J., Bugiel, M., Jannasch, A., and Schäffer, E. (2020). Germanium nanospheres for ultraresolution picotensiometry of kinesin motors. *bioRxiv*. Publisher: Cold Spring Harbor Laboratory _eprint: https://www.biorxiv.org/content/early/2020/06/20/2020.06.18.159640.full.pdf.

[Sullan et al., 2013] Sullan, R. M. A., Churnside, A. B., Nguyen, D. M., Bull, M. S., and Perkins, T. T. (2013). Atomic force microscopy with sub-piconewton force stability for biological applications. *Methods*, 60(2):131–141.

[Sumlin et al., 2018] Sumlin, B. J., Heinson, W. R., and Chakrabarty, R. K. (2018). Retrieving the aerosol complex refractive index using PyMieScatt: A Mie computational package with visualization capabilities. *Journal of Quantitative Spectroscopy and Radiative Transfer*, 205:127–134. Publisher: Elsevier.

[Sun et al., 2009] Sun, Y., McKenna, J. D., Murray, J. M., Ostap, E. M., and Goldman, Y. E. (2009). Parallax: high accuracy three-dimensional single molecule tracking using split images. *Nano Letters*, 9(7):2676–2682.

[Sun et al., 2010] Sun, Y., Sato, O., Ruhnow, F., Arsenault, M. E., Ikebe, M., and Goldman, Y. E. (2010). Single-molecule stepping and structural dynamics of myosin X. *Nature Structural & Molecular Biology*, 17(4):485–491.

[Svoboda and Block, 1994] Svoboda, K. and Block, S. M. (1994). Force and velocity measured for single kinesin molecules. *Cell*, 77(5):773–784.

[Tapster et al., 1987] Tapster, P., Rarity, J., and Satchell, J. (1987). Generation of sub-poissonian light by high-efficiency light-emitting diodes. *EPL (Europhysics Letters)*, 4(3):293.

[Taute et al., 2015] Taute, K. M., Gude, S., Tans, S. J., and Shimizu, T. S. (2015). High-throughput 3D tracking of bacteria on a standard phase contrast microscope. *Nature Communications*, 6(1):1–9.

[Taylor and Sandoghdar, 2019] Taylor, R. W. and Sandoghdar, V. (2019). Interferometric scattering microscopy: seeing single nanoparticles and molecules via rayleigh scattering. *Nano letters*, 19(8):4827–4835.

[Thompson et al., 2002] Thompson, R. E., Larson, D. R., and Webb, W. W. (2002). Precise nanometer localization analysis for individual fluorescent probes. *Biophysical Journal*, 82(5):2775–2783.

[Veneziano et al., 2018] Veneziano, R., Shepherd, T. R., Ratanalert, S., Bellou, L., Tao, C., and Bathe, M. (2018). In vitro synthesis of gene-length single-stranded DNA. *Scientific Reports*, 8(1):6548. Number: 1 Publisher: Nature Publishing Group.

[Vilfan et al., 2008] Vilfan, I. D., Candelli, A., Hage, S., Aalto, A. P., Poranen, M. M., Bamford, D. H., and Dekker, N. H. (2008). Reinitiated viral RNA-dependent RNA polymerase resumes replication at a reduced rate. *Nucleic acids research*, 36(22):7059–7067.

[Virtanen et al., 2020] Virtanen, P., Gommers, R., Oliphant, T. E., Haberland, M., Reddy, T., Cournapeau, D., Burovski, E., Peterson, P., Weckesser, W., Bright, J., van der Walt, S. J., Brett, M., Wilson, J., Jarrod Millman, K., Mayorov, N., Nelson, A. R. J., Jones, E., Kern, R., Larson, E., Carey, C., Polat, I., Feng, Y., Moore, E. W., Vand erPlas, J., Laxalde, D., Perktold, J., Cimrman, R., Henriksen, I., Quintero, E. A., Harris, C. R., Archibald, A. M., Ribeiro, A. H., Pedregosa, F., van Mulbregt, P., and Contributors, S. . . (2020). SciPy 1.0: Fundamental Algorithms for Scientific Computing in Python. *Nature Methods*, 17:261–272.

[von Ahsen et al., 2001] von Ahsen, N., Wittwer, C. T., and Schutz, E. (2001). Oligonucleotide melting temperatures under PCR conditions: nearest-neighbor corrections for Mg2+, deoxynucleotide triphosphate, and dimethyl sulfoxide concentrations with comparison to alternative empirical formulas. *Clinical Chemistry*, 47(11):1956–1961.

[von Diezmann et al., 2017] von Diezmann, A., Shechtman, Y., and Moerner, W. E. (2017). Three-Dimensional Localization of Single Molecules for Super-Resolution Imaging and Single-Particle Tracking. *Chemical reviews*, 117(11):7244–7275.

[Wallace et al., 2010] Wallace, E. V., Stoddart, D., Heron, A. J., Mikhailova, E., Maglia, G., Donohoe, T. J., and Bayley, H. (2010). Identification of epigenetic DNA modifications with a protein nanopore. *Chemical communications*, 46(43):8195–8197.

[Wang et al., 1998] Wang, M. D., Schnitzer, M. J., Yin, H., Landick, R., Gelles, J., and Block, S. M. (1998). Force and velocity measured for single molecules of RNA polymerase. *Science*, 282(5390):902–907.

[Wang et al., 1997] Wang, M. D., Yin, H., Landick, R., Gelles, J., and Block, S. M. (1997). Stretching DNA with optical tweezers. *Biophysical journal*, 72(3):1335.

[Wang et al., 2020] Wang, Z., Maluenda, J., Giraut, L., Vieille, T., Lefevre, A., Salthouse, D., Radou, G., Moulinas, R., Astete-Morales, S., Smith, G., et al. (2020). Detecting genetic variation and base modifications together in the same single molecules of DNA and RNA at base pair resolution using a magnetic tweezer platform. *bioRxiv*.

[Whitley et al., 2017] Whitley, K. D., Comstock, M. J., and Chemla, Y. R. (2017). Elasticity of the transition state for oligonucleotide hybridization. *Nucleic acids research*, 45(2):547–555. Publisher: Oxford University Press.

[Whitley et al., 2016] Whitley, K. D., Comstock, M. J., Jia, H., Lohman, T. M., and Chemla, Y. R. (2016). Direct Observation of the Stepping Behavior of E. Coli UvrD Helicase. *Biophysical Journal*, 110(3):561a.

[Wooddell and Burgess, 1996] Wooddell, C. I. and Burgess, R. R. (1996). Use of asymmetric PCR to generate long primers and single-stranded DNA for incorporating cross-linking analogs into specific sites in a DNA probe. *Genome research*, 6(9):886–892.

[Woodside et al., 2006a] Woodside, M. T., Anthony, P. C., Behnke-Parks, W. M., Larizadeh, K., Herschlag, D., and Block, S. M. (2006a). Direct measurement of the full, sequence-dependent folding landscape of a nucleic acid. *Science*, 314(5801):1001–1004.

[Woodside et al., 2006b] Woodside, M. T., Behnke-Parks, W. M., Larizadeh, K., Travers, K., Herschlag, D., and Block, S. M. (2006b). Nanomechanical measurements of the sequence-dependent folding landscapes of single nucleic acid hairpins. *Proceedings of the National Academy of Sciences*, 103(16):6190–6195.

[Wu and Hickson, 2006] Wu, L. and Hickson, I. D. (2006). DNA helicases required for homologous recombination and repair of damaged replication forks. *Annu. Rev. Genet.*, 40:279–306.

[Yakovchuk et al., 2006] Yakovchuk, P., Protozanova, E., and Frank-Kamenetskii, M. D. (2006). Base-stacking and base-pairing contributions into thermal stability of the DNA double helix. *Nucleic acids research*, 34(2):564–574. Publisher: Oxford University Press.

[Yasuda et al., 1998] Yasuda, R., Noji, H., Kinosita Jr, K., and Yoshida, M. (1998). F1-ATPase is a highly efficient molecular motor that rotates with discrete 120 steps. *Cell*, 93(7):1117–1124.

[Ybert et al., 2007] Ybert, C., Barentin, C., Cottin-Bizonne, C., Joseph, P., and Bocquet, L. (2007). Achieving large slip with superhydrophobic surfaces: Scaling laws for generic geometries. *Physics of fluids*, 19(12):123601.

[Yin et al., 1995] Yin, H., Wang, M. D., Svoboda, K., Landick, R., Block, S. M., and Gelles, J. (1995). Transcription against an applied force. *Science*, 270(5242):1653–1657.

[Yoneyama and Fujita, 2009] Yoneyama, M. and Fujita, T. (2009). RNA recognition and signal transduction by rig-i-like receptors. *Immunological reviews*, 227(1):54–65.

[Zheng et al., 2015] Zheng, X., Bi, C., Li, Z., Podariu, M., and Hage, D. S. (2015). Analytical methods for kinetic studies of biological interactions: A review. *Journal of pharmaceutical and biomedical analysis*, 113:163–180.

[Zlatanova et al., 2000] Zlatanova, J., Lindsay, S. M., and Leuba, S. H. (2000). Single molecule force spectroscopy in biology using the atomic force microscope. *Progress in biophysics and molecular biology*, 74(1-2):37–61.

List of Figures

List of Tables